

University of Quebec  
Institut national de la recherche scientifique  
Centre Énergie, Matériaux et Télécommunications

# Oxide Perovskites for Solar Energy Conversion

by

Joyprokash Chakrabartty

Dissertation submitted for the partial fulfillment of the requirements of the degree,  
*Doctor of philosophy*, Ph.D.  
in science of energy and materials

## Jury d'évaluation

<b>Research supervisor</b>	Federico Rosei, Professor and Director, INRS-EMT.
<b>Research co-supervisor</b>	Riad Nechache, Principal Investigator, École de Technologie Supérieure (ETS), Montréal.
<b>Internal examiner and the president of the Jury</b>	Mohamed Chaker, Professor, INRS-EMT.
<b>External examiner</b>	Nazir P. Kherani, Professor, University of Toronto.
<b>External examiner</b>	Jerome Claverie, Professor, University of Sherbrooke.

## Abstract

Inorganic ABO<sub>3</sub> perovskite materials exhibit exotic physical and chemical properties due to their exceptional crystal structures and thus offer exciting opportunities for spintronics, computer memories, sensors, microwave and photovoltaic (PV) device applications. Since the discovery of bulk photovoltaic (BPV) effect in non-centrosymmetric crystals, the perovskite oxides including BaTiO<sub>3</sub> (BTO), LiNbO<sub>3</sub> (LNO), BiFeO<sub>3</sub> (BFO), BiMnO<sub>3</sub> (BMO), and Pb(Zr,Ti)O<sub>3</sub> (PZT) drew enormous interest in fundamental science research, as they exhibit either a suitable band gap or larger than band gap photovoltages (up to 1000 V) under homogeneous light illumination. However, owing to their insulating characteristics retain even at the dimensions down to nanometer scale, the charge carrier conduction in polar perovskites is extremely poor resulting in the generation of low photocurrent density, typically in the  $\mu\text{A}/\text{cm}^2$  range and below. Driven by the challenges of improving photocurrent density, in this project, we have investigated BMO and BFO compounds in view of their integration as active materials in PV devices in order to improve the photocurrent density and thus solar power conversion efficiency (PCE). BMO in thin film form possesses ferroelectric behavior i.e. a remnant polarization of  $\sim 6 \mu\text{C}/\text{cm}^2$  at room temperature and its low band gap value ( $\sim 1.2 \text{ eV}$ ) efficiently absorbs light wavelengths exceeding the visible wavelengths of the solar spectrum. In contrast, BFO thin films exhibit strong ferroelectricity with a remnant polarization of  $\sim 55 \mu\text{C}/\text{cm}^2$  and a band gap of  $\sim 2.7 \text{ eV}$  that corresponds to visible light of solar spectrum. Although the physical and chemical properties of various forms of BFO, from bulk to nanoparticles are widely investigated in solar cells, the potential of BMO alone or in combination with other perovskites is rarely investigated and reported so far in the field of solar energy conversion.

In the first part of this thesis, we demonstrate a bilayer-stacking scheme, more specifically a heterostructure based on BFO/BMO epitaxial bilayer thin films grown by pulsed laser deposition (PLD) onto Niobium doped (111)-oriented SrTiO<sub>3</sub> (STO) substrates. The BFO/BMO bilayers as photoactive materials in solid-state PV devices show remarkable PCEs up to 1.43% under 1 sun solar radiation (AM 1.5G), which is higher than those reported values for individual BFO or BMO thin films. The fill factor (FF) is determined to be 0.72 which is a remarkable value for ferroelectric perovskite-based devices. The bilayers exhibit prominent ferroelectric behavior ( $\sim 100 \mu\text{C}/\text{cm}^2$ ) compared to individual BFO or BMO films. To describe the PV responses, we use a traditional interfacial model where an interface generated electric field is significantly modulated by spontaneous polarization of the materials.

In the second part, we demonstrate a PV device based on Bi-Mn-O composite thin films which exhibits a PCE of 4.20%. The composite materials are made of two different types of crystal phases: BMO and BiMn<sub>2</sub>O<sub>5</sub>. The former is ferroelectric with a band gap of  $\sim 1.20$  eV as specified previously, while BiMn<sub>2</sub>O<sub>5</sub> is semiconducting with a band gap of  $\sim 1.23$  eV. The composite films are grown by PLD on (100) oriented Niobium doped STO single crystal substrates. The crystal structure of both phases in the composite films is characterized by transmission electron microscopy (TEM) and further confirmed by Raman spectroscopy (RS) analysis. Conductive atomic force microscopy (C-AFM) and Kelvin probe force microscopy (KPFM) under illumination show the increased photocurrent and photovoltage generations across BMO /BiMn<sub>2</sub>O<sub>5</sub> grain boundaries (GB) compared to the interior of the grains. The ferroelectricity of BMO does not play a significant role in the PV effect, as confirmed by combined Piezoresponse force microscopy (PFM) and KPFM measurements. The results are described in the framework of GB barrier potentials.

In the last part, we describe the photocatalytic properties of BMO thin films and nanostructures, both grown epitaxially on (111) oriented Niobium doped STO substrates by PLD. The nanostructures were achieved using nanostencils i.e. shadow masks with a periodic array of nanometer-scale circular features. Photoelectrochemical properties of films and nanostructures as working electrodes are investigated by linear sweep voltammetry (LSV) measurements under chopped illumination. The nanostructures exhibit photocurrent density of  $\sim 0.9 \text{ mA/cm}^2$  at 0.8 V vs Ag/AgCl (1.38 V vs reverse hydrogen electrode (RHE)) which is substantially higher than the values recorded in thin films,  $\sim 10 \text{ }\mu\text{A/cm}^2$  at 0.4 V vs Ag/AgCl (0.98 V vs RHE) under 1 Sun radiation. Band alignments with respect to the redox potential of water and gas chromatograph measurements demonstrate that the BMO photoelectrodes (both films and nanostructures) are suitable for oxygen evolution reactions.

## **Acknowledgement**

I am truly fortunate to spend around four years at Institut national de la recherche scientifique (INRS), University of Quebec, Canada, that provided me the great opportunity to accomplish my PhD studies in a friendly environment. I would like to express my sincere gratitude to Professor Federico Rosei, my supervisor, for his generous supports throughout my PhD studies. I would like to give thanks to Dr. Riad Nechache, my co-supervisor, for his supervision. I am also grateful to Dr. Catalin Harnagea for his scientific comments on some parts of my works and for his comments on my dissertation. I am indebted to some of my colleagues (officemates) including Mr. Cui Daling, Mr. Nathanael Komba, and Mr. Ali Almesrati, from whom I got unconditional supports during the frustrating period of my studies. I am also grateful to all group members, lab technicians, administrative staffs, and all professors of EMT-INRS for their direct and indirect supports.

Last, but not the least, I thank my family members who gave me true love and unwavering support during these four years. Therefore, I am honored to dedicate my dissertation to my family members.

# Table of Contents

<b>Abstract.....</b>	<b>01</b>
<b>Acknowledgement.....</b>	<b>04</b>
<b>List of Figures.....</b>	<b>10</b>
<b>List of Tables.....</b>	<b>19</b>
<b>Introduction.....</b>	<b>20</b>
<b>Chapter 1 Background Literature Review .....</b>	<b>26</b>
1.1 Oxide perovskites.....	26
1.2 Ferroelectricity.....	27
1.3 Magnetism.....	30
1.4 Multiferroic materials: coexistence of ferroelectricity and magnetism .....	31
1.4.1 Lone pair induced ferroelectric polarization in multiferroic perovskites.....	35
1.4.2 Magnetic order in multiferroic oxide perovskites .....	36
1.5 Multiferroic BiMnO <sub>3</sub> .....	37
1.5.1 Synthesis and crystal structures.....	37
1.5.2 Ferroelectric and magnetic properties .....	38
1.6 Multiferroic BiFeO <sub>3</sub> .....	40
1.6.1 Synthesis and crystal structures.....	41
1.6.2 Ferroelectric and magnetic properties .....	43
1.7 Photovoltaic effect for solar energy conversion .....	45
1.7.1 Basics and advances of p-n junction solar cells .....	45
1.7.2 Photovoltaic effect in ferroelectric perovskite materials.....	50
1.7.3 Advances of ferroelectric materials in photovoltaic devices .....	56

1.8	Photocatalytic properties of materials for water splitting applications.....	58
1.8.1	Basics and advances of photocatalytic process in water splitting.....	59
1.8.2	Advances of oxide perovskites as photoelectrodes in water splitting.....	63
1.9	Objectives of the thesis .....	66
1.10	Structure of the thesis.....	68
<b>Chapter 2 Experimental Methods .....</b>		<b>70</b>
2.1	Growth of thin films.....	70
	Pulse laser deposition.....	70
2.2	Characterization methods.....	72
2.2.1	X-ray diffraction.....	72
2.2.2	Scanning electron microscope.....	73
2.2.3	Transmission electron microscopy.....	74
2.2.4	Atomic force microscopy and Piezoresponse force microscopy .....	75
2.2.5	Conductive atomic force microscopy.....	76
2.2.6	Kelvin probe force microscopy .....	77
2.2.7	Macroscopic ferroelectric hysteresis loop measurement .....	78
2.2.8	Ultraviolet photoemission spectroscopy .....	78
2.2.9	Ellipsometry .....	78
2.2.10	Photoluminescence spectroscopy.....	79
2.2.11	Solar simulator .....	80
2.2.12	External quantum efficiency measurement.....	80
<b>Chapter 3 Enhanced Photovoltaic Properties in Bilayer BiFeO<sub>3</sub>/Bi-Mn-O Thin Films... 81</b>		<b>81</b>
3.1	Introduction.....	81

3.2	Experimental methods .....	82
3.2.1	Thin film growth .....	82
3.2.2	Current-voltage measurements.....	83
3.3	Characterizations.....	83
3.3.1	Crystal structures.....	83
3.3.2	Surface roughness and interfaces .....	85
3.3.3	Ferroelectric properties .....	86
3.3.4	Optical properties .....	89
3.3.5	Photovoltaic properties: measurement of current density-voltage (J-V) curves .....	89
3.3.6	Band edge energy: ultraviolet photoemission spectroscopy (UPS) measurement.....	92
3.4	Discussion .....	94
3.5	Conclusions and perspectives .....	101
<b>Chapter 4 Mixed Crystal Phases in Oxide Perovskite Thin Films for Improved Photovoltaic Performance .....</b>		<b>102</b>
4.1	Introduction.....	102
4.2	Experimental methods .....	104
4.2.1	Synthesis of thin films and device fabrication .....	104
4.3	Characterizations.....	105
4.3.1	Crystal structures.....	105
4.3.2	Ferroelectric properties .....	110
4.3.3	Surface charge measurements with and without illumination .....	114
4.3.4	Photovoltaic properties: measurement of current density-voltage (J-V) curves .....	116
4.3.5	External quantum efficiency (EQE) measurement.....	119

4.3.6	Ellipsometry measurements .....	120
4.3.7	Photovoltaic effect by scanning probe microscopy (SPM) measurements .....	121
4.4	Discussion .....	129
4.5	Conclusions and perspectives .....	133
<b>Chapter 5 Photoelectrochemical Properties of BiMnO<sub>3</sub> Thin Films and Nanostructures.....</b>		<b>135</b>
5.1	Introduction.....	135
5.2	Experimental methods .....	136
5.2.1	Thin film growth .....	136
5.2.2	Nanostructure growth.....	137
5.2.3	Sample preparation for PEC experiments .....	138
5.3	Characterizations.....	139
5.3.1	Crystal structures.....	139
5.3.2	Average heights of nanostructures .....	142
5.3.3	PEC cell performance.....	143
5.3.4	Calculation of total surface area of the BMO nanostructures .....	145
5.3.5	Photocurrent density as a function of time.....	147
5.3.6	Incident photon to current efficiency measurements .....	148
5.3.7	Optical transmittance spectra analysis .....	150
5.3.8	Mott–Schottky analysis .....	152
5.4	Discussion .....	154
5.5	Conclusions and perspectives .....	158
<b>Chapter 6 Conclusions and Perspectives .....</b>		<b>160</b>

6.1	Conclusions.....	160
6.2	Perspectives.....	162
	<b>References .....</b>	<b>164</b>
	<b>Appendix A: List of Acronyms.....</b>	<b>192</b>
	<b>Appendix B: Résumé (in French).....</b>	<b>195</b>

## List of Figures

Figure 1-1 Schematic diagram of two typical views of cubic $ABO_3$ perovskite unit cells with the origin centered at the B-site cation (a) and at the A-site cation (b) respectively .....	26
Figure 1-2 Atomic structures of BTO exhibiting paraelectric and FE phase. FE phase shows upward ( $P_{up}$ ) and downward ( $P_{down}$ ) polarization vector, respectively .....	28
Figure 1-3 Schematic of a ferroelectric (a) and a magnetic (b) hysteresis loop showing the coercive field, spontaneous and remnant polarization or magnetization. Associated current loops during FE hysteresis measurement indicated by red in (a). .....	30
Figure 1-4 Schematics of different types of magnetic properties exhibiting orientation of electron's spin (a) paramagnetism (b) ferromagnetism (c) antiferromagnetism, (d) ferrimagnetism and (e) canted antiferromagnetic where the magnetic components in different directions are represented by solid lines. ....	31
Figure 1-5 MF materials combine magnetic and ferroelectric properties.....	32
Figure 1-6 Comparison of maximum polarization values among several single-phase multiferroic materials .....	35
Figure 1-7 (a) Schematic representation of the mechanism of breaking inversion symmetry in $ABO_3$ perovskite structures (b) Lone-pair $2s^2$ in the ammonia molecule .....	36
Figure 1-8 The monoclinic unit cell of BMO .....	38
Figure 1-9 FE hysteresis loops of the Pt/SrTiO <sub>3</sub> /BiMnO <sub>3</sub> /SrTiO <sub>3</sub> /Pt and Pt/SrTiO <sub>3</sub> /BiMnO <sub>3</sub> /SrTiO <sub>3</sub> /Pt capacitors .....	40
Figure 1-10 Atomic structure of BFO. (a)Two pseudocubic cells with cation shifts and octahedra rotations along $[1\ 1\ 1]_{pc}$ direction are joined to form (b) the rhombohedral unit cell. A site $Bi^{3+}$ and B site $Fe^{3+}$ cations are displaced towards $[111]_{pc}$ directions.....	42

Figure 1-11 Strain engineering in BFO thin films exhibits various crystal structures .	43
Figure 1-12 FE hysteresis loop of 400 nm thick monodomain BFO thin films with Pt top and SrRuO <sub>3</sub> bottom electrodes. The blue curve represents the polarization fatigue after 10 <sup>6</sup> switching cycles	44
Figure 1-13 Schematic of a p-n junction with band alignments (a,b). Current density vs voltage (J-V) curve under dark and illumination (c).	47
Figure 1-14 Best efficiencies of different solar cells	49
Figure 1-15 Schematic representation of developing J <sub>SC</sub> and V <sub>OC</sub> .	52
Figure 1-16 (a) Schematic of the electrical measurements of a poled ceramic sample under illumination (b) schematic of the series summation of developed photovoltage across the individual grain. Potential across the sample under dark (c) and illumination (d).	53
Figure 1-17 (a) The interfacial effect on the photovoltage in FE materials showing the depolarizing field (E <sub>dp</sub> ) (b,c,d) Diagram of a metal-film-metal electrode having symmetric and asymmetric Schottky contacts, indicating the effect of interface electric field E <sub>i</sub>	54
Figure 1-18 Schematic of DWs (a) and associated band structure in dark condition (b). Schematic of band structure upon illumination (c) and accumulation of photoexcited charges at single DW (d).	55
Figure 1-19 Best cell efficiencies in oxide perovskite solar cells (green curve).	58
Figure 1-20 Schematics of PEC cell exhibiting energy band alignment in water splitting using (a) a photoanode, (b) photocathode, and (c) both photoanode and photocathode in the tandem configuration.	59
Figure 1-21 Alignment of energy band positions of prominent semiconductors in contact with aqueous electrolyte at pH 1. NHE means normalized hydrogen electrode.	60

Figure 1-22 Theoretical photocurrent densities estimated for few semiconductors under one-sun illumination.....	63
Figure 1-23 (a) Photocurrent density of BFO/SRO/STO(001) with BFO thickness of 223 nm under 121 mW/cm <sup>2</sup> (dark, red) and 250 mW/cm <sup>2</sup> (blue, green) illumination. The inset shows the magnified portion of the onset of photocurrent density (b) impact of ferroelectric polarization. Black and red curves show negative and positive polarization charges on the surface, respectively. ....	65
Figure 1-24 Photocurrent densities of epitaxial BFCO/CRO/STO heterostructure without (a) and with ferroelectric poling (b,c) under chopped simulated sunlight illumination (AM1.5G). Schematic illustrations are shown on the right of each figure. ....	66
Figure 2-1 Schematic diagram of basic pulse laser deposition (PLD) system. ....	71
Figure 2-2 Schematic of diffraction of X-rays by the periodic arrangement of planes of atoms. ....	73
Figure 2-3 Experimental setups for a typical PFM measurement. ....	76
Figure 3-1 (a) XRD $\theta$ -2 $\theta$ scans of bear NSTO substrates, the as-deposited BMO, BFO and BFO/BMO layer respectively. The respective films grown on (111) oriented NSTO substrate shows (1/2, 1/2, 1/2) reflections of BFO, BMO and small percentages of (101) <sub>t</sub> orientation of Mn <sub>3</sub> O <sub>4</sub> phases. The inset clearly shows (111) <sub>pc</sub> and (111) <sub>pc</sub> orientation of BMO and BFO phases. The symbol ‘*’ indicates tungsten contamination of the x-ray tube source (b) $\Phi$ scan measurements show three-fold symmetry of BMO, BFO and NSTO respectively, demonstrating the epitaxial nature of the films (c) RSM around NSTO (312) reflections shows the two spots related to the coexistence of BMO and BFO lattice. ....	84

Figure 3-2 AFM surface topography image of BMO (a) and BFO (b) respectively. The inset shows respective surface profile analysis of each. (c) Cross sectional TEM image taken at the resolution of 10 nm shows sharp interfaces at BFO/BMO interface. .... 86

Figure 3-3 Local scale (a,b) and microscopic (c,d) FE characterization of one of the samples measured on the top BFO surface. (a) Out of plane PFM image shows switching of polarization direction after subsequent poling the area encircled with +10V/-10V/+10V voltage pulses. (b) Corresponding in-field hysteresis loops of z-PFM signals. (c) Voltage vs polarization curve recorded on the heterostructure in two different frequencies. (d) Voltage vs polarization curve recorded on the top of BMO layer. The blue curve exhibits the corresponding current which represents the switching of polarization. .... 88

Figure 3-4 (a) Optical absorption spectra of the BFO/BMO film (b) Plots of  $(\alpha E)^2$  versus E for BMO, BFO/BMO and BFO films respectively which are used to extract the direct band gap of BMO and BFO. .... 89

Figure 3-5 (a) J-V characteristic curves of the heterostructure, with positive and negative poling demonstrating the PV effect. (b) The time vs  $J_{SC}$  shows stable photocurrent generation. Bottom left inset shows the geometry of the tested structure. Top right inset shows the dynamics of short circuit photocurrent recorded for 70 s under light on (off) conditions. The top left and bottom right inset shows good stability of photocurrent generation taken for 500 sec. .... 90

Figure 3-6 (a) J-V characteristic curves of ITO/BFO/NSTO heterostructure, with positive and negative poling demonstrating the FE PV effect (b) Time dynamics of voltage under dark and illumination. The inset of (b) shows the voltage stability for longer period of time (5 to 200 sec). .... 92

Figure 3-7 UPS spectra of BFO, BMO and Au (reference). The inset shows the magnification of low binding energy edge.....	94
Figure 3-8 (a) Energy band alignment of isolated ITO, BFO, BMO and doped STO films (b) Energy band alignment of the ideal ITO/BFO/BMO/Nb:STO interface at thermal equilibrium which also shows corresponding polarization effect with the direction of current flow.....	99
Figure 3-9 Mechanism of band modulation by polarization (a) upward and (b) downward polarization direction respectively.....	100
Figure 4-1 Schematic of device connections for electrical measurements.....	105
Figure 4-2 (a) XTEM image of a sample device (b) higher magnification of the selected area between 1 and 2 indicated in ‘a’ showing the interface between BMO and BiMn <sub>2</sub> O <sub>5</sub> . Both clearly indicate the formation of two different crystalline phases on the substrates (c) magnification of the selected area of ‘1’ in ‘a’ shows epitaxial growth of the BMO phase. The inset shows the result of respective Fast Fourier Transform (FFT) of the image (d) magnification of the selected area of ‘2’ in ‘a’ shows the growth of the BiMn <sub>2</sub> O <sub>5</sub> phase, with its respective FFT in the inset.....	107
Figure 4-3 (a) SAED of TEM recorded from another random area along the film-interfaces indicates the presence of another orientations of BiMn <sub>2</sub> O <sub>5</sub> crystal structure (b) reconstructed diffraction pattern of BiMn <sub>2</sub> O <sub>5</sub> at same beam orientation (B=[-130]) using lattice parameters obtained from the XRD database.....	109
Figure 4-4 (a) Room temperature Raman spectra of Bi-Mn-O films and of NSTO substrates (b) only film response obtained by subtracting the substrate response.....	110
Figure 4-5 Contact topography AFM image (a) simultaneously recorded with the OP-PFM image (b). Out of plane hysteresis loop (d) recorded from different grains, such that encircled in red in topography image (c). Current response as a function of applied DC voltage (e) recorded from the	

green encircled grain in the topography image (c). Hysteresis loops (g) recorded from the same grains (such that red encircled in topography image (c) with higher voltage demonstrating FE fatigue. Contact topography AFM image of the same grain (f) recorded after hysteresis loops showing changes in grain morphology. .... 112

Figure 4-6 (a) Macroscopic voltage vs polarization curve recorded on the BMO/NSTO heterostructure at two different frequencies. The curve demonstrates the FE character of the sample and (b) the corresponding voltage vs current loops confirms the switching of polarization. .... 114

Figure 4-7 (a) Schematics of electrical connection for PFM experiments (b,c) Simplified schematics of KPFM experimental setup conducted on virgin area and poled area (up/down) respectively. Surface potential measured by KPFM performed on the virgin sample: (d) and (f) Topography, (e and g) CPD image measured with (f, g) and without (d, e) illuminating the sample. (h) CPD profiles of line 1 indicated in e & g. The inset shows CPD profiles of line 2 indicated in e & g..... 115

Figure 4-8 (a) J-V curves recorded in best sample under illumination after switching with a bipolar voltage pulses (b)  $J_{SC}$ -V curve recorded under illumination for different orientations of polarization (c) Plot of  $J_{SC}$  as a function of time recorded on the samples poled by a bipolar voltage pulse. 118

Figure 4-9 (a) J-V curve recorded on BMO films. The inset shows the schematic of electrical connections (b) J-V curve recorded on  $BiMn_2O_5$  thin films. Both films were deposited on (100) oriented NSTO substrates. .... 119

Figure 4-10 EQE measurements on a single sample reveal highest efficiencies of ~ 42% under UV illumination. .... 120

Figure 4-11 (a) Optical absorption spectra of the films contained BMO- $BiMn_2O_5$ , BMO, and  $BiMn_2O_5$  phases respectively. Corresponding penetration depth spectra (b) and estimated band

gaps (c) of the films contained BMO-BiMn<sub>2</sub>O<sub>5</sub> (red), BMO (green), and BiMn<sub>2</sub>O<sub>5</sub> (blue) phases respectively. .... 121

Figure 4-12 Surface photocurrent measurements by C-AFM performed on as-grown samples (a) Topographic image (b) current image recorded while switching the illumination on/off at 0 V bias (c) current line profile across the image. Topographic image (d) and current image under illumination at 0 V bias (e) recorded in another area on the surface of the sample, (f) line profiles of topographic and corresponding current showing a high current at GBs. The same measurements performed while illuminating the sample surface at high intensity (g) Topographic image (h) short circuit current image (i) comparison of line profiles extracted from the short circuit current and topographic images. Higher resolution topography (j) and short circuit current (k) images under illumination, and (l) comparison of line profiles extracted from the short circuit current and topographic images. Scan sizes: (5x5)  $\mu\text{m}^2$  in a,b; (3x2)  $\mu\text{m}^2$  in d, e; (3x3)  $\mu\text{m}^2$  in g and h; and (0.54x0.54)  $\mu\text{m}^2$  in j and k. .... 123

Figure 4-13 Surface potential measured by KPFM performed on as-grown samples: (a) and (c) Topography, (b, and d) CPD image measured with (c, d) and without (a, b) illuminating the sample. (e, f) line profiles of the topography demonstrated as black curves extracted from (a) and (c) exhibit the same features, while the corresponding CPD profiles demonstrated as red curves clearly show a distinct photovoltage generation across grains and grain boundaries. (g) Comparison of CPD distributions over the surface of the films under dark and illumination conditions. .... 126

Figure 4-14 (a) Sequence of applied number of bipolar voltage pulses and corresponding recorded J-V curves (b) J-V curves recorded after applying different bipolar voltages pulses under dark. (c) Plot of resistance as a function of the number of applied pulses. .... 131

Figure 4-15 (a)  $J_{SC}$ -V curve recorded under illumination before and after poling (with 6 and 8 voltage pulses) respectively (b) Plot of the  $J_{SC}$  as a function of time recorded on the samples cycled 10 times. The inset shows associated  $V_{OC}$ . (c) Variation of PV parameters ( $J_{SC}$  and  $V_{OC}$ ) as a function of the number of pulses. .... 133

Figure 5-1 Schematic of a basic PEC cell set up. .... 139

Figure 5-2 (a) XRD  $\theta$ - $2\theta$  scans of BMO films deposited on (111) oriented NSTO substrates. The symbol ‘#’ indicates tungsten contamination of the x-ray tube sources. The inset shows SEM image of as-deposited BMO films (b)  $\Phi$  scan measurements show three-fold symmetry of BMO, demonstrating the epitaxial nature of the films (c) SEM image of BMO nanostructures grown on (111)<sub>c</sub> oriented NSTO using a stencil mask (d) XRD  $\theta$ - $2\theta$  scans exhibit (111)<sub>pc</sub> orientation of BMO nanostructures. .... 141

Figure 5-3 (a)  $10 \times 10 \mu\text{m}^2$  AFM image of the as-deposited nanostructures exhibiting the formation of a hexagonal nanoscale pattern on the NSTO substrate (b) Line profile of image (a) exhibits the average height of  $\sim 70$  nm of each nanostructure with  $5 \times 5 \mu\text{m}^2$  AFM imaging (c) the high resolution associated line profiles of the nanostructures (d) that further confirms the average height of each. The nanostructures’ height and size distributions are reported in (e) & (f) respectively. .... 142

Figure 5-4 (a) Variations of current density with applied voltage (vs Ag/AgCl) in 1 M  $\text{Na}_2\text{SO}_4$  at  $\text{p}^H$  6.8 under chopped 1 Sun and 2 Sun illumination of BMO films. The inset shows the response of the open circuit voltage under dark and at 1 sun illumination (b) Variations of current density with applied voltage (vs Ag/AgCl) in 1 M  $\text{Na}_2\text{SO}_4$  at  $\text{p}^H$  6.8 under chopped 1 Sun illumination of BMO nanostructures. The inset shows the response of the open circuit voltage under dark and under 1 Sun illumination..... 144

Figure 5-5 (a) AFM image of the as-deposited nanostructures exhibiting the formation of a hexagonal nanoscale pattern on the NSTO substrate (b) Low magnification SEM images of slots wherein the nanostructures are formed (c) high magnification SEM image covering the intersection of two neighboring slots. The red circle indicates a number of blocked pores that did not participate in forming nanostructures. The presence of the same blocked pores is indicated by a red circle in another slot (d). ..... 146

Figure 5-6 (a) Line profile image of nanostructures depicted in Fig.5-3c (b) magnifying image of one of the line profiles of nanostructures suggesting the triangular shapes of nanostructures... 147

Figure 5-7 Photocurrent density as the function of time observed in both BMO films (a) and nanostructures (b) under 1 sun (AM1.5G) while applying a constant potential of + 0.98 V and + 1.38 V vs RHE in 1M Na<sub>2</sub>SO<sub>4</sub> respectively..... 148

Figure 5-8 Plot of IPCE as a function of wavelength for BMO nanostructures (black) at 1.2 V vs Ag/AgCl and films (red) at 0.4 V vs Ag/AgCl respectively..... 150

Figure 5-9 (a) Optical transmittance spectra of STO with (black) and without (red) NS-BMO (b) calculated direct band gap of NS-BMO. The inset shows high magnification exhibiting a band gap of ~ 1.2 eV. .... 151

Figure 5-10 Mott–Schottky analysis ( $1/C^2$  versus applied potential, where  $C$  is the capacitance) of BMO thin films (a) and nanostructures (b) photoelectrodes. The intercept of the dashed line ( $1/C^2 = 0$ ) can be used to determine the  $V_{fb}$  of the BMO photoelectrodes..... 154

Figure 5-11 Calculated energy-level diagram based on Mott–Schottky results showing the energy levels of  $V_{fb}$ , valence band edge (VB), and conduction band edge (CB) of the respective BMO film (a) and nanostructures (b) photoelectrodes. .... 157

Figure 5-12 Amount of hydrogen and oxygen evolved by BMO nanostructures (a) and thin films (b) respectively recorded at 0.4 V vs Ag/AgCl under 1 sun illumination. Dot line (red and black) in both images shows the trend of respective gas generation in time. .... 158

## List of Tables

Table 3-1 Comparison of the PV properties of BFO, BMO and bilayer BFO/BMO films..... 91

Table 3-2 UPS data extracted to build the band diagram. .... 93

Table 4-1 Efficiencies calculated from different samples after switching with a bipolar voltage pulse. .... 116

## List of Journal Publications Based on This Thesis

- [1] Joyprokash Chakrabartty et al., Enhanced photovoltaic properties in bilayer BiFeO<sub>3</sub>/Bi-Mn-O thin films. Nanotechnology 2016, 27, 215402. (Chapter 3)
- [2] Joyprokash Chakrabartty et al., Improved photovoltaic performance from inorganic perovskite oxide thin films with mixed crystal phases. Nature Photonics 2018, 12, 271. (Chapter 4)
- [3] Joyprokash Chakrabartty et al., Photoelectrochemical properties of BiMnO<sub>3</sub> thin films and nanostructures. J. of Power Sources 2017, 365, 162. (Chapter 5)

# Introduction

With increasing population on our planet, the world energy consumption rate is also increasing, expected to be more than doubled (~27.6 TW) by 2050 and more than tripled (~43.0 TW) by 2100 with respect to the present energy consumption rate [1]. Currently around 86% of total energy of the earth is generated by the combustion of fossil fuels (oil, coal and natural gas) [2]. Since the traditional fossil fuel based energy generation has become a growing public concern due to environmental issues, an immense interest is booming towards clean and sustainable energy sources. Solar energy is regarded as one of the most reliable and abundant renewable energy sources to replace fossil fuels. This is because sunlight is “free”, abundant and widely distributed which is available to every country and person on the planet. The photovoltaic (PV) effect [3,4] is used to directly convert solar energy into electricity. However, the effective conversion of solar energy into electricity completely depends on the development of PV technologies. Current commercial PV markets are mainly dominated by silicon-based solar cells. Driven by technological advancements, a record performance of solar to electrical power conversion efficiency (PCE) of about 27% under 1 sun illumination (AM1.5G) has been achieved in single crystalline silicon solar cells [5]. However, the performances of this p-n junction based solar cells are still under their predicted potentials and limited by several practical disadvantages such as high materials cost compared with conventional fossil fuel-based energy generation and complex material processing steps. The quest for new materials alongside the developments and optimizations of existing materials are required for next-generation PV devices.

The discovery of optoelectronic properties in inorganic  $ABO_3$ -perovskites recently draws enormous interest in the scientific community because of their fundamentally new approaches for

direct conversion of solar radiation into electricity. Specifically, the PV mechanism in oxide perovskites is completely different from that occurring at the p-n interface in traditional semiconductors [4]. In traditional PV devices, an internal electric field is developed across the p-n junction which separates the photogenerated charge carriers. However, non-centrosymmetric perovskite crystals enable spontaneous ferroelectric (FE) polarization accompanied by an internal electric field (depolarizing field) in the opposite direction which is used to separate the charge carriers. The effective magnitude of the polarization-induced internal electric field is about one order of magnitude higher than that of a p-n junction [6]. Usually, the photovoltages in p-n junction based PV cells are limited by the band gaps of semiconductors (typically  $\leq 1$  V) [7]. However, FE perovskites can develop larger than band gap photovoltages which are referred to as anomalous photovoltage (APV). The PV effect was first observed in FE BaTiO<sub>3</sub> (BTO) crystals in 1956 [8]. Afterwards, the PV effect with an APV as large as 1000 V was recorded in LiNbO<sub>3</sub> (LNO) crystals which was described by light-induced refractive index changes under light illumination [9,10]. Epitaxial BiFeO<sub>3</sub> (BFO) thin films with ordered periodic FE domains yield APV up to 16 V which was described by an exciting theory-the theory of domain walls (DW) [11]. According to DW theory, the photogenerated charge carriers are separated by the high electric field developed across each DW. The total photovoltage is the sum of individual photovoltages developed across each DW. However, the DW theory was brought under scrutiny when the APVs of up to 28 V was reported in BFO films with a single FE domain [12]. The understanding of the exact physical phenomena that underpin the APV in FEs is in fact a subject of ongoing debate. The APV, which does not occur exclusively in FEs, was first observed on PbS films in 1946, amounting to 2 V [13]. It was later detected in other semiconductors including polycrystalline CdTe, ZnTe, and InP films [14,15], thus essentially contradicting the theory of band gap limited photovoltage in conventional

p-n junctions. The phenomenon was described by postulating the existence of barriers at grain boundaries (GBs), arising from the asymmetric concentration of impurity centers at the interfaces. The superposition of oriented grains in series was considered to be at the origin of the APVs. Despite exhibiting large APV, FE perovskites exhibit low values of photocurrent density ( $J_{SC}$ ), typically in the range of  $nA/cm^2$  to  $\mu A/cm^2$  [11,12], thus limiting their PCE. FE perovskites are typically insulators resulting in extremely low charge carrier transport (limiting their  $J_{SC}$ ) in their crystal structures. Therefore, the challenges to improve the PCE are mainly related to the enhancement of  $J_{SC}$ . So far, the highest value of  $J_{SC}$ ,  $\sim 30$   $mA/cm^2$  was observed in FE lead zirconate titanate (PZT) thin films under pulsed laser illumination [16]. More recently,  $J_{SC}$  values up to  $11.70$   $mA/cm^2$  (open circuit voltage,  $V_{OC} = 0.79$  V) were achieved in FE double perovskite  $Bi_2FeCrO_6$  (BFCO) thin films under 1 sun ( $100$   $mW/cm^2$ ), leading to a PCE of up to 3.30% in single layers [17]. In addition, a breakthrough efficiency of 4.80% under 1 Sun illumination was recently reported in  $BaTiO_3$  (BTO) crystals describing the observation of ballistic transport of non-thermalized carriers i.e. hot carriers in FE insulators [18]. Using nanoscale electrode probing,  $J_{SC}$  and  $V_{OC}$  of up to  $\sim 19.10$   $mA/cm^2$  and  $\sim 0.35$  V respectively, were obtained in BTO.

The application of perovskite materials has recently been extended to photocatalytic hydrogen and oxygen production. In contrast to electric power generation using solid-state PV devices, the photocatalytic approach to chemical fuel production in the gas form i.e. known as photoelectrochemical (PEC) cells is being widely studied as a potential method to harness solar energy [19,20,21] which is easier to store than electricity [22,23]. The photocatalytic process occurs in PEC cells, where a photoactive semiconducting material forms a junction in contact with a liquid electrolyte. The photogenerated charge carriers are then driven mainly by the junction induced electric field into the electrolytes, which activates the PEC reactions [24,25]. The

performance of PEC cells depends on several material-related factors, including the following parameters: high light absorption coefficient, high mobility of charge carriers, chemical stability in contact with reactants, and suitable matching of band-edge energies with redox potential of water for favorable hydrogen ( $H_2$ ) and oxygen ( $O_2$ ) evolution reactions [26,27,28,29]. Perovskite materials have shown unique photophysical properties and offer distinct advantages over many other material systems. Particularly, they exhibit the suitable band energy alignment with the redox potential of water in aqueous solutions and their semiconducting band gap corresponds to visible light, which makes them attractive candidates for hydrogen and oxygen evolution reactions. For instance, titanate perovskite  $MTiO_3$  compounds (where  $M = Sr, Ba, Ca, Mn, Co, Fe, Pb, Cd, Ni$ ) have high band gaps ( $>3.5$  eV) and exhibit good photocatalytic behavior under ultra-violet (UV) radiation of the solar spectrum [30,31,32,33,34,35]. However, titanates decorated with co-catalysts (Rh or Ru, or  $NiO_x$ ) can harness a visible range of solar radiation which are good examples of catalysts for hydrogen evolution reactions. In contrast, without the need for co-catalysts, most of the ferrite-based perovskites ( $LaFeO_3$ ,  $BiFeO_3$ ,  $GaFeO_3$ , and  $YFeO_3$ ) possess relatively low band gaps ( $< 3$  eV) corresponding to the large range of visible wavelength of solar spectrum. Therefore, ferrite perovskites exhibit superior photophysical properties over hematite and iron oxide compounds [36]. For example, FE BFO thin films with a band gap of  $\sim 2.7$  eV can act as photoanodes in PEC cells and exhibit  $J_{SC}$  values of up to  $\sim 5 \mu A/cm^2$  under 1 sun radiation (AM1.5G) [37,38,39]. It is worth mentioning that the modulation of band bending occurs at film-electrolyte interfaces due to the FE polarization of BFO leading to a faster electron-hole separation process and thus exhibits an enhanced photocatalytic performance. Similarly, FE band energy modulation and thus an enhancement of PEC performance were also observed in BFCO thin films. In fact, BFCO exhibits even higher PEC performance ( $J_{SC}$  up to  $\sim 1 mA/cm^2$  under 1 sun

illumination) than the performance of BFO films [40]. To improve further the PEC performances, it is required to explore such type of perovskite-based materials which are stable in electrolytes (less corrosive), possess low band gaps (corresponds to visible wavelengths of solar spectrum) and can straddle the reduction and oxidation potentials of water.

This thesis aims to study the physical and chemical properties of complex inorganic oxide perovskites to improve the solar energy conversion efficiency. Two multiferroic perovskite compounds: BiMnO<sub>3</sub> (BMO) and BFO are chosen for this study where the perovskite crystal phases are stabilized onto appropriate substrates by pulsed laser deposition (PLD). Among all FE perovskites, BFO is widely investigated for PV applications. It exhibits a good FE remnant polarization ( $\sim 55 \mu\text{m}/\text{cm}^2$ ) and a low band gap value (2.4-2.8 eV) compared to the band gap values of traditional FEs ( $>3 \text{ eV}$ ). However, the PCE of BFO thin films is still poor ( $< 0.1\%$ ) under 1 sun illumination. In contrast, thin film BMOs with thicknesses of several hundreds of nanometers exhibit weak FE property ( $\sim 6 \mu\text{m}/\text{cm}^2$ ), low band gap (1.1-1.2 eV) and high optical absorption coefficient (in the order of  $10^5 \text{ cm}^{-1}$ ) at room temperature. Because of these physical properties, we first investigated BMO as an active visible light absorber in solar energy research to the best of our knowledge. A PCE of 0.11% was obtained in multiphase Bi-Mn-O thin films i.e. composite films made of BMO and Mn<sub>3</sub>O<sub>4</sub> phases. However, we believe that the full potentials of single or multiphase BMO as active components in solar energy conversion are yet to be explored which motivates to continue our investigations. In addition, driven by the concept of multi-junction solar cells, and considering the fabrication flexibility of PLD grown multi-stacking (heterostructures) thin films, we choose bilayer perovskite thin films (BFO/BMO) to investigate the potential improvements of PCE of FE PV devices. Nevertheless, we predicted a good photocatalytic behavior of BMO due to its low band gap values which should straddle the oxidation and/or

reduction potential of water to hydrogen gas production. In the photocatalytic process, the size effects (thin films vs. nanostructures) or crystal morphologies of materials are extremely sensitive to electrochemical reactions, as described in numerous reports. Driven by this concept, we extend our study and investigate the photocatalytic property of BMO thin films and nanostructures as working electrodes in PEC cells.

In conclusion, we describe a PV device based on bilayer thin films (BFO/BMO) which show a significant improvement of PCE under 1 Sun illumination, which is higher than any PCE ever reported in individual BFO and BMO thin films. In addition, we demonstrate the concept of a PV device based on composite thin films made of two different types of crystal phases: BMO and  $\text{BiMn}_2\text{O}_5$ , which show a record PCE in inorganic oxide perovskites based PV devices. In the last part of the thesis, we discuss the PEC performances of BMO photoanodes for  $\text{H}_2$  and  $\text{O}_2$  evolution reactions. Specifically, we compare the PEC performances of BMO thin films and nanostructures and report a superior PEC performance in nanostructures over films.

# Chapter 1 Background Literature Review

## 1.1 Oxide perovskites

Among all complex oxide materials, oxide perovskites are most extensively studied and widely used crystal structures due to their exceptional physical and chemical properties. The chemical formula of a perovskite is  $ABO_3$ , where A & B represents the cation, and O represents the oxygen. In a perovskite, the A-site cation is surrounded by the eight corner-sharing  $BO_6$  octahedra with a coordination number of twelve, and the B-site cation usually a transition metal with a coordination number of six is surrounded by the octahedron of negatively charged oxygen ions. More specifically, the B-site cation is located in the center of the octahedron (Fig. 1-1).

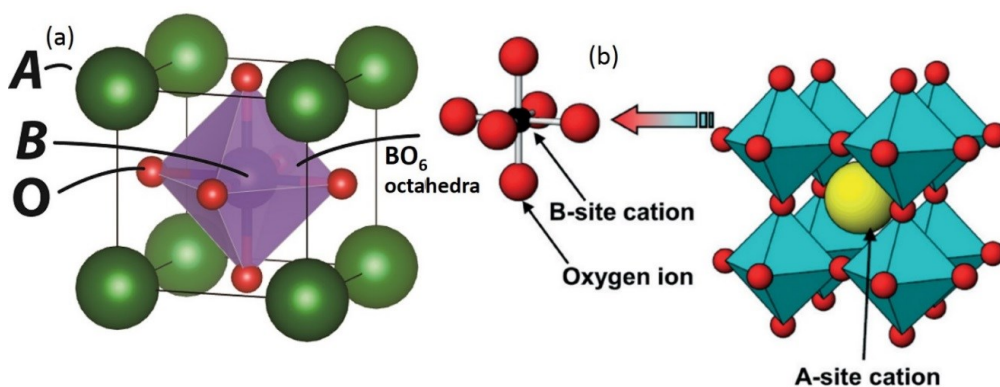


**Figure 1-1** Schematic diagram of two typical views of cubic  $ABO_3$  perovskite unit cells with the origin centered at the B-site cation (a) and at the A-site cation (b) respectively [41].

As shown in Fig. 1-1, the B-site cations are strongly bonded to the oxygen anions while the A-site cations have relatively weak interactions to oxygen. The cationic interactions with oxygen anions change with the ionic radii and the electronegativity of the cations (A and/or B-site) resulting in octahedral tilting in their crystal structures. Perovskites exhibit lattice distortion due to the

octahedral tilting resulting in the transformation of crystal phases from cubic to orthogonal or rhombohedral or tetragonal or monoclinic or triclinic phase. The lattice distortion has an important impact on crystal field which may change the electronic (band alignment, electron and/or hole transport through material systems) and optical properties (absorption coefficient, photoluminescence etc). Since octahedral tilting gives rise to the reduction of crystal symmetry, the stability of different crystal symmetries is determined by the tolerance factor ( $t$ ), as follows,

$$t = \frac{r_A + r_O}{\sqrt{2}(r_B + r_O)}$$

where  $r_A$ ,  $r_B$  and  $r_O$  indicate the ionic radii of A & B cations, and O anions, respectively. The most stable cubic lattice is obtained when  $t = 1$ . When  $t \geq 1$ , the crystal lattice is tetragonal. The lattice changes to rhombohedral or orthorhombic when  $t \leq 1$  [42,43]. The best examples of oxide perovskites are  $\text{PbZrO}_3$  (PZO),  $\text{BaTiO}_3$  (BTO),  $\text{PbTiO}_3$  (PTO),  $\text{BiFeO}_3$  (BFO),  $\text{SrTiO}_3$  (STO) and  $\text{BiMnO}_3$  (BMO).

## 1.2 Ferroelectricity

Since the discovery of ferroelectricity in Rochelle salt in 1920, ferroelectric (FE) materials gradually permeated every aspect of the modern microelectronic industry by means of their versatile chemical and physical properties [44]. Particularly FEs are increasingly being used as vital components in next-generation logic devices, memories, sensors and electro-optic elements for waveguide devices. Ferroelectricity is a characteristic of some specific materials which exhibit a spontaneous electric polarization vector ( $P$ ) in the absence of an external electric field ( $E$ ), and the orientation of the polarization can be switched by an applied electric field. Therefore, the distinct characteristic of a FE material is its spontaneous polarization, which is a reversible polar

vector. It develops as a result of symmetry reducing phase transformation that displaces positive and negative charges along with a restricted family of crystallographic directions, resulting in a permanent electric dipole moment [45]. BTO is one of the classical examples of FE perovskites depicted in Fig. 1-2. In BTO, a dipole moment occurs due to the relative displacements of the  $\text{Ti}^{4+}$  and  $\text{O}^{2-}$  ions from their symmetrical positions.

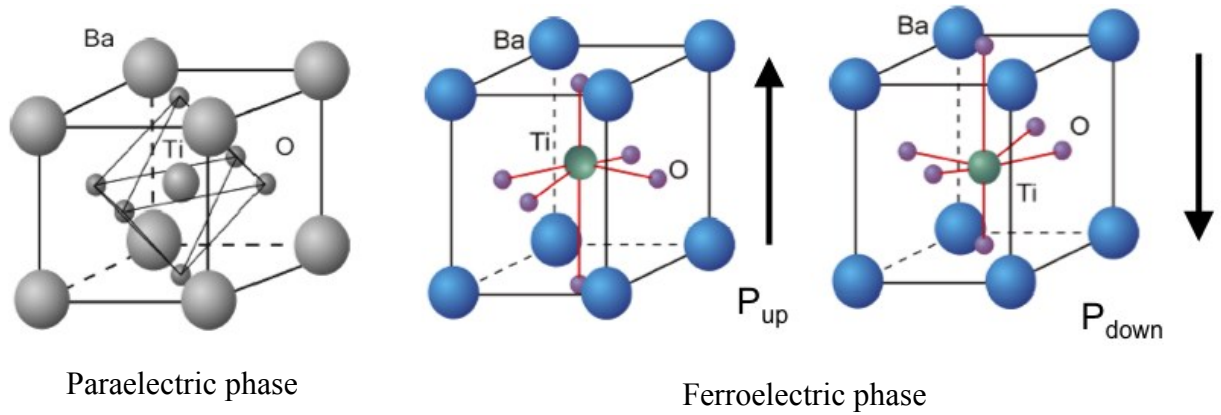


**Figure 1-2** Atomic structures of BTO exhibiting paraelectric and FE phase. FE phase shows upward ( $P_{up}$ ) and downward ( $P_{down}$ ) polarization vector, respectively [46].

FE materials are characterized mainly by analyzing their electric polarization response under an external electric field i.e. by measuring macroscopic hysteresis loops, as depicted by black in Fig. 1-3a. In macroscopic FE measurements, hysteresis loops are constructed by integrating the current (in the external circuit) over time under the application of a varying bias voltage. The current includes polarization switching currents in addition to the linear capacitive and the undesired leakage currents. Since FEs possess at least two stable polarization states which can be controlled by applying a suitable electric field, some specific regions in a FE material with different orientations of the polarization vector may coexist and the FE domains appear to minimize the free energy. Initially, the domains in FE materials are randomly oriented and no net polarization is

observed in the absence of an external applied electric field. With increasing the field, the total polarization gradually increases towards a saturation value ( $P_s$ ). If the field is reduced back to zero, the net polarization does not disappear but rather decreases only slightly from the saturation value. This polarization value is called remnant polarization ( $P_r$ ). When the field sweeps in reverse direction, the polarization state switches suddenly at a specific field intensity called the negative coercive field ( $-E_c$ ) (Fig. 1-3a). Further increasing the negative field results in a polarization increase in absolute value up to the saturation value  $|-P_s|$ , but opposite orientation. The same behavior is observed if the direction of the field is changed again. Generally, ideal hysteresis loops are symmetric (the positive and negative values of polarization are identical, ( $|+P_r| = |-P_r|$  and  $|+P_s| = |-P_s|$ )) where the remnant polarization and coercive fields are well-defined. However, several effects, such as charge accumulation in the presence of internal fields and the electrode materials with different work functions, can lead to domain pinning, and thus to an asymmetric hysteresis loop. This phenomenon is known as the imprint. The polarization switching phenomenon can also be identified by two symmetric switching peaks in the hysteresis of the current – field loop as illustrated by the red curve in Fig. 1-3a.

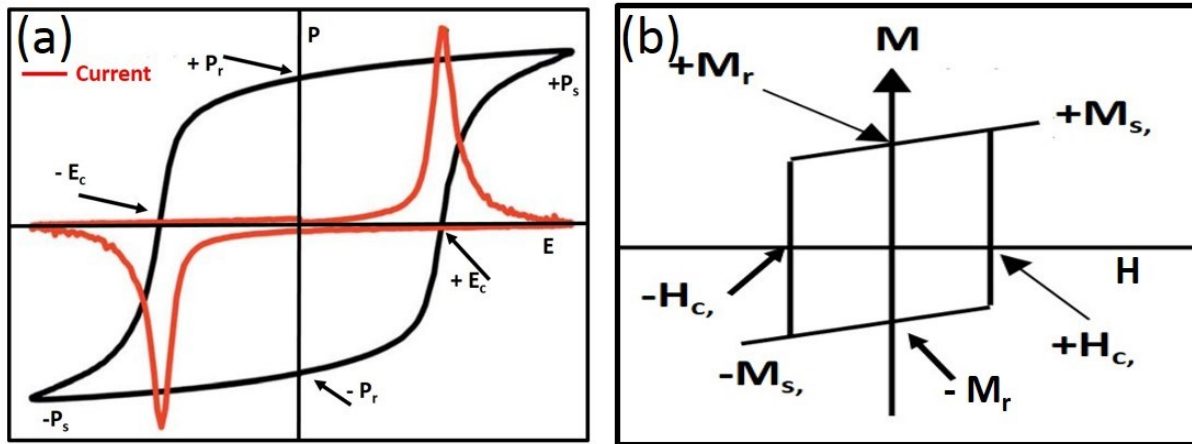


**Figure 1-3** Schematic of a ferroelectric (a) and a magnetic (b) hysteresis loop showing the coercive field, spontaneous and remnant polarization or magnetization. Associated current loops during FE hysteresis measurement indicated by red in (a).

### 1.3 Magnetism

Magnetism is a physical phenomenon of materials which is described by the orbital and spin motions of electrons and the way of interaction of electrons with one another. Magnetic behavior lies in the collective interactions of atomic magnetic moments oriented in a particular direction. The materials composed of atomic elements with partially filled *d* or *f* orbitals mainly exhibit magnetic characteristics. Similar to FEs, the magnetic materials are also characterized by analyzing magnetic hysteresis loops as depicted in **Fig. 1-3b**. The classical examples of magnetic materials are iron, cobalt, nickel, and Gadolinium [47]. On the basis of the orientation of magnetic moments with respect to each other in the crystalline lattice, magnetic materials are classified into four different categories such as paramagnetic, ferromagnetic, antiferromagnetic and ferrimagnetic (**Fig. 1-4**). In paramagnetic materials, the magnetic moments of neighboring atoms are oriented randomly resulting in no net magnetization in the absence of a magnetic field. In ferromagnetic

materials, the electron spins of neighboring atoms are parallel with each other which leads to a high net magnetic moment. When the neighboring sublattices exhibit anti-parallel alignment of electron spins with respect to each other (ideally zero net magnetization), the materials are known as antiferromagnetic materials. Ferrimagnetic behavior is described by the competition of parallel and anti-parallel magnetic moments with un-equal magnitudes. Like ferrimagnetism, the residual magnetism can appear in materials due to the canting of antiparallel spin arrangements along with parallel spin vectors. These weak ferromagnetic materials are known as canted antiferromagnetic materials (Fig. 1-4e).

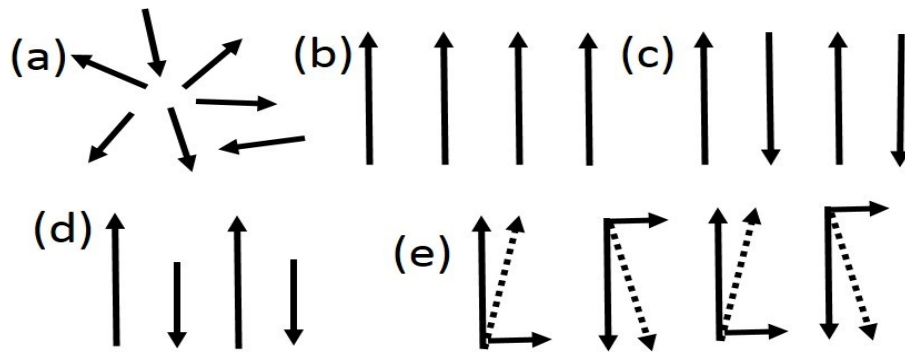


**Figure 1-4** Schematics of different types of magnetic properties exhibiting orientation of electron's spin (a) paramagnetism (b) ferromagnetism (c) antiferromagnetism, (d) ferrimagnetism and (e) canted antiferromagnetic where the magnetic components in different directions are represented by solid lines.

#### 1.4 Multiferroic materials: coexistence of ferroelectricity and magnetism

Like spontaneous alignment of polarization by the applied electric field in FE materials, the spontaneous alignment of electron spins can be switched by a magnetic field in magnetic materials (more precisely, in ferromagnetic materials). Similarly, the spontaneous alignment of strain can

also be switched by a stress field in ferroelastic materials. With these three primary types of ferroic ordering (ferromagnetism, ferroelectricity, and ferroelasticity), the concept of ferrotoroidicity (a new ferroic ordering of toroidal moments which should be switchable by crossed electric and magnetic fields) is also considered as one of the primary type of ferroic ordering in materials [48]. The material which exhibits two or more primary ferroic order parameters in the same phase in the absence of the external applied field is called multiferroic (MF) materials [49]. The first known MF was perhaps boracites ( $\text{Ni}_3\text{B}_7\text{O}_{13}\text{I}$ ) [50], thereafter followed by many others either found in nature or synthesized artificially [51]. In recent years, the materials which exhibit ferroelectricity and magnetism (either ferro, ferri or antiferromagnetic order) in their single or multiphase crystal structures are called MFs, regardless of the presence of other ferroic properties [52,53] as illustrated in Fig. 1-5.

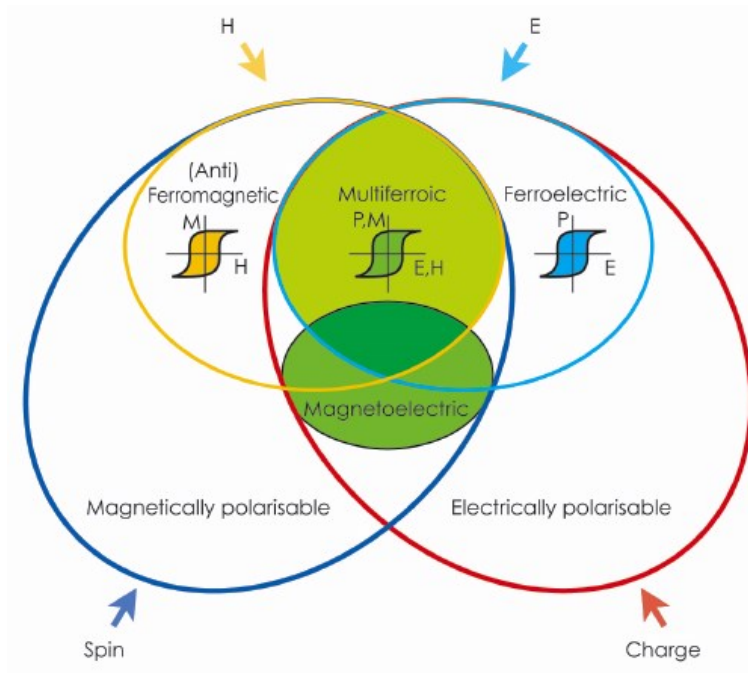


Figure 1-5 MF materials combine magnetic and ferroelectric properties [54].

MFs are particularly appealing not only because they have more than one ferroic properties in parent compounds, but also offer extra degrees of freedom in device design, due to the possible interactions between the magnetic order and ferroelectric polarization (Fig. 1-5) which essentially leads to additional functionalities. For example, the magnetoelectric effect i.e. the induction of a magnetization by an electric field, or of a polarization by a magnetic field, can be used entirely in new device paradigms, such as multiple states data storage devices, actuators, and transducers [55,56,57,58]. Although MFs are appealing in electronic device applications, there are very few MF materials that exist in reality. This is because a material must be a robust insulator to sustain the ferroelectric polarization, while, on the contrary, most of the magnetic materials are metals, i.e. good electric conductors. In fact, attempts to introduce magnetic order (by introducing impurities or unequal ratios of atoms) in a ferroelectric material resulted in increased electrical conduction (most appropriately named leakage) which is proven to be severely detrimental for ferroelectric properties. The scarcity of MF materials can also be explained by their electronic structure. Generally, ferroelectricity originates in the off-center shifting of transition metal ions (with empty  $d$  orbitals) from the center of their surrounding anions. However, magnetism needs partially filled  $d$  or  $f$  orbitals which have a corresponding localized spin, or magnetic moment. Exchange interactions between the localized moments lead to magnetic order. Thus the presence of  $d$  electrons of transition metals suppresses FE properties in magnetic materials. That is why the coexistence of ferroelectricity and magnetism in a single-phase material is in fact very rare and indeed a complex phenomenon to describe.

The most extensively studied and widely used MFs are the perovskite crystals. The complex perovskite compounds possess highly localized transition-metal  $3d$  electrons leading to exotic magnetic behavior, however, there are several mechanisms that may induce ferroelectricity. For

example, ferroelectricity can originate via electronic lone pairs [59,60,61,62,63,64], charge ordering [65], geometric effect [66] and even magnetism [67,68]. In the first three cases, the magnetic and ferroelectric orders occur independently, although a weak coupling between them often occurs. These are denoted as type-I multiferroics. The spontaneous remnant polarization in type-I MFs is relatively high [54] compared to other class of MFs. In the last class, the ferroelectric and magnetic order emerge jointly, implying a strong coupling between them in which case the MF material is denoted as type-II. The values of ferroelectric polarization in type-II MFs are usually much smaller. Type-II MFs are classified into another two groups: the first one in which ferroelectricity is induced by a particular type of magnetic spiral and second in which ferroelectricity appears even for collinear magnetic structures. A summary of single-phase multiferroics with their typical values of spontaneous ferroelectric polarization is depicted in Fig. 1-6. As shown in Fig. 1-6, the largest spontaneous polarization reported so far is in BiFeO<sub>3</sub> (relaxed,  $P_s \approx 100 \mu\text{C}/\text{cm}^2$ ; strained,  $P_s \leq 150 \mu\text{C}/\text{cm}^2$ ) [59]. Nonetheless, charge ordering due to different valence states in transition metal oxides was also found to be the source of ferroelectricity in compounds such as LuFe<sub>2</sub>O<sub>3</sub>, Pr<sub>1/2</sub>Ca<sub>1/2</sub>MnO<sub>3</sub> and in RNiO<sub>3</sub>. Among them, the largest polarization is recorded in LuFe<sub>2</sub>O<sub>4</sub> ( $25 \mu\text{C}/\text{cm}^2$ ) but this value is still controversial [69]. In YMnO<sub>3</sub>, ferroelectricity appears due to a geometric effect in where the tilting of octahedra moves the oxygen ions closer to small Y ions resulting in ferroelectricity. Orthorhombic (o-) TbMnO<sub>3</sub> is a typical example of spin-driven ferroelectricity generation in MFs which experiences a transition from a spiral order ( $P_s \leq 0.1 \mu\text{C}/\text{cm}^2$ ) to a collinear antiferromagnetic order ( $P_s \approx 1 \mu\text{C}/\text{cm}^2$ ) under pressure [70]. The largest spin-spiral-driven polarization has been observed in CaMn<sub>7</sub>O<sub>12</sub> ( $P_s \approx 0.3 \mu\text{C}/\text{cm}^2$ ) [71].

In the next section, we elaborate the lone pair mediated mechanism of ferroelectricity generation that occur in BFO, and BMO MFs, because these two Bi-based perovskite compounds and their physical properties are the ultimate focus of this thesis.

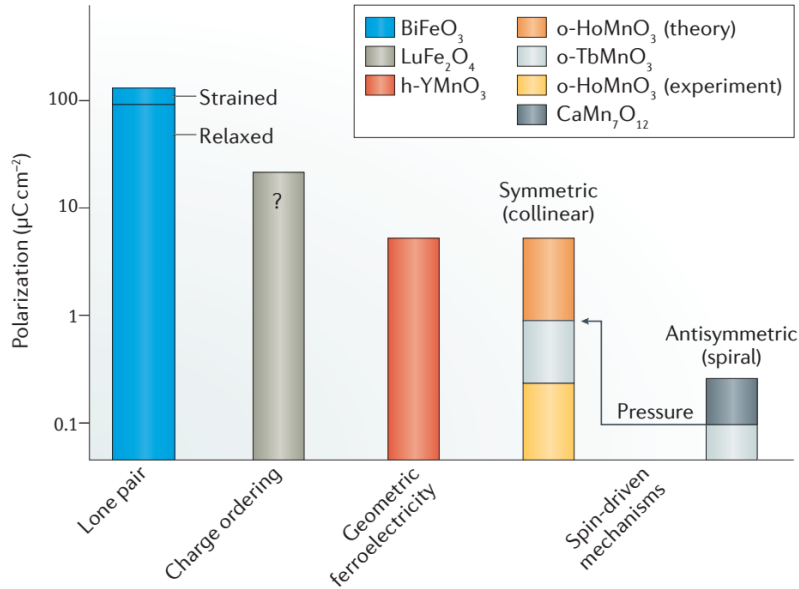


**Figure 1-6** Comparison of maximum polarization values among several single-phase multiferroic materials [52].

#### 1.4.1 Lone pair induced ferroelectric polarization in multiferroic perovskites

Among all MF perovskites, Bi containing oxide compounds such as BFO and BMO are practically attractive in electronic device applications because they are chemically inert and nontoxic, and their constituent elements are earth abundant. The two ferroic orders occur simultaneously in BFO or BMO because of the following reasons: *A* site cation ( $\text{Bi}^{3+}$ ) induces ferroelectricity due to its lone pairs of electrons while the *B* site cation (Fe or Mn) induces magnetism due to their partially filled *d* orbitals. The electronic configuration of  $\text{Bi}^{3+}$  is  $[\text{Xe}] 4f^{14}5d^{10}6s^26p^0$  where empty *6p* states form covalent bonds with the surrounding oxygen anions while the outer shell electrons of the *6s*

orbitals do not participate in chemical bonds. The lone-pairs are nearly spherical in the absence of any interactions. When the lone pairs are surrounded by oxygen anions, they move away from the centrosymmetric position due to Coulombic electrostatic repulsions thus forms a localized lobe-like distribution, like the ammonia molecule [72,73] (Fig. 1-7). The results provide the net displacement of the Bi cation with respect to the surrounding oxygen anions which breaks the spatial inversion symmetry of the lattice and leads to the formation of spontaneous polarization, as depicted in Fig.1-7. When the perovskites are stabilized onto the substrates, the induced strain in their thin films may severely affect the direction of the spontaneous polarization vectors.

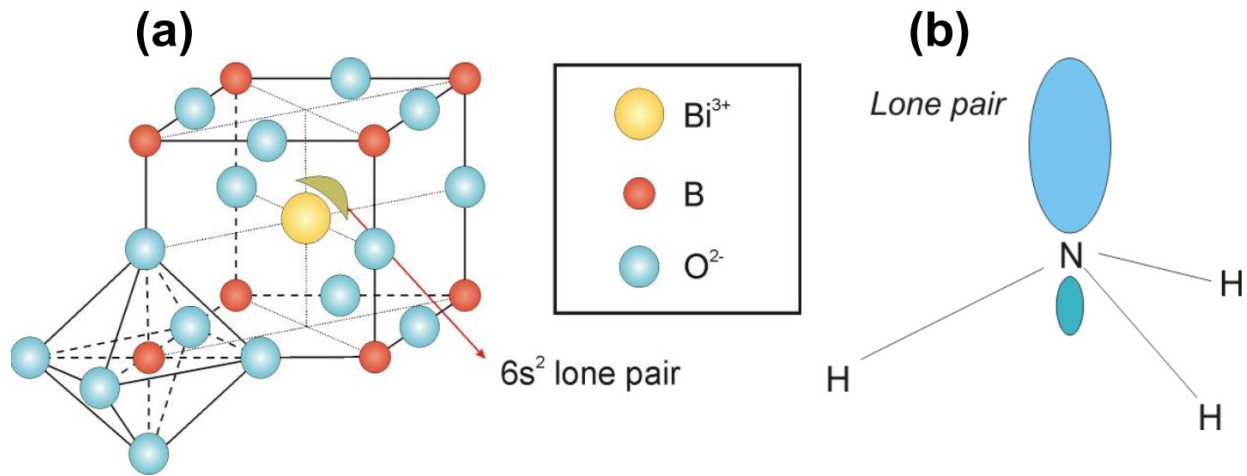


Figure 1-7 (a) Schematic representation of the mechanism of breaking inversion symmetry in  $ABO_3$  perovskite structures (b) Lone-pair  $2s^2$  in the ammonia molecule [72].

#### 1.4.2 Magnetic order in multiferroic oxide perovskites

As discussed previously for Bi containing MFs, the Bi<sup>3+</sup> cation is located always at the  $A$  site and the location of a magnetic transition metal cation with a partially occupied outer electron  $d$  shell is at the  $B$ -site. Generally, the  $d$ -states energetically degenerate in absence of any Coulomb interactions. Since the  $d$ -orbitals of transition metal is located at the center of the octahedron, the

$d$ -orbitals split into two energy states,  $e_g$  ( $d_{x^2-y^2}$  and  $d_{3z^2-r^2}$ , the high-energy levels) and  $t_{2g}$  ( $d_{xy}$ ,  $d_{yz}$ , and  $d_{zx}$ , the low-energy levels) depending on Coulomb repulsion with fully occupied  $p$ -orbitals of neighboring oxygen ions [74,75]. The oxygen octahedron of the  $B$  site cation interrupts the long-range  $B$  site cationic ordering, however, the long-range magnetic ordering arises from the magnetic superexchange interactions arbitrated by oxygen. The magnetic order in perovskite materials (whether ferro, ferri or antiferromagnetic) mainly depends on the filling of the  $e_g$  orbitals according to the Goodenough-Kanamori's (GK) rules [76]. Since  $B$  site of single perovskites is occupied by only one type of cation with the same oxygen states and same  $e_g$  orbital filling, the single multiferroic materials in principle should exhibit the antiferromagnetic ordering. In the case of ideal perovskites, GK rules are deduced by considering the B-O-B bond angle of  $180^\circ$ . However, lattice distortion (due to the rotation of oxygen octahedra) may change this bond angle which may yield different magnetic interactions in the lattice [76].

## 1.5 Multiferroic BiMnO<sub>3</sub>

### 1.5.1 Synthesis and crystal structures

BiMnO<sub>3</sub> (BMO) is a metastable compound which is commonly synthesized in bulk form under high pressure ( $\sim 3$  GPa to  $\sim 6$  GPa) and high temperature ( $\sim 600 - 700$  °C) [77,78,79]. It can also be stabilized on various substrates in thin film form under low ambient gas pressure conditions (in the range of 1 to 10 Pa) [80,81,82]. However, the highly volatile character of Bi element and the high tendency of BMO compound to decompose makes the synthesis of BMO extremely sensitive to temperature and pressure, entailing a critical environment to stabilize only single-phase BMO even in thin film form despite the availability of a large number of synthesis techniques. Moreover,

even multiphases BMO require highly optimized growth conditions to synthesize as they are extremely sensitive to the growth parameters.

The crystal structure of BMO belongs to the highly distorted non-centrosymmetric monoclinic  $C2$  space group at room temperature ( $< 450$  K) with the lattice parameters,  $a = 9.52 \text{ \AA}$ ,  $b = 5.61 \text{ \AA}$ ,  $c = 9.85 \text{ \AA}$ ,  $\alpha = \gamma = 90^\circ$ , and  $\beta = 110.67^\circ$  (Fig. 1-8). BMO exhibits two structural phase transitions at  $\sim 450$  K and  $\sim 770$  K, respectively. At  $\sim 450$  K, BMO is still indexed as monoclinic  $C2$  space group while exhibit a significant change in lattice parameters ( $a = 9.58 \text{ \AA}$ ,  $b = 5.58 \text{ \AA}$ , and  $c = 9.75 \text{ \AA}$ , and  $\beta = 108^\circ$ ). At  $\sim 770$  K, BMO undergoes a phase transition from monoclinic to centrosymmetric orthorhombic crystal structure with  $Pbnm$  space group [63].

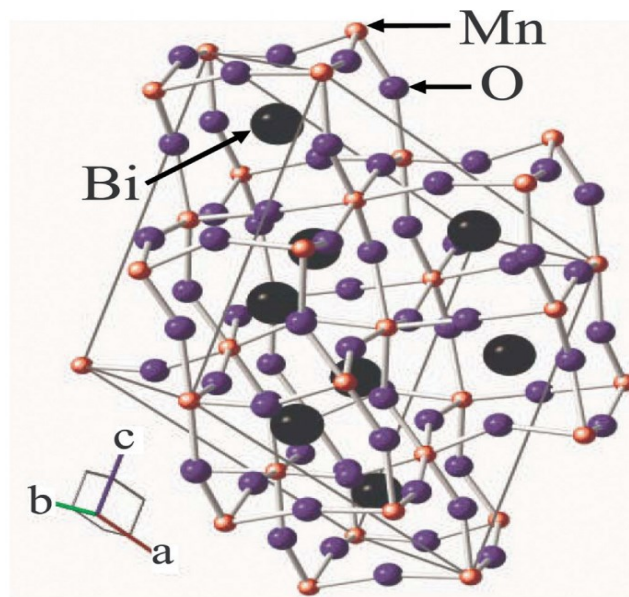


Figure 1-8 The monoclinic unit cell of BMO [83].

## 1.5.2 Ferroelectric and magnetic properties

As discussed in Section 1.4.1, lone pair electrons ( $6s$ ) of  $A$  site cation ( $\text{Bi}^{3+}$ ) induces ferroelectricity in Bi-based perovskite compounds. The highly distorted monoclinic BMO with  $C2$  space group

exhibits ferroelectricity [84]. BMO retains ferroelectric (FE) behavior below Curie temperature of  $\sim 770\text{K}$ . Santos et. al. first reported a low remnant polarization value ( $\sim 62\text{ nC/cm}^2$ ) in polycrystalline BMO in the temperature range of 80 K to 400 K [85]. FE measurement of BMO is extremely difficult because it exhibits high electrical leakage current under applied bias. BMO thin films often possess defects such as bismuth or oxygen vacancies which are considered to be the possible reason for this high leakage current behavior. To minimize the undesired leakage current, BMO thin films were sandwiched between two insulators. As result, a good FE remnant polarization up to  $\sim 16\text{ }\mu\text{C/cm}^2$  were recorded at room temperature [86] (Fig.1-9). However, the presence of ferroelectricity in BMO is still a subject of ongoing debate. Some theoretical and experimental observations [87,88,89,90,91] questioned the existence of ferroelectricity in BMO compounds describing BMO as monoclinic  $C2/c$  space group (centrosymmetric), which exhibits an antiparallel arrangement of the electric dipoles of the lone-pair electrons of  $\text{Bi}^{3+}$  [87].

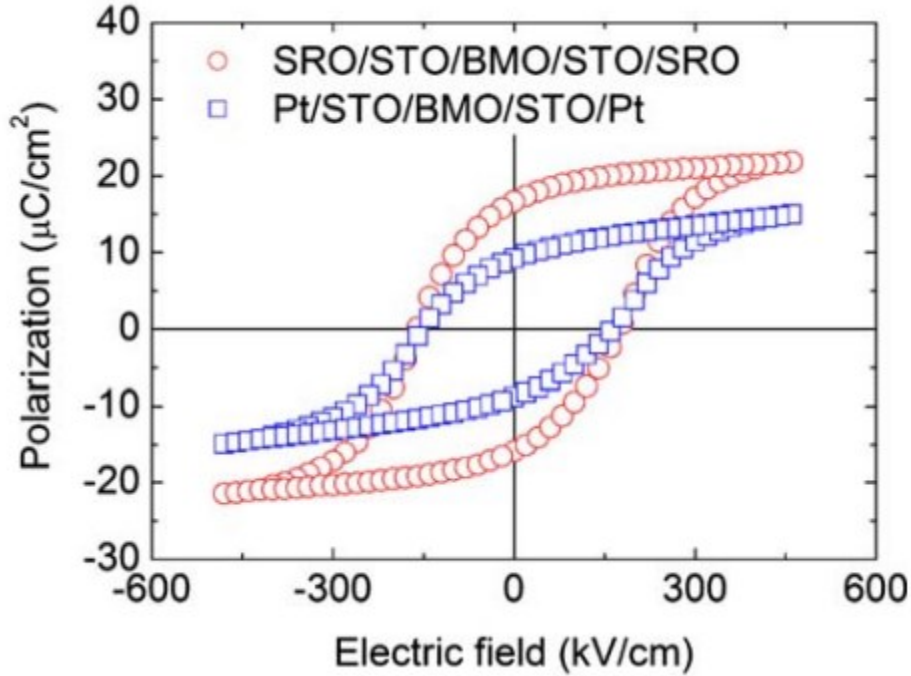


Figure 1-9 FE hysteresis loops of the Pt/SrTiO<sub>3</sub>/BiMnO<sub>3</sub>/SrTiO<sub>3</sub>/Pt and Pt/SrTiO<sub>3</sub>/BiMnO<sub>3</sub>/SrTiO<sub>3</sub>/Pt capacitors [86].

BMO should exhibit antiferromagnetic ordering (described in Section 1.4.2) as observed in similar orbital ordering compound LaMnO<sub>3</sub>, however in practice two out of three Mn - O - Mn orbital configurations in BMO favor ferromagnetic interactions along the monoclinic *b*-axis which results in an overall long-range net ferromagnetism [78]. BMO exhibits ferromagnetism under the Neel temperature of ~105K [80,92]. The theoretical saturated magnetization is estimated to be  $4 \mu_B/f.u$  where  $\mu_B$  and *f.u* denote Bohr magnetron and formula unit respectively. Experimentally, the saturated magnetization is reported to be  $\sim 3.6 \mu_B/f.u$  in bulk BMO [63] and  $\sim 2.2 \mu_B/f.u$  in thin films [81]. The saturated magnetization is reached up to  $3.9 \mu_B/f.u$  at 5 K which is very close to the theoretical value [93].

## 1.6 Multiferroic BiFeO<sub>3</sub>

### 1.6.1 Synthesis and crystal structures

The most widely investigated multiferroic oxide is bismuth ferrite,  $\text{BiFeO}_3$  (BFO). It has been drawing immense interest in scientific research since the first successful growth of BFO thin films on crystalline substrates by Ramesh's group [59]. In thin film form, BFO exhibits the coexistence of remarkable ferroelectric, magnetic and optical properties at room temperature, and the existence of a cross-coupling between them endows BFO with a unique potential for multifunctional devices in several fields (electronics, spintronics, photonics, etc) that offers a fantastic playground to engineering the novel physical properties in epitaxial thin films [94].

Michel et al. in 1969 [95] first unveil the atomic structures of BFO which belong to  $R3c$  space group with a highly distorted perovskite structure in rhombohedral symmetry containing two formula unit cells. The structure is depicted in Fig. 1-10. The lattice parameters of pseudocubic BFO structure (in true sense rhombohedral) are determined to be  $a_{pc} = 3.96 \text{ \AA}$  and  $\alpha_{pc} = 89.4^\circ$ . The rhombohedral symmetry is also equivalent to hexagonal crystal symmetry which comprises six formula units of BFO. The lattice constants of the hexagonal symmetry are equal to  $a_{\text{hex}} = 5.579 \text{ \AA}$  and  $c_{\text{hex}} = 13.869 \text{ \AA}$ .

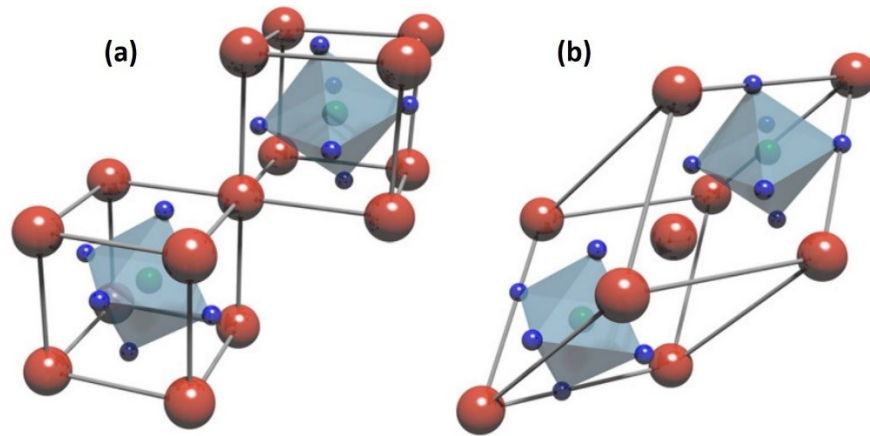


**Figure 1-10** Atomic structure of BFO. (a) Two pseudocubic cells with cation shifts and octahedra rotations along  $[1\ 1\ 1]_{pc}$  direction are joined to form (b) the rhombohedral unit cell [94]. A site  $\text{Bi}^{3+}$  and B site  $\text{Fe}^{3+}$  cations are displaced towards  $[111]_{pc}$  directions.

Although the structure of bulk BFO is rhombohedral, the methods of stabilizing high quality epitaxial thin films on the single crystal substrates have brought enormous opportunities to tune the crystal structures of BFO compounds. The lattice mismatch between substrates and deposited films introduces strain (compressive or tensile) in the films and thus allows to stabilize different types of crystal structures (Fig. 1-11). Examples of BFO structures in thin films include tetragonal [96,97,98], rhombohedral [99,100], orthorhombic [101, 102], monoclinic [103,104,105,106], and triclinic [107]. These structural changes yield numerous physical and chemical properties in the films.

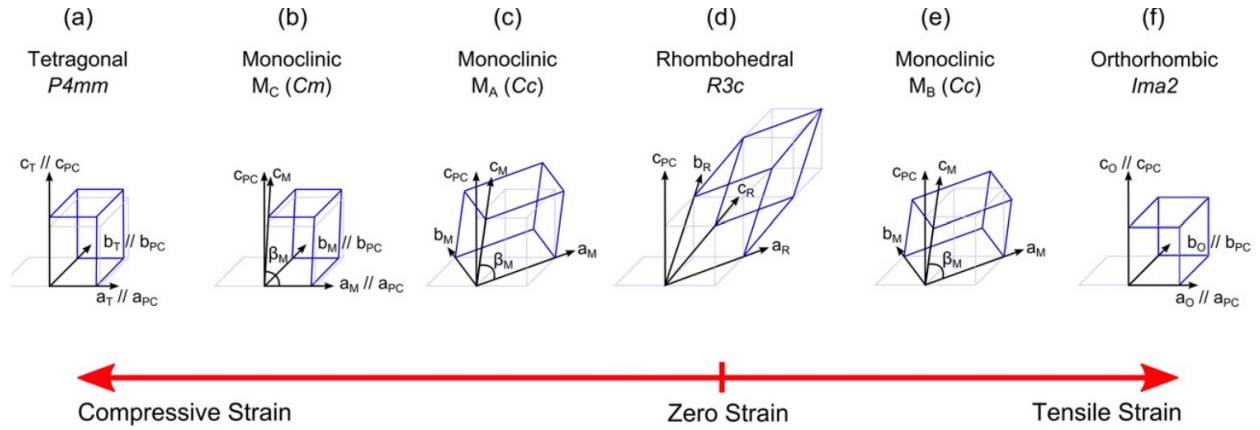
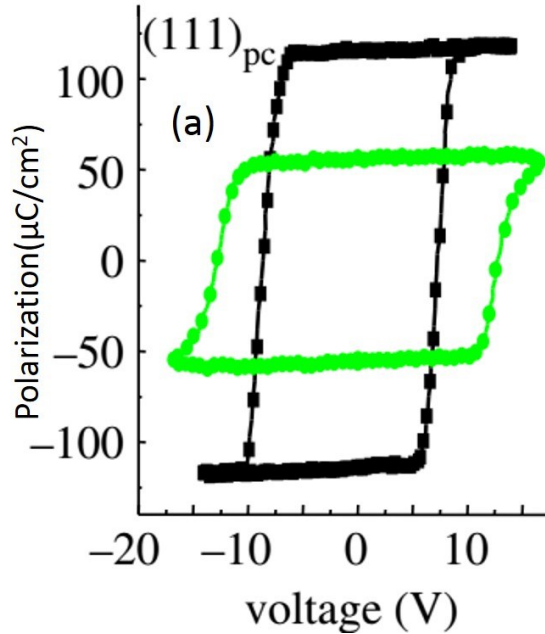


Figure 1-11 Strain engineering in BFO thin films exhibits various crystal structures [94].

### 1.6.2 Ferroelectric and magnetic properties

Like BMO, BFO exhibits ferroelectric (FE) behavior due to the lone pair electrons (6s) of A-site cation ( $\text{Bi}^{3+}$ ), as described in Section 1.4.1. The FE behavior of bulk BFO i.e. rhombohedrally distorted perovskite with  $R3c$  space group was first characterized by hysteresis loops under liquid nitrogen conditions (spontaneous polarization,  $P_s = 6.1 \mu\text{C}/\text{cm}^2$ ) [108]. At 294 K, Kubel & Schmid reported FE properties in a monodomain single crystal. For the same crystal structure, the  $P_s$  of  $100 \mu\text{C}/\text{cm}^2$  was reported in bulk BFO at room temperature by Lebeugle et. al. [109], which is the highest  $P_s$  value reported so far in a single crystal. However, the bulk BFO is unstable in their crystal structures and extremely leaky i.e. high leakage current under applied bias perhaps as a result of defects and nonstoichiometry, which prevents the application of this material in real electronic devices. In thin film form, BFO exhibits a giant FE remnant polarization ( $\sim 55 \mu\text{C}/\text{cm}^2$ ) at room temperature (Fig. 1-12). The polarization values higher than  $100 \mu\text{C}/\text{cm}^2$  at room temperature have been reported in BFO thin films till to date [110]. The ferroelectric Curie temperature of BFO is  $\sim 1100$  K.



**Figure 1-12** FE hysteresis loop of 400 nm thick monodomain BFO thin films with Pt top and SrRuO<sub>3</sub> bottom electrodes. The blue curve represents the polarization fatigue after 10<sup>6</sup> switching cycles [110].

As described in [section 1.4.2](#), the single perovskite (ABO<sub>3</sub>) generally exhibits antiferromagnetic ordering, however, the rotation of octahedron may cause the lattice distortion which results in different magnetic ordering in the lattice. In case of BFO (G-type antiferromagnetic with Neel temperature of 643 K), the magnetic moment of each iron atom (Fe<sup>3+</sup>) is surrounded by antiparallel spins of six neighboring iron atoms. Due to the lattice distortion, the neighboring spins are not perfectly antiparallel, rather canted away from the rotation plane by up to one degree resulting in a weak magnetism. In bulk BFO, spins of iron atoms order in a G-type antiferromagnetic structure with a long-wavelength (620 Å) of cycloidal modulation i.e. a spiral spin structure occurred due to the rotation of the antiferromagnetic axis in the crystal. Destruction of this cycloidal modulation either by applying large magnetic fields [111] or chemical substitution [112] result in the formation

of weak-ferromagnetic order with a remnant magnetization of  $0.01 \mu B/\text{Fe}$  [113]. A gigantic enhancement of the magnetic moment ( $1 \mu B/\text{unit cell}$ ) has been reported in BFO thin films compared to its bulk counterpart at room temperature [59] which is described by induced strain in the films due to the lattice mismatch between substrates and films. Relaxed films normally exhibit cycloidal spin order [114,115] while strained films show weak ferromagnetic ordering [116,117,118].

## 1.7 Photovoltaic effect for solar energy conversion

### 1.7.1 Basics and advances of p-n junction solar cells

The photovoltaic (PV) effect occurs in photoactive materials under illumination. When an internal electric field develops across the material, photogenerated electrons and holes are being separated by this electric field. Under short circuit condition, photogenerated carriers flow through the external electric circuit and produce currents. One of the earliest examples to develop an internal electric field i.e. asymmetric electric potential in photoactive semiconductor materials was sandwiching the materials between two metallic electrodes with different work functions. This asymmetric electric potential developed at the metal-semiconductor interfaces is known as *Schottky* barrier induced internal electric field [119]. An alternative mechanism to develop an internal electric field in semiconductor materials is described by the *p-n* junction theory which is widely used and regarded as the classical theory in PV sciences and technologies. According to this theory, the Fermi level alignment of both *p*-type and *n*-type materials at thermodynamic equilibrium implies band bending at the interfaces resulting in a built-in electric field. This field ultimately drives the photogenerated electron-hole pairs to the electrodes as described in Fig. 1-13. However, the *Schottky* field is also present in real devices depending on the type of electrodes

used therefore the net field in the devices is the resultant of both contributions. The performance of the PV cells is mainly characterized by plotting current density ( $J$ ) as a function of applied voltage ( $V$ ). The PV parameters such as open-circuit voltage ( $V_{OC}$ ), short-circuit current ( $J_{SC}$ ) and the fill-factor ( $FF$ ) are extracted from the  $J$ - $V$  curve as shown in Fig. 1-13c. Those parameters are used to calculate light to electrical power conversion efficiency (PCE),

$$PCE = \frac{FF * V_{OC} * J_{SC}}{P_{in}} \dots\dots\dots (1.1)$$

where FF is determined by the following equation,

$$FF = \frac{(V_m * J_m)}{(V_{oc} * J_{sc})} \dots\dots\dots (1.2)$$

In high efficient PV devices, photogenerated charges (electrons and holes) must be separated as efficiently as possible and transport them independently to the electrodes before recombination. Therefore, the active materials used in PV devices should have the following properties: high photoabsorption coefficient, narrow energy band gap, high rate of electron-hole pair generation, the long diffusion length of charge carriers, low recombination rate, and high carrier mobility.

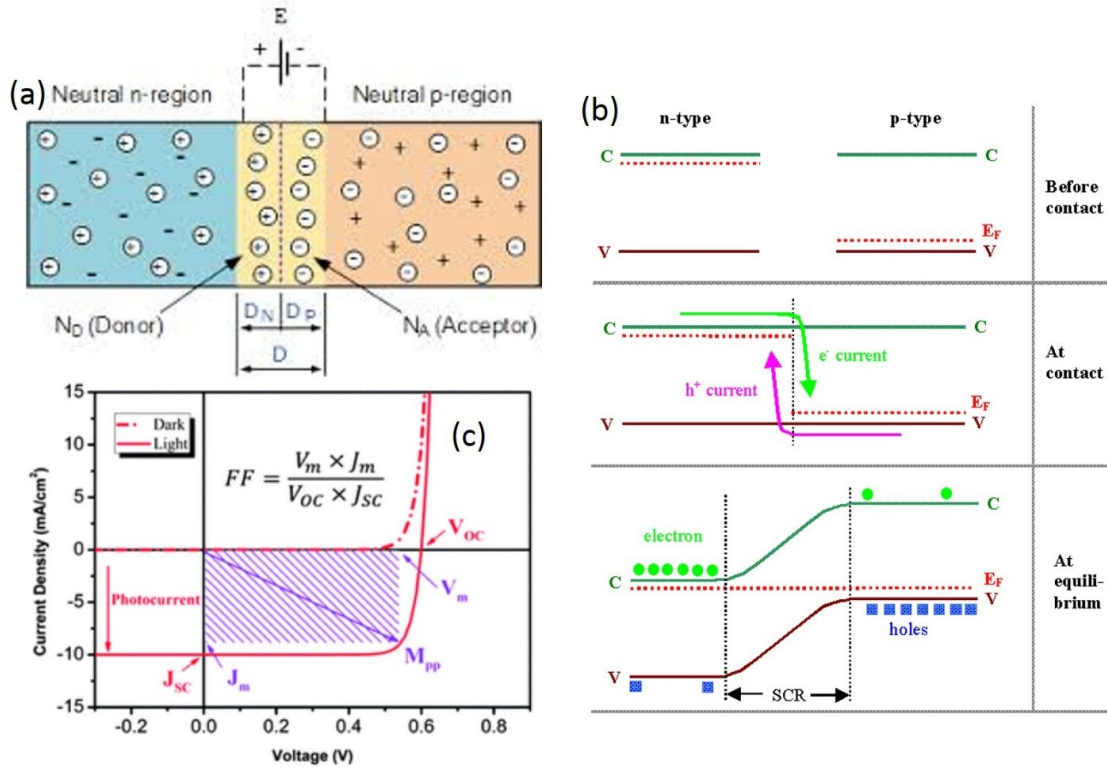


Figure 1-13 Schematic of a p-n junction with band alignments (a, b). Current density vs voltage (J-V) curve under dark and illumination (c). [119]

In 1954, the first silicon solar cell with a PCE of  $\sim 6\%$  was reported by Chapin et al. [120]. Driven by the technological advances, single *p-n* junction based silicon solar cells have led efficiencies of up to 27%. Silicon technologies are presently dominating the commercial market with a share of over 90%. The remaining share is being taken up mainly by CdTe and CuInSe<sub>2</sub> based solar cells. Thin film solar cells considered as second generation solar technology shows huge potentials towards cost reduction in the manufacturing process due to drastic materials savings, low-temperature cell integration and high automation level in series production, in contrast to the bulk silicon wafer technology. For example, CdTe/CdS [121], Cu(In,Ga)Se<sub>2</sub> (CIGS) [122], GaAs based cells exhibit efficiencies of up to 20% to date. Third generation solar cells are mainly dominated

by nanoscience and nanotechnology because of the extraordinary optoelectronic properties yielded by quantum physical effects. For example, theoretical efficiencies of 65% (double the efficiency of existing solar cells) were estimated for solar cells made of three-dimensional grids of quantum dots [123] whereas the experimental efficiencies were found to be only ~12% so far. The limited charge transport through the *p-n* junction and the presence of energy barriers at the interfaces are the major detrimental factors affecting the PCEs of these solar cells. New types of PV cells in addition to the developments of second and third generation solar cells are presently being studied intensively to enhance the PV performances and simultaneously reduce the manufacturing cost. In this regard, the emerging solar cells involving dye-sensitized, organic & inorganic, hybrid-halide perovskite, quantum dot etc are currently being investigated. The efficiencies so far achieved in those cells are in the range of about 4% to 20% till to date. The best efficiency solar cells are summarized in the following chart (Fig. 1-14).

# Best Research-Cell Efficiencies

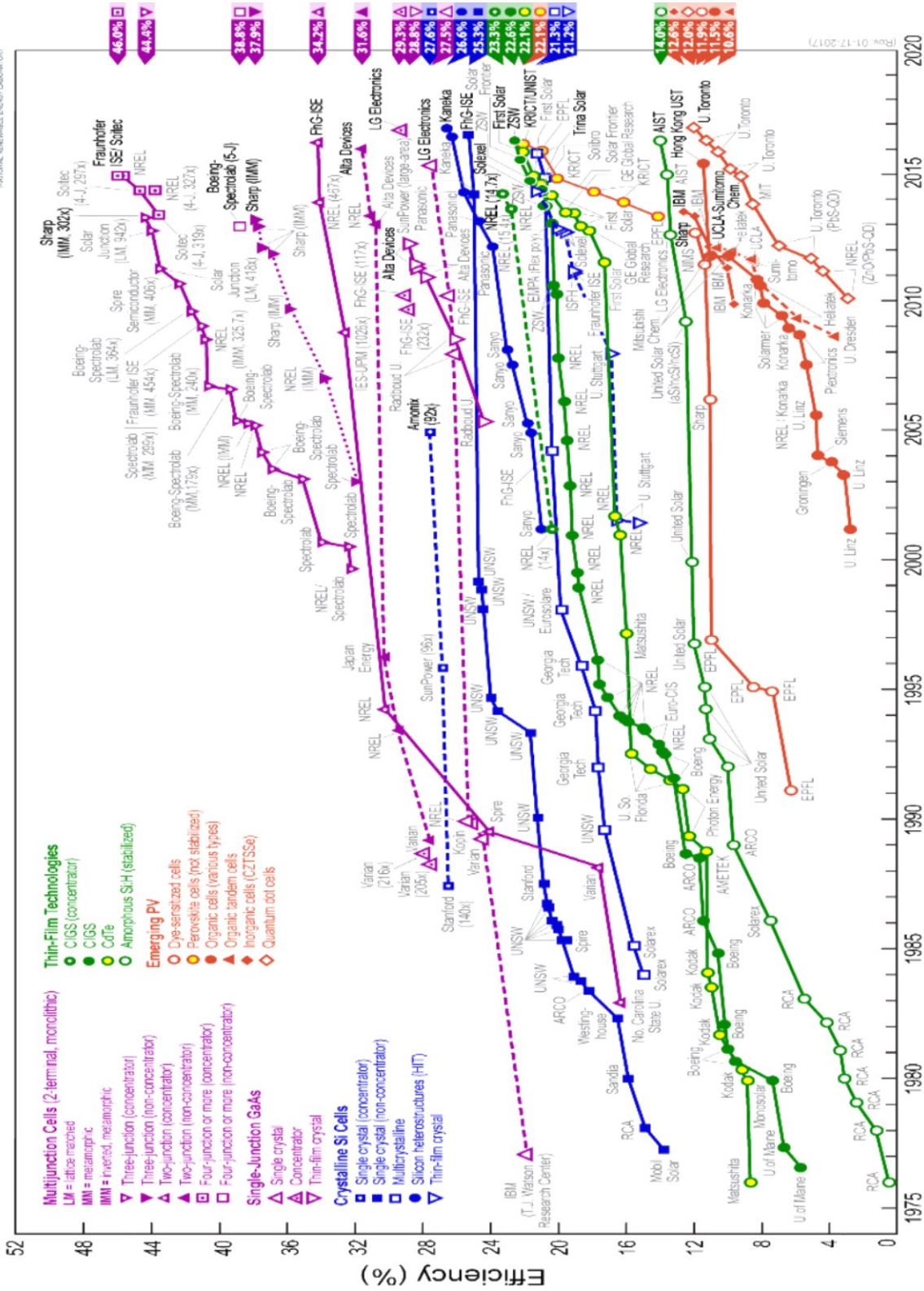


Figure 1-14 Best efficiencies of different solar cells [124].

### 1.7.2 Photovoltaic effect in ferroelectric perovskite materials

Although the solar energy conversion efficiencies of the inorganic oxide perovskites are not competitive with the commercial *p-n* junction based solar cells (described in [section 1.7.1](#)), they usually draw enormous interest in scientific research due to their fundamentally new approaches for solar energy conversion (i.e. completely different from that occur in *p-n* junctions). The PV effect is observed in non-centrosymmetric perovskite crystals under homogeneous illumination [[9,8,125,126](#)] which is referred to as bulk photovoltaic (BPV) effect. BPV effect has two characteristic features [[126](#)]. First, the values of photocurrent density depend on the polarization of light and second, the ability to yield larger than band gap photovoltage (up to 1000 V) [[10](#)] which is significantly different from the band gap limited photovoltages in *p-n* junctions (typically  $\leq 1\text{V}$ ). Among all FE perovskites, the PV effect was first observed in BaTiO<sub>3</sub> (BTO) and explained by the formation of space charge layers [[8](#)]. Later, it was unveiled that the BPV effect in BTO shows the changes of photovoltages with the polarization direction of incident light which might be parallel or perpendicular to the polar axis of materials [[127](#)]. Dalba et al. [[128](#)] then described the direct relation between the polarization of incident light and photocurrent generation by the third rank tensor property. Later, many theories were proposed to explain the BPV effect in polar materials, however, there is no unique one till to date that can explain all aspects of experimental results. The most cited theories are described below for better understanding.

Glass et.al. [[129](#)] described the PV effect in FE perovskites by photoabsorption of impurity states. More specifically, they demonstrated the local asymmetry of impurities in the pyroelectric host that can lead to a steady-state photocurrent generation in LiNbO<sub>3</sub> (LNO) [[10](#)]. The probability of intervalence charge transfer between host-impurity atoms in the  $\pm c$  directions differs, as a result,

the photoexcited charge carriers move through the crystals. The relation between  $J_{SC}$  and the incident light intensity can be expressed by the following equation,

$$J_{SC} = J_e - J_r = G\alpha I_L \quad \dots\dots\dots (1.3)$$

where  $J_e$ ,  $J_r$ ,  $G$ ,  $\alpha$ , and  $I_L$  are the current density due to the excitation of the charge carriers, the recombination current density, the Glass coefficient, the absorption coefficient of light, and the light intensity, respectively [10, 130]. The value of  $G$  depends on the material in choice.

When the circuit is connected to an external load, the additional voltage is dropped across the device which is estimated by  $V = E\delta$ , where  $E$  and  $\delta$  denote the electric field and thickness respectively. The eq. [1.3] can then be modified as follows,

$$J_{SC} = J_e - J_r = G\alpha I_L - \sigma E \quad \dots\dots\dots (1.4)$$

Where  $\sigma$  represents the electrical conductivity. If the electrodes are disconnected, the open circuit electric field can be described by eq. [1.5],

$$E_{OC} = \frac{V_{OC}}{\delta} = \frac{G\alpha I_L}{\sigma} \quad \dots\dots\dots (1.5)$$

The phenomenology of the BPV describes the photocurrent density as a function of the tensor property of materials [126]. It is observed that the photocurrent density ( $J_i$ ) depends on the polarization of light. Considering linear and circular polarization of light, the  $J_i$  can be expressed as follows,

$$J_i = \alpha G_{ijk}^L e_j e_k^* I_L + i G_{ik}^C (e e^*)_i I_L \dots\dots\dots (1.6)$$

Or

$$J = \alpha G I_L \text{ (in scalar form)}$$

The first and second term in eq. [1.6] represents the BPV effect for linearly and circularly polarized light respectively, where  $e$ ,  $G_{ijk}^L$ , and  $G_{ik}$  denote the unit vector for polarized light, third rank and second rank tensor of materials. For linearly polarized light, the BPV effect is nonzero only in non-centrosymmetric crystal structures and  $G_{ijk}^L$  denotes the piezoelectric tensor. For circularly polarized light, BPV effect is nonzero only for gyrotropic (optically active) noncentrosymmetric crystals [126].

As illustrated in Fig. 1-15, when the electrodes are disconnected (open-circuit condition),  $J$  leads the photovoltage generation in the medium which is described by the following equation [1.7],

$$V_{OC} = \frac{Jl}{\sigma_d + \sigma_{ph}} \dots\dots\dots (1.7)$$

As illustrated in eq. [1.5] and eq. [1.7], if the conductivity (dark or photoconductivity) is low, a high photovoltage is developed in the materials. This photovoltage is proportional to the distance between electrodes and is not limited by the band gap. Although the phenomenology of the BPV is a powerful tool to realize the general relationship between the polarization of light and crystal structures, it actually cannot describe the actual PV mechanism along with the magnitude of photovoltaic response [130].

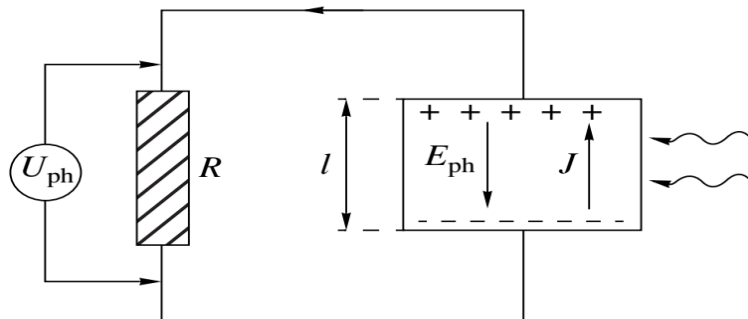
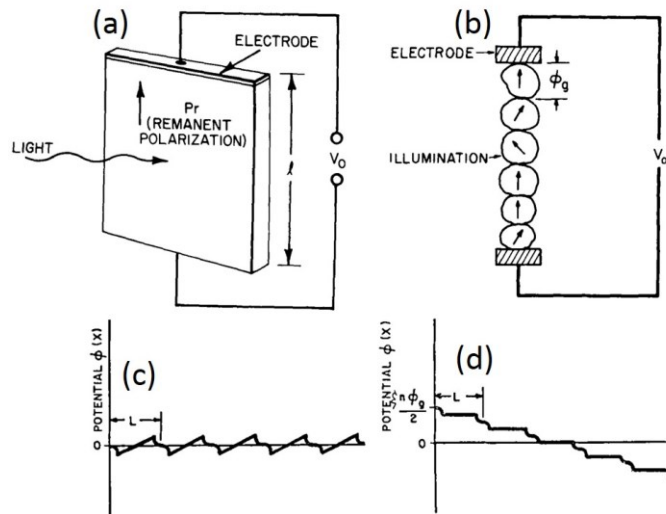


Figure 1-15 Schematic representation of developing  $J_{SC}$  and  $V_{OC}$ . [126]

Brody and Crowne [131] proposed another theory to demonstrate the large photovoltage in poled ceramic FEs where the photovoltages are proportional to remnant polarization and distance between the two electrodes. When poled FEs are illuminated, the photoinduced carriers screen the internal electric field of the bulk grain but do not screen the fields within the surface regions of grains where spontaneous polarization begins or is terminated. As a result, a tiny voltage will develop, independently, across each grain under illumination. The series sum of those small photovoltages leads to the development of a high photovoltage across the whole sample which is thus proportional to the distance between two electrodes of the sample (Fig. 1-16).



**Figure 1-16** (a) Schematic of the electrical measurements of a poled ceramic sample under illumination (b) schematic of the series summation of developed photovoltage across the individual grain. Potential across the sample under dark (c) and illumination (d). [131]

One of the most exciting theories to describe the PV effect in FE perovskite thin films is the depolarization field theory. FE polarization induces an internal electric field in the films in opposite direction (with respect to polarization) which is called depolarization field ( $E_{DP}$ ) [132]. Since the thickness of thin films is of the order of tens to few hundreds of nanometers, the effect of  $E_{DP}$  in

films is very strong compared with that in bulk form. However, the bound charges of FE polarization can be screened by either free charges that may be present in FE materials, or by external electrodes. Nevertheless, the screening of polarization by charges, even if partial, helps to stabilize the FE domains i.e. the  $E_{DP}$ , resulting in the development of a net electric field in the films [133] (Fig. 1-17).

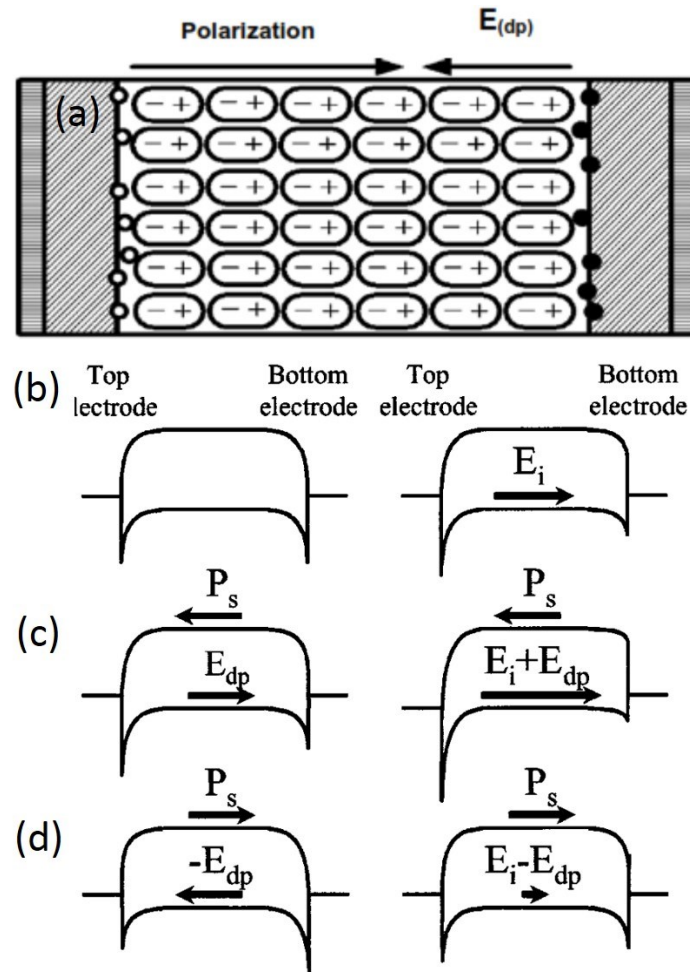
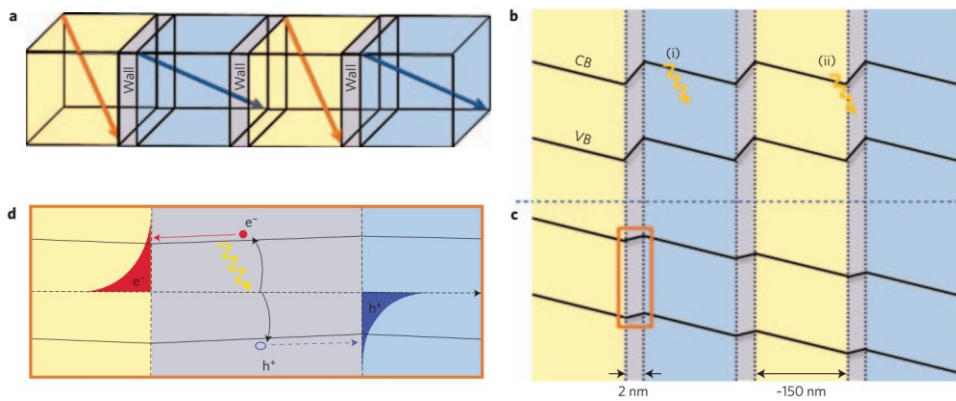


Figure 1-17 (a) The interfacial effect on the photovoltage in FE materials showing the depolarizing field ( $E_{dp}$ ) [134] (b,c,d) Diagram of a metal-film-metal electrode having symmetric and asymmetric Schottky contacts, indicating the effect of interface electric field  $E_i$  [135].

The PV effect in FE perovskite thin films can also be described by the domain wall (DW) theory [11]. The theory describes the anomalous photovoltaic effect (large photovoltage) in FE thin films by the series summation of the potential steps developed across domain walls, as shown Fig. 1-18. According to DW theory, the built-in potential steps may arise from the polarization vector perpendicular to the domain walls (theoretically predicted in  $\text{PbTiO}_3$ , and confirmed later experimentally in BFO) [136,137]. The associated charge density forms an electric dipole, leading to an electric field within the wall accompanied by the associated potential step from one side to the other (Fig.1-18a,b). The photoexcited carriers are separated mainly at the domain wall by the local electric field (Fig. 1-18c,d). This mechanism is analogous to the model proposed by Brody and Crowne for polycrystalline samples. However, the anomalous PV effect is also observed in epitaxial FE thin film (without any domain), thus contradicting the DW theory [138].



**Figure 1-18** Schematic of DWs (a) and associated band structure in dark condition (b). Schematic of band structure upon illumination (c) and accumulation of photoexcited charges at single DW (d). [11]

### 1.7.3 Advances of ferroelectric materials in photovoltaic devices

The PV effect is described in several FE perovskites such as  $\text{LiNbO}_3$  [10],  $\text{Pb}(\text{Zr},\text{Ti})\text{O}_3$  [139],  $\text{BaTiO}_3$  [127], and  $(\text{Pb},\text{La})(\text{Zr},\text{Ti})\text{O}_3$  (PLZT) [134]. Although FEs can yield large photovoltage under illumination (up to 1000 V), the  $J_{\text{SC}}$  is extremely poor (in the range of  $\text{nA}/\text{cm}^2$ ) leading to a very low PCE (in the order of  $10^{-4}$  to  $10^{-6}$ ). One of the major obstacles to improve the  $J_{\text{SC}}$  is the insulating property of FEs which shows intrinsically low bulk conductivity of FE domains. Besides, FEs possess large band gaps ( $> 3$  eV) therefore they can only harness electricity from ultraviolet part of the solar spectrum. The highest efficiency of  $\sim 0.28\%$  was achieved in PLZT thin films [134] which is far below the theoretical limit of  $19.5\%$  [133]. It is worth mentioning that the incorporation of traditional semiconductors in FE based PV devices can significantly improve the efficiency. For example, an *n*-type  $\text{Cu}_2\text{O}$  layer between the  $\text{PbZr}_x\text{Ti}_{1-x}\text{O}_3$  film and the Pt contact leads to a 120-fold enhancement of the  $J_{\text{SC}}$  ( $4.80 \text{ mA}/\text{cm}^2$ ), corresponding to a PCE of  $0.57\%$  under AM1.5G ( $100 \text{ mW}/\text{cm}^2$ ) illumination [140]. The efficiency up to  $\sim 1.25\%$  is obtained in PV devices made of  $\text{PbZr}_x\text{Ti}_{1-x}\text{O}_3$  and *a-Si* [141]. Most recently, a breakthrough efficiency of  $4.8\%$  has been recorded in  $\text{BaTiO}_3$  crystals by nano-scale probing [18].

The FE property of multiferroic (MF) perovskites is used to describe the PV effect in MFs. Therefore, the theories described above (section 1.7.2) are also employed in describing the PV effect in MFs. One of the major advantages of MFs is their relatively low band gap (1.1 to 2.7 eV) compared with conventional FE materials, which therefore makes them more effective candidates for harnessing a wide range of visible light of solar spectrum. The band gaps in perovskites are determined by accounting a charge transfer from the oxygen (O)  $2p$  states at the valence band maximum to the transition-metal  $d$  states at the conduction band minimum. The charge transfer process is solely dependent on the fundamental characteristics of cation–oxygen bonds:  $A\text{--}O$  and

*B–O*. Owing to a large difference in electronegativity between the oxygen and transition-metal cations, the bandgaps in FE perovskites such as LNO, BTO and PZT are quite large (3–5 eV) compared with the band gaps (1.1–2.8 eV) of well-known multiferroic perovskites such as BFO, BMO and BFCO. The best examples of MFs exhibiting PV effect are BFO, BMO, and BFCO. BFO is most widely investigated in the form of thin films, which show a good FE property [11] leading to a high photovoltage of up to 50 V [138]. However, the photocurrent is still poor, in the range of nanoamperes, resulting in low PCE. The PV effect in multi-phase BMO thin films have also been reported, exhibiting a PCE of up to 0.11% under 1 sun illumination. A significant PV response was also observed in epitaxial MF BFCO thin films with a quantum efficiency of 6.5% under the illumination of a red laser light [142]. The significant enhancements of efficiencies in perovskite materials are depicted in Fig. 1-19. In recent years, the lead halide perovskites (organic-inorganic halide perovskites) draw enormous interest because of their high efficiencies (above 20%), however, they are highly unstable at ambient atmosphere. In contrast, inorganic oxide perovskites are highly stable in air. Among all oxide perovskites, the most significant advancement has been obtained in BFCO thin films, which exhibited a large  $J_{SC}$  value (11.7 mA/ cm<sup>2</sup>) and relatively a high PCE (3.3%) in single layers under 1sun illumination [17]. Moreover, it was found that the Fe/Cr cationic ordering and their distribution in the films can tune the band gap of BFCO in the range of 2.1–1.4 eV. This led to the concept of designing a multi-absorber system comprising three stacking layers with different band gaps, leading to a solar cell with a breakthrough PCE of 8.1%. The PV effect in BFCO has been described by the depolarization field induced by the spontaneous FE polarization.

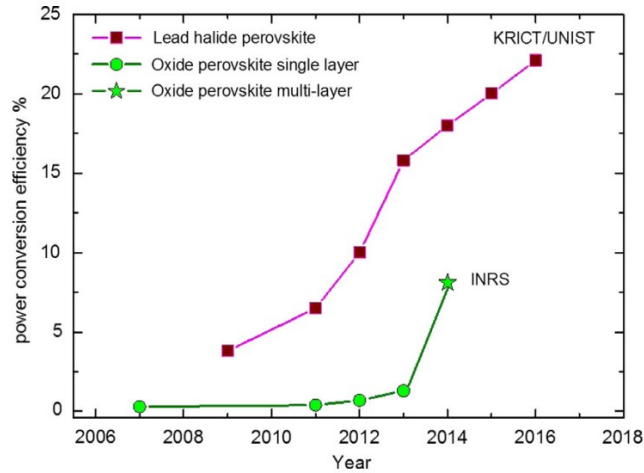


Figure 1-19 Best cell efficiencies in oxide perovskite solar cells (green curve). [143]

## 1.8 Photocatalytic properties of materials for water splitting applications

Now a day, the photovoltaic industries are dominated by solid-state junction based devices where the electric fields at the interfaces of *p*-type and *n*-type materials are the driving forces for photogenerated carriers towards electrodes. The same interfacial effect can be achieved at the semiconductor-liquid interfaces while the semiconductor surfaces (*n*-type or *p*-type) are in contact with a liquid electrolyte, thereby forming a photoelectrochemical (PEC) cell. In a PEC cell, the photocatalytic process occurs which is similar to the photosynthesis in plants [144]. In contrast with solid-state PV processes, PEC cells convert solar energy into a chemical fuel (hydrogen gas), which is easier to store than electricity [22,23]. Apart from the clean chemical fuel generation, conversion of CO<sub>2</sub> to hydrocarbons (fuels) is also of significant interest, since it appears to be a viable solution to reduce CO<sub>2</sub> emissions across the globe [145,146]. Nonetheless, the applications of photocatalysis process largely depend on the development of a variety of materials systems which are suitable for specific applications [147,148,149]. The following section describes, in

brief, the photocatalytic process that occurs in PEC cell during hydrogen and oxygen evolution reactions.

### 1.8.1 Basics and advances of photocatalytic process in water splitting

In PEC cells, the semiconductors as photoelectrodes are exposed to radiation and thus photocharge carriers are generated in the semiconductors [19,20,21,150]. These carriers are then driven into the surface of the semiconductors by the electric field that occurs at semiconductor-electrolyte junction. The charge carriers promote a redox reaction at semiconductor-electrolyte interfaces resulting in hydrogen and oxygen through decomposition of water molecules (electrolytes contain water) [24,25], as described in Fig. 1-20. The decomposition of water molecules into hydrogen and oxygen takes place due to the following reaction:



According to this equation, an energy of roughly  $\sim 1.23 \text{ eV}$  is required to dissociate the water molecules into chemical fuels i.e. hydrogen and oxygen.

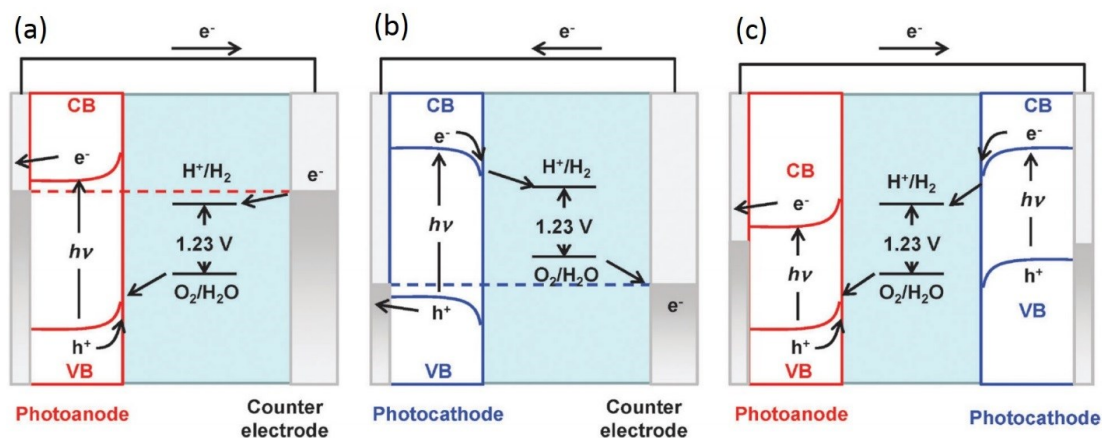


Figure 1-20 Schematics of PEC cell exhibiting energy band alignment in water splitting using (a) a photoanode, (b) photocathode, and (c) both photoanode and photocathode in the tandem configuration. [151]

Major challenges of photoelectrolysis in PEC cells are mainly related to the properties of the semiconductors. These include the efficiency of their light absorption, their chemical stability in contact with reactants, and the difficulty of matching their band-edge energies with hydrogen ( $H_2$ ) and oxygen ( $O_2$ ) evolution reactions [26,27,152]. In particular, the evolution of either hydrogen or oxygen, or both, is entirely dependent on the alignment of the valence band (VB) and conduction band (CB) edges of the semiconductor with respect to the redox potential of water [28,29]. The most prominent semiconductors with suitable band alignment with the redox potential of water are shown in the Fig. 1-21.

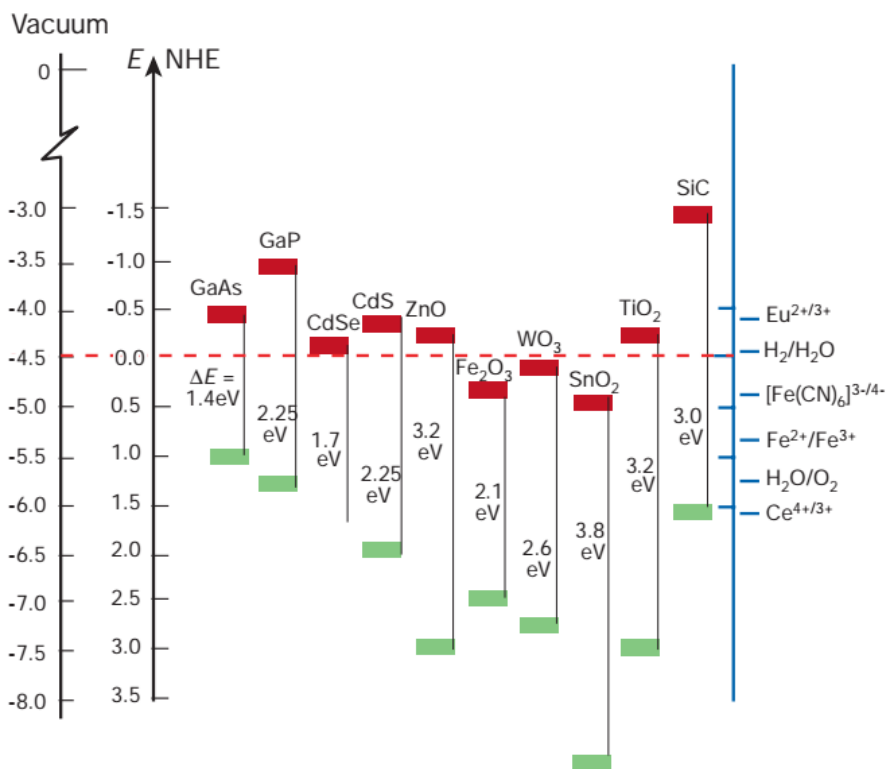


Figure 1-21 Alignment of energy band positions of prominent semiconductors in contact with aqueous electrolyte at  $p^H$  1 [26]. NHE means normalized hydrogen electrode.

In principle, the water splitting reaction occurs in three steps: (1) photons with energy higher than the band gap energy are absorbed in the semiconductor photocatalysts and the photocharge carriers are generated (2) the charge carriers are then separated and swift away to the surfaces (one type of charge carrier in semiconductor surface and another migrate to the external circuit thus reaches to the counter electrode surfaces), and (3) finally the adsorbed species on semiconductor surfaces (and on counter electrode surfaces) are reduced and oxidized by the photogenerated electrons and holes to produce H<sub>2</sub> and O<sub>2</sub>, respectively [19]. All these steps are strongly dependent on the structural and electronic properties of the semiconductor material. For example, the high crystallinity implies a reduced density of defects and thus allows the fast transport of photocarriers to the semiconductor surface while reducing the recombination centers. Sometimes, co-catalysts are deposited onto the semiconductor surfaces to promote the photocatalytic activities. The novel metals (Pt, Rh) or metal oxides (NiO, RuO<sub>2</sub>) are typically used as co-catalysts to produce more reactive sites on the surfaces, targeting to reduce the activation energy for gas evolution. Therefore, both bulk and surface properties of the materials are crucial for photocatalytic water splitting reactions.

In the 1970s, metal oxide semiconductors such as n-type TiO<sub>2</sub> were first studied as photocatalysts for water splitting [24, 153]. Since then, rigorous investigations were carried out on TiO<sub>2</sub> and TiO<sub>2</sub> based photocatalysts for water splitting reactions, partly because they offer good photostability in electrolytes (less corrosive in chemical reactions). Afterwards, the high photocatalytic activity of K<sub>4</sub>Nb<sub>6</sub>O<sub>17</sub> has also been reported due to its unique nanostructures [154]. In the late 1990s, many tantalates have also been reported to be highly active as photocatalysts [155,156,157]. Tungsten-based metal oxides, with generic formula AMWO<sub>6</sub> [A: Rb, Cs; M: Nb, Ta] also exhibit good photocatalytic performance for hydrogen gas evolution [158]. However, such oxide materials

mainly harvest ultraviolet (UV) light due to their inherently large band gap ( $>3.5$  eV) [159]. Another drawback of these metal oxide semiconductors is their low valence band edge with respect to the water oxidation potential (1.23 V vs. NHE) which requires an enormous overpotential for a redox reaction. Semiconductors such as  $\alpha$ -Fe<sub>2</sub>O<sub>3</sub> [160] and WO<sub>3</sub> [161] are also investigated extensively as potential candidates as photocatalysts in water splitting.  $\alpha$ -Fe<sub>2</sub>O<sub>3</sub> has a suitable band gap of 2.1 eV; however, its long-range antiferromagnetic order results in low charge-carrier mobility ( $\sim 10^{-2}$  to  $10^{-1}$  cm<sup>2</sup> V<sup>-1</sup> s<sup>-1</sup>) [162] and a short hole-diffusion length (of the order of 2–20 nm) [163] which limits its PEC performance. In contrast, WO<sub>3</sub> is diamagnetic, therefore the hole mobility and diffusion lengths are higher (10 cm<sup>2</sup> V<sup>-1</sup> s<sup>-1</sup> and 0.15  $\mu$ m, respectively) [164]. However, it exhibits a high band gap of 2.7 eV, and it is only stable under acidic conditions. The theoretical predictions of the maximum limit of photocurrent density that can be achieved using contemporary semiconductors in water splitting reactions are depicted in Fig. 1-22.

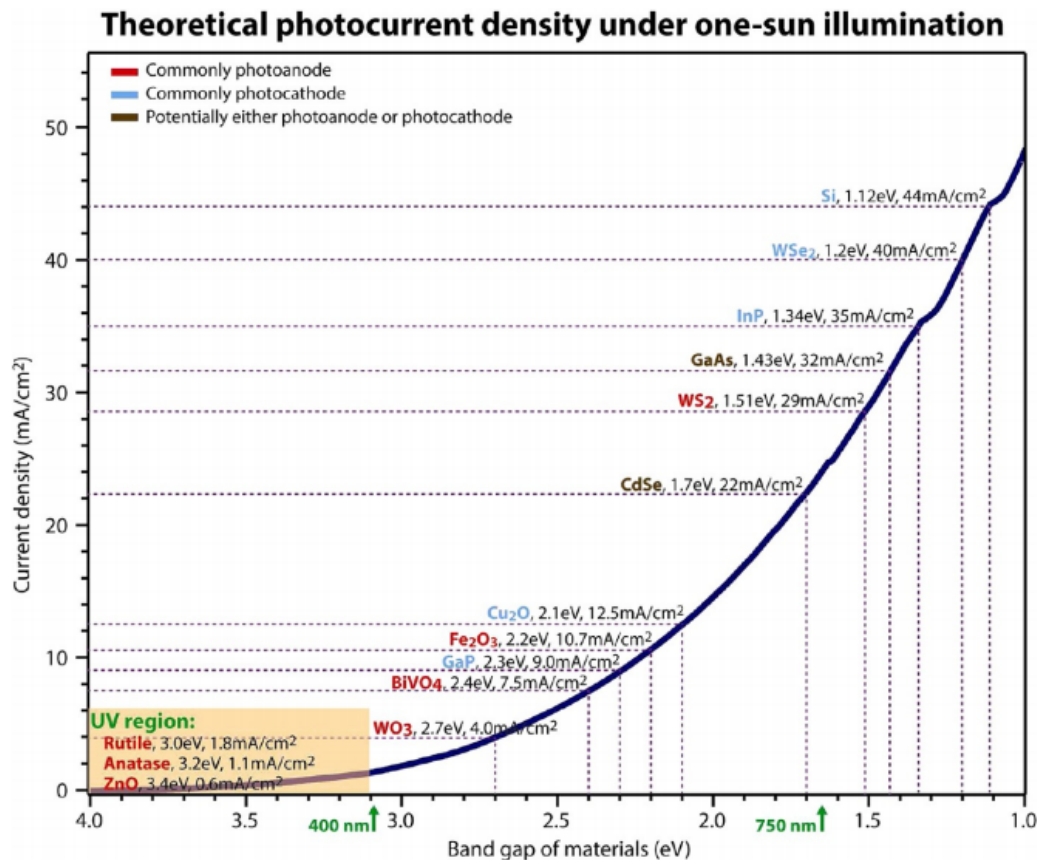


Figure 1-22 Theoretical photocurrent densities estimated for few semiconductors under one-sun illumination. [165]

### 1.8.2 Advances of oxide perovskites as photoelectrodes in water splitting

Although TiO<sub>2</sub> –based material systems are widely studied in photocatalytic applications, ternary and other complex oxide systems have been increasingly explored as photocatalysts. Among the various classes of materials, perovskite-based photocatalysts have unique photophysical properties and offer distinct advantages over other material systems. Generally, perovskites exhibit good photostability and corrosion resistance in aqueous solutions. Many perovskites offer favorable band edge potentials to initiate photoinduced reactions for hydrogen evolution. The degree of octahedral tilting in their lattice may alter the photophysical properties and band structures of

perovskites. For example,  $\text{TiO}_2$  is able to absorb UV light and the conduction band (CB) positions are above the water reduction level. However, replacement of Ti sites by suitable dopants with stoichiometric chemical ratio converts host  $\text{TiO}_2$  into perovskite crystal structures (i.e.  $\text{MTiO}_3$  where  $M = \text{Sr, Ba, Ca, Mn, Co, Fe, Pb, Cd, Ni}$ ). The changes of octahedral tilting enable more negative CB energy which makes them more suitable candidates for hydrogen generation [30,31,32,33]. Adding co-catalysts such as Rh, Ru, or  $\text{NiO}_x$  loaded on the surface of the titanate perovskites leads to an increased absorption of visible light and thus enhances the rate of the gas evolution reaction from water molecules [166,167]. Similar to  $\text{TiO}_2$  based materials, alkali tantalate perovskites ( $\text{NaTiO}_3$ ,  $\text{AgTiO}_3$ ,  $\text{KTiO}_3$ ) offer efficient photoreaction under UV irradiation [168,169,170], however, they can be altered their absorption edge from UV to visible range under the effect of doping and the inclusion of co-catalysts [171,172].

Most of the ferrite-based perovskites such as  $\text{LaFeO}_3$ ,  $\text{BiFeO}_3$ ,  $\text{GaFeO}_3$ , and  $\text{YFeO}_3$  have their native band gaps ( $< 3$  eV) in the visible region [173,174,175,176] and exhibit superior electronic properties (high exciton diffusion length, increased electron conductivity, and low conduction band edge potential) over hematite and other iron oxide compounds [36]. Among them, BFO (ferroelectric with the band gap of  $\sim 2.7$  eV) in thin film form yields a photocurrent density of up to  $\sim 5 \mu\text{A}/\text{cm}^2$  under 1 sun radiation (AM1.5G) [37]. The ferroelectric properties of BFO films could be utilized to modulate the band bending at BFO-electrolyte interfaces which can further enhance the electron-hole separation and improve the photocatalytic performances (Fig. 1-23). Additionally, the effect of doping and adding co-catalysts in BFO are widely investigated with emphasis on enhancing its photocatalytic activities.

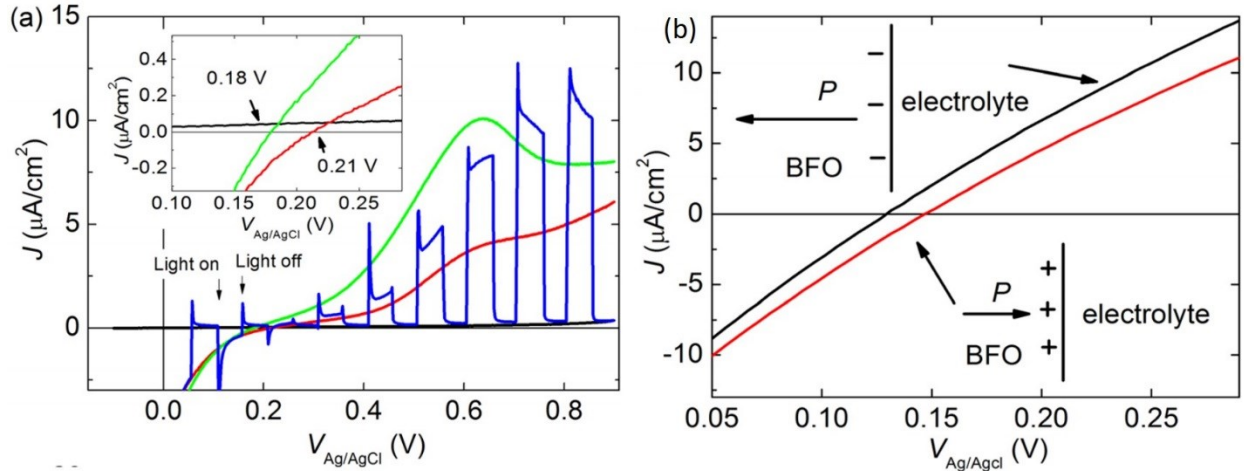


**Figure 1-23** (a) Photocurrent density of BFO/SRO/STO(001) with BFO thickness of 223 nm under 121 mW/cm<sup>2</sup> (dark, red) and 250 mW/cm<sup>2</sup> (blue, green) illumination. The inset shows the magnified portion of the onset of photocurrent density (b) impact of ferroelectric polarization. Black and red curves show negative and positive polarization charges on the surface, respectively. [37]

In addition, double perovskites (chemical formula  $A_2BB'O_6$  including  $Sr_2FeNbO_6$  [177],  $La_2FeTiO_6$  [178] and BFCO [40]) are also used as visible light absorbers which are chemically stable in aqueous solutions during photocatalytic reactions. Li et al. demonstrated the superior photocatalytic properties of BFCO thin films over BFO films. They showed that the ferroelectric property of BFCO can be used to modulate the band bending which improves the photocurrent density (Fig. 1-24).

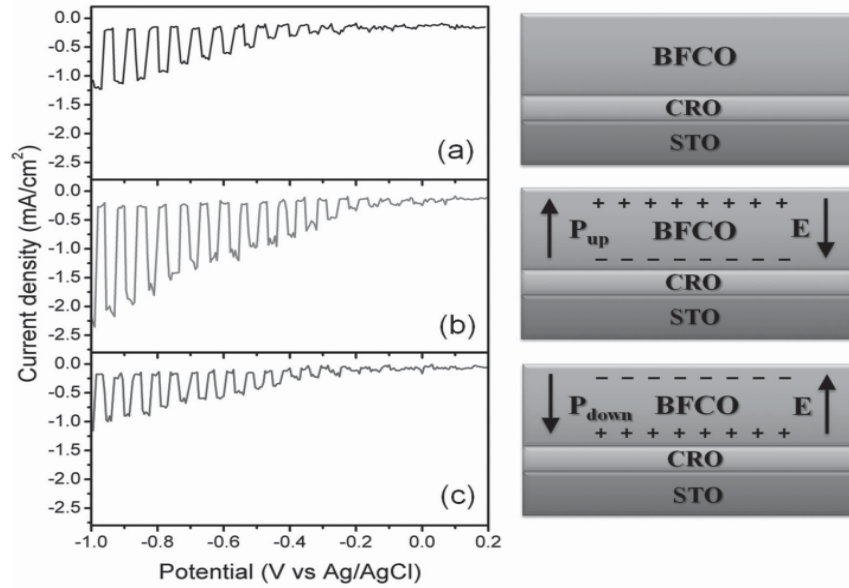


**Figure 1-24** Photocurrent densities of epitaxial BFCO/CRO/STO heterostructure without (a) and with ferroelectric poling (b,c) under chopped simulated sunlight illumination (AM1.5G). Schematic illustrations are shown on the right of each figure. [40]

## 1.9 Objectives of the thesis

For efficient conversion of solar energy into electricity, the exploration, discovery, and optimization of materials are required. Although the power conversion efficiency (PCE) of PV devices based on inorganic oxide perovskites is still not competitive with commercial PV devices, they already have shown some unique features such as larger than bandgap photovoltages and the changes of photocurrents with polarization direction which are fundamentally different from the conventional p-n junction based PV devices. In addition, inorganic oxide perovskites are particularly attractive in PV research, as their crystal structures and PV parameters (photovoltages and photocurrents) are highly stable at ambient atmosphere whereas organic-inorganic halide perovskites are reported to be highly unstable in air. Moreover, many inorganic perovskites are referred to as multifunctional materials, therefore, their applications can also be extended into new

applications including transducers, photodetectors, light emitting diodes (LEDs), microwave devices, computer memories etc. In this project, we study the inorganic oxide perovskites as active materials for solar energy conversion. In particular, we describe ferroelectric properties, grain boundaries and size effects of perovskite materials and their positive impacts on the performances of PV devices. We choose  $\text{BiMnO}_3$  (BMO) and  $\text{BiFeO}_3$  (BFO) as active material components for solar energy harvesting due to the following reasons:

BFO thin film is most widely investigated as active material components in FE PV devices. It exhibits good FE polarization ( $\sim 55 \mu\text{m}/\text{cm}^2$ ) and low band gap value (2.4-2.8 eV) compared to the band gap values of traditional FE materials ( $> 3$  eV). Although the band gap of BFO corresponds to the large visible range of the solar spectrum, it exhibits low photocurrent density ( $\text{nA}/\text{cm}^2$ ) resulting in a poor PCE ( $< 0.1\%$ ). The high insulating behavior of BFO limits the charge carrier conduction in its crystal structure thus lowering the photocurrent density. In contrast, BMO exhibits FE polarization of  $\sim 6 \mu\text{m}/\text{cm}^2$  and a band gap of  $\sim 1.2$  eV which can be used as visible and infrared light absorber in PV devices. Generally, FE perovskites with low band gap values are required in improving the performances of FE PV devices. On this basis, we previously studied FE PV effect in multiphase BMO thin films and reported a PCE of  $\sim 0.11\%$ . However, it is essential to investigate rigorously their physical and chemical properties both at the nanoscale and macroscopically to explore the overall potential of BMO compounds in solar energy research. Moreover, it is also important to assess their overall potential to be integrated with other material systems to improve the solar energy conversion efficiency. In these contexts, the objectives of this thesis are outlined as follows,

- (1) Synthesis of BMO thin films (single and multiphase) and study their ferroelectric and PV properties;
- (2) Study the electrical and optical properties of grain boundaries in multiphase BMO

thin films; (3) Synthesis of BFO/BMO bilayer thin films and study their ferroelectric and PV properties; (4) Investigate the photocatalytic behavior of BMO thin films and explore strategies to enhance photocatalytic performance of BMO based photoelectrodes in solar energy research.

## **1.10 Structure of the thesis**

The structure of the thesis is outlined as follows:

Chapter 1 describes the background literature of oxide perovskite materials for solar energy conversion.

Chapter 2 describes briefly the main experimental methods and characterization techniques used throughout this work. Starting with the pulsed laser deposition technique (PLD), the chapter covers the different types of characterizations methods such as X-ray diffraction (XRD), transmission electron microscopy (TEM), atomic force microscopy (AFM), scanning electron microscopy (SEM), piezoresponse force microscopy (PFM), solar simulator and photoluminescence (PL) spectroscopy.

Chapter 3 presents the synthesis of BiFeO<sub>3</sub>/Bi-Mn-O bilayer thin films deposited on niobium doped SrTiO<sub>3</sub> substrates by PLD and shows an enhanced PV efficiency. The bilayer made of two different band gap materials are stacked vertically on the substrates to absorb the large range of visible wavelengths of sunlight thus enhanced PCE.

Chapter 4 describes the PV effect in Bi-Mn-O composite thin films composed of two different types of crystalline phases: BMO and BiMn<sub>2</sub>O<sub>5</sub>. The results show a record PCE in the composite films. A model based on grain boundary (GBs) barrier potentials is employed to describe the physics behind the PV effect in these composites.

Chapter 5 describes the photoelectrochemical (PEC) properties of BMO thin films and nanostructures. BMO nanostructures exhibit superior PEC performance over films.

Chapter 6 outlines the conclusions and future perspectives.

## Chapter 2 Experimental Methods

### 2.1 Growth of thin films

#### Pulse laser deposition

A pulsed laser deposition (PLD) system consists of a high vacuum chamber equipped with the facilities needed for rotating a target and a substrate material (s). The target holder is located in front of the substrate holder. The schematic of a typical PLD system is shown in Fig. 2-1. In PLD systems, an external laser beam with sufficiently high energy density is focused on the surface of the targeted material. Each laser pulse ablates a small amount of material from the target, creating a plasma plume in front of the surface. The plume expands adiabatically towards the substrate, where the material is deposited. Generating and expanding plasma plume undergoes three consecutive processes: interaction of the laser beam with the target material resulting in evaporation of a thin surface layer, interaction of the evaporated material with the incident laser beam resulting in an isothermal plasma formation and expansion, and anisotropic adiabatic expansion of the plasma leading to the characteristic nature of the laser deposition process [179]. This plume supplies sufficient material to the substrate for film growth. The important parameters of PLD that might affect the morphology and crystal quality of thin films are as follows: the vacuum base pressure (typically  $10^{-5}$ - $10^{-10}$  mbar), the background gas pressure (for most complex oxide materials 1-100 mbar), substrate temperature during deposition (500-1000 °C), laser fluence (1-3 J/cm<sup>2</sup> for most perovskite oxide materials), laser frequency (repetition rate of the pulses, 1-20 Hz), the distance between the target material and substrate distance, and laser spot size on the target material. All parameters are interdependent. Despite exhibiting the presence of few droplets on the thin films, the ability to transfer stoichiometric atomic composition from target materials

even from a complex compound into plasma plume makes PLD a suitable candidate for complex materials synthesis [180]. More detail description of PLD is provided in the reference [181].

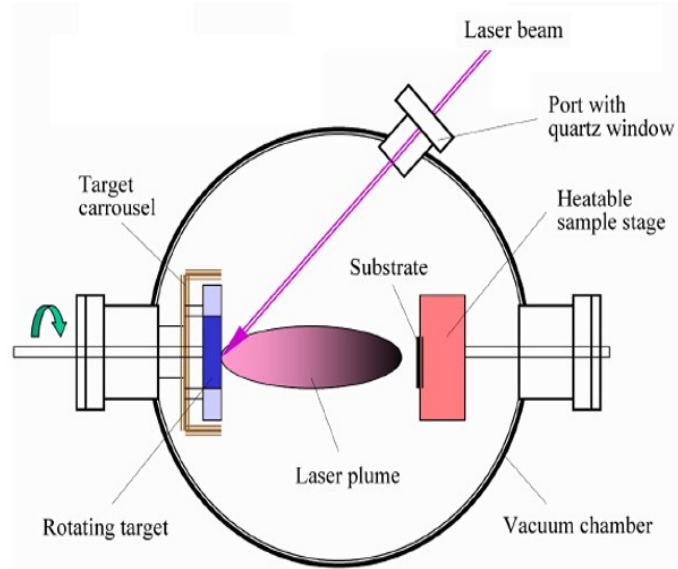


**Figure 2-1** Schematic diagram of basic pulse laser deposition (PLD) system. [182]

In this study, we have used a PLD system consisting of a GSI Lumonics KrF excimer Laser ( $\lambda = 248$  nm with a pulse FWHM  $\tau = 15.4$  ns) and a vacuum chamber. The chamber is evacuated to reach our required background vacuum pressure ( $\sim 10^{-5}$  mbar) by using a mechanical and turbo pump establishing outside of the chamber. The laser pulses enter into an optical system made of mirrors and lenses, then enter into the chamber through a quartz window and finally strikes the target material at an angle of  $45^\circ$  from the normal of the material surface. A numerical computer control system has been employed to control and measure the laser parameters, particularly pulse repetition rate, laser energy and the number of laser pulses. The substrate temperature is monitored using a K-type thermocouple during film deposition. The other parameters are substrate temperature, substrate-target distance, and flow rate of oxygen during deposition.  $\text{BiFeO}_3$ ,

$\text{Bi}_{1.4}\text{MnO}_3$ , and indium doped tin oxide (ITO) targets were purchased from MTI Corporation. 0.5% Nb-doped  $\text{SrTiO}_3$  substrates were purchased from Crys Tec. Inc.

## 2.2 Characterization methods

### 2.2.1 X-ray diffraction

X-ray diffraction (XRD) scan is employed to determine the crystal structures of the as-grown perovskite thin films and nanostructures. **Figure 2-2** illustrates the working principle of XRD. Geometrically, the distance between two parallel planes of periodically arranged planes ( $d$ ), the wavelength of a monochromatic X-ray source ( $\lambda$ ) and the diffraction angle ( $\theta$ ) are being correlated with each other by the following equation (known as Bragg's law),

$$n\lambda = 2d \sin\theta \dots\dots\dots(2.1)$$

where  $n$  is the order of reflection. Since the wavelength ( $\lambda$ ) is roughly equal to the distance between two atoms (approx.  $0\text{-}5 \text{ \AA}$ ), the XRD technique is an extremely powerful tool for measuring the crystalline structure of a given material. In this thesis, we have used XRD system named High-resolution PANalytical X'Pert Pro MRD 4-circle diffractometer system. The system is designed for several measurements such as  $\theta$ - $2\theta$  scan (Bragg-Brentano), grazing incidence, Phi scan, texture analysis, high-resolution reciprocal space mapping (RSM), high resolution rocking curve measurement, residual stress analysis, and X-ray reflectivity measurement. In our study, we used extensively  $\theta$ - $2\theta$ , Phi scan and RSM measurements. Phi scan measurements are used to observe the cube on cube epitaxy of the films whereas RSM measurements around the (204) reflection of the substrate are used to identify the crystal structure of the obtained films, and to calculate the lattice parameters.

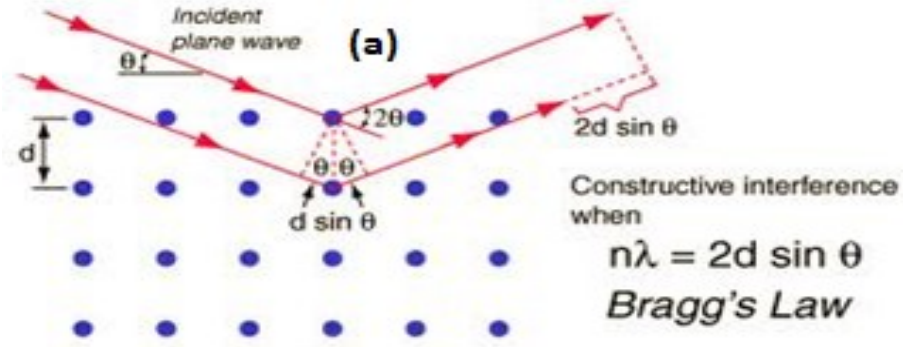


Figure 2-2 Schematic of diffraction of X-rays by the periodic arrangement of planes of atoms. [183]

### 2.2.2 Scanning electron microscope

Scanning electron microscope (SEM) is used to record the images of the surfaces of the objects. In SEM, a focused electron beam scans over the surface of the sample in vacuum to extract structural and chemical information point-by-point from a region of interest in the sample. The typical beam diameter of the SEM is in the range of 5 nm to 2  $\mu$ m and the working (accelerating) voltage is in the range of 2 to 50 KV. SEM deals with basically three types of electrons: secondary electrons, backscattered electrons, and elemental X-ray. In SEM, secondary and backscattered electron signals are used for the visualization of the surface of a specimen. Secondary electrons, a result of inelastic collisions, are used to image the surface structure of a sample with the resolution of 10 nm or better. Nevertheless, backscattered electrons, a result of the elastic collision, help to resolve topographical contrast and atomic number contrast with a lateral resolution better than 1 micron. While secondary electron imaging infers an energy of the emitted electrons below 50 eV, the backscattered electrons have an energy greater than 50 eV [184]. SEM can only deal with conductive specimens and provides surface imaging. In addition, it cannot detect the materials which have an atomic number smaller than that of carbon. More detail description is provided in

the reference [181]. In this thesis, the SEM (FESEM, JEOL JSM7401F) set up with an acceleration voltage of 5 kV is used to record the images.

### **2.2.3 Transmission electron microscopy**

Transmission Electron Microscopy (TEM) is a very powerful technique to extract information about the crystalline structure of the specimen. TEM provides different types of diffraction patterns such as dots, regions or circles which are originated from the irradiated area of the sample. Dotted, center-circled and diffuse-circled diffraction pattern indicate mono-crystalline, the polycrystalline and amorphous structure of the specimen, respectively. In TEM, a beam of electrons scatters through a crystalline specimen according to the Bragg's law. The scattered beams at small angles are focused by the objective lens to form a diffraction pattern at its back focal plane. The scattered beams are recombined to form an image in the image plane [184]. In the case of diffraction patterns, the whole illuminated area of sample generates electrons, and, in order to protect the screen, a virtual image of the specimen is produced by placing a small aperture in the image plane of the objective lens. The pattern obtained by placing this aperture is called selected area diffraction (SAD). In this thesis, we used JEOL 2100F TEM at 200 KV to analyze the crystal quality and crystal orientations of the film-substrate interface (cross-sectional image). To perform TEM analysis, the samples were prepared by Focused Ion Beam using a Hitachi FB2000A. To obtain crystallographic information of a phase, the sample was tilted to a certain zone axis using Kikuchi patterns as guidelines. The zone axis is the direction that is parallel to the intersection of two or more families of lattice planes. Therefore, tilting the beam direction parallel to a certain zone axis will maximize the number of diffraction spots (planes) in a diffraction pattern. To facilitate the

analysis, diffraction patterns were also drawn via crystallography software (Carine Crystallography) by comparison with the actual diffraction patterns obtained from TEM data.

#### **2.2.4 Atomic force microscopy and Piezoresponse force microscopy**

Atomic force microscopy (AFM) imaging relies on the measurement of the forces either attractive or repulsive between a sharp fine tip on a cantilever and a sample. The tip is attached to the free end of a flexible cantilever. The force acting on the tip is transmitted to the cantilever, which deflects a laser beam reflected off from its back onto a segmented photodiode that gives signals which can be used to obtain the deflection of the cantilever. AFM has three different types of operating mode which are contact mode, non-contact mode and tapping mode i.e. intermittent contact mode. In Piezoresponse force microscopy (PFM) measurements, AFM with a conductive tip is used to probe the local ferroelectric polarization states and the electromechanical properties of the samples via converse piezoelectric effect. In this process, the local lattice vibrations of the ferroelectric samples induced by an applied AC signal between conductive tip and the bottom electrodes are detected to construct the image. A lock-in system is employed to extract the induced local oscillations of the sample surfaces to eliminate the noise together with all harmonic components from the actual deflection signal. The remaining signal provides only the sample response and is referred to as piezoresponse signal. The schematic of PFM circuitry is depicted in

**Fig. 2-3.**

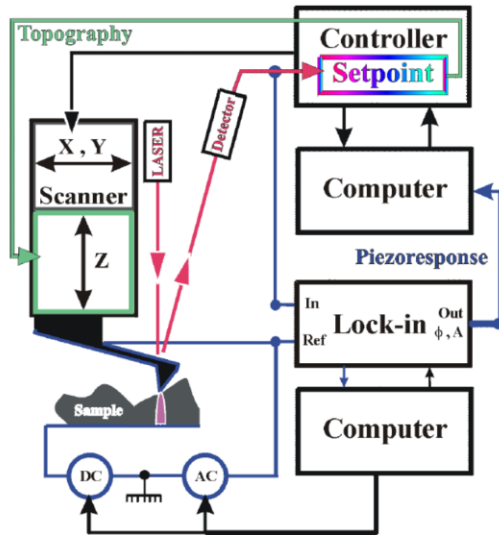


Figure 2-3 Experimental setups for a typical PFM measurement. [185]

In our work, we have used tapping mode of operation of AFM to image the surface of the as-grown thin films. In PFM experiments, the bias voltage between the top BMO surface and the NSTO substrates was applied using a C-AFM tip while scanning. The experimental set up was composed of an AFM Enviroscope system (Veeco Instruments, now Bruker), equipped with conductive silicon cantilever with Co/Cr coated tip (MESP, Bruker), and the model 7265 DSP dual Lock-in from Signal Recovery (a division of AMETEK, Inc, USA), to both excite electrically the sample and detect the response. The amplitude of the applied AC modulation was 0.5 V at 20 kHz. Hysteresis loop measurements were performed using a computer controlled Keithley 2400 Digital SourceMeter (Cleveland, OH) which supplied the DC voltage (-5 V to +5 V), connected in series with the AC source.

### 2.2.5 Conductive atomic force microscopy

Conductive atomic force microscopy (C-AFM) is a scanning probe technique capable of imaging the surface of the samples using contact mode of AFM operation under in which the electrostatic

interaction is minimized by application of an appropriate bias voltage during topographic imaging. The same kind of tip is used as used in PFM experiments. The topography and associated current image both under dark and illumination were measured by photoconductive AFM (Pc-AFM) (Smart SPM1000 from AISTNT, Inc.). Pc-AFM was conducted by illuminating the sample locally with a laser (632 nm wavelength, 4 mW power, 0.4 NA objective) to confirm the presence of the bulk photovoltaic effect. The current is measured with a pre-amplifier with a choice of three measurement scales (1 nA, 100 nA, and 10  $\mu$ A) and four choices of integration frequencies (100 Hz, 1 kHz, 7 kHz, 30 kHz).

### **2.2.6 Kelvin probe force microscopy**

Kelvin probe force microscopy (KPFM) is a non-contact AFM operation mode in which the electrostatic interaction is minimized by the application of an appropriate bias voltage during topographic imaging. In the case of metallic samples, the bias voltage is applied accounting the local work function difference between tip and sample surface i.e. the contact potential difference (CPD). However, it provides information about the surface charges in the case of insulating surfaces. In our experiments, the KPFM set up was equipped with a similar tip as for PFM (radius at the apex below 30 nm). KPFM was implemented using a PLLproII controller from RHK Technology. We used a double modulation scheme, mechanically oscillating the cantilever at its first (fundamental) resonance (around 55 kHz, tip-dependent) for topography imaging, while the second resonance ( $\sim$ 310 kHz) was used for electrostatic modulation, as described in reference [186]. Both topography and surface potential (SP) were measured simultaneously, in a single pass. The double-pass technique was not used since preliminary experiments showed worsening of the lateral resolution when using lift mode. The amplitude of the AC excitation applied was again 0.5 V.

### **2.2.7 Macroscopic ferroelectric hysteresis loop measurements**

Macroscopic ferroelectric measurements were performed using a Thin Film Analyzer (TFA 2000) at room temperature to record polarization-voltage (P-V) hysteresis loops. A triangular wave was applied to bias the sample while recording the hysteresis response.

### **2.2.8 Ultraviolet photoemission spectroscopy**

Ultraviolet photoemission spectroscopy (UPS) is a quantitative spectroscopic technique extensively used to measure the kinetic energy spectra of photoelectrons emitted by surface atoms of the respective samples which have absorbed ultraviolet photons, in order to determine the absolute value of the work function (Fermi level,  $E_F$ ) and ionization potential (equivalent to valence band edge,  $E_V$ ) of semiconductor materials. UPS spectra were taken using ESCA Escalab 220i XL with a monochromated Al K $\alpha$  X-ray source (1486.6 eV). UPS measurements were carried out using He I (21.22 eV) photon lines from a discharge lamp.

### **2.2.9 Ellipsometry**

Ellipsometry is a non-destructive optical technique which is used for the measurement of the optical properties of a sample material. The principle is based on the change of the polarization state of the light after reflection at oblique incidence on the sample surface. The measurement provides two independent parameters,  $\psi$ , and  $\Delta$ , which gives all relevant information about the polarization state of light at a given wavelength. Based on the values of  $\psi$  and  $\Delta$ , the thickness, refractive index, surface roughness, and extinction coefficient  $k$  of the materials are determined. The absorption coefficient  $\alpha$ , one of the important parameters of optical properties of the films is deduced from the extinction coefficient  $k$  by using the following formula:

$$\alpha = \frac{4\pi k}{\lambda} \dots\dots\dots (2.2)$$

Where  $\lambda$  is the wavelength of incident light.

In our experiments, the optical behavior of thin films was investigated by analyzing the absorption spectra collected by variable angle spectroscopic ellipsometry (VASE, J. A. Woollam Company) at room temperature. To obtain the ellipsometric data ( $\psi$  and  $\Delta$ ), the measurements were performed in the photon energy range of 1.22 to 3.45 eV at five angles of incidence (55, 60, 65, 70 and 75°). The ellipsometric data were collected for the naked substrates and the films on substrates respectively. The optical response of the naked substrate, employed later to extract the optical response of the films, was demonstrated using a Gaussian oscillator model which shows the Kramer-Kronig consistency of the real and imaginary parts of dielectric constants. Subsequently, the optical response functions (n, k) were extracted by fitting the ellipsometric spectra to the corresponding optical model consisting of substrate/film/surface roughness/air ambient structure. By varying the parameters of the models in the fitting procedure, the root mean square error (RMSE) was minimized. The three sets of data extracted for optical functions of three different samples were averaged to estimate the absorption coefficient.

**2.2.10 Photoluminescence spectroscopy**

Photoluminescence (PL) is an optical phenomenon which involves absorption of energy and subsequent emission of light. The PL spectra can be used to determine the optical band gaps, identify surface, interface and impurity levels in the material systems. The PL intensity and its dependence on the level of photo-excitation and temperature are directly related to the dominant recombination process. Analysis of PL helps to understand the underlying physics of the recombination mechanism. In our experiment, the samples were measured using an excitation

wavelength of 405 nm using the PL experimental set up (Horiba Jobin Yvon). The photoemission spectra of the wavelength of 400 nm to 800 nm were collected.

### **2.2.11 Solar simulator**

Depending on the tilting of earth's surface, The American Society for Testing and Materials (ASTM) publishes three spectra: AM0, AM1.5 Direct, and AM1.5 Global. Among them, AM1.5 Global is used to characterize the terrestrial solar cells because the radiation of AM1.5G is as equivalent to the radiation intensity of sunlight in the earth surface. In our experiment, we used SS50AAA solar simulator (class AAA) which consists of a high-pressure Xenon Lamp (Xenon Short Arc) with 150 W power and a built-in touch panel color display system controller. Matching the sun's spectra of AM 1.5G, the output power of the system on the sample located on the flat surface is  $100 \text{ mW/cm}^2$  (with an error of  $\pm 15\%$ ). Solar spectra of our system are matched to American Society for Testing and Materials (ASTM) E927 standard (with the error of  $\pm 25\%$ ). The lifetime of the lamp is 1000 hours. The system provides controls on the intensity of Xenon lamp having additional shutter controlling the steady state light source.

### **2.2.12 External quantum efficiency measurement**

External quantum efficiency (EQE) measurements were performed using an Oriel IQE 200 certified systems equipped with a 250 W QTH lamp as monochromatic light source covering the spectral range of 300-1800 nm with a resolution of 10 nm. The system meets the ASTM E1021-12 standard test method for spectral responsivity measurements of PV devices. The system was calibrated with Si and Ge detectors.

# Chapter 3 Enhanced Photovoltaic Properties in Bilayer BiFeO<sub>3</sub>/Bi-Mn-O Thin Films

## 3.1 Introduction

Photovoltaic (PV) devices must harvest the wide range of visible light of solar spectrum to improve the solar energy conversion efficiency. Among all inorganic oxide perovskites, multiferroics (MF) exhibit relatively low energy band gaps (1.1-2.8 eV) compared to the band gap values ( $> 3$  eV) of traditional ferroelectric (FE) materials including LiNbO<sub>3</sub> (LNO), BaTiO<sub>3</sub> (BTO) and Pb(Zr,Ti)O<sub>3</sub> (PZT), thus promising to harvest visible part of sunlight. So far, the most widely investigated MF material for PV device applications is BiFeO<sub>3</sub> (BFO). BFO exhibits FE property at room temperature and offers a comparatively small band gap (2.4–2.8 eV) compared to traditional FE materials [187]. Although BFO can yield large anomalous open-circuit voltage ( $V_{oc}$ ) [11,12,188] under illumination that exceeds several times of its band gap, the photocurrent density of pure BFO-based PV devices is extremely low (in the range of nA/cm<sup>2</sup>). BiMnO<sub>3</sub> (BMO) is another MF which, in contrast to BFO, exhibits weak FE property at room temperature and has a smaller band gap ( $\sim 1.2$  eV) [189], resulting in the absorption of the large wavelength range of the solar spectrum. Overall BMO [189] and BFO [190] thin films exhibit extremely low power conversion efficiency (PCE) under 1 sun (0.11% and below), which limits their individual application in PV devices. A recent report showed that Fe and Cr cation ordering in Bi<sub>2</sub>FeCrO<sub>6</sub> (BFCO) thin films can substantially tune the band gaps from 2.4-1.4 eV offering great potential to fabricate multilayer FE PV devices with graded band gaps in perpendicular stacking to substrates. The absorbance of a large range of the solar spectrum by grading the band gap of BFCO in a device named multi-absorber leads to a high photocurrent generation and a corresponding high PCE (up to 8.1%) [17].

In addition, the formation of a band discontinuity including a Schottky barrier at electrode-FE interface increases the driving force that effectively separates photocarriers in the devices [191,192].

Inspired by the multi-absorber concept, in this chapter, we combine BFO and BMO by growing BFO/BMO bilayer thin films sandwiched between top Sn-doped indium oxides (ITO) electrodes and bottom conducting Nb (0.5%) doped SrTiO<sub>3</sub> substrates (NSTO). A PCE of ~1.43% is recorded in BFO/BMO bilayer thin films under 1 Sun illumination, which is higher than any PCE ever reported in individual BFO or BMO thin films i.e. 14.3 times higher than relatively higher PCE of BMO. Ferroelectricity plays a crucial role in the PV effect, as shown by the dependence of the photocarrier transport properties on the orientation of the spontaneous polarization. We describe the observed PV behavior by developing a model based on the energy band structure of all device components and show that the band alignment is modulated by polarization switching. This work opens new perspectives towards the enhancement of the PCE and fill factor in bilayer FE PV devices, which are promising candidates for future use in low power electronic device applications.

## **3.2 Experimental methods**

### **3.2.1 Thin film growth**

Heteroepitaxial BFO/BMO structures were grown on (111) oriented single crystal NSTO substrates by pulse laser deposition (PLD). Bi<sub>1.4</sub>MnO<sub>3</sub> and 10% Bi-rich BFO targets were used to first deposit epitaxial BMO films on NSTO substrates, followed by BFO films. The PLD chamber was pumped to a vacuum level of  $1 \times 10^{-6}$  mbar prior to deposition in both cases. In the case of BMO films, the deposition parameters were set as follows: laser fluence and pulse frequency ~1.5 J/cm<sup>2</sup> and ~ 3 Hz respectively. The substrate temperature was kept constant at ~ 600 °C under a

partial oxygen pressure of  $\sim 10$  mTorr. Subsequently, the as-prepared epitaxial BMO films were used as a template to grow BFO films. In this case, the laser fluence, pulse frequency, substrate temperature and partial oxygen pressure were  $\sim 1.5$  J/cm<sup>2</sup>,  $\sim 6$  Hz, 600 °C and  $\sim 15$  mTorr, respectively. The target to substrate distance was  $\sim 5.5$  cm in both cases. After each deposition, the as-grown films were cooled down to room temperature under vacuum in both cases. The thickness of both films was  $\sim 60 \pm 10$  nm, as estimated from x-ray reflectivity and transmission electron microscopy (TEM) measurements. For electrical measurements, Sn-doped In<sub>2</sub>O<sub>3</sub> (ITO) top electrodes were deposited by PLD through masks on the surface of the as-grown film at  $\sim 200$  °C. The surface area of the octagonal shaped ITO electrode for all devices was  $\sim 0.003$  mm<sup>2</sup> to  $0.0009$  mm<sup>2</sup>.

### 3.2.2 Current-voltage measurements

The PV properties of the BFO/BMO heterostructures were investigated by performing current density–voltage (J-V) measurements both in dark and under light illumination with a maximum power density of 100 mW/cm<sup>2</sup> (AM 1.5 G). A computer controlled Keithley 2400 Digital Source Meter was used for applying external bias. Prior to each measurement, the pristine samples were poled by applying 1  $\mu$ s 5 voltage pulses of magnitude  $-15$  V ( $+15$  V). To record J-V curves, the bias was swept between  $+1$  V and  $-1$  V, far below the ferroelectric coercive voltage to prevent changing the polarization direction during measurement.

## 3.3 Characterizations

### 3.3.1 Crystal structures

**Figure 3-1a** shows the  $\theta$ - $2\theta$  scan of X-ray diffraction (XRD) which reveals the preferential pseudocubic structure of  $(111)_{pc}$  oriented BMO phases and  $(111)_{pc}$  oriented BFO phases following

the cubic (111) direction of NSTO substrates. BMO films also contain a small quantity of the  $\text{Mn}_3\text{O}_4$  (MO) phase, oriented along the tetragonal  $(101)_t$  direction, similar to that previously found in BMO composite films [189]. The  $\Phi$  scan analysis around the NSTO (101) reflection suggests epitaxial growth of both films with a threefold symmetry, as shown in Fig. 3-1b. In addition, the presence of the two phases, i.e. BFO and BMO in the film is further confirmed by reciprocal space mapping (RSM) around the STO (312) reflections, which clearly demonstrates two distinct spot reflections, as shown in Fig. 3-1c. The calculated in plane and out of plane lattice parameters of BFO ( $a = b \approx 3.924 \text{ \AA}$ ,  $c \approx 4 \text{ \AA}$ ) and BMO ( $a = b \approx 3.932 \text{ \AA}$ ,  $c \approx 4.1503 \text{ \AA}$ ) from RSM measurements suggests pseudo-cubic tetragonal structure on the NSTO substrates.

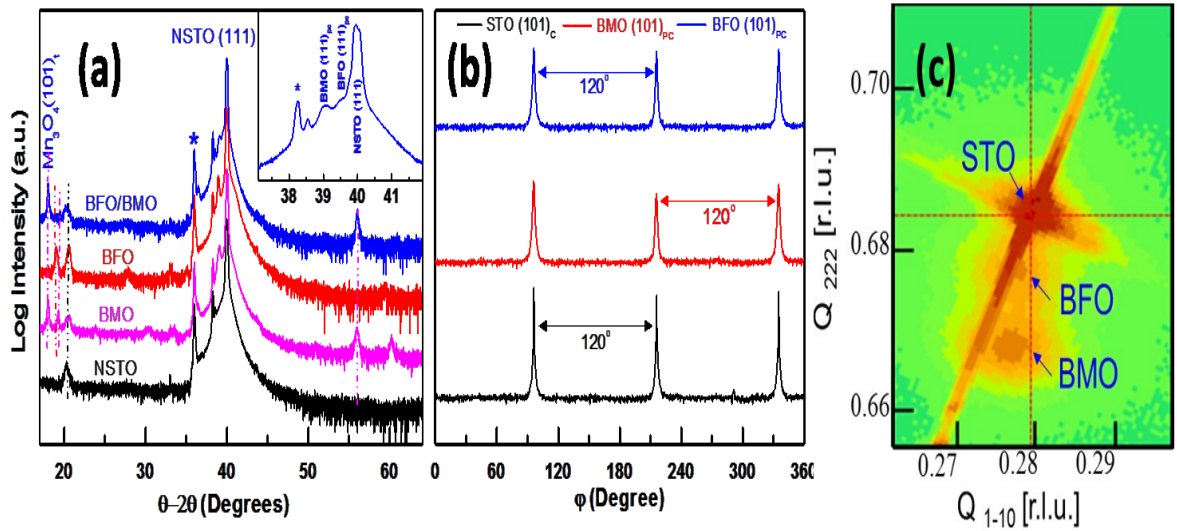


**Figure 3-1** (a) XRD  $\theta$ - $2\theta$  scans of bear NSTO substrates, the as-deposited BMO, BFO and BFO/BMO layer respectively. The respective films grown on (111) oriented NSTO substrate shows  $(1/2, 1/2, 1/2)$  reflections of BFO, BMO and small percentages of  $(101)_t$  orientation of  $\text{Mn}_3\text{O}_4$  phases. The inset clearly shows  $(111)_{pc}$  and  $(111)_{pc}$  orientation of BMO and BFO phases. The symbol ‘\*’ indicates tungsten contamination of the x-ray tube source (b)  $\Phi$  scan measurements

show three-fold symmetry of BMO, BFO and NSTO respectively, demonstrating the epitaxial nature of the films (c) RSM around NSTO (312) reflections shows the two spots related to the coexistence of BMO and BFO lattice.

### 3.3.2 Surface roughness and interfaces

A typical Atomic Force Microscopy (AFM) image of the BMO surface and the corresponding top BFO surface are illustrated in Fig. 3-2a,b. The surface roughness of BMO film is  $\sim 2.5$  nm (RMS) with a peak to valley around  $\sim 8$  nm over a  $10 \times 10 \mu\text{m}^2$  area. The top BFO surface exhibits a surface roughness of  $\sim 5.6$  nm (RMS) and a peak to valley of  $\sim 17$  nm (Fig. 3-2b). The surface roughness of BMO may promote the intermixing phenomena at the interface, especially when 2D growth conditions are not achieved. The intermixing between Fe and Mn might lead to the formation of an additional pure phase of  $\text{Bi}(\text{Fe}_{1-x},\text{Mn}_x)\text{O}_3$  (BFMO) or solid solution of BFO and BMO at the interface. These types of intermixing phenomena are also observed in other metastable alloys or solid solutions by synthesis the films with sequential PLD [193,194]. Although the existence of  $\text{Bi}(\text{Fe}_{1-x},\text{Mn}_x)\text{O}_3$  phase at the interface due to intermixing has been predicted in BFO buffered BMO films achieved after post-annealing [195] however cross-sectional TEM images (Fig. 3-2c) shows sharp interfaces at BFO/BMO interfaces in our cases.

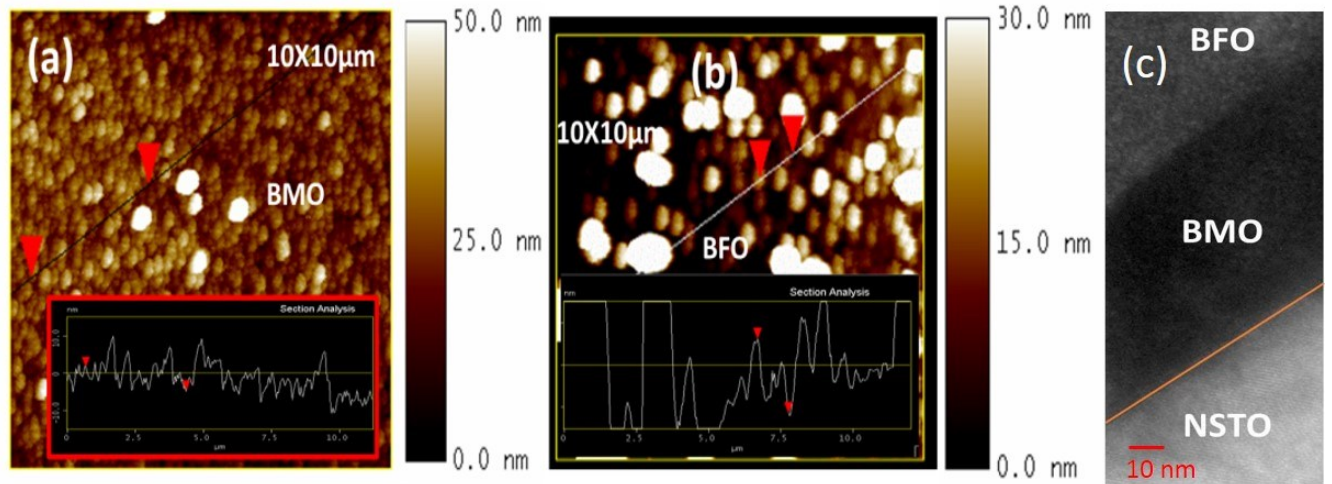


**Figure 3-2** AFM surface topography image of BMO (a) and BFO (b) respectively. The inset shows respective surface profile analysis of each. (c) Cross sectional TEM image taken at the resolution of 10 nm shows sharp interfaces at BFO/BMO interface.

### 3.3.3 Ferroelectric properties

The presence of ferroelectricity in the samples at grain level is demonstrated by local electromechanical measurements using piezoresponse force microscopy (PFM), as shown in **Fig. 3-3a,b**. The FE domains can be individually or partially switched by applying  $\pm 10$  V voltage pulses, as shown in the marked area of **Fig. 3-3a**. In addition, the recorded PFM hysteresis loop shown in **Fig. 3-3b** demonstrates a strong PFM response of the top BFO layer ( $2d_{zz}^{\text{BFO/BMO}} \sim 34$  pm/V) compared with single layer BMO ( $2d_{zz}^{\text{BMO}} \sim 1$  pm/V) [189], indicating that the top BFO layer contributes more to the PFM signal. This can be explained as follows: first, it is well-known that the PFM signal originates within the topmost few 10 s of nanometers under the tip, due to the highly non-uniform electric field [196,197]. Second, the room temperature permittivity of BFO films is significantly smaller than that of the BMO ( $\sim 130$  [198] compared to  $\sim 500$  [199]) at frequencies comparable to our PFM measurement (10 kHz). Therefore, even in the case of a

uniform electric field across the heterostructure, the relative voltage drop would occur mainly across the BFO layer. In our films, we inferred the permittivities from the slope of the FE hysteresis loops, measurements which also confirm the FE behavior at macroscopic scale. The plots in Fig. 3-3c,d show the macroscopic polarization hysteresis of the as-deposited bilayer heterostructures and of the as-grown BMO single layer, respectively. As can be clearly seen, the slope is almost zero (with an absolute error estimated around 20, due to the leakage currents) for the heterostructure (Fig. 3-3c) while we estimate a value of  $\sim 50$  for the BMO layers only (Fig. 3-3d). Furthermore, the fact that the polarization of the heterostructure is much higher than that of BMO, and it switches, means that the voltage drops across the BFO component is sufficient to reverse polarization, implying (from the electrostatic boundary condition at the interface) that its permittivity is sufficiently low. This confirms our previous supposition that the PFM response comes mainly from the BFO layer. The BMO layer alone (Fig. 3-3d) exhibits a low remnant polarization (without leakage current compensation) of  $\sim 1.33 \mu\text{C}/\text{cm}^2$ , well below that previously reported for similar films at room temperature [189]. The positive and negative coercive voltages measured are around  $\sim 2.5 \text{ V}$  and  $\sim -3 \text{ V}$  respectively. The loops in Fig. 3-3c exhibit almost the same coercive voltages ( $\sim +3 \text{ V}$  and  $\sim -4 \text{ V}$  respectively) at two different frequencies. In both P-V loops, an imprint was observed which likely originates from the presence of a small leakage or the effect of using different types of top and bottom electrodes. Therefore, we conclude from the above discussion that the heterostructure exhibits large FE contributions from BFO films rather than from BMO itself.

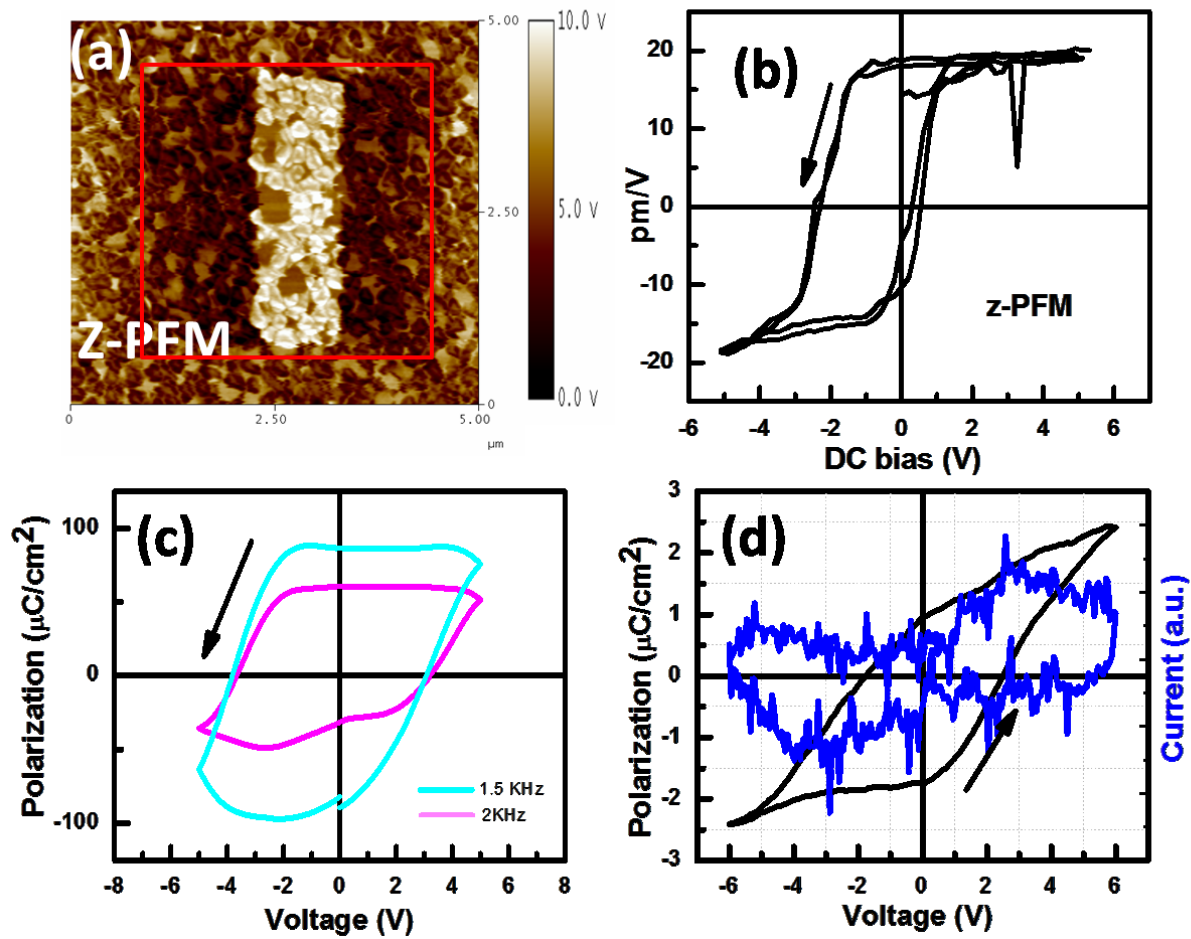


**Figure 3-3** Local scale (a,b) and microscopic (c,d) FE characterization of one of the samples measured on the top BFO surface. (a) Out of plane PFM image shows switching of polarization direction after subsequent poling the area encircled with +10V/-10V/+10V voltage pulses. (b) Corresponding in-field hysteresis loops of z-PFM signals. (c) Voltage vs polarization curve recorded on the heterostructure in two different frequencies. (d) Voltage vs polarization curve recorded on the top of BMO layer. The blue curve exhibits the corresponding current which represents the switching of polarization.

### 3.3.4 Optical properties

Optical measurements were performed to study the absorption properties of the films. The absorption coefficient ( $\alpha$ ) is presented as a function of photon energy (E) in Fig. 3-4. As seen in Fig. 3-4a, the optical absorption threshold of BMO is  $\sim 1.50$  eV while that of BFO is  $\sim 2.40$  eV. From the  $(\alpha E)^2$  versus E plot, we calculate a band gap,  $1.2 \pm 0.1$  eV for BMO, and  $2.7 \pm 0.1$  eV for BFO respectively. These values are roughly equal to the values reported previously in the analysis of BFO [200] and BMO [189] optical absorption.

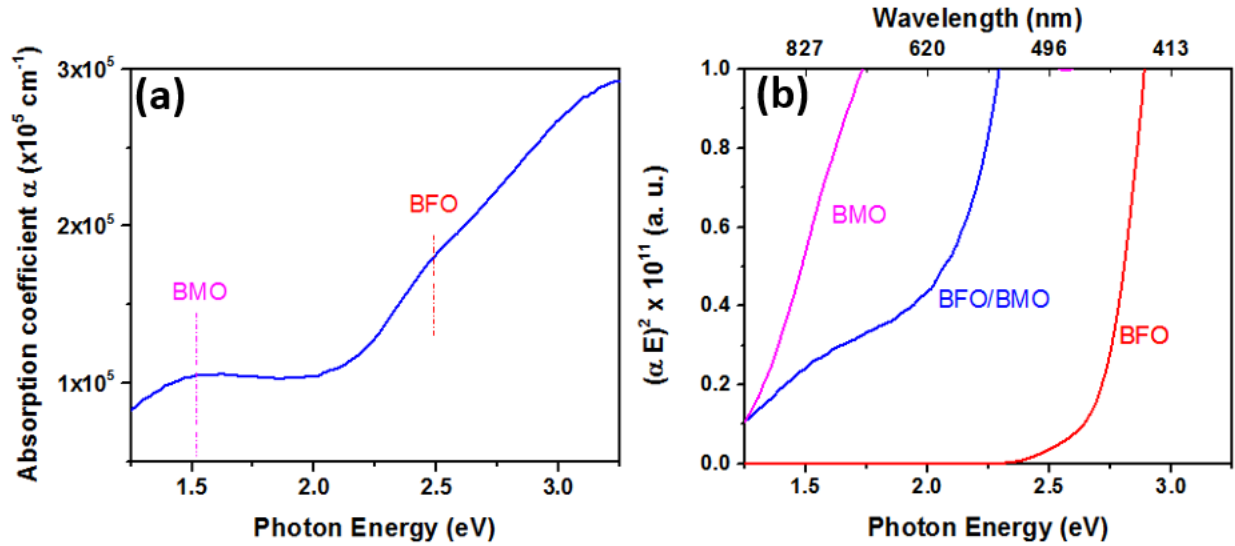
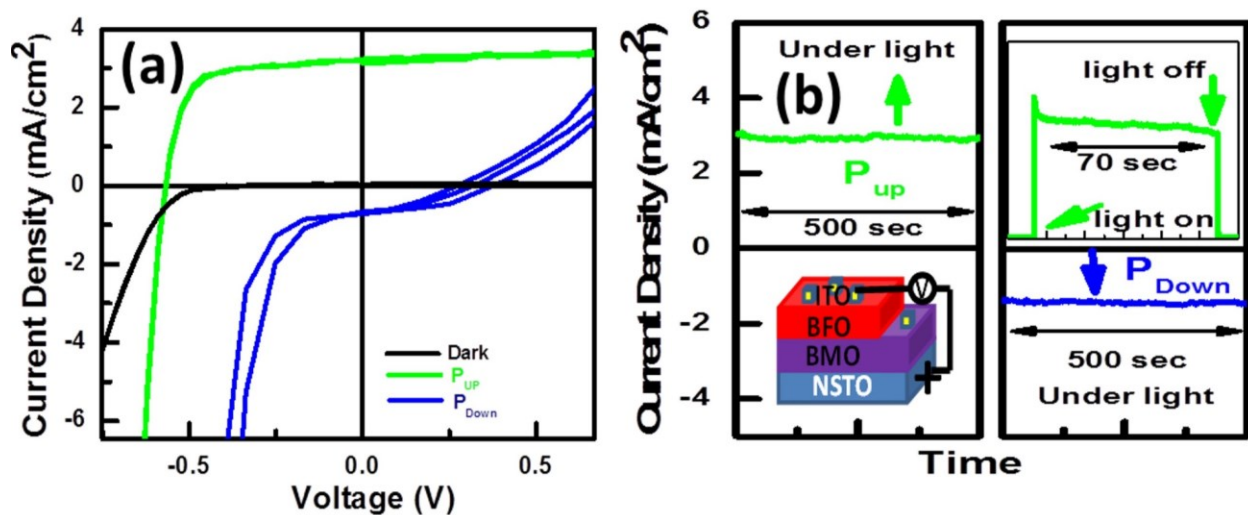


Figure 3-4 (a) Optical absorption spectra of the BFO/BMO film (b) Plots of  $(\alpha E)^2$  versus E for BMO, BFO/BMO and BFO films respectively which are used to extract the direct band gap of BMO and BFO.

### 3.3.5 Photovoltaic properties: measurement of current density-voltage (J-V) curves

The PV measurements were conducted by applying an appropriate voltage between top ITO electrode and the bottom NSTO electrode. The schematic diagram of electrical connection and the J-V curve of the samples are shown in Fig. 3-5. The recorded short-circuit photocurrent density

( $J_{SC}$ ) and open circuit voltage ( $V_{OC}$ ) are  $\sim 3.5 \text{ mA/cm}^2$  and  $\sim 0.56 \text{ V}$ , respectively. The calculated PCE is  $\sim 1.43\%$  with a high fill factor (FF) of  $\sim 0.72$ . The observed FF is slightly higher than that previously reported in FE oxide-based PV devices ( $\sim 0.71$  in BMO films). To evaluate the stability of the short-circuit photocurrent, we observed its evolution over time as shown in Fig. 3-5b. We recorded the photocurrent as a function of time after each poling, under illumination. The top right inset of Fig. 3-5b shows the time dynamics of  $J_{SC}$  at the onset of solar spectrum on (off). The bottom left inset shows the schematic diagram of electric circuit connection.



**Figure 3-5** (a) J-V characteristic curves of the heterostructure, with positive and negative poling demonstrating the PV effect. (b) The time vs  $J_{SC}$  shows stable photocurrent generation. Bottom left inset shows the geometry of the tested structure. Top right inset shows the dynamics of short circuit photocurrent recorded for 70 s under light on (off) conditions. The top left and bottom right inset shows good stability of photocurrent generation taken for 500 sec.

To elucidate further the individual contribution from each film to PV responses, we performed the J-V curve in each film separately. The  $J_{SC}$  and  $V_{OC}$  of ITO/BMO/NSTO heterostructures were  $\sim 0.23 \text{ mA/cm}^2$  and  $\sim 0.56 \text{ V}$  respectively (PCE 0.1%) which we previously reported [189]. The

recorded  $J_{SC}$  and  $V_{OC}$  of ITO/BFO/NSTO heterostructure are  $\sim 0.032 \text{ mA/cm}^2$  and  $\sim 0.42 \text{ V}$  respectively at the state of up poling as shown in Fig. 3-6. Figure 3-6a shows the J-V curves of ITO/BFO/NSTO heterostructure under 1 sun illumination (AM1.5G). The bias was swept between + 1 V and - 1 V during measurements. The recorded  $J_{SC}$ ,  $V_{OC}$  and FF are  $\sim 0.032 \text{ mA/cm}^2$ ,  $\sim 0.42 \text{ V}$  and  $\sim 0.44$  respectively at the state of up poling. At down poling,  $J_{SC}$  is decreased down to  $\sim 0.011 \text{ mA/cm}^2$  while  $V_{OC}$  is increased to  $\sim 0.55 \text{ V}$ . The calculated PCE is  $\sim 6 \times 10^{-4} \%$ . Figure 3-6b shows the plot of photovoltage as a function of time under chopped illumination which further confirms the PV response clearly. The PV parameters of ITO/BFO/NSTO, ITO/BMO/NSTO, and ITO/BFO/BMO/NSTO heterostructures are summarized in Table 3-1.

**Table 3-1** Comparison of the PV properties of BFO, BMO and bilayer BFO/BMO films.

	Up Polarization ( $P_{UP}$ )		Down Polarization ( $P_{DOWN}$ )	
	$J_{sc}$ [ $\text{cm}^{-2}$ ]	$V_{oc}$ [V]	$J_{sc}$ [ $\text{cm}^{-2}$ ]	$V_{oc}$ [V]
ITO/BFO/NSTO	$\sim 0.032 \text{ mA}$	$\sim 0.42$	$\sim 0.011 \text{ mA}$	$\sim 0.55$
ITO/BMO/NSTO [189]	$\sim 0.15 \text{ mA}$	$\sim 0.53$	$\sim 0.23 \text{ mA}$	$\sim 0.56$
ITO/BFO/BMO/NSTO	$\sim 3.50 \text{ mA}$	$\sim 0.56$	$\sim 0.70 \text{ mA}$	$\sim 0.35$

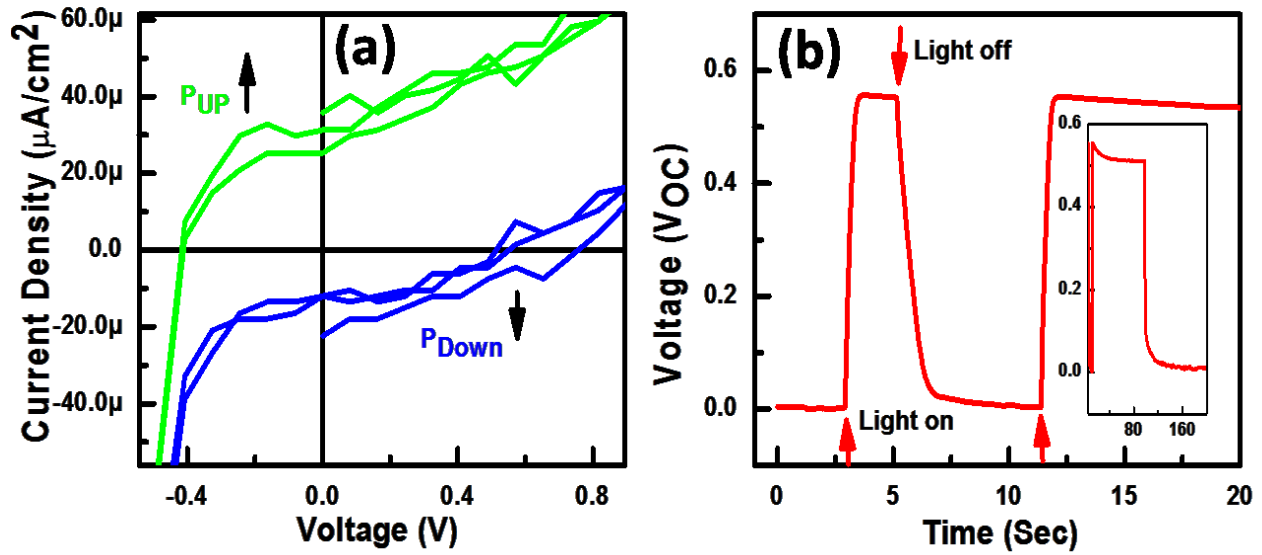


Figure 3-6 (a) J-V characteristic curves of ITO/BFO/NSTO heterostructure, with positive and negative poling demonstrating the FE PV effect (b) Time dynamics of voltage under dark and illumination. The inset of (b) shows the voltage stability for longer period of time (5 to 200 sec).

### 3.3.6 Band edge energy: ultraviolet photoemission spectroscopy (UPS) measurement

Band edges energy has been studied by UPS on the bilayer device. To remove surface contamination, the sample was etched for 4 min using an Ar ion beam prior to UPS measurements. The procedure reported in reference [201] was followed to determine the numerical values of the parameters. Figure 3-7 shows the UPS spectrum of BFO, BMO and that of a gold reference, using a 21.22 eV source for excitation. The extracted parameters from UPS data are shown in Table 3-2.

**Table 3-2** UPS data extracted to build the band diagram.

	<b>Band Gap (<math>E_g</math>) [eV]</b>	<b>Work Function (<math>\Phi</math>) [eV]</b>	<b>Fermi Energy (<math>E_F</math>) [eV]</b>	<b>Valence Band Energy (<math>E_v</math>) [eV]</b>	<b>Conduction Band Energy (<math>E_c</math>) [eV]</b>
ITO[202]	-	4.7	-	-	-
BFO	$2.7 \pm 0.1$	$4.53 \pm 0.1$	$4.53 \pm 0.1$	$6.73 \pm 0.1$	$4.03 \pm 0.1$
BMO	$1.2 \pm 0.1$	$4.7 \pm 0.1$	$4.7 \pm 0.1$	$5.85 \pm 0.1$	$4.65 \pm 0.1$
NSTO[203]	3.2	4.08	7.2	7.2	4

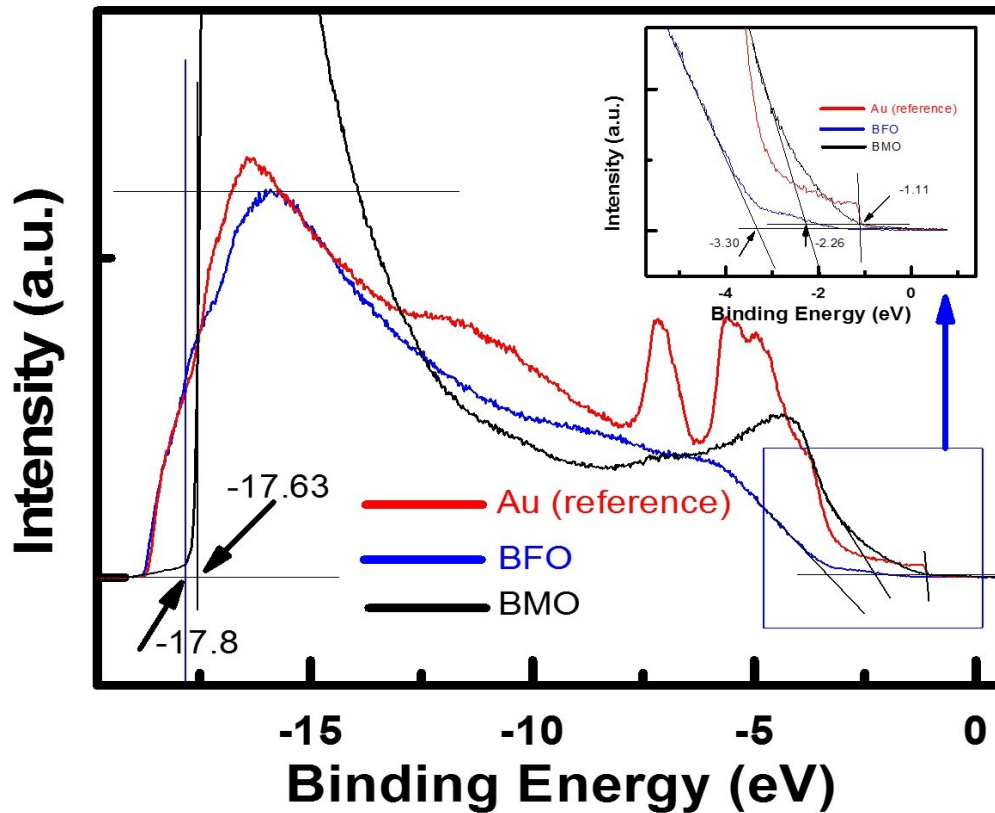


**Figure 3-7** UPS spectra of BFO, BMO and Au (reference). The inset shows the magnification of low binding energy edge.

### 3.4 Discussion

The resistance of BFO/NSTO structure is believed to be higher than that of BMO/NSTO structure (appears from the polarization modulation of the barrier height and width at electrode interfaces) because of higher density of bound charges of BFO (higher polarization). In addition, BFO has a high band gap ( $\sim 2.7$  eV) as compared with BMO ( $\sim 1.2$  eV). Therefore, the photocurrent generation in BFO alone is lower than that of BMO, consistent with our results. The BFO/BMO bilayer device generates higher  $J_{SC}$  values ( $\sim 3.50$  mA/cm<sup>2</sup>). Each layer in the device absorbs light

at its own characteristic wavelength. High energy photons ( $\sim 2.7$  eV in the visible range) are absorbed by BFO while BMO absorbs photons in the infrared spectrum ( $\sim 1.2$  eV). As a result, the total photocarrier generation in the whole device structure is much higher. The presence of secondary  $\text{Mn}_3\text{O}_4$  phase within BMO is detrimental for PV and FE performances [189] mainly because of increased trap densities and thus changes the photorecombination rate, as well as the electric field distribution. Therefore, achieving a single-phase BMO in the BFO/BMO bilayers may improve further the PV device performance. However, the single-phase  $\text{BiMnO}_3$  films exhibit  $V_{\text{OC}}$  and  $J_{\text{SC}}$  of  $\sim 0.46$  V and  $\sim 0.35$   $\text{mA}/\text{cm}^2$  respectively (described in Section 4.3.4, Chapter 4) which are roughly equal to the multiphase films (the films described in this Chapter). To obtain a high effective photocurrent, an efficient photocarrier separation process is mandatory before recombination. In our case, charge separation is achieved by the total electric field across the device generated by the band discontinuity at the interfaces along with the depolarization field of BFO and BMO (detailed in Fig. 3-8).

The FF depends on the parasitic resistance (shunt and series resistance of typical electrical circuit model) of a solar cell [204]. The series ( $R_{\text{Series}}$ ) and shunt resistances ( $R_{\text{Shunt}}$ ) extracted from the J-V curve of BFO/BMO bilayer devices are  $\sim 25$   $\Omega\cdot\text{cm}^2$  and  $\sim 1.2$   $\text{k}\Omega\cdot\text{cm}^2$  respectively. The J-V curve of BFO/NSTO device exhibits  $R_{\text{Series}} = \sim 4.6$   $\text{k}\Omega\cdot\text{cm}^2$  and  $R_{\text{Shunt}} = \sim 45$   $\text{k}\Omega\cdot\text{cm}^2$  while BMO/NSTO shows  $R_{\text{Series}} = \sim 220$   $\Omega\cdot\text{cm}^2$  and  $R_{\text{Shunt}} = \sim 30$   $\text{k}\Omega\cdot\text{cm}^2$ . Generally, low series resistance and high shunt resistance are required to achieve high FF. Series resistance appears in the cell mainly due to the movement of carriers across the cell, the contact resistance at electrodes, and the resistance of the electrodes themselves. Conversely, the presence of a shunt resistance is typically due to the defects present either inside the film or at interfaces which may provide an alternate path for the light-generated current, thus lowering the generated power in the device. The

efficiency of charge collection inside a structure before carrier recombination, which can be tuned by the parasitic resistance depends on the charge carrier mobility of the films, the internal electric field sweeping the carriers to their respective contacts and the carrier recombination rate. In our devices (BMO, BFO and bilayer-based), we used the same electrodes (thus we assume the similar order of magnitude of electrode resistance), however, the contact and film resistances are different. Considering the electric field that arises at the interfaces from Schottky contact and band discontinuity (Fig. 3-8), single BMO and BFO/BMO bilayer based devices exhibit similar total electric field. Thus, the contact resistance at thermal equilibrium should be equal in both cases. Although BFO exhibits low contact resistance, it has high film resistance compared to BMO. Therefore, it is expected to exhibit a high photocarrier recombination rate in BFO, which lowers the device's FF. Nonetheless, generally the carriers tend to accumulate at the interfaces in the case of low carrier mobility materials, with low internal field and sharp, high-quality interfaces across the structure [205], and the charge trapping at the interface increases recombination loss, thus further lowering the FF. In the case of BFO/BMO bilayer structure, we measured a relatively low surface roughness of the bottom BMO layer of 2.5 nm over an area of  $10 \times 10 \mu\text{m}^2$  (Fig. 3-2a,b). This is a prerequisite factor for the establishment of a smooth, defect-free interface. The smooth interface between BMO and BFO was also proven by preliminary cross-sectional TEM experiments (Fig. 3-2c). Given that the top BFO layer is epitaxially grown (Fig. 3-1) and taking into account the relatively low lattice mismatch between BMO and BFO we believe that the possibility of high charge trapping at the BFO/BMO interface is low and that this leads to a lower recombination loss resulting in an improved FF (0.72).

To further elucidate the characteristics of  $V_{OC}$ , and  $J_{SC}$ , we studied the possible interface effects of the built-in-fields and the depolarization fields within the BFO and BMO layer. Based on the UPS

measurements, we constructed the energy band diagram of our ITO/BFO/BMO/NSTO heterostructure as shown schematically in Fig. 3-8. We assumed ideal interfaces, neglecting the charge traps at the film/electrode interfaces [4]. Based on the position of the Fermi Energy ( $E_F$ ) and the band gap of BFO and BMO extracted from ellipsometry measurements, we considered the BFO and BMO layers as n-type semiconductors. This assignment is justified by the very likely presence of oxygen vacancies, generally observed in Bi-based perovskite thin films [206,207]. In the case of doped STO, we used the electron affinity and band gap from previous reports [202] that depict this material as an n-type semiconductor, since it is able to generate excitons under illumination [208,209]. At thermal equilibrium, band bending and band discontinuities occurred at all interfaces of our heterostructure due to the differences in work functions, valence band, and conduction band offsets. Each of these discontinuities has an associated electric field, as illustrated in Fig. 3-8b, where we show the Schottky barrier induced field ( $E_1$ ), band discontinuity induced electric fields ( $E_2$  &  $E_3$ ), the possible orientation of spontaneous polarization and its associated depolarization field ( $E_{dp}$ ). These electric fields influence the movement of photogenerated electron-hole pairs and thus control the direction of the photogenerated current flow. According to our model, the net effect resulting from the formation of the interfacial junction between layers and the Schottky junction at the film/top electrode is an electric field oriented upward (towards ITO), which is crucial for the separation of photogenerated charge carriers. The theoretically calculated net internal potential is  $\Delta\Phi_{B=ITO/BFO/BMO/NSTO} = \sim 0.62$  eV. This value is slightly higher than our experimentally measured photovoltage ( $V_{OC}$ ) of  $\sim 0.56$  eV, and we attribute the difference to the finite shunt resistance, surface states and other parasitic effects i.e. connecting wire resistance, capacitance, inductance etc that are likely to appear while characterizing the devices.

Our estimations show that the Schottky field (ITO/BFO) is the highest among the other fields in the whole structure. Generally, the current flow is dominated by one type of carrier and typically, if the barrier height for holes is  $\sim 0.2$  eV larger than that of electrons, the hole current will be approximately a factor of  $10^4$  smaller than the electron current [210]. Therefore, since the barrier height for holes is larger than the electron barrier height in our structure, current flow is dominated by electrons driven towards STO. Additionally, the net depolarization field originating from the spontaneous polarization of BFO and BMO layers modulates the Schottky barrier and interface-generated electric fields, further increasing the shortcircuit current when the polarization is oriented towards STO.

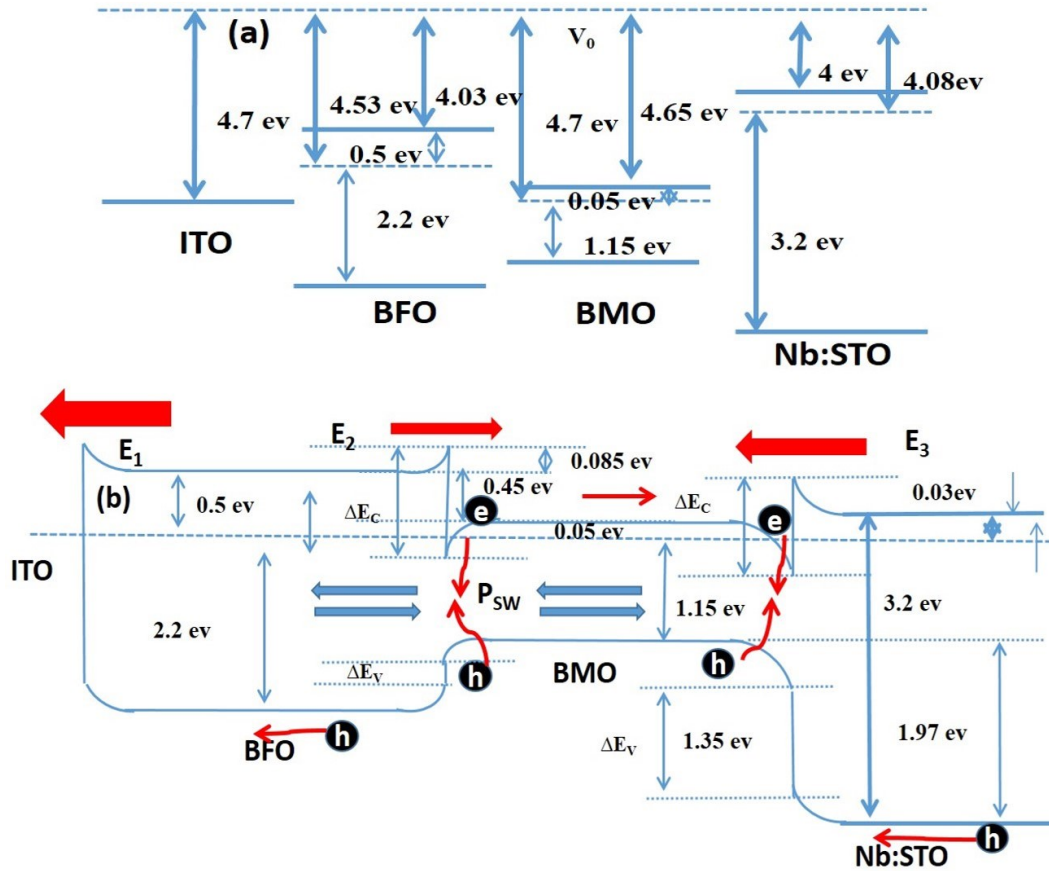


**Figure 3-8** (a) Energy band alignment of isolated ITO, BFO, BMO and doped STO films (b) Energy band alignment of the ideal ITO/BFO/BMO/Nb:STO interface at thermal equilibrium which also shows corresponding polarization effect with the direction of current flow.

We denote the polarization in BMO and BFO films  $P_1$  and  $P_2$  respectively, where  $P_2 > P_1$ . If  $P_2 = P_1 = 0$  at thermal equilibrium, space charges accumulate at interfaces, as shown in Fig. 3-9, resulting in the electric fields depicted in Fig. 3-8b. When  $P_2, P_1 \neq 0$  and polarization aligned towards the top or bottom electrodes as depicted in Fig. 3-9, the polarization bound charges accumulate at ITO/BFO, BFO/BMO and BMO/NSTO interfaces.

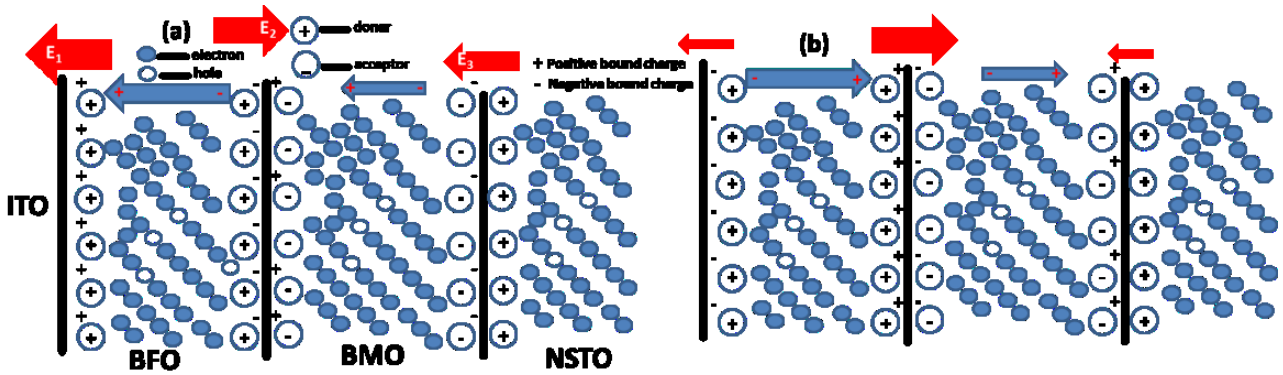


Figure 3-9 Mechanism of band modulation by polarization (a) upward and (b) downward polarization direction respectively.

Due to the incomplete screening of these bound charges, a depolarization field with opposite direction to the polarization is developed in both layers thus leading to an additional energy band bending at the interfaces [211]. In the case of up poling (towards ITO), the Schottky barrier will be higher, resulting in a higher magnitude of  $E_1$  due to the effect of bound charges. Similarly, the bound charges at the BFO/BMO interface will reduce the electric field  $E_2$ , while at the interface with the substrate,  $E_3$  is slightly increased. Since  $P_1$  is relatively small, the modulation effect on  $E_3$  will not be significant. For opposite poling,  $E_1$  and  $E_3$  will be lower, whereas  $E_2$  will be higher. As a result, the net electric field will be flipped down towards bottom electrodes. Therefore, during up poling the shortcircuit photocurrent will be higher, as shown in Fig. 3-5a. For the same reason, the shortcircuit photocurrent is relatively smaller while down poling. In addition, the incomplete polarization switching together with the relatively high resistance developed at the BFO/BMO interface due to polarization modulation [212] might explain the reduced values of  $J_{sc}$  and  $V_{oc}$ , as evidenced in the J-V curve in Fig. 3-5a. When comparing the band alignment of the ITO/BMO/BFO/NSTO with that of ITO/BFO/BMO/NSTO, we find that in both cases, the net internal potential is equal ( $\Delta\Phi_B = \sim 0.62$  eV) however the photocurrent generation will be higher

in BFO/BMO structure due to the grading of the band gap (illuminated from ITO side). However, the estimation of the magnitude of each built-in field set up, including the depolarization field is needed to measure the exact magnitude of the net electric field set up across the device structure. This will be the subject of future studies.

### **3.5 Conclusions and perspectives**

In this chapter, we described enhanced PV properties in epitaxial BFO-BMO heterostructures deposited by PLD on (111)-oriented NSTO substrates. We measured a PCE of  $\sim 1.43\%$  under 1 sun simulator illumination (AM 1.5G). Besides the comparatively high PCE ( $\sim 14.3$  times higher than BMO), a relatively high FF ( $\sim 0.72$ ) along with a high PFM response were observed, compared with individual single layers of BFO and BMO. To describe the PV effect in this system, we employed a traditional interfacial model (interface generated electric field), which is significantly affected by the spontaneous polarization. However, the optimization of thickness of each layer, and the possible interfacial layer formation (due to interface mixing) could be an interesting topic in terms of obtaining high absorption of sunlight. In addition, the coupling of two FE layers at their interface could be an interesting study and may open many opportunities for multilayer FE materials based electronic devices.

## Chapter 4 Mixed Crystal Phases in Oxide Perovskite Thin Films for Improved Photovoltaic Performance

### 4.1 Introduction

As described in Chapter 1, the photovoltaic (PV) effect in single crystal ferroelectric (FE) materials is known as bulk photovoltaic (BPV) effect [126,213]. FEs can yield a large photovoltage (1000 V) under illumination which can exceed the band gap of materials [10] (referred to as anomalous photovoltage (APV)) with negligible photocurrent density that clearly distinguish them from conventional semiconductors. The APVs in FEs are described by the BPV effect [8,127] invoked for  $\text{LiNbO}_3$  (LNO),  $\text{BaTiO}_3$  (BTO) and  $\text{Pb}(\text{Zr},\text{Ti})\text{O}_3$  (PZT) thin films, depolarization field theory or the theory of domain walls (DW) [11] used in epitaxial  $\text{BiFeO}_3$  (BFO) films. Therefore the exact physical phenomena that underpin the APV in FEs is still a subject of ongoing discussion. Although FEs yield APV, they exhibit low photocurrent density, typically in the range of  $\text{nA}/\text{cm}^2$ . The APV which does not occur exclusively in FEs was first observed in PbS films (2 V) [13] and later detected in other semiconductors including polycrystalline CdTe, ZnTe and InP films [14,15]. Generally, the accommodation of a large number of grain boundaries (GB) in the thin films promotes the charge carrier recombination centers and thus reduces the PV device performances. Therefore, the polycrystalline films (large number of GBs) are considered to be inferior compared with their single crystalline counterparts. However, few exceptions have been reported in traditional semiconductors including CdTe, ZnTe and InP films [14,15] where polycrystalline films exhibited superior performances than their single crystalline counterparts. The phenomena were described by postulating the existence of potential barriers at GBs, arising from the asymmetric concentration of impurity centers at the interfaces.

The electrical degradation in FE thin films is associated with the gradual increase of dielectric leakage current under DC field stress. The electrical degradation phenomenon is described by GB model [214,215] suggesting that GBs in dielectrics exhibit higher resistance compared to their bulk grains. Therefore, high electric fields are evolved across GBs under DC bias which may cause local electrical breakdown or field assisted emission of trapped charge carriers. The electrical degradation can also be described by the migration of oxygen vacancies in FE oxide materials. Under DC field stress, oxygen vacancies pile up at the cathode electrodes and are compensated by the electrons. In polycrystalline or multiphase materials, these processes occur at GBs. As result, the potential barrier height of GBs decreases with reducing the density of states at GBs. Since the potential barrier height of GBs can control the current level at GBs, the resultant leakage current start to increase. The superior PV performances observed in traditional polycrystalline semiconductor-based PV devices compared to their single crystalline counterparts are described by the potential barrier heights across GBs [216,217]. However, no reports previously described the role of GBs in improving the PV performances in inorganic oxide perovskite thin films to the best of our knowledge.

In this chapter, we demonstrate the concept of a PV device based on a composite material made of two different types of crystal phases: BiMnO<sub>3</sub> (BMO) and BiMn<sub>2</sub>O<sub>5</sub>. The former is ferromagnetic [63] below ~105 K and FE [86] with an experimental band gap of ~1.20 eV at room temperature (RT) while BiMn<sub>2</sub>O<sub>5</sub> is semiconducting with a theoretical band gap of ~1.23 eV [218]. We show that incorporating FE grains in non-FE semiconducting materials (FE-semiconducting matrix) in the same device can enhance the short circuit current density ( $J_{SC} = \sim 7.03 \text{ mA/cm}^2$ ) while exhibiting an APV ( $V_{OC} = \sim 1.48 \text{ V}$ ), leading to a record PCE of ~4.20% in a single layer FE thin film based composite PV device. So far, the highest PCE of ~ 3.30% is reported in single layer FE

$\text{Bi}_2\text{FeCrO}_6$  (BFCO) thin films under 1 Sun illumination [17]. In our cases, in contrast to BFCO, the recorded  $V_{\text{OC}}$  exceeds the band gap of individual phases in the films. We found that photoexcited charge carriers accumulate mainly across GBs rather than in the interior of the grains. The results are described in the framework of GB barrier potentials.

## 4.2 Experimental methods

### 4.2.1 Synthesis of thin films and device fabrication

Bi-Mn-O composite hetero-structures were grown on 0.5% Nb-doped (100)-oriented  $\text{SrTiO}_3$  single crystal (NSTO) substrates by pulse laser deposition (PLD). The deposition parameters were set as follows: laser fluence and pulse frequency were  $\sim 3.5 \text{ J/cm}^2$  and  $\sim 3 \text{ Hz}$  respectively and the substrate temperature was kept at  $\sim 620 \text{ }^\circ\text{C}$  under a partial oxygen pressure of  $\sim 10 \text{ mTorr}$ . The target to substrate distance was  $\sim 5.5 \text{ cm}$ . After deposition, the as-grown films were cooled to room temperature under vacuum. The thickness of the films was of  $110 \pm 10 \text{ nm}$ , estimated from cross-section transmission electron microscopy (TEM). For electrical measurements, two-dimensional arrays of 120 nm thick indium tin oxide (ITO) top transparent electrodes were deposited by PLD through masks with circular apertures ( $\sim 0.5 \text{ mm}$  in diameter) on the surface of the as-grown film at  $\sim 300 \text{ }^\circ\text{C}$  under 10 mTorr  $\text{O}_2$  pressure.

The same target was used to deposit the individual BMO and  $\text{BiMn}_2\text{O}_5$  thin films. The deposition parameters for BMO films were as follows: laser fluence  $\sim 1 \text{ J/cm}^2$ , pulse frequency  $\sim 1 \text{ Hz}$ , and the substrate temperature was kept constant at  $\sim 620 \text{ }^\circ\text{C}$  under the partial oxygen pressure of  $\sim 8 \text{ mTorr}$ . The target to substrate distance was  $\sim 6 \text{ cm}$ . After deposition, the as-grown films were annealed for 40 min under the same oxygen pressure before cooling down to room temperature under vacuum. The PLD parameters for  $\text{BiMn}_2\text{O}_5$  films were set as follows: laser fluence  $\sim 2 \text{ J/cm}^2$

, pulse frequency  $\sim 5$  Hz, and the substrate temperature was kept constant at  $\sim 750$  °C under the partial oxygen pressure of  $\sim 10$  mTorr. The target to substrate distance was  $\sim 6$  cm. After deposition, the as-grown films were cooled to room temperature under vacuum.

The device schematics and circuit connections for macroscopic electrical measurements are illustrated in Fig. 4-1.

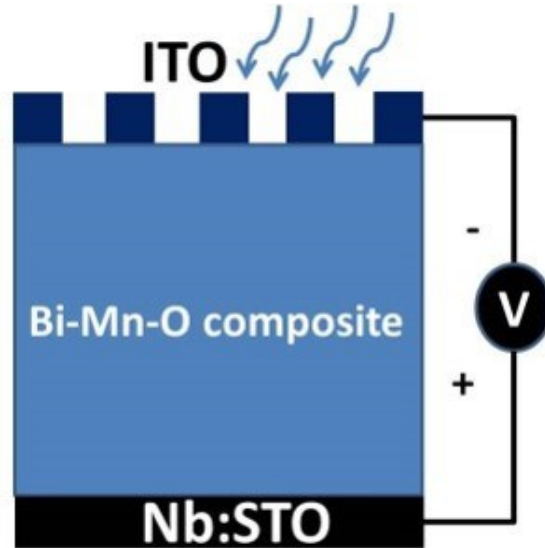


Figure 4-1 Schematic of device connections for electrical measurements.

## 4.3 Characterizations

### 4.3.1 Crystal structures

The composite films with a thickness of  $\sim 110$  nm were grown on NSTO substrates by PLD. As mentioned above, the composite films contain both BMO and  $\text{BiMn}_2\text{O}_5$  phases, yielding GBs and interfaces, as evidenced by TEM images (Fig. 4-2). Raman spectroscopy (RS) (Fig. 4-4) further confirms the presence of the two distinct BMO and  $\text{BiMn}_2\text{O}_5$  phases.

#### 4.3.1.1 Transmission Electron Microscopy (TEM) Analysis

Cross-sectional TEM (XTEM) was used to analyze the crystal quality of the interface. **Figure 4-2a** displays a low magnification XTEM image of the sample device used in this study. The high-resolution image of the selected area indicates the presence of two distinct microstructural phases with a clear interface (GB) between them (**Fig. 4-2b**). To identify the phases, we first carried out Electron diffraction (EDX) analysis in TEM. EDX analysis performed in the selected area 1 shows almost equal atomic percentages of Bi and Mn ( $\text{Mn/Bi} = \sim 1.08$ ), while area 2 exhibits almost a double atomic percentage of Mn than Bi ( $\text{Mn/Bi} = \sim 0.60$ ). Therefore, we assign  $\text{BiMn}_2\text{O}_5$  crystal phases to bright contrast and BMO to relatively dark contrast in TEM images.

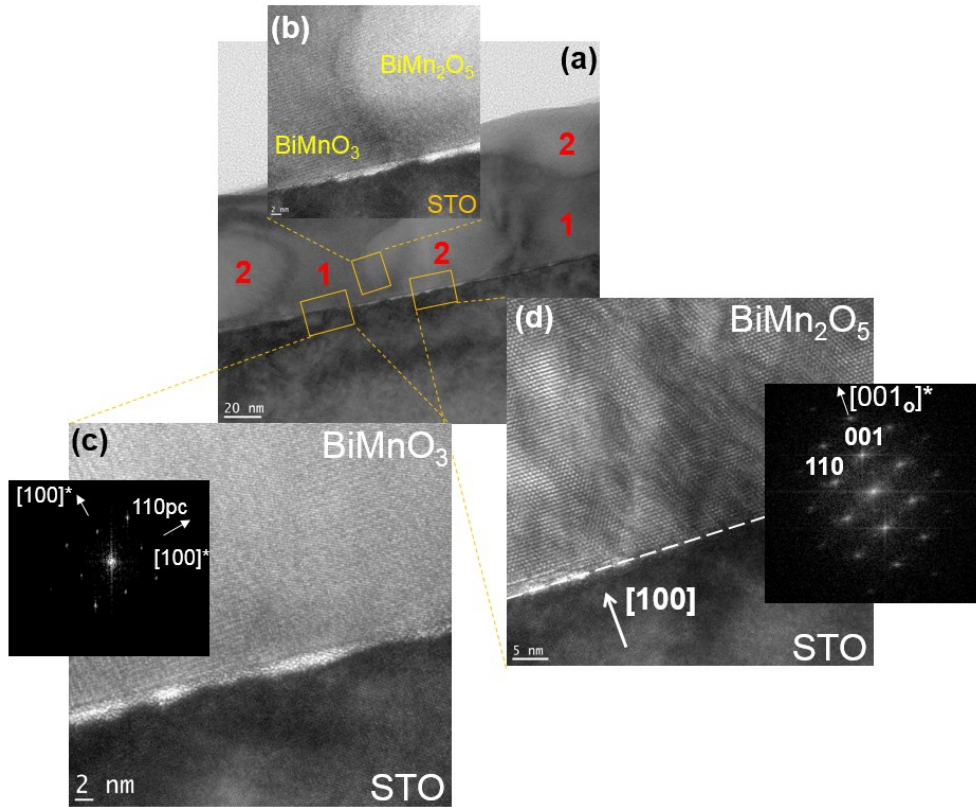


**Figure 4-2** (a) XTEM image of a sample device (b) higher magnification of the selected area between 1 and 2 indicated in ‘a’ showing the interface between BMO and BiMn<sub>2</sub>O<sub>5</sub>. Both clearly indicate the formation of two different crystalline phases on the substrates (c) magnification of the selected area of ‘1’ in ‘a’ shows epitaxial growth of the BMO phase. The inset shows the result of respective Fast Fourier Transform (FFT) of the image (d) magnification of the selected area of ‘2’ in ‘a’ shows the growth of the BiMn<sub>2</sub>O<sub>5</sub> phase, with its respective FFT in the inset.

We performed high-resolution TEM (HRTEM) analysis at different locations on the sample. **Figures 4-2c,d** display typical HRTEM images showing an interface between STO/BMO and STO/BiMn<sub>2</sub>O<sub>5</sub> for a <100>STO zone axis orientation, respectively. The zone-axis in TEM analysis defines the direction of a direct-space lattice-vector [219]. The corresponding FFT patterns are displayed in the inset of each figure. The FFT pattern obtained from the perovskite BMO phase

(Fig. 4-2c) looks similar to that obtained from the substrate with in-plane and out-of-plane lattice parameters in the film close to 3.9 Å, which indicates a pseudo “cube-on-cube” growth of this phase onto the STO substrate. These relationships are similar to those previously reported for the epitaxial growth of BMO thin films on (100) STO. The low symmetry nature of the BMO (i.e. monoclinic) makes the following relationship possible: first (111)BMO // (100)STO with  $\sim$ [-101]BMO // <010>STO and second (10-1)BMO // (100)STO with  $\sim$ [121]BMO // <010>STO [80]. The HRTEM of STO/BiMn<sub>2</sub>O<sub>5</sub> interface and corresponding FFT pattern are illustrated in Fig. 4-2d. These results are in good agreement with the orthorhombic crystal structure of BiMn<sub>2</sub>O<sub>5</sub> (Bi<sub>2</sub>Mn<sub>4</sub>O<sub>10</sub>) with lattice parameters a = 7.54 Å, b = 8.534 Å and c = 5.766 Å, where the orthorhombic (00l)<sub>O</sub> family of planes is parallel to the surface. However, a more detailed selected area diffraction (SAED) analysis in different regions of the samples revealed that BiMn<sub>2</sub>O<sub>5</sub> crystal grains are differently oriented. As shown in Fig. 4-3, the SAED pattern of the film and the substrate, taken with the incident electron beam along the same direction, identifies an epitaxial relationship between cubic STO and the orthorhombic phase of BiMn<sub>2</sub>O<sub>5</sub> as follows: (200)<sub>C</sub> || (310)<sub>O</sub>; (0 $\bar{2}$ 0)<sub>C</sub> || (003)<sub>O</sub>; (001)<sub>C</sub> || ( $\bar{1}$ 30)<sub>O</sub>. A small lattice mismatch of  $\sim$ 1 % between d<sub>003</sub> BiMn<sub>2</sub>O<sub>5</sub> = 1.92 Å and d<sub>0-20</sub> SrTiO<sub>3</sub> = 1.94 Å is observed and the angle mismatch between these two planes was found to be  $\sim$ 1.8°.

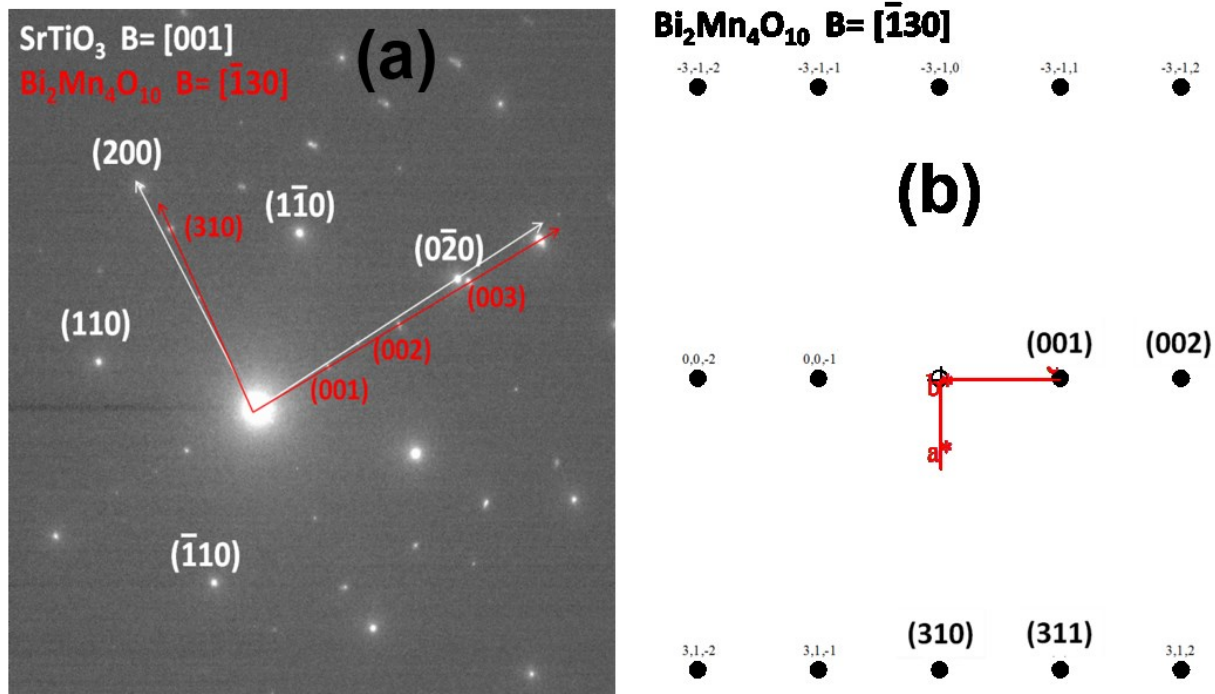


**Figure 4-3** (a) SAED of TEM recorded from another random area along the film-interfaces indicates the presence of another orientations of  $\text{BiMn}_2\text{O}_5$  crystal structure (b) reconstructed diffraction pattern of  $\text{BiMn}_2\text{O}_5$  at same beam orientation ( $B = [\bar{1}30]$ ) using lattice parameters obtained from the XRD database.

#### 4.3.1.2 Raman spectroscopy analysis

The presence of these two crystal phases was also confirmed by RS measurements. **Figure 4-4** shows room temperature RS of the as-deposited films. The RS recorded on BMO films and on bare substrates are shown in **Fig. 4-4a**. **Figure 4-4b** exhibits only the spectra of the film constructed by separating the substrate's response. The Raman active modes (**Fig. 4-4 b**) correspond to the Pbam structure of  $\text{BiMn}_2\text{O}_5$  and C2 structure of BMO, both obtained from TEM analysis. The peaks at  $\sim 651 \text{ cm}^{-1}$ ,  $\sim 607 \text{ cm}^{-1}$ ,  $\sim 320 \text{ cm}^{-1}$ , and  $\sim 192 \text{ cm}^{-1}$  are assigned to the Pbam structure, similarly to what was reported in references [220,221]. The modes of the C2 structure of BMO

were observed at  $\sim 651 \text{ cm}^{-1}$  and  $\sim 540 \text{ cm}^{-1}$  along with other modes reported in [222]. Our RS results exhibit all the Raman active modes reported previously in individual BMO and  $\text{BiMn}_2\text{O}_5$  crystals. We, therefore, conclude that the RS of the films originates from two distinct phases of BMO mullite.

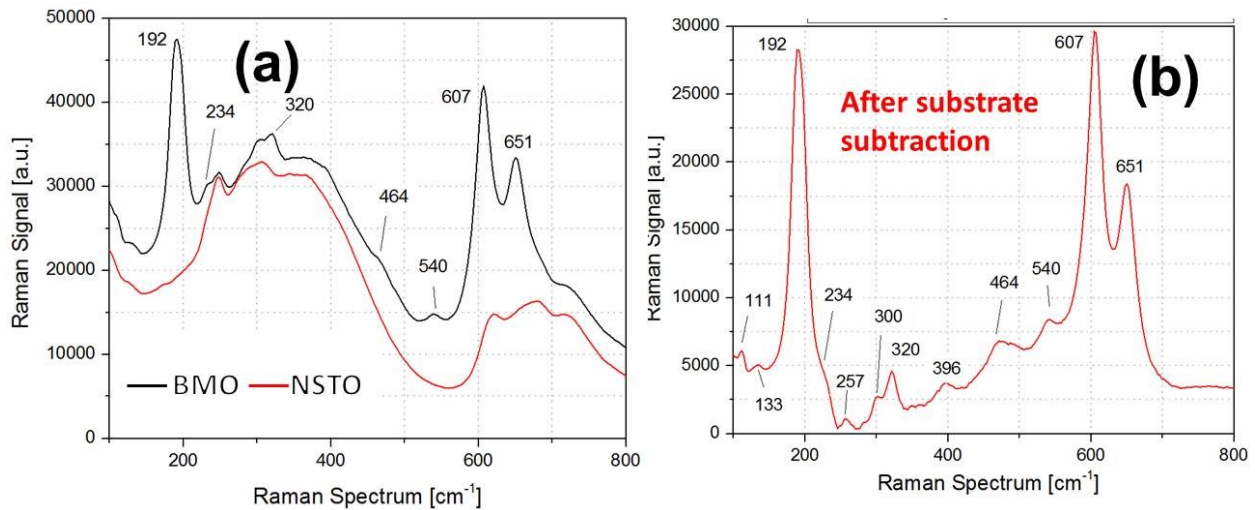


**Figure 4-4** (a) Room temperature Raman spectra of Bi-Mn-O films and of NSTO substrates (b) only film response obtained by subtracting the substrate response.

## 4.3.2 Ferroelectric properties

### 4.3.2.1 Composite films

The presence of ferroelectricity in the samples is demonstrated by recording piezoresponse force microscopy (PFM) images and piezoelectric hysteresis loops using PFM, which has a lateral resolution well-below the grain level as shown in Fig. 4-5a,b. Out of plane PFM image shows switching of polarization direction after subsequent poling the red encircled area with +5V/-5V voltages (Fig. 4-5a,b). The on (off) field hysteresis loops are only obtained from specific grains which we assigned as BMO grains (Fig. 4-5d). The rest of the remaining grains show only a linear behavior (Fig. 4-5e), consistent with the  $\text{BiMn}_2\text{O}_5$  phase which is not FE [223]. From the PFM

measurements, we observed, in few specific area of the samples, that some of neighboring grains exhibit a same electrical behavior (i.e. FE or semiconducting). This suggests that BMO/BMO and BiMn<sub>2</sub>O<sub>5</sub>/BiMn<sub>2</sub>O<sub>5</sub> GBs coexist with the majority of BMO/BiMn<sub>2</sub>O<sub>5</sub> GBs in the composite films. The results presented in Fig. 4-5d,e,g are a summary of the many individual grains probed at different places of the same sample. The topographic images recorded before and after measuring hysteresis loops show no morphological changes in the grains (red circled in Fig. 4-5c), excluding any irreversible electrochemical reactions. The hysteresis loops recorded from FE grains either show a saturated character (black curve in Fig. 4-5d) or non-saturated character (such as the red curve shown in Fig. 4-5d) and asymmetric due to the imprint effect. Typically, the off-field measurements are more reliable since they minimize the strong electrostatic interactions between the tip and sample during measurements [224]. Additionally, the off-field loops in our case were measured at a very low frequency, each data point representing a voltage pulse of 0.1 s followed by a delay of 0.8 s for signal measurements. The resulting cycling frequency of the loops is thus 11 MHz, which clearly proves the local FE character of the grains. The current measured simultaneously with the PFM hysteresis is negligible through FE grains (region encircled in red), while it is significant (Fig. 4-5e) in the non-FE grains associated with BiMn<sub>2</sub>O<sub>5</sub> (obtained from the green encircled grain). There was no detectable in-plane polarization in any grains as confirmed by x-PFM measurements. When the voltage range was increased (between +8 V to -8 V) to acquire hysteresis loops, we observed the occurrence of fatigue, in the form of changes in the shape of the hysteresis loop. The fatigue is confirmed by calculating the area of the loops. After the fifth sweep, the grain is observed to be deformed as shown in Fig. 4-5g. We found the same characteristics in different individual grains in different places of the same sample.

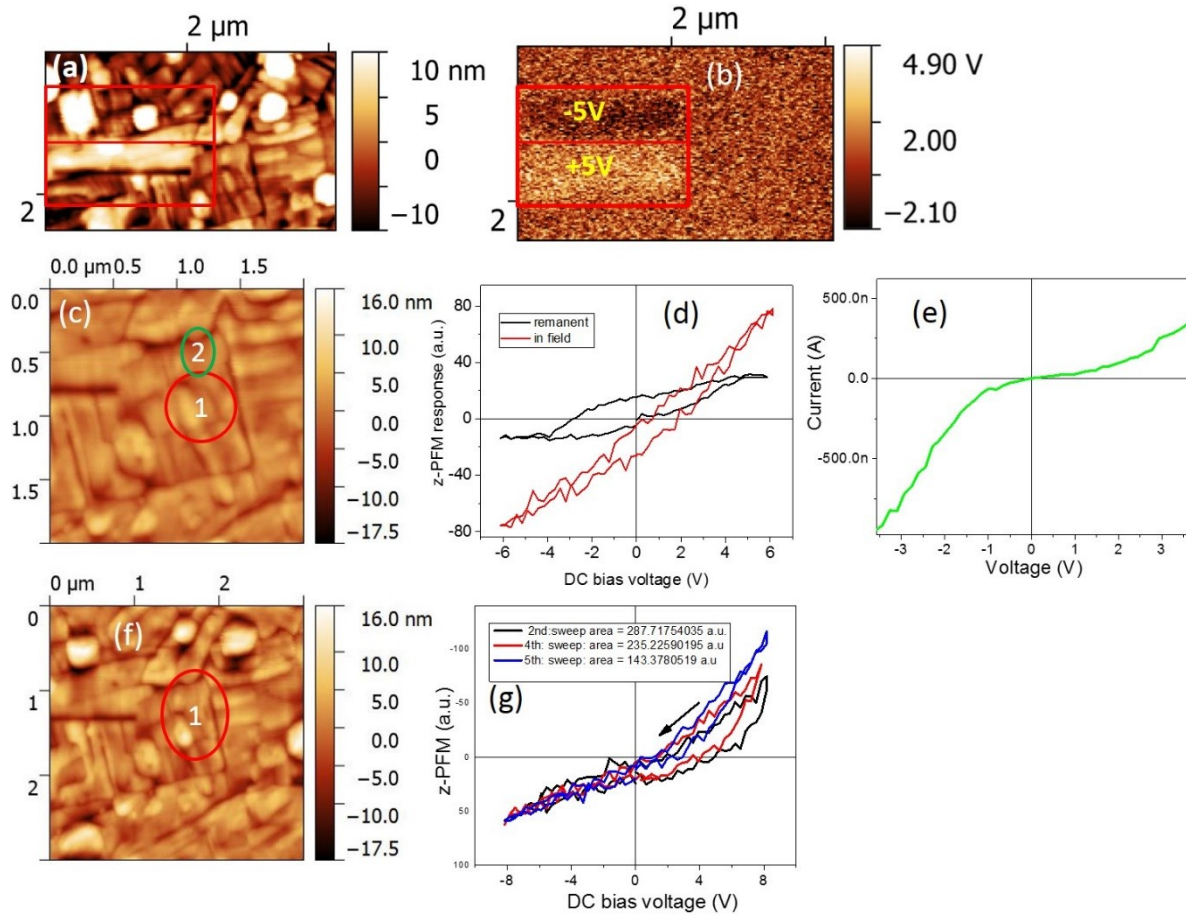


**Figure 4-5** Contact topography AFM image (a) simultaneously recorded with the OP-PFM image (b). Out of plane hysteresis loop (d) recorded from different grains, such that encircled in red in topography image (c). Current response as a function of applied DC voltage (e) recorded from the green encircled grain in the topography image (c). Hysteresis loops (g) recorded from the same grains (such that red encircled in topography image (c) with higher voltage demonstrating FE fatigue. Contact topography AFM image of the same grain (f) recorded after hysteresis loops showing changes in grain morphology.

#### 4.3.2.2 BiMnO<sub>3</sub> (BMO) thin films

The plots in Fig. 4-6a show macroscopic polarization hysteresis curves of the as-grown BMO films at two different frequencies exhibiting a remnant polarization of  $\sim 1 \mu\text{C}/\text{cm}^2$ , well below values previously reported for BMO films at room temperature [189,225]. The positive and negative coercive voltages measured are around  $\sim 1 \text{ V}$  and  $\sim -3 \text{ V}$  respectively. The FE switching peaks are clearly visible in the associated current loops, as shown in Fig. 4-6b. This behavior represents polarization switching, which is a typical characteristic of ferroelectricity. The hysteresis loop shows a more pronounced electrical leakage character of BMO films. This leakage behavior of BMO was also observed in the previous measurements [85,226]. This is probably due to a larger density of interphase boundaries that denote a higher density of defects, but the existence of a switchable FE polarization in BMO films (i.e. in this report) is certain, as demonstrated by measurements at different cycling frequencies (Fig. 4-6a,b). The fact that the hysteresis loop parameters do not change significantly when modifying the cycling frequency shows that the measured charge flow originates in their switching of polarization and is not due to other effects [227,228]. Another important property that can be extracted from the FE loops is the imprint of polarization. An imprint is observed which likely originates from the presence of a leakage or the effect of using different types of top and bottom electrodes.

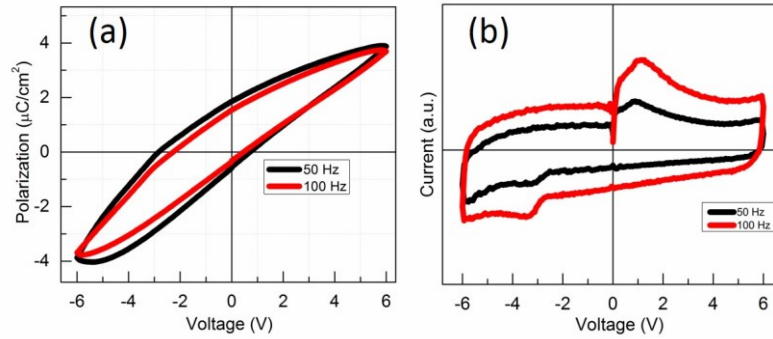


**Figure 4-6** (a) Macroscopic voltage vs polarization curve recorded on the BMO/NSTO heterostructure at two different frequencies. The curve demonstrates the FE character of the sample and (b) the corresponding voltage vs current loops confirms the switching of polarization.

### 4.3.3 Surface charge measurements with and without illumination

To investigate the FE effect on photocharge generation at the nanoscale, we conducted Kelvin probe force microscopy (KPFM) experiments under dark and illumination conditions. A specific region of the composite sample was first poled by applying consecutive positive and negative 5V DC voltages using a conductive AFM tip during piezoresponse force microscopy (PFM) experiments (Fig. 4-7a). No changes in the surface were observed afterward (Fig. 4-7d,f). Polarization was confirmed by recording a new PFM image of the surrounding area. CPD images were obtained with non-contact-AFM, using KPFM mode. The geometry of the KPFM experiment is described in Fig. 4-7b,c. While applying positive (negative) voltages, polarization is oriented up (down), since in our circuit the tip was grounded. Therefore, in KPFM images,  $P_{\text{up}}$  (positive) domains appear as dark contrast while  $P_{\text{down}}$  (negative) domains appear as bright contrast (red marked rectangle in Fig. 4-7e). Under illumination, the photo-induced electronic charges move towards the top surface of the films, which results in the decrease of the CPD (recorded as an

increase due to the grounded tip configuration, Fig. 4-7g,h). If ferroelectricity were to dominate the PV effect, the photogenerated electronic charges should move in opposite directions for  $P_{up}$  and  $P_{down}$  (Fig. 4-7c). However the CPD profile (Fig. 4-7h) recorded under illumination shows a positive shift everywhere compared to that recorded under dark, irrespective of the polarization direction, thus excluding the role of ferroelectricity in the PV effect.

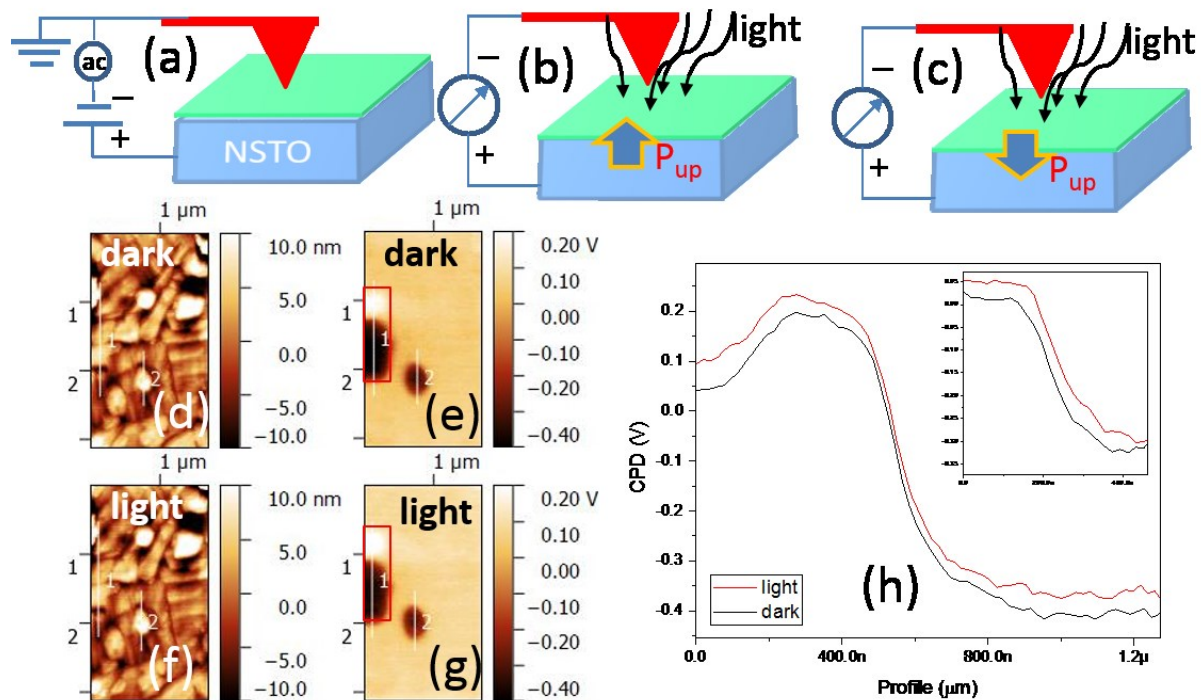


**Figure 4-7** (a) Schematics of electrical connection for PFM experiments (b,c) Simplified schematics of KPFM experimental setup conducted on virgin area and poled area (up/down) respectively. Surface potential measured by KPFM performed on the virgin sample: (d) and (f) Topography, (e and g) CPD image measured with (f, g) and without (d, e) illuminating the sample. (h) CPD profiles of line 1 indicated in e & g. The inset shows CPD profiles of line 2 indicated in e & g.

#### 4.3.4 Photovoltaic properties: measurement of current density-voltage (J-V) curves

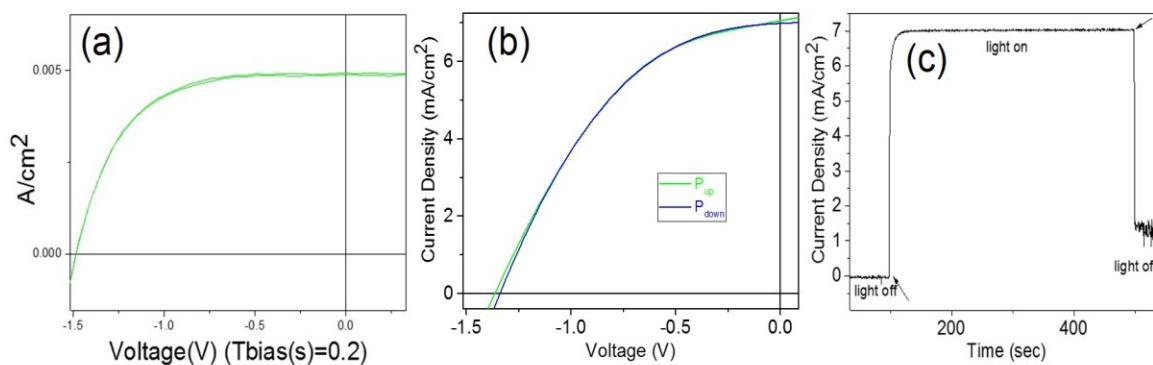
To assess the PV effect, we recorded the  $J_{SC}$  as a function of external applied DC voltage, both in dark and under 1 sun (AM1.5G) illumination conditions. The electrodes were connected using needle probes (25  $\mu\text{m}$  in diameter) attached to xyz micro-positioners. We compared PV measurements performed with and without masking. We used a stripe mask applied under an optical microscope to cover the area surrounding the electrode. We found a negligible difference. This means that the light reaching the active area originates from a very narrow region around the top electrode. The current generated from this scattered light is negligible compared to that generated by direct light. In the course of these studies, 5 samples were randomly selected to measure PV responses from a set of 10 samples. The samples exhibited efficiencies of  $\sim 4.20\%$ ,  $\sim 4.0\%$ ,  $\sim 3.90\%$ ,  $\sim 3.8\%$  and  $\sim 3.96\%$  respectively. The best performance device ( $\sim 4.20\%$ ) exhibited the fill factor (FF) of  $\sim 0.58$  (Fig. 4-8a). A survey of the efficiencies calculated from different samples is provided in Table 4-1, indicating an average PCE of  $\sim 3.97\%$ . In the rest of the texts, we discussed the sample exhibiting  $\sim 3.96\%$  PCE since it is the closest to the average efficiency. The variation of the efficiencies in different samples may arise from several factors including different film uniformity, top electrode size, uniformity of the incident light, thereby variation in current and voltage measurements in each sample.

Table 4-1 Efficiencies calculated from different samples after switching with a bipolar voltage pulse.

Sample No.	PCE (%)
1	4.20
2	4.00

3	3.90
4	3.80
5	3.96
Average	3.97

Prior to the measurement of the characteristic J-V curves, the polarization of pristine samples was switched by applying sequences of bipolar voltage pulses with a magnitude of 6 V and duration of 0.1 s each (depicted in Fig. 4-14), such that the polarization remained oriented either towards STO (hereafter  $P_{\text{down}}$ ) or towards ITO ( $P_{\text{up}}$ ). The purpose of this poling is to observe the macroscopic FE effect on PV effect if any. The J-V curves of the poled samples were then recorded under illumination, as shown in Fig. 4-8b. The  $J_{\text{SC}}$  and  $V_{\text{OC}}$  of one of the devices were  $\sim 7.03 \text{ mA/cm}^2$  and  $\sim 1.36 \text{ V}$ . The calculated PCE is  $\sim 3.96\%$  at a FF of  $\sim 0.42$ . The  $J_{\text{SC}}$  recorded as a function of time in this state is shown in Fig. 4-8c. However, both  $J_{\text{SC}}$  and  $V_{\text{OC}}$  varied only slightly (almost negligible) when the device was poled with a reverse bias voltage (polarization in the  $P_{\text{down}}$  state) as depicted by the blue curve in Fig. 4-8b. No hysteresis was observed while recording I-V curves suggesting no effect of charge injection over time during measurements.



**Figure 4-8** (a) J-V curves recorded in best sample under illumination after switching with a bipolar voltage pulses (b)  $J_{SC}$ -V curve recorded under illumination for different orientations of polarization (c) Plot of  $J_{SC}$  as a function of time recorded on the samples poled by a bipolar voltage pulse.

To determine the individual contributions of the BMO and BiMn<sub>2</sub>O<sub>5</sub> phases to the observed PV parameters, we performed separate measurements on films crystallized in each phase. BMO films exhibit  $V_{OC}$  and  $J_{SC}$  of  $\sim 0.46$  V and  $\sim 0.35$  mA/cm<sup>2</sup> respectively in the state of down poling under 1 sun illumination (Fig. 4-9a). Polycrystalline BiMn<sub>2</sub>O<sub>5</sub> films also showed a PV response under an illumination of 1 sun, with  $V_{OC}$  of  $\sim 0.22$  V and a much lower  $J_{SC}$  of  $\sim 0.20$   $\mu$ A/cm<sup>2</sup> (Fig. 4-9b). Therefore, both individual films exhibited a much weaker PV effect compared with that of the composite films previously illustrated in Fig. 4-8b.

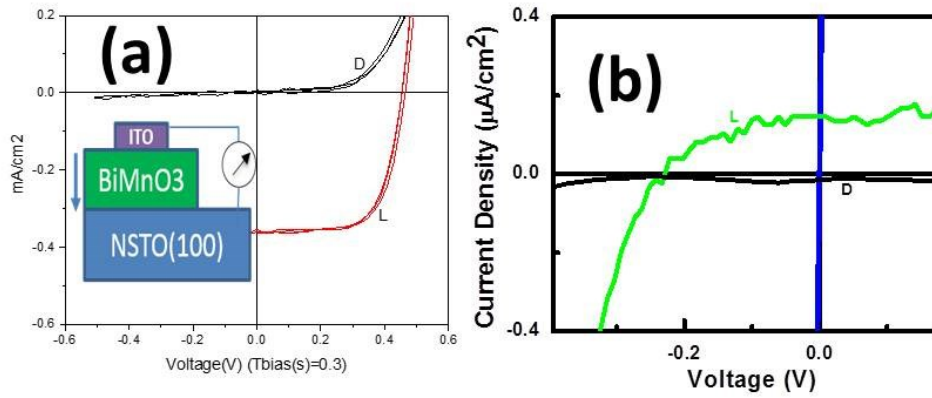


**Figure 4-9** (a) J-V curve recorded on BMO films. The inset shows the schematic of electrical connections (b) J-V curve recorded on BiMn<sub>2</sub>O<sub>5</sub> thin films. Both films were deposited on (100) oriented NSTO substrates.

#### 4.3.5 External quantum efficiency (EQE) measurement

To observe the photoexcited charge carriers and their separation efficiency, we performed EQE measurements (Fig. 4-10). A maximum EQE of ~ 42% is observed in the ultraviolet region of the solar spectrum while ~ 23% is obtained in the visible region. The J<sub>SC</sub> calculated from the EQE is ~7.20 mA/cm<sup>2</sup>, which is slightly higher than the J<sub>SC</sub> observed in the J-V curves (~7.03 mA/cm<sup>2</sup>). The EQE spectra contain an average EQE data for a set of five contact points on the same sample. The average EQE data to construct a single spectrum was reported previously in BiFeO<sub>3</sub> thin films [190].

The J<sub>SC</sub> was calculated using the equation:

$$J_{SC} = \sum_{\lambda} S(EQE, \lambda) * S(AM1.5G, \lambda) * \left(\frac{\lambda}{hc}\right) * q \text{ or } \int_{\lambda_1}^{\lambda_2} \left(EQE(\lambda) * AM(1.5G)(\lambda) * q * \left(\frac{\lambda}{hc}\right)\right) d\lambda$$

where EQE(λ), AM(1.5G)(λ), q, h, c, and λ represent the external quantum efficiency, solar irradiance, electron charge, Planck constant, light constant and wavelength of light respectively.

The integration yields a  $J_{SC}$  of  $\sim 7.20 \text{ mA/cm}^2$  which is slightly higher than the values obtained from J-V curves ( $\sim 7.03 \text{ mA/cm}^2$ ).

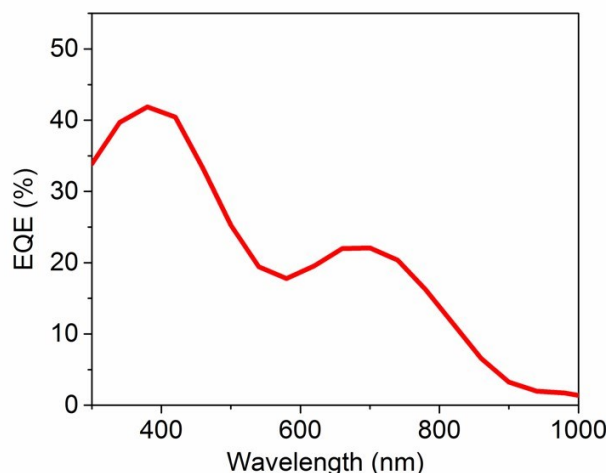


**Figure 4-10** EQE measurements on a single sample reveal highest efficiencies of  $\sim 42\%$  under UV illumination.

#### 4.3.6 Ellipsometry measurements

Optical ellipsometry measurements were performed to study the absorption properties of the films. The absorption coefficients ( $\alpha$ ) estimated for the different films are presented as a function of photon energy (E) in Fig. 4-11a. As observed in Fig. 4-11a, the peaks appear in the region of 1.60-1.75 eV for all films. These near-infrared features of perovskite manganites have been widely investigated [229,230,231]. Related peaks were thus assigned to charge transfer excitations between mixed O 2p and Mn 3d states. The procedure to investigate the optical properties of thin films is well reported in the literature [17,40,189,225,232,233,234,235]. The optical penetration depth ( $\alpha^{-1}$ ) of our investigated films is depicted in Fig. 4-11b. To determine the energy band gap,  $(\alpha E)^2$  versus E was plotted according to Tauc's equation [236], as shown in Fig. 4-11c. The plots

indicate a direct band gap of all films ( $\text{BMO} = \sim 1.27 \pm 0.05 \text{ eV}$ ;  $\text{BiMn}_2\text{O}_5 = \sim 1.24 \pm 0.05 \text{ eV}$ ;  $\text{BMO-BiMn}_2\text{O}_5 = \sim 1.25 \pm 0.05 \text{ eV}$ ). The results are close to the estimated band gaps of BMO which are in the range of  $\sim 1.15\text{-}1.20 \text{ eV}$  [40,189,225,218,237]. Despite the very close values of their bandgaps, the composite films efficiently absorb light wavelengths exceeding 850 nm (Fig. 4-11b) which also contributes to enhancing their PV properties. The contribution of NSTO substrate to the measured PV performance is excluded since the incident photons with energy  $E \geq 3.2 \text{ eV}$  (band gap of NSTO) are mainly absorbed in the films (Fig. 4-11b).

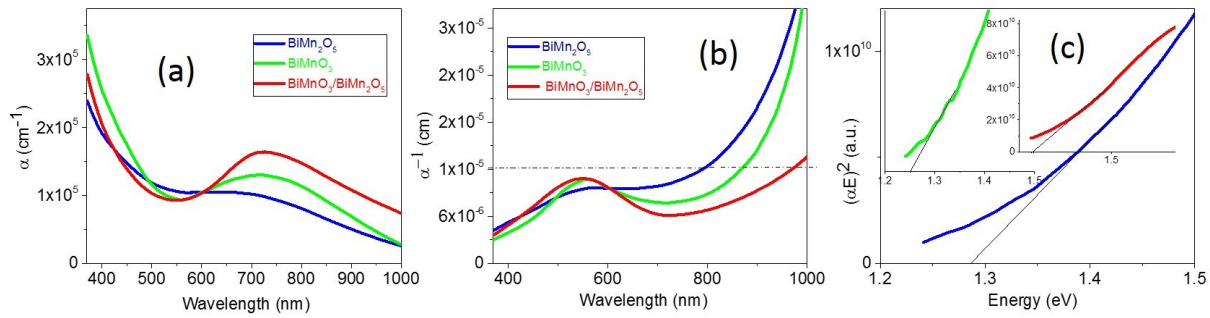


**Figure 4-11** (a) Optical absorption spectra of the films contained BMO-BiMn<sub>2</sub>O<sub>5</sub>, BMO, and BiMn<sub>2</sub>O<sub>5</sub> phases respectively. Corresponding penetration depth spectra (b) and estimated band gaps (c) of the films contained BMO-BiMn<sub>2</sub>O<sub>5</sub> (red), BMO (green), and BiMn<sub>2</sub>O<sub>5</sub> (blue) phases respectively.

### 4.3.7 Photovoltaic effect by scanning probe microscopy (SPM) measurements

#### 4.3.7.1 Conductive atomic force microscopy (C-AFM) measurements

To describe the effect of grain interfaces, we investigate the PV behavior of both bulk grain and grain boundaries at the nanoscale using conductive atomic force microscopy (C-AFM). The photocurrent generation properties of GBs were investigated using C-AFM and are presented in Fig. 4-12. Figure 4-12a,b show the topography and the corresponding photocurrent image recorded

simultaneously. During acquisition, the illumination of the sample (provided by a laser source with the wavelength of  $\sim 632$  nm) underneath the AFM tip was initially OFF (top of image) then turned ON (middle stripe) and OFF again (bottom). As can be seen in the current profile (Fig. 4-12c), the current generation is negligible under dark and there is a sizable short circuit current measured during the illumination period. This clearly demonstrates the occurrence of the PV effect in our films, and also excludes any topographic artefacts [238]. In a higher magnification measurement performed in another area under constant laser illumination (Fig. 4-12d,e), we observe that the contrast is not evenly distributed over the film's surface, but is rather most prominent around the locations corresponding to GB interfaces. At GBs, the magnitude of the current reaches values of 25 pA, one order of magnitude higher than in the bulk grain, as illustrated in a line scan profile crossing the GBs (Fig. 4-12e,f). Further investigations show that the magnitude of the photocurrent increases in absolute value with light intensity, reaching  $\sim 1000$  pA (Fig. 4-12h,i), while still remaining confined in the vicinity of the GBs. To verify the effect of any possible topographic artifact, the result is further confirmed by high-resolution photocurrent measurements, as shown in Fig. 4-12h-l. The magnitude of the photocurrent (which reaches  $\sim 600$  pA in this area), is highest at GBs and is not correlated with surface topography nor with the local slope. This can be clearly inferred by comparing the encircled regions. The green circle marks a "smooth" GB, where the photocurrent is high all across the GB, while in the red circle, indicating a steep GB, the current is high only where the adjacent grains are in direct contact. These observations show that the current spikes do not depend on the geometry of the tip-sample contact and we thus exclude the possible role of topographic artifacts in our measurements.

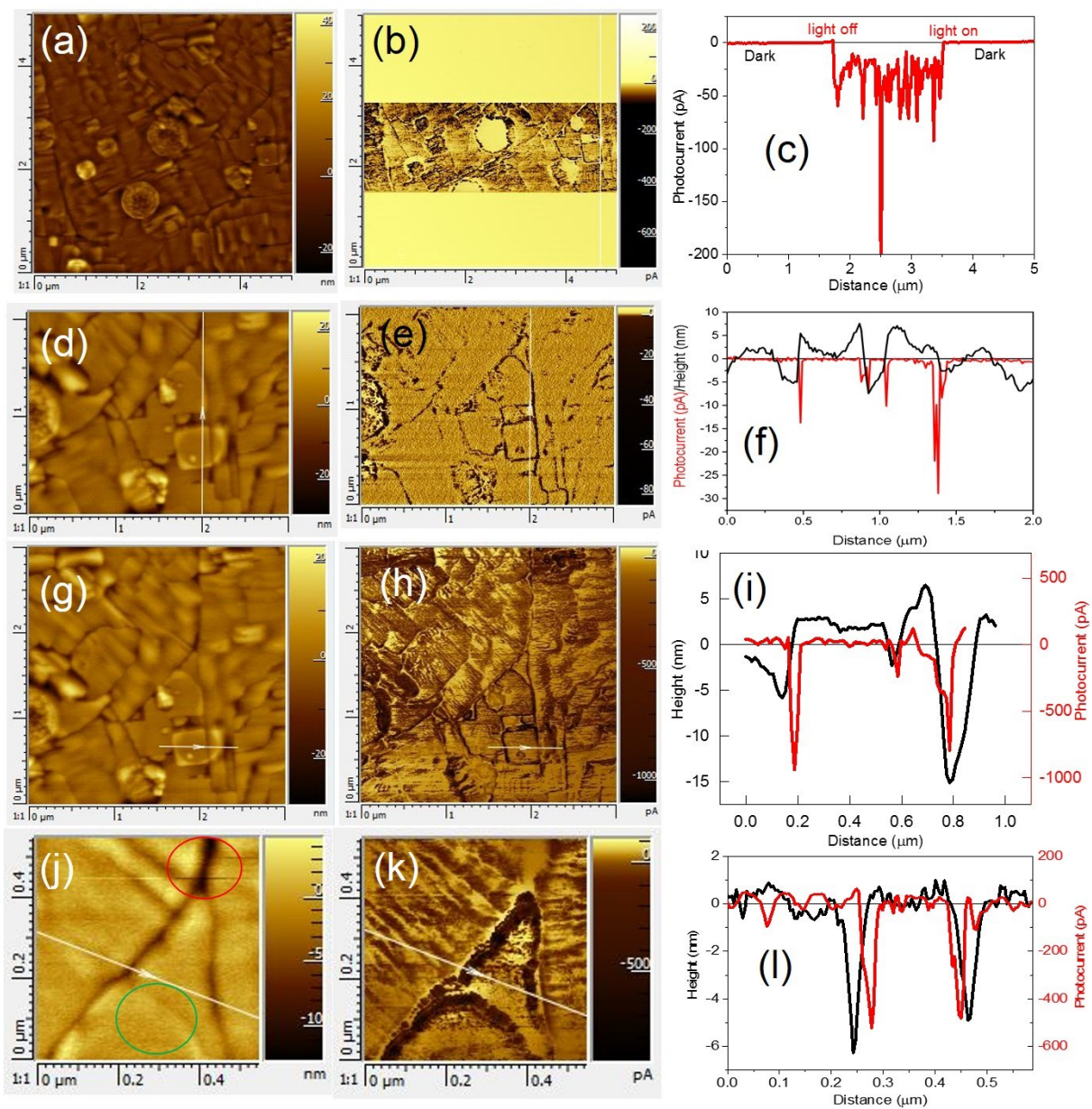


**Figure 4-12** Surface photocurrent measurements by C-AFM performed on as-grown samples (a) Topographic image (b) current image recorded while switching the illumination on/off at 0 V bias (c) current line profile across the image. Topographic image (d) and current image under illumination at 0 V bias (e) recorded in another area on the surface of the sample, (f) line profiles of topographic and corresponding current showing a high current at GBs. The same measurements

performed while illuminating the sample surface at high intensity (g) Topographic image (h) short circuit current image (i) comparison of line profiles extracted from the short circuit current and topographic images. Higher resolution topography (j) and short circuit current (k) images under illumination, and (l) comparison of line profiles extracted from the short circuit current and topographic images. Scan sizes: (5x5)  $\mu\text{m}^2$  in a,b; (3x2)  $\mu\text{m}^2$  in d, e; (3x3)  $\mu\text{m}^2$  in g and h; and (0.54x0.54)  $\mu\text{m}^2$  in j and k.

#### 4.3.7.2 Kelvin probe force microscopy (KPFM) measurements

The PV activity was further studied by assessing the induced photovoltage. We mapped the surface potential using KPFM, both in dark conditions and under illumination, as shown in Fig. 4-13. Again, there is no correlation between topographic images (Fig. 4-13a,c) and the corresponding contact potential difference (CPD) (Fig. 4-13b,d). These observations allow us to exclude possible artefacts that may arise from non-local capacitive contributions [239]. The contrast in CPD images does not reveal changes at GBs as observed in the C-AFM experiments described above. We attribute this observation to the conductivity of the sample which allows the charge carriers to move in the film's plane (thus flattening the surface potential), and to the screening of charges by adsorbed layers, formed in the ambient atmosphere. To test the second hypothesis, we analyzed the CPD in an area previously scanned in contact mode, where the adsorbed layers have been partially removed (area marked with rectangles in Fig. 4-13a,c). Comparing cross-section profiles within this area in the dark and during illumination (Fig. 4-13e,f) reveals that CPD values differ at GBs, being highest under illumination ( $\sim 45$  mV) compared with the values in the bulk grain ( $\sim 30$  mV). While it may seem low, this difference of  $\sim 15$  mV is higher than that observed at GBs in  $\text{Sb}_2\text{Se}_3$  ( $< 10$  mV) thin films [240]. Statistical data analysis shows that while the roughness of both topographic images acquired in the dark and under light is equal to  $\sim 5$  nm, the full width at half

maximum (FWHM) of the CPD distribution calculated from the CPD image under illumination is broader by  $\sim 50$  mV (Fig. 4-13g). This  $\sim 150\%$  increase in CPD distributions (from dark to illumination) is a clear indication that the distribution of charges at the surface is broader and thus photo charge generation is not uniform. Additionally, this shows that the CPD distribution differs significantly from the dark. The recorded low CPDs at GBs in the dark and the C-AFM studies unveil a downward bend bending at GBs, similar to values found in previous reports [238]. The results suggest a very little decrease of the  $V_{OC}$  at GBs due to charge accumulation under illumination. The high or low  $V_{OC}$  at GBs depends on the potential barrier height at GBs [216,217], consistent with our results. The regions of similar heights do not exhibit the same potentials and vice versa, which confirms that the measured potential in our work is not an artifact that may originate from convolution with topography [216,241].

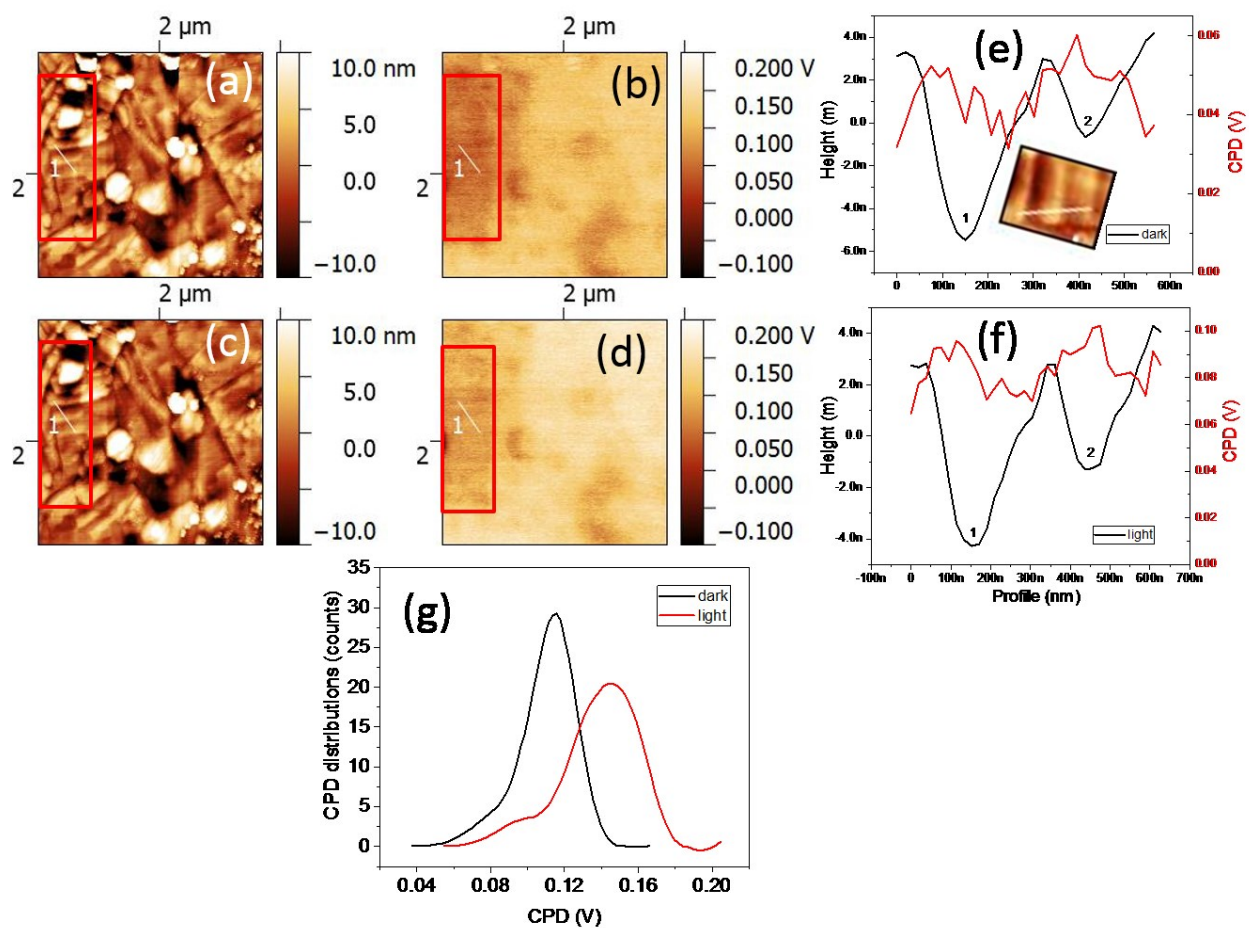


**Figure 4-13** Surface potential measured by KPFM performed on as-grown samples: (a) and (c) Topography, (b, and d) CPD image measured with (c, d) and without (a, b) illuminating the sample. (e, f) line profiles of the topography demonstrated as black curves extracted from (a) and (c) exhibit the same features, while the corresponding CPD profiles demonstrated as red curves clearly show a distinct photovoltage generation across grains and grain boundaries. (g) Comparison of CPD distributions over the surface of the films under dark and illumination conditions.

#### 4.3.7.3 Possible artifacts in SPM based measurements

SPM-based experiments are dynamic measurement techniques whereby a tip scans (typically at constant speed) across a surface while exerting a constant force against it. This condition is

achieved using an actuator (the piezoelectric scanner) controlled with a feedback loop. SPM-based measurements are complex and thus prone to be influenced by artifacts. Below we describe several possible artifacts and taken approaches to minimize such effects in the measurements.

(i) **Topographic artifacts:** At GBs, the tip may touch the sample in two or more contact points, and since this increases the total contact area, the measured current may be higher. This kind of artifact cannot be completely ruled out. However, a careful analysis of the current over several GBs may allow to assess its relative importance. In our case, for example, the images in [Fig. 4-12 j,k](#) showed that similar GB contact geometry exhibit very different current levels, as discussed in the main text. This type of artifact should not depend on the geometry of sample illumination i.e. illumination angle with respect to sample surface. Since in our experiments the short circuit current increases drastically under illumination, we do not believe that topographic artifacts play a significant role in our observations.

(ii) **Indirect topographic artifacts:** When the SPM tip crosses over GBs, there are spikes in the error signal (i.e. the difference between the actual force and the set point/desired force) meaning that the contact force also undergoes fast variations, which are dependent on the sensitivity of the feedback loop. These spikes in the contact force may result, via different mechanisms, in an increased current. We anticipate two such mechanisms: (a) Changes in tip/cantilever – sample capacitance, since the force is known to be proportional to the cantilever displacement (proportional to the contact force), in cantilever-based AFMs. If the capacitance is kept at a constant potential (the CPD between tip and sample), then there will be a flow of charge to re-establish charge equilibrium. (b) Increased charge scrapping: since the tip scans in contact with the surface, it continuously scraps charges from the surface, and charges from ambient re-screen the surface, as described in references [\[242,243\]](#).

These charges, collected by the conductive tip may be detected by the current amplifier and thus could appear in the current image. At GBs, where the geometry of the surface changes, we believe the bound charge to be different from that found in the adsorbed layers on top of grains, possibly resulting in spikes of the measured current.

Since the deflection signal spikes at the surfaces depend on the scan parameters, particularly on scanning speed, they can be easily identified. Similarly, the removal of bound charges depends linearly on speed [242]. We performed the SPM measurements at several different relatively low speeds to minimize these effects [242,244]. We did not observe significant changes in the measured current due to changes in the scan speed. On this basis, we exclude this effect as a possible artifact in C-AFM measurements.

**(iii) Pyroelectric effect:** Although the incident photon flux on the sample is constant, the AFM tip may change the local flux underneath due to the local shadowing by the tip and/or cantilever, resulting in a local change of thermal equilibrium (either cooling or warming if the tip absorbs more heat). If the material is pyroelectric (non-centrosymmetric), cooling may result in a local change of polarization, which could, in principle, result in a flow of charges to re-equilibrate surface charges. This effect was analyzed in detail by Alexe and Hesse [138] and it was found to be negligible in the case of the prominent ferroelectric BiFeO<sub>3</sub>. In our case, however, the material is a composite film, made of two phases, namely semiconducting BiMn<sub>2</sub>O<sub>5</sub> and the weak FE BMO (which very likely exhibits a low pyroelectric coefficient). Estimates for the perovskite BiFeO<sub>3</sub> concluded a pyroelectric contribution of  $\sim 2 \times 10^{-15}$  A, roughly six orders of magnitude below the measured photocurrent [12]. In our case, we measured higher photocurrents (1 nA vs 0.3 nA) using a much lower laser power (4 mW as opposed to 80 mW in [12]) and therefore conclude that the

pyroelectric contribution to the measured current is negligible compared to the photovoltaic response.

(iv) **Photostimulated electron emission from the electrode:** In principle, the photoelectric effect could take place at the bottom electrode, resulting in electrons reaching into the film and arriving at the surface via transport through the bulk or the more conductive paths at GBs. However, in our case, the absorption length at 632 nm wavelength (the C-AFM measurement) is less than 100 nm (Fig. 4-11b). In addition, the STO substrate, which has a bandgap of  $\sim 3.2$  eV and electron affinity of  $\sim 4$  eV starts to absorb at wavelengths below 400 nm [245]. We, therefore, believe that we can safely exclude this effect in our measurements.

#### 4.4 Discussion

The occurrence of an APV (i.e. a  $V_{OC}$  larger than the band gap of either individual phases) in the composite films can be described either in relation to GB barrier potentials existing in mainstream semiconductors [14] or by spontaneous polarization in FE materials [131]. The presence of both semiconducting ferroelectric BMO and non-FE semiconductor  $\text{BiMn}_2\text{O}_5$  phases are also demonstrated by nanoscale measurements (Fig. 4-7, showing that some grains exhibit FE hysteresis loops, while others do not). We then conducted nanoscale ferroelectricity measurements, which showed that ferroelectricity does not govern the observed APV. We first investigated the occurrence of ferroelectricity in selected grains by recording FE hysteresis loops using PFM, as shown in Fig. 4-5. Subsequently, we oriented the polarization in two FE grains in opposite directions, then measured the CPD both in dark and under illumination. Since we did not observe a significant effect of polarization orientation on the CPD even for grains which were demonstrated to be FE (Fig. 4-7), we conclude that ferroelectricity does not play a significant role

in the observed APV. Therefore, we believe that band bending occurring at GBs (evidenced by C-AFM and KPFM) plays a crucial role in the behavior observed in our nanocomposite films. Following this observation, we take into account the concept of GB barrier potentials to describe our results. To better understand the processes that take place in our composite films, we then analyzed the J-V curves taken under dark and illumination conditions by repeatedly applying voltage pulses in the sample. The series of bipolar applied DC pulses is shown in Fig. 4-14a. We recorded J-V curves first for both  $P_{up}$  and  $P_{down}$  polarization states that are shown in Fig. 4-8b. Then we applied pairs of positive/negative (bipolar) pulses to cycle the polarization orientation and recorded a J-V curve after each, both under illumination and under dark. We found the same J-V curves under the light until 6 polarization cycles and similarly no significant changes were observed in the J-V curve taken under dark conditions until 6 pulses were applied. In contrast, the J-V curves recorded at or more than 6 polarization cycles clearly demonstrate the increased current density by the effect of increased number of pulses (4-14b and Fig 4-15a). The calculated resistances (the slope at zero applied voltage) after each bipolar pulse are shown in Fig. 4-14c.

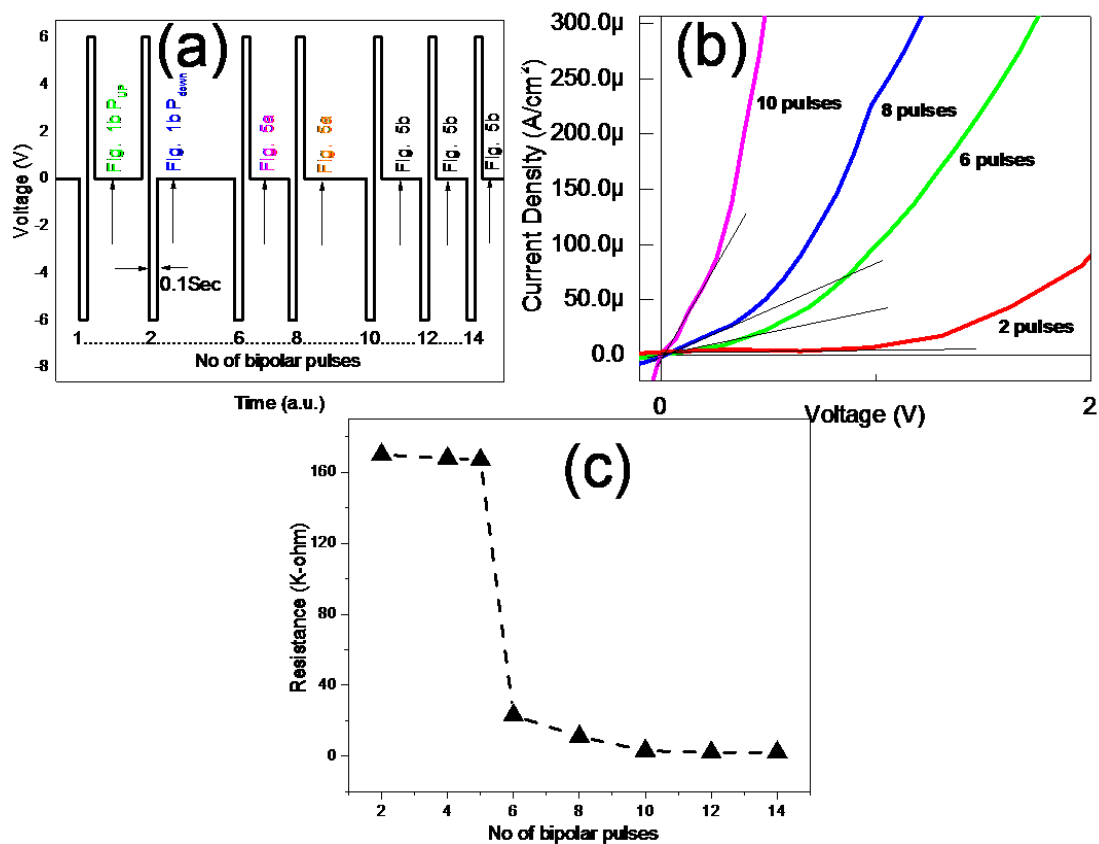


**Figure 4-14** (a) Sequence of applied number of bipolar voltage pulses and corresponding recorded J-V curves (b) J-V curves recorded after applying different bipolar voltages pulses under dark. (c) Plot of resistance as a function of the number of applied pulses.

The effect of pulses on photovoltage and photocurrents is described in [Fig. 4-15](#). In the pristine samples, (before applying any voltage pulse), we measured a low  $J_{SC}$  of  $330 \mu\text{A}/\text{cm}^2$  ([Fig. 4-15a](#)). After the first cycling of polarization (i.e. the application of one negative and one positive voltage pulse, see [Fig. 4-14a](#))  $J_{SC}$  increased dramatically to  $7.03 \text{ mA}/\text{cm}^2$  and remained close to this value until six voltage pulses, after which it decreased again ([Fig. 4-15c](#)). Nonetheless, the J-V curves recorded under dark showed a gradual increase of the current with the number of applied voltage pulses ([Fig. 4-14b](#)).

On the basis of these results, we propose the following scenario for the PV behavior observed in our films: the PV effect is present over the whole film surface, yet it is much stronger at the GB where the conductivity is higher due to the local barrier potentials. Initially,  $J_{SC}$  is low, because the carrier conduction paths are narrow. With voltage pulses applied to switch the direction of polarization, charge carriers are injected and accumulated mainly along the conduction paths further contributing to conductivity, similar to the fatigue mechanism observed in  $\text{BiFeO}_3$  [246] and causing the initial increase of  $J_{SC}$ . With increasing the number of bipolar pulses, the space charge region extends further away from GBs into the bulk of the grains. The growth of the space charge region leads to the saturation (with the number of pulses) of the PV effect taking place at the boundary, possibly by reducing the GB potential barrier. Additionally, the space charge region expanding into the bulk grain becomes more conductive, providing (internal) short-circuit paths through which the photocurrent leaks back, thus reducing the  $J_{SC}$  and  $V_{OC}$  measured in the external circuit. This scenario is consistent with the model developed by Metzger and Gloeckler who found that charge accumulation at GB essentially controls their mobility within the GBs [247].

The increase of the dark conductivity with the number of applied voltage pulses was also related to FE fatigue [248,249]. The fatigue mechanism is often described in the framework of the GB model [214,215] and in the model of defect trapping at electrode-semiconductor interfaces [250,251]. As depicted in Fig. 4-15, our results show first an increase, then a plateau followed by the deterioration of the device PV parameters ( $V_{OC}$  and  $J_{SC}$ ), in agreement with the GB model described above. According to charge trapping model, the effective thickness of the PV active film would decrease continuously with the number of bipolar pulses, eventually leading to a complete short-circuit of the film. However, in our samples, we observe that the PV parameters do not collapse to zero, but rather reach the second plateau after 10 bipolar pulses (Fig. 4-15b,c and Fig.

4-14c). The PV parameters in this degraded (fatigued) state were also found to be stable in time and returned to the same values upon switching the light on/off (Fig. 4-15b). Therefore, we conclude that the effect of the successive voltage pulses on the  $V_{OC}$  and  $J_{SC}$  observed in our experiments proves the GB effect on PV performance.

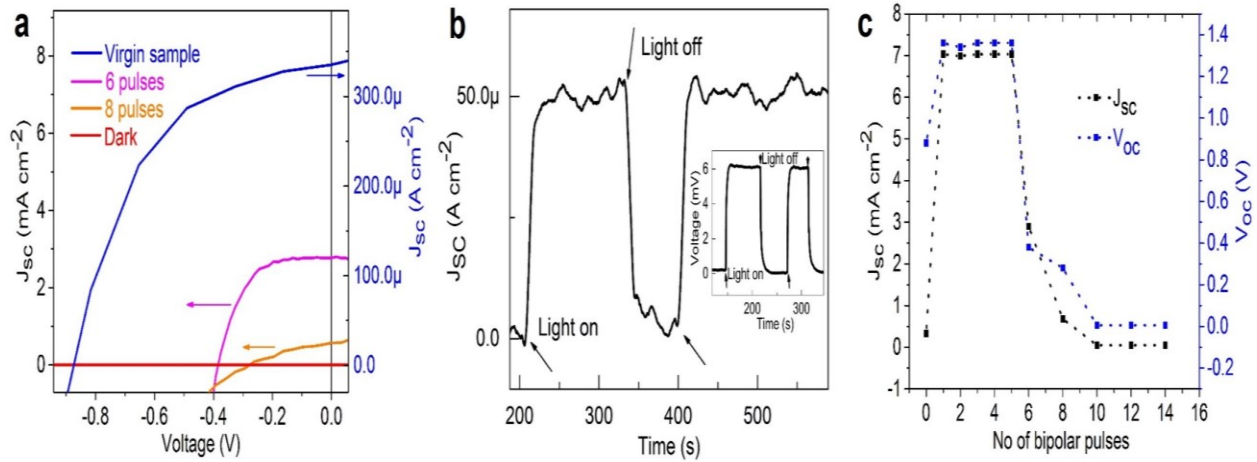


**Figure 4-15** (a)  $J_{SC}$ -V curve recorded under illumination before and after poling (with 6 and 8 voltage pulses) respectively (b) Plot of the  $J_{SC}$  as a function of time recorded on the samples cycled 10 times. The inset shows associated  $V_{OC}$ . (c) Variation of PV parameters ( $J_{SC}$  and  $V_{OC}$ ) as a function of the number of pulses.

## 4.5 Conclusions and perspectives

We presented an approach based on GB engineering in  $ABO_3$ -perovskite oxide thin films to control and stabilize the PCE. We showed that the inclusion of GBs in such oxide absorbers enhances optical absorption, a surprising phenomenon for multiferroic and perovskite-based PV devices. In contrast, most devices based on polycrystalline absorbers in mainstream silicon or III-V semiconductor-based solar technologies exhibit worse performance compared to their single-crystalline counterparts, partly because GBs tend to contain numerous defects, thereby enhancing

carrier recombination which in turn degrades optical absorption. However, fast photocarrier separation/transport and improved PCE can be achieved in polycrystalline devices by means of the atomic vacancies at GBs, positively charged GBs and proper electrode positioning near the GBs. Polycrystalline CIGS and CdTe solar cells are best-suited examples which exhibit superior device performances regarding their single crystalline counterparts. Here, we showed a record 4.20% PCE under 1 sun illumination (AM1.5G) recorded for Bi-Mn-O composite films, accommodating a large number of GBs promoted by the coexistence of BMO and BiMn<sub>2</sub>O<sub>5</sub> perovskite crystal phases. We find that this efficiency for a single layer perovskite oxide film is primarily controlled by the accumulation of charge carriers at GBs which can be modified by applying bipolar voltage pulses. The results demonstrate a fundamentally new way to enhance PCE in perovskite oxide thin film based PV devices. These concepts are promising for further developments in the emerging area of perovskite oxide photovoltaics, which have the evident advantage of long-term stability, since they are inorganic oxides.

# Chapter 5 Photoelectrochemical Properties of BiMnO<sub>3</sub> Thin Films and Nanostructures

## 5.1 Introduction

The discovery of the photovoltaic (PV) effect in semiconducting ferroelectric (FE) oxides creates interesting opportunities in solar energy research due to the characteristic band gaps of FEs (in the range 1.1-3.5 eV) and their spontaneous polarization (originating from their non-centrosymmetric crystal structure) induced internal electric field which extends across the whole volume of material. This electric field can be used to drive photogenerated charge carriers towards their respective electrodes, without the need for a p-n junction [12,252,253]. Reports on anomalous photovoltages (up to 1000 V) [10] and high power conversion efficiency (PCE) (up to 8.1%) [17,18] in solid-state FE PV devices highlight the promising properties of such materials for next-generation solar cells. The application of FE materials has also recently been extended to photocatalytic hydrogen production. It was shown that multiferroic BiFeO<sub>3</sub> (BFO) [37,38,39] and Bi<sub>2</sub>FeCrO<sub>6</sub> (BFCO) [40] can act as photoelectrodes for H<sub>2</sub> and O<sub>2</sub> evolution through dissociation of water in photoelectrochemical (PEC) cells. In such bismuth-based perovskites, ferroelectricity modulates the band bending in favor of efficient carrier collection from semiconductor to electrolyte, thus increasing the photocurrent. Similarly, multiferroic BiMnO<sub>3</sub> (BMO) films exhibit FE behavior at room temperature (RT) and devices based on BMO convert radiation into electricity through the FE PV effect [189]. Typical BMO films have a small band gap (~ 1.2 eV) which promotes photon absorption from a broad range of the solar spectrum, including visible light. This feature prompted our study of BMO compounds as photoelectrodes in PEC cells. In addition, FE materials including BFO and BFCO retain their RT multifunctional (FE and magnetic) character even when shrinking

their dimensions to the submicrometer range, often referred to as size effects, [254,255,256] thereby offering exciting opportunities to miniaturize solid state device architectures. Additionally, the size effects in FEs enable large surface to volume ratio that could be useful in PEC solar cells to transfer a large number of charge carriers from semiconductors to electrolytes.

In this chapter, we demonstrate the controlled growth of BMO nanostructures (NS-BMO) through nanostencils [257,258,259] i.e. shadow masks with a periodic array of nanometer-scale circular features, on (111) oriented Niobium (Nb)-doped SrTiO<sub>3</sub> (NSTO) substrates by pulse laser deposition (PLD). More specifically, we demonstrate the proof of concept of stabilization of crystalline BMO nanostructures on the substrates by PLD. Conducting NSTO was chosen as a substrate to promote epitaxial growth of BMO, which is favored by the small lattice mismatch. In addition, its conductivity makes it a good candidate for a bottom electrode for electrical measurements. We study the optical and PEC properties of the NS-BMO and compare them with BMO thin films (TF-BMO) deposited on NSTO substrates by PLD. We show that size effects (i.e. thin films vs. nanostructures) allow to favorably tailor the energy band alignment with respect to the redox potential of water. We demonstrate that BMO photoelectrodes can obtain variable band position in favor of hydrogen and oxygen evolution, respectively. According to the band alignment with respect to the redox potential of water, we conclude that both types of photoelectrodes are suitable for oxygen evolution reaction.

## **5.2 Experimental methods**

### **5.2.1 Thin film growth**

BMO thin film heterostructures were grown on single crystal NSTO (111) substrates by PLD. A Bi<sub>1.4</sub>MnO<sub>3</sub> target was used to deposit Bi-Mn-O films on NSTO substrates. The PLD chamber was

pumped to a vacuum level of  $1 \times 10^{-6}$  mbar prior to deposition. The deposition parameters were set as follows: laser fluence  $\sim 1.5$  J/cm<sup>2</sup>, pulse frequency  $\sim 1$  Hz, and the substrate temperature  $\sim 620^\circ\text{C}$ . Oxygen pressure in the deposition chamber was kept constant at  $\sim 10$  mTorr. The target to substrate distance was  $\sim 6$  cm. After deposition, the as-grown films were annealed for 20 mins under same oxygen pressure before cooling to RT under vacuum. The thickness of the films was  $60 \pm 10$  nm, as estimated by X-Ray Reflectivity.

### 5.2.2 Nanostructure growth

Nanostructured BMO was grown on NSTO (111) substrates using the same target and PLD chamber as for the BMO thin films. The PLD chamber was pumped to the same vacuum level ( $1 \times 10^{-6}$  mbar) prior to deposition. A stencil mask with nanoscale apertures acquired from Aqua Marijn Filtration (The Netherlands) was mechanically mounted on the substrate to grow the patterned NS. Patterning via nanostenciling [260,261] is an unconventional approach which does not require post-deposition etching processes compared to traditional methods such as electron-beam lithography and focused ion beam lithography. The fabrication of nanostenciling experiments was conducted using laser interference lithography-based stencil masks, with built-in 500 nm thick Si<sub>3</sub>N<sub>4</sub> nanosieves with circular apertures. The stencils had hexagonal arrays of pores (350 nm in diameter) with a periodicity of 700 nm and were patterned on 14 free-standing, low-stress (LS- Si<sub>3</sub>N<sub>4</sub>) membranes (2 mm in length and 100  $\mu\text{m}$  in width each, 100  $\mu\text{m}$  apart). The 0.5  $\mu\text{m}$  Si<sub>3</sub>N<sub>4</sub> membranes were prepared on single crystalline Si (100) wafers 380  $\mu\text{m}$  thick and the stencil's dimension was  $5 \times 5$  mm<sup>2</sup> with an active area of  $2 \times 2.7$  mm<sup>2</sup>. The stencils were mechanically clamped and temporarily fixed onto the substrates. It was desirable that the gap between the sieve and substrate be as small as possible and as uniform as possible over the whole shadowed area, which was achieved using a proper mechanical fixture for the stencil–substrate

assembly. The deposition parameters were set as follows: laser fluence  $\sim 3 \text{ J/cm}^2$ , pulse frequency  $\sim 10 \text{ Hz}$ , and the substrate temperature  $\sim 620 \text{ }^\circ\text{C}$  under a partial oxygen pressure of  $\sim 10 \text{ mTorr}$ . The target to substrate distance was  $\sim 5.5 \text{ cm}$ . After deposition, the as-grown structures were cooled to RT under vacuum.

### 5.2.3 Sample preparation for PEC experiments

The films and nanostructures of BMO were deposited by PLD on the one-sided polished thus one-sided conducting niobium doped STO substrates with the dimension of  $(10 \times 5 \times 0.5) \text{ mm}^3$ . The BMO samples were attached to the FTO coated glass substrate using silver paste so that the photogenerated carriers can easily transfer from the sample to the FTO coated glass. The entire sample except the specific BMO film surface area was then covered with insulating epoxy to reduce current leakage. The FTO was then connected to the measurement instrument as working electrodes, as illustrated in [Fig. 5-1](#). The PEC properties of BMO thin films and nanostructures were investigated using linear sweep voltammetry experiments (scan rate of  $25 \text{ mV/sec}$ ), in a three-electrode configuration, which consists of an Ag/AgCl reference electrode, a Pt counter electrode, and as prepared BMO samples as working electrodes. All PEC measurements were conducted in an aqueous solution of  $1.0 \text{ M Na}_2\text{SO}_4$ . The samples were illuminated through a quartz window with a sun simulator (AM1.5G) with the irradiance of  $100 \text{ mW/cm}^2$  (1 sun) and  $200 \text{ mW/cm}^2$  (2 sun) at a distance of  $2 \text{ cm}$  from the lamp case ( $7 \text{ cm}$  distance from the bulb). The sun simulator was manually turned on/off to record the chopped current.

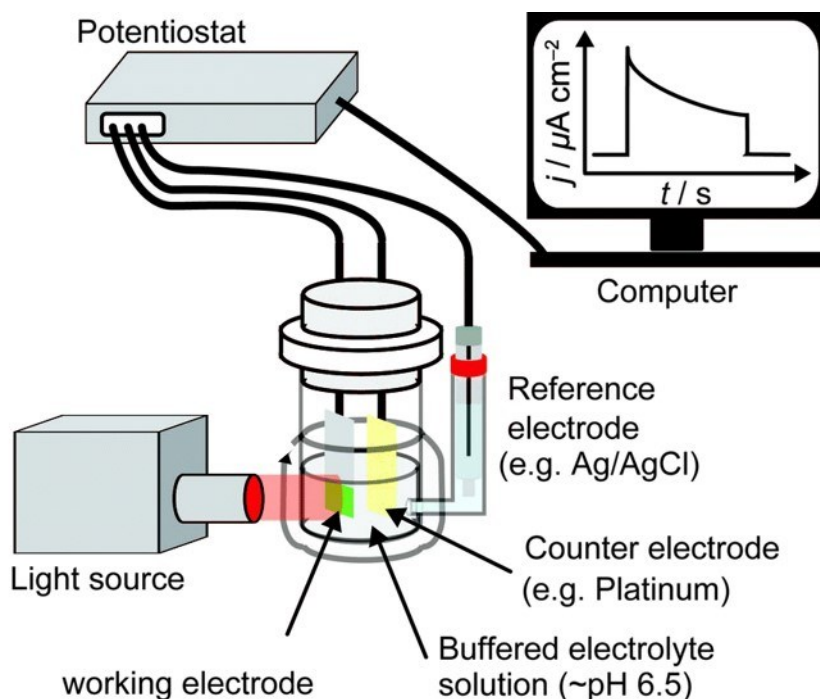


Figure 5-1 Schematic of a basic PEC cell set up. [262]

## 5.3 Characterizations

### 5.3.1 Crystal structures

Figure 5-2a shows a typical  $\theta$ - $2\theta$  scan X-ray diffraction (XRD) pattern of the obtained films. The pattern reveals that the BMO crystal phase has a preferential orientation along the pseudocubic  $(111)_{pc}$  direction. The films exhibit the additional  $(1/2, 1/2, 1/2)$  reflections of BMO, which correspond to monoclinic structure. The  $\Phi$ -scan analysis around the NSTO (101) reflection suggests epitaxial growth of the films with threefold symmetry (Fig. 5-2b.). The monoclinic unit cell of BMO ( $a_m = 0.954 \text{ nm}$ ,  $b_m = 0.561 \text{ nm}$ ,  $c_m = 0.986 \text{ nm}$ , and  $\beta = 110.7^\circ$ ) is composed of the superposition of strongly distorted perovskite units with the pseudocubic lattice parameter of  $a_{pc} = 3.95 \text{ \AA}$ . Therefore the lattice mismatch between BMO and NSTO is only  $\sim 1.13\%$  [263,264]. A large lattice mismatch (the difference in the atomic spacing between the film and substrate

materials) and the difference in thermal expansion rate induces strain and stress during film growth, thus affecting crystallization process and hindering epitaxy. The small mismatch between BMO and NSTO promotes the heteroepitaxial growth of single-phase BMO. The results are consistent with previous work on BMO films [225]. Figure 5-2c displays scanning electron microscopy (SEM) images of NS-BMO samples. The crystal structures are confirmed by XRD  $\theta$ - $2\theta$  scans (Fig. 5-2d) which show highly  $(111)_{pc}$  oriented BMO crystal phases. The results indicate the same crystal structures as obtained in the films. A similar procedure for patterning nanostructures and their structural characterization has been also described in the case of FE BFCO materials [256].

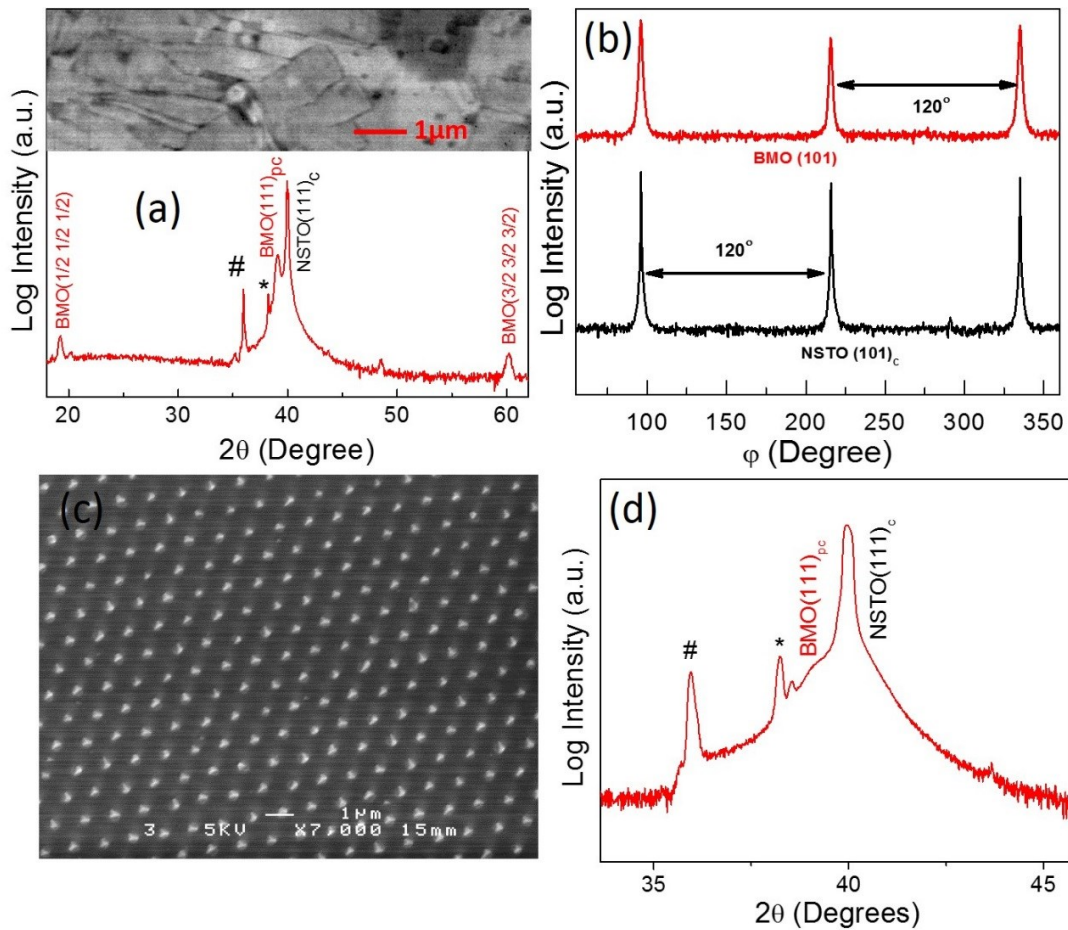


**Figure 5-2** (a) XRD  $\theta$ - $2\theta$  scans of BMO films deposited on (111) oriented NSTO substrates. The symbol '#' indicates tungsten contamination of the x-ray tube sources. The inset shows SEM image of as-deposited BMO films (b)  $\Phi$  scan measurements show three-fold symmetry of BMO, demonstrating the epitaxial nature of the films (c) SEM image of BMO nanostructures grown on (111)<sub>c</sub> oriented NSTO using a stencil mask (d) XRD  $\theta$ - $2\theta$  scans exhibit (111)<sub>pc</sub> orientation of BMO nanostructures.

### 5.3.2 Average heights of nanostructures

A typical Atomic Force Microscopy (AFM) images of the as-deposited BMO nanostructures are illustrated in Fig. 5-3a,c. The average height of each nanostructure is estimated from the line profile measurements of AFM images (Fig. 5-3b,d) to be  $\sim 70$  nm. The average heights and size distributions of nanostructures are depicted in Fig. 5-3e,f.

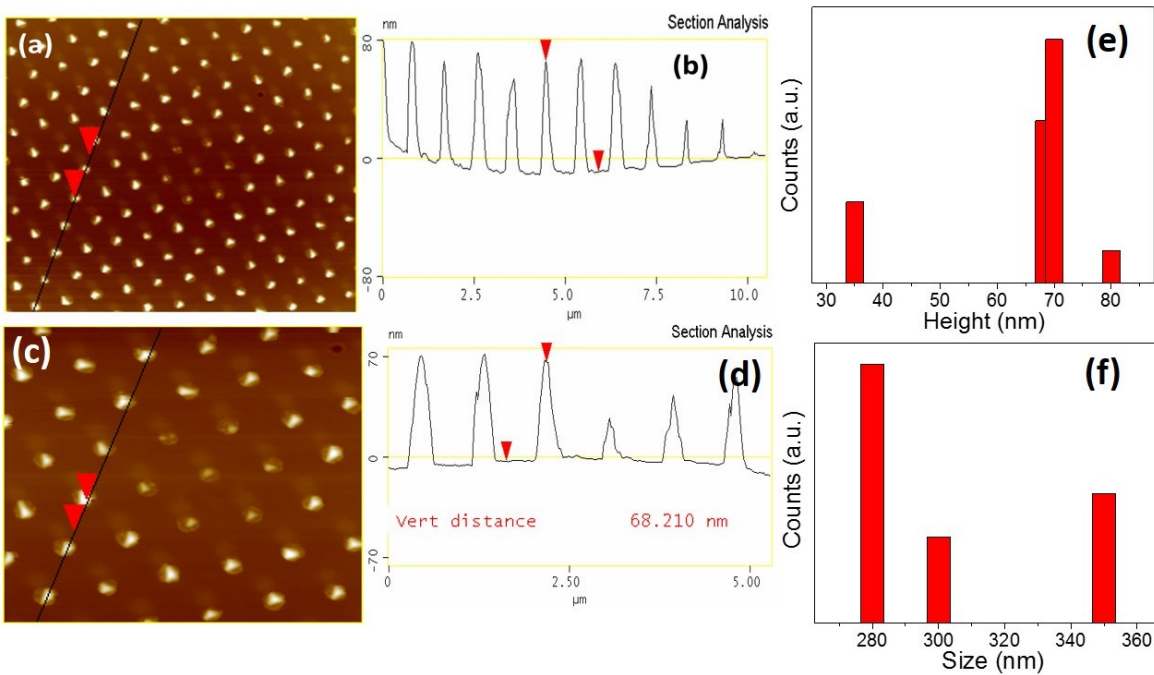


**Figure 5-3** (a)  $10 \times 10 \mu\text{m}^2$  AFM image of the as-deposited nanostructures exhibiting the formation of a hexagonal nanoscale pattern on the NSTO substrate (b) Line profile of image (a) exhibits the average height of  $\sim 70$  nm of each nanostructure with  $5 \times 5 \mu\text{m}^2$  AFM imaging (c) the high resolution associated line profiles of the nanostructures (d) that further confirms the average height of each. The nanostructures' height and size distributions are reported in (e) & (f) respectively.

### 5.3.3 PEC cell performance

For a simultaneous monitoring of the dark and light current in our devices, the PEC properties of TF-BMO and NS-BMO were investigated by linear sweep voltammetry (LSV) under chopped light illumination (Fig. 5-4). The fast increase and decrease of the current density ( $J_{SC}$ ) under chopped light illumination signals the presence of effective photocharge carrier extraction with reduced probability of critical charge trapping and discharging effect [265]. Figure 5-4a,b display the  $J_{SC}$  as a function of applied potential recorded in TF-BMO and NS-BMO respectively. The onset potential is determined to be  $\sim -0.6$  V vs. Ag/AgCl ( $\sim -0.02$  V vs RHE, reverse hydrogen electrode) for the films whereas a shift to more negative potentials  $\sim -0.9$  V vs. Ag/AgCl ( $\sim -0.30$  V vs. RHE) is observed in nanostructured BMO. In comparison, the shifting of onset potentials of anodic photocurrent from  $-0.209$  V vs. Ag/AgCl to  $-0.366$  V vs. Ag/AgCl is described by the effect of Ti doping on the improved photocurrent in BFO films [266]. In TF-BMO, the highest  $J_{SC}$  of  $\sim 10$   $\mu\text{A}/\text{cm}^2$  at  $0.4$  V vs Ag/AgCl ( $0.98\text{V}$  vs RHE) was recorded at 1 Sun illumination ( $100$   $\text{mW}/\text{cm}^2$ ). The  $J_{SC}$  increased to  $\sim 40$   $\mu\text{A}/\text{cm}^2$  at  $0.4$  V vs Ag/AgCl when the same films were exposed to 2 Sun illumination. In epitaxial  $223$  nm-thick BFO films, the highest  $J_{SC}$  of  $\sim 10$   $\mu\text{A}/\text{cm}^2$  were reported under illumination with intensities of  $250$   $\text{mW}/\text{cm}^2$  (2.5 Sun) [37]. In our case, the  $60$  nm-thick BMO film yields the same values of  $J_{SC}$  as BFO under 1 Sun illumination and increases up to 4 times under 2 Sun illumination. The observed open circuit voltage ( $V_{OC} = \sim 0.38$  V) increases from positive potential to negative potential under illumination (inset of Fig. 5-4a) which are the typical characteristics of n-type semiconductor photoelectrodes [267]. As illustrated in Fig. 5-4b, the highest  $J_{SC}$  of  $\sim 900$   $\mu\text{A}/\text{cm}^2$  at  $0.8$  V vs Ag/AgCl ( $1.38$  V vs RHE) was recorded under 1 Sun in NS-BMO. Similarly, the highest photocurrent density of  $0.4$   $\text{mA}/\text{cm}^2$  and  $2.7$   $\text{mA}/\text{cm}^2$  both at  $1.4$  V vs RHE was reported in Ti-doped  $\alpha\text{-Fe}_2\text{O}_3$  films and  $\text{WO}_3$  films respectively

[268,269]. The quantitative estimate of the surface area of the nanostructures exposed to electrolytes is described in following section 5.3.4. The photocurrent density of BMO nanostructures is quite small ( $\sim 12 \mu\text{A}/\text{cm}^2$ ) in negative potential and significantly increases in positive potentials ( $\sim 900 \mu\text{A}/\text{cm}^2$ ). Similarly to BMO films, the photovoltage of BMO nanostructures increases towards negative potential ( $V_{\text{OC}} = \sim 0.32 \text{ V}$ ). This suggests that the deposited nanostructures behave as n-type photoanode materials. The saturated  $J_{\text{SC}}$  values measured in NS-BMO are similar to those observed in BFCO films [40]. Negligible PEC responses were observed from ‘naked’ NSTO substrates (green color in Fig. 5-4a), implying that the observed PEC properties mainly originate from films.

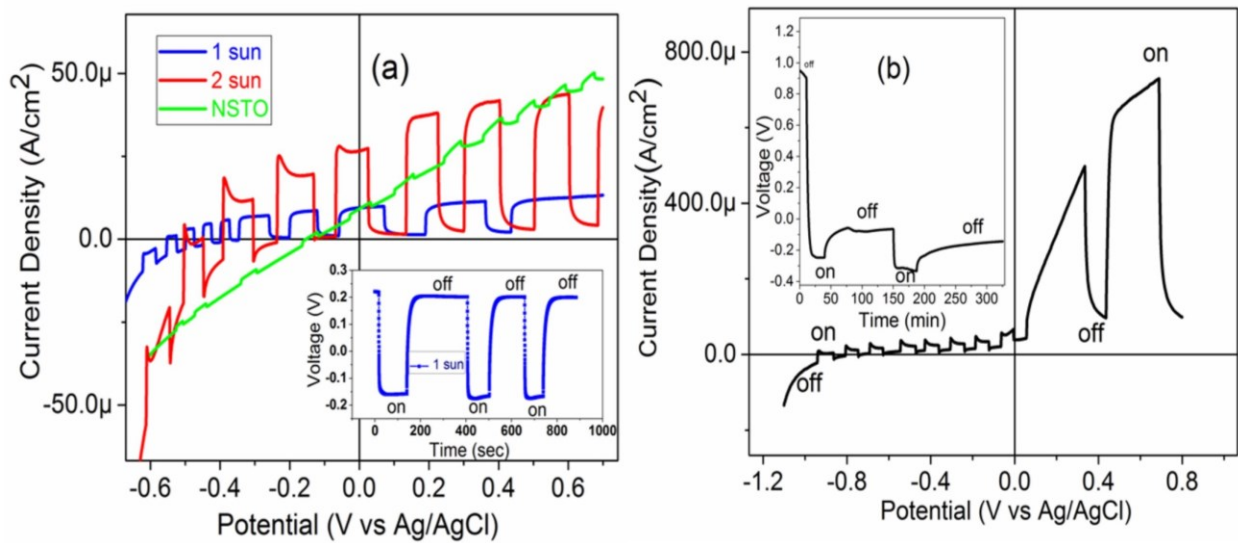


**Figure 5-4** (a) Variations of current density with applied voltage (vs Ag/AgCl) in 1 M  $\text{Na}_2\text{SO}_4$  at  $\text{p}^{\text{H}}$  6.8 under chopped 1 Sun and 2 Sun illumination of BMO films. The inset shows the response of the open circuit voltage under dark and at 1 sun illumination (b) Variations of current density with applied voltage (vs Ag/AgCl) in 1 M  $\text{Na}_2\text{SO}_4$  at  $\text{p}^{\text{H}}$  6.8 under chopped 1 Sun illumination of BMO nanostructures. The inset shows the response of the open circuit voltage under dark and under 1 Sun illumination.

### 5.3.4 Calculation of total surface area of the BMO nanostructures

We calculated the current density described in Fig. 5-4 by the following equation,

$$\text{Current density} = \frac{\text{measured current}}{\text{total surface area exposed to electrolytes}} \dots\dots\dots (5.1)$$

The procedure that followed to calculate the total surface area exposed to electrolytes is described as follows:

$$\text{Area of hexagon} = \frac{[(3\sqrt{3})a^2]}{2} \dots\dots\dots (5.2)$$

where a = 700 nm as estimated from Fig. 5-5a. Therefore the density of nanostructures is  $\sim 2.36 \times 10^8 \text{ cm}^{-2}$ . As shown in Fig. 5-5b, there are overall 14 slots, and the patterning of the nanostructures is located in each slot. The area of one slot is estimated to be  $\sim 0.0022 \text{ cm}^2$ , yielding a total area of 14 slots of  $\sim 0.0308 \text{ cm}^2$ . Therefore the total number of nanostructures in our samples is  $\sim 7268800$ . To simplify the calculation, we used this number of nanostructures. However, in practice, not all pores of the stencil mask contributed to form nanostructures because many were blocked due to residual material clogging from successive depositions. This was confirmed by SEM imaging of the bare stencil mask (Fig. 5-5c,d).

To estimate the surface area of an individual nanostructure, we assumed a triangular shape of each nanostructure on the basis of their typical line profile image (Fig. 5-6). The surface area of a single nanostructure can then be estimated by calculating the surface area of a triangle,

$$\text{Surface area} = \left(\frac{1}{2}\right)*b*h \dots\dots\dots (5.3)$$

where h and b indicate the height and base of each nanostructure which are 70 and 280 nm respectively (Fig. 5-6b). The calculated surface area of one side of one nanostructure is  $\sim 9.80 \times 10^{-11} \text{ cm}^2$ . Since it is a triangle, it has two other triangular facets. Therefore the total surface area of

one nanostructure is  $\sim 2.94 \times 10^{-10} \text{ cm}^2$  which yield a total surface area of all nanostructures of  $\sim 0.0021 \text{ cm}^2$ . As mentioned above in relation to the actual number of nanostructures, the total surface area will be somewhat lower and consequently, the photocurrent density will be higher than that calculated in the text.

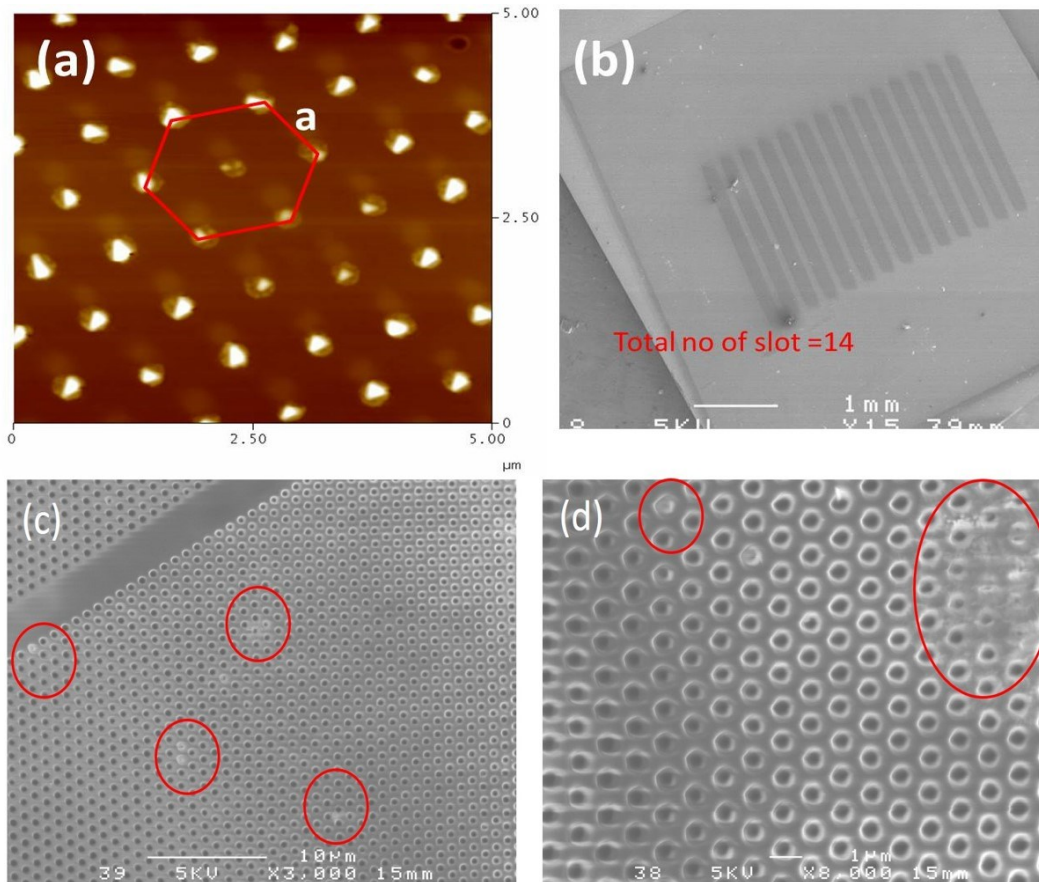


**Figure 5-5** (a) AFM image of the as-deposited nanostructures exhibiting the formation of a hexagonal nanoscale pattern on the NSTO substrate (b) Low magnification SEM images of slots wherein the nanostructures are formed (c) high magnification SEM image covering the intersection of two neighboring slots. The red circle indicates a number of blocked pores that did not participate in forming nanostructures. The presence of the same blocked pores is indicated by a red circle in another slot (d).

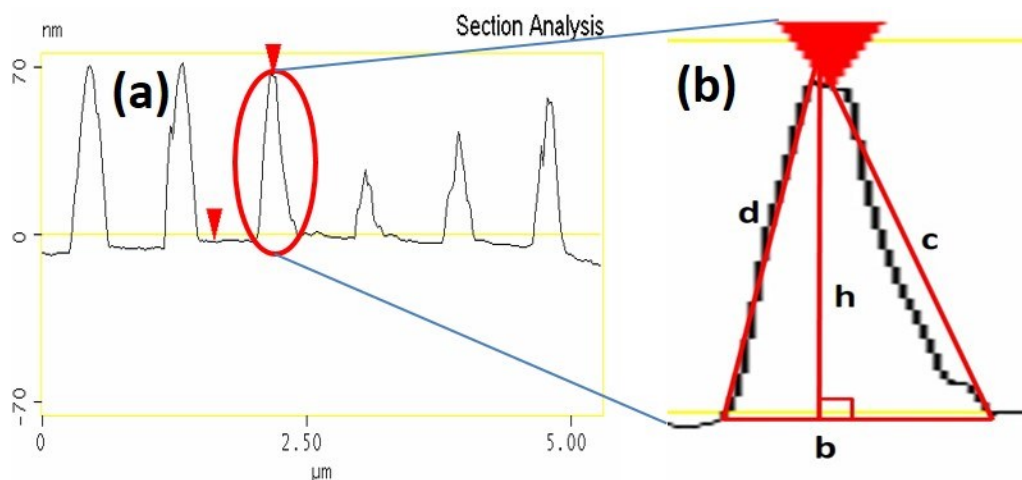


**Figure 5-6** (a) Line profile image of nanostructures depicted in Fig.5-3c (b) magnifying image of one of the line profiles of nanostructures suggesting the triangular shapes of nanostructures.

### 5.3.5 Photocurrent density as a function of time

Figure 5-4 shows the chopped  $J_{SC}$ , which essentially refers to the transient characteristics of the photocurrent density. It is important however to measure and compare the steady state characteristics of photocurrent density for both films and nanostructures. To confirm the steady state characteristics of  $J_{SC}$ , we recorded the photocurrent in both types of samples as a function of time (Fig. 5-7) while applying a constant bias of + 0.4 V (films) and + 0.8 V (nanostructures) vs Ag/AgCl (0.98 V vs RHE and 1.38 V vs RHE) in 1 M  $\text{Na}_2\text{SO}_4$  respectively. The photocurrent on both films and nanostructures tends to stabilize after a rapid initial decrease, then remains roughly stable up to  $\sim 1000$  s of testing under illumination. Specifically, TF-BMO samples exhibit  $\sim 9\%$  drop of  $J_{SC}$  while NS-BMO samples show roughly equal steady-state characteristics as observed in Fig. 5-7. Alike BMO films, nanocrystalline  $\text{WO}_3$  films exhibit around 10% drop of photocurrent density prior to reaching steady-state condition [270] whereas  $\alpha\text{-Fe}_2\text{O}_3$  films show the same steady-state behavior [271] of BMO nanostructures. These results indicate that both BMO

photoanodes can effectively separate photogenerated carriers over long periods of time to achieve the dissociation of water molecules into H<sub>2</sub> and O<sub>2</sub>. Additionally, the sharp transition of J<sub>SC</sub> during light on-off (off-on) condition (Fig. 5-7) exhibits quick charge separation characteristics in both films and nanostructures.

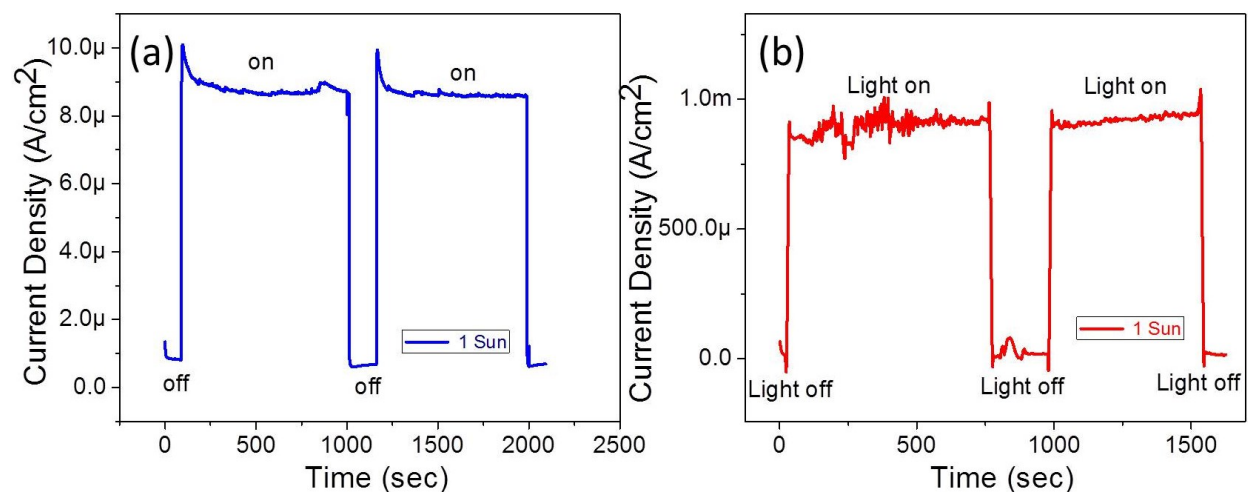


**Figure 5-7** Photocurrent density as the function of time observed in both BMO films (a) and nanostructures (b) under 1 sun (AM1.5G) while applying a constant potential of + 0.98 V and + 1.38 V vs RHE in 1M Na<sub>2</sub>SO<sub>4</sub> respectively.

### 5.3.6 Incident photon to current efficiency measurements

The incident photon to current efficiency (IPCE) describes the ratio of photogenerated electrons collected by the electrodes over the number of incident monochromatic photons. To derive the IPCE values, we performed current–voltage measurements using different band-pass optical filters. IPCE is calculated by using the following equation [272].

$$\text{IPCE}(\%) = \frac{c \times h}{e} \frac{J(\text{A}/\text{cm}^2)}{\lambda(\text{nm}) \times P(\text{w}/\text{cm}^2)} \times 100 \dots\dots\dots (5.4)$$

Where  $J$  is the photocurrent density,  $P$  is the incident radiation intensity at a given wavelength,  $\lambda$  is the wavelength of the incident photon,  $c$ ,  $h$ , and  $e$  are the speed of light, Planck's constant, and the elementary electric charge, respectively. To confirm the contribution of infrared photons to the photocurrent, band-pass filters which have wavelength center at 400, 500, 600, 700, and 800 nm respectively. For each filter, the incident radiation intensity at the position of sample was measured using a power meter.

To measure the IPCE, we recorded the current–voltage measurements under specific radiation wavelengths (Fig. 5-8). To avoid band-to-band absorption in the NSTO substrate (around 387 nm) and promote the contribution from BMO, the measurements were carried out by varying the incident wavelength from 400 to 800 nm. The results indicate that the absorbed photons of different energies are successfully converted into photocurrents. In particular, the IPCE values are more pronounced in the wavelength range of 400 to 600 nm, confirming the high photon to current conversion rate in the visible region of the solar spectrum. The high IPCE values are recorded in BMO nanostructures compared with films thus indicate a high photon to current conversion efficiency in nanostructures. As a result, BMO nanostructures yield a higher photocurrent density than the films, in good agreement with the results shown in Fig. 5-4. By comparison,  $\text{Fe}_2\text{O}_3$  and  $\text{WO}_3$  semiconducting films exhibit IPCEs of 0.5% and 22% respectively at 1.6 V vs RHE [273,274], whereas an IPCE of 22% is obtained in Ti-doped BFO films at 1.4 V vs RHE [268].

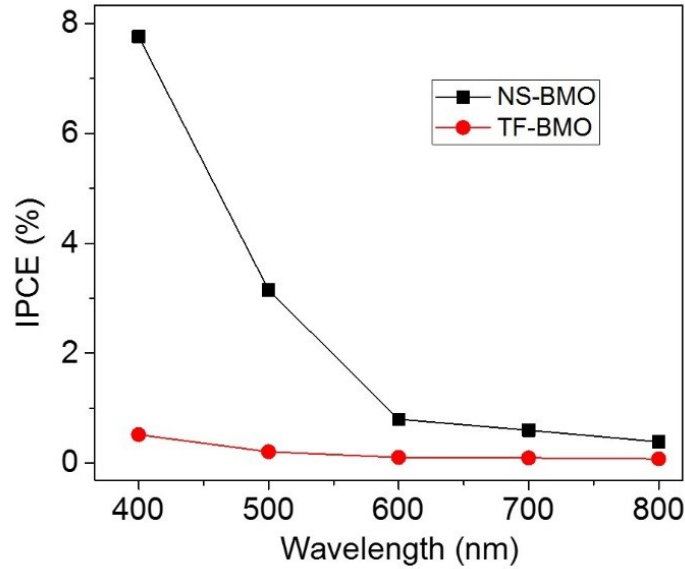


Figure 5-8 Plot of IPCE as a function of wavelength for BMO nanostructures (black) at 1.2 V vs Ag/AgCl and films (red) at 0.4 V vs Ag/AgCl respectively.

### 5.3.7 Optical transmittance spectra analysis

Figure 5-9 shows the UV-Vis transmittance spectra and the associated optical band gap of NS-BMO grown on double-sided polished STO substrates by PLD. Figure 5-9a clearly displays the transparent nature of the NS-BMO and naked un-doped STO crystals for comparison. The transmittance decreases to 55% in NS-BMO compared to naked STO (70%), as expected. As the optical transmittance is directly related to the band gap of the material, we estimated the optical band gap of NS-BMO using these transmittance spectra (Fig.5-9b).

The optical band-gap can be inferred from UV-Vis spectra using Tauc's equation [236]:

$$\alpha E = A(E-E_g)^n \dots\dots\dots(5.5)$$

where  $E$  is the photon energy,  $A$  is the proportionality constant i.e. function of the refractive index and hole/electron effective masses,  $n$  is equal to 1/2 or 2 for direct or indirect gap materials respectively. The absorption coefficient  $\alpha$  is determined by using the following equation,

$$\alpha = - \frac{\ln(T)}{d} \dots\dots\dots (5.6)$$

where  $T$  and  $d$  are the transmittance and height of the nanostructures respectively. The band gap values are determined by the linear extrapolation approach. The linear extrapolation intersects the  $X$ -axis at  $\sim 3.2$  eV which corresponds to the optical band gap of STO single crystals [225]. The linear extrapolation of additional optical transition yields a photon energy of  $\sim 1.2$  eV which is the optical band gap of NS-BMO (Fig. 5-9b). The calculated band gap of NS-BMO is the same as previously observed in TF-BMO, we, therefore, do not observe significant changes in band gap with the BMO morphology change.

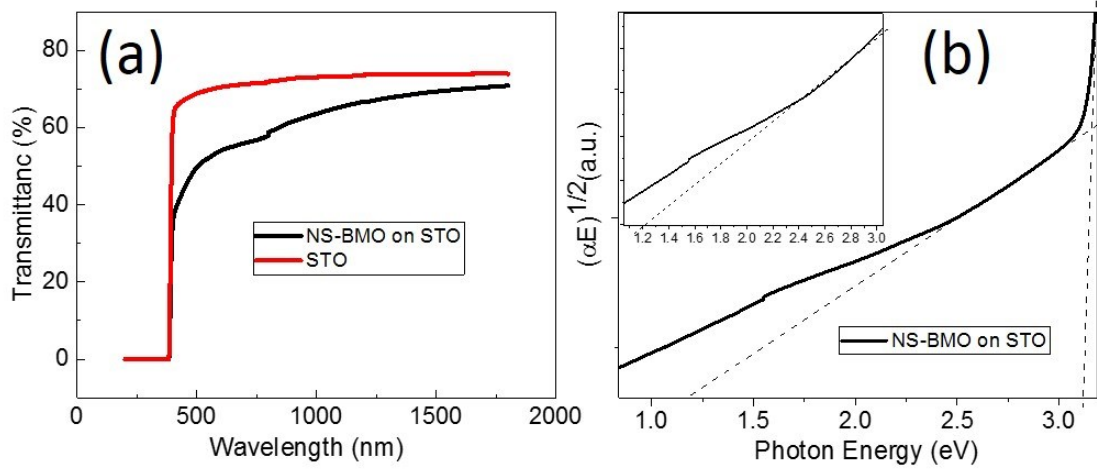


**Figure 5-9** (a) Optical transmittance spectra of STO with (black) and without (red) NS-BMO (b) calculated direct band gap of NS-BMO. The inset shows high magnification exhibiting a band gap of  $\sim 1.2$  eV.

### 5.3.8 Mott–Schottky analysis

The flat band potential ( $V_{fb}$ ) of both BMO films and nanostructures was obtained by performing a Mott–Schottky analysis [275] using capacitance impedance measurements on the electrode/electrolyte in dark conditions. The flat band potential is deduced from the Mott-Schottky equation using the potential of the x-axis intercept where  $1/C^2 = 0$  in Mott-Schottky equation,

$$\frac{1}{C_{SC}^2} = \left( \frac{2}{e\epsilon\epsilon_0 N_D A^2} \right) \left( V - V_{fb} - \frac{k_B T}{e} \right) \dots\dots\dots (5.7)$$

where  $C_{SC}$  is the capacitance of the space charge region,  $e$  is the elementary charge of an electron,  $\epsilon_0$  is the permittivity of vacuum,  $\epsilon$  is the dielectric constant of BMO ( $\epsilon = 50$ ) [225], ‘ $A$ ’ is the electrochemically active surface area,  $V$  is the applied voltage,  $V_{fb}$  is the flat band potential,  $k$  is Boltzmann’s constant,  $T$  is the temperature expressed in Kelvin (300 K) and  $N_D$  is the ionized donor dopant concentration.  $N_D$  is calculated from the slope of the Mott-Schottky curve at 5 kHz frequency. The extrapolation of the Mott-Schottky curve where  $1/(C_{SC})^2 = 0$  is used to derive the flat band potential  $V_{fb}$ . Therefore the flat band potential is,

$$V_{fb} = V - \frac{k_B T}{e} \dots\dots\dots (5.8)$$

The calculated  $V_{fb} = -0.24$  V/NHE for films and  $-0.14$  V/NHE for nanostructures respectively and the donor density,

$$N_D = \frac{2}{e\epsilon\epsilon_0(\text{slope})A^2} \dots\dots\dots (5.9)$$

where  $N_D = 1.30 \times 10^{21}$  cm<sup>-3</sup> for films and  $5.51 \times 10^{21}$  cm<sup>-3</sup> for nanostructures, respectively. The conduction band edge ( $E_{CB}$ ) is calculated using the following equation [276] which is valid for n-type materials,

$$E_{CB} = V_{fb} + k_B T \ln\left(\frac{N_D}{N_{CB}}\right) \dots\dots\dots (5.10)$$

where  $N_{CB}$  is the effective density of states in the conduction band. Therefore the calculated values,  $E_{CB} = - 0.34$  eV/NHE for films and  $- 0.27$  eV/NHE for nanostructures respectively.  $N_{CB}$  is calculated from the following equation,

$$N_{CB} = 2 \left[ \frac{(2\pi m_e^* K_B T)}{h^2} \right]^{3/2} \dots\dots\dots (5.11)$$

where  $m_e^* = 1.1 m_0$  [277] ( $m_0 = 9.1 \times 10^{-31}$  Kg), and  $h$  is Planck's constant. The calculated value of  $N_{CB}$  is  $2.89 \times 10^{19}$  /cm<sup>3</sup>.

The width of the space charge region is calculated from the following formula,

$$W_{SC} = \left[ \frac{(2\varepsilon\varepsilon_0\Delta\Phi_{SC})}{qN_D} \right]^{1/2} \dots\dots\dots (5.12)$$

where  $\Phi_{SC} = V - V_{fb}$ , the potential drop across the space charge region. For BMO films, the calculated value of  $W_{SC}$  is in the range of 0.40 to 1.90 nm with  $\Phi_{SC}$  from ranging 0.1 to 1 V vs RHE. For BMO nanostructures, the calculated value of  $W_{SC}$  is in the range of 0.24 to 0.87 nm with  $\Phi_{SC}$  from 0.05 to 0.75 V vs RHE.

The x-axis intercept potential of films (Fig. 5-10a) and nanostructures (Fig. 5-10b) are  $\sim + 0.18$  V and  $\sim + 0.28$  V vs RHE respectively, yielding a  $V_{fb(\text{film})}$  of  $\sim - 0.24$  V and a  $V_{fb(\text{nanostructure})}$  of  $\sim - 0.14$  V vs NHE (normalized hydrogen electrode). Mott-Schottky plots show the positive characteristic slopes which are typical of *n*-type semiconductors. These slopes are used to calculate the donor density ( $N_D$ ) of both BMO films and nanostructures which are roughly equal to  $1.30 \times 10^{21}$  cm<sup>-3</sup> and  $5.51 \times 10^{21}$  cm<sup>-3</sup> respectively. The calculated space charge regions ( $W_{SC}$ ) for films and nanostructures are in the range of 0.40 to 1.90 nm with  $\Phi_{SC}$  from 0.1 to 1 V vs RHE and 0.24 to 0.87 nm with  $\Phi_{SC}$  from 0.05 to 0.75 V vs RHE, respectively.

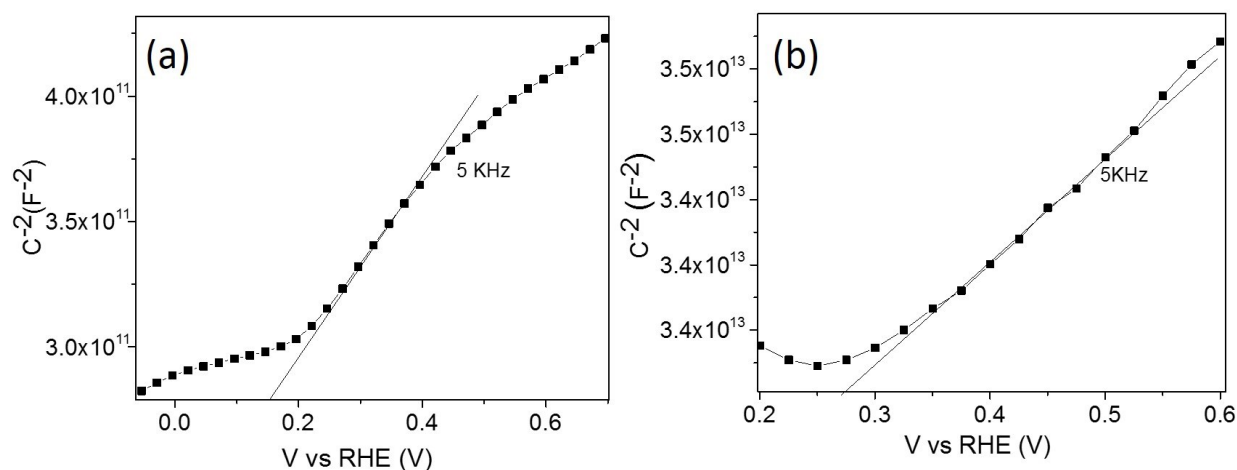


**Figure 5-10** Mott–Schottky analysis ( $1/C^2$  versus applied potential, where  $C$  is the capacitance) of BMO thin films (a) and nanostructures (b) photoelectrodes. The intercept of the dashed line ( $1/C^2 = 0$ ) can be used to determine the  $V_{fb}$  of the BMO photoelectrodes.

## 5.4 Discussion

The ferroelectric properties of PLD-grown BMO films are well known and were reported in our previous work [189,225]. To investigate the FE effect of BMO films on photocurrent generation in the PEC cell, we followed the same approach used in the case of BFCO films to prepare the top electrodes for electrical connections [40]. We poled the samples by applying voltage pulses with amplitude in the range of  $\pm 5$  V to  $\pm 8$  V and pulse width of 25  $\mu$ s. Although FE properties exert a significant influence on the enhancement of the photocurrent in BFCO films, we did not observe any FE effect in the PEC performances of BMO films. This may result from the bound surface charges [278] of FE polarization which are neutralized in the presence of electrolytes. As a result, the internal electric field is reduced to below the detection limit. In contrast to thin films, no ferroelectricity is observed in NS-BMO as characterized by piezoresponse force microscopy

(PFM). This is probably due to the high conductivity of the nanostructures (Mott-Schottky analysis of Fig. 5-10b), or alternatively to size effects.

On this basis, the internal electric field induced by the depletion zone formed at the substrate-film interface can be the origin of the PV response in the films [279,189]. The same interfacial effect can account for the superior PEC performance of nanostructures over films. However, the space charge region in thin films is larger than in the nanostructures (based on the calculation described in Section 5.3.8). Since the films cover more substrate surface than the nanostructures, the interface effect would be more pronounced in the films, thereby generating a higher photocurrent. This is in contrast with the obtained results indicating that the contribution of the in-built internal electrical field formed at the interface to the observed photocurrent is not predominant. Since the reduced radial dimension of NS-BMO favors electron conductivity (on the basis of calculated values of  $N_{CB}$  mentioned in Section 5.3.8) and drastically increases the surface to volume ratio, we conclude that these properties promote a rapid diffusion of photocarriers to the surfaces and thus improve the separation efficiency of charge carriers [280]. This then leads to an enhancement of the PEC performance in NS-BMO.

To achieve the best PEC performance, the band energy levels of semiconductor electrodes and electrolytes need to be properly aligned. The BMO energy levels are aligned with water redox levels, as shown in Fig. 5-11. To draw a complete picture of the band alignment of BMO, the energy gaps between flat band potential and conduction band potential are estimated to be -0.10 eV for thin films and - 0.13 eV for nanostructures vs. NHE. To calculate these energy gaps, one of the energy levels of either VB or CB of both TF-BMO and NS-BMO should be known. In our case, we estimated the conduction band position of both TF-BMO and NS-BMO using the equation [5.10]. The band gap of TF-BMO was set to  $\sim 1.2$  eV, according to previous work [225]. In the

case of NS-BMO, the optical band gap is determined from transmittance spectra of UV-Vis spectroscopy measurement which was found to be  $\sim 1.2$  eV, similar values observed in TF-BMO. Ideally, the bandgap of the semiconductor materials should straddle the reduction and oxidation potentials of water in order to achieve photocatalytic water splitting using a single photocatalyst, which is +0 V and +1.23 V vs normal hydrogen electrode (NHE) at  $p^H=0$ , equivalent to the energy of 238 KJ/mol [24,26]. However, the design of a practical device remains a formidable challenge as it is important to carefully control both the band gaps and relative band edge positions of the photoanode and photocathode to meet the thermodynamic considerations for water splitting, and absorb complementary photons to increase device efficiency. In low band gap materials such as Si (1.1 eV) and InP (1.3 eV), the required overpotentials are the key factors for the placement of the VB and CB edge positions of a semiconductor with respect to the potentials for oxygen and hydrogen evolution reactions respectively [281]. According to the complete band alignment with respect to oxygen and hydrogen evolution reactions, it shows that TF-BMO and NS-BMO both are suitable for  $O_2$  evolution reaction (Fig. 5-11).

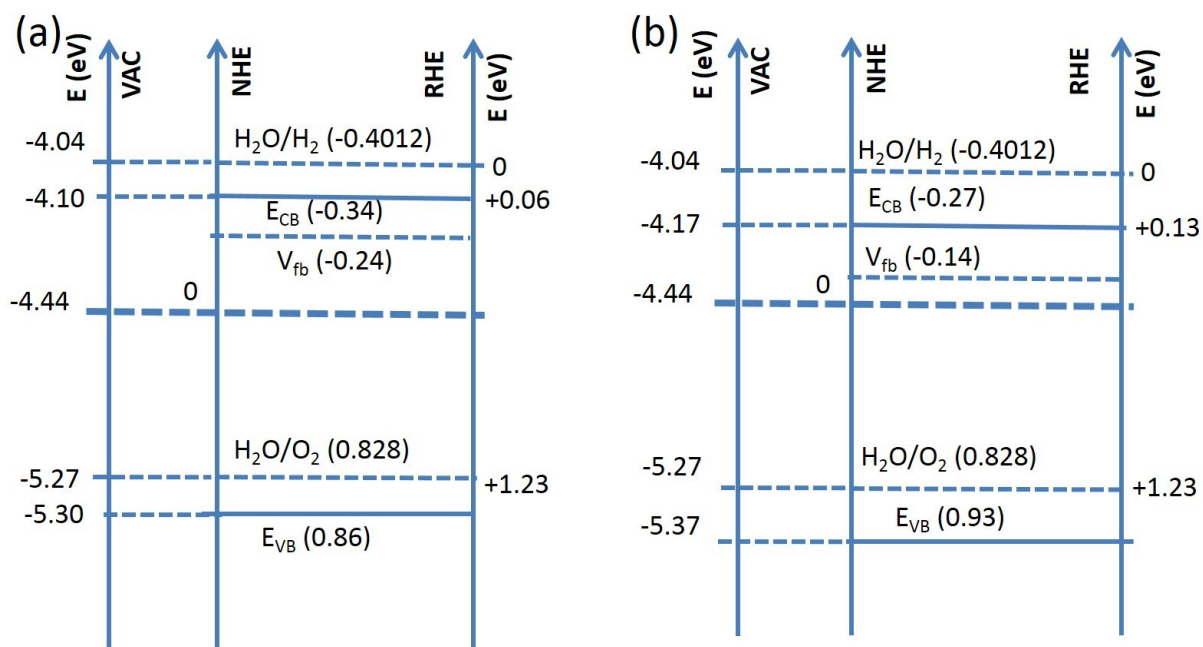


**Figure 5-11** Calculated energy-level diagram based on Mott–Schottky results showing the energy levels of  $V_{fb}$ , valence band edge (VB), and conduction band edge (CB) of the respective BMO film (a) and nanostructures (b) photoelectrodes.

The experiments related to hydrogen and oxygen gas evolution in a gas chromatograph are demonstrated in Fig. 5-12 to confirm the above analysis (Fig. 5-11). After a certain interval of time, the generated gas in the experimental chamber was collected using a vacuum tight syringe and injected into a gas chromatograph which was calibrated to quantify oxygen and hydrogen gas, respectively. The results clearly show the enhancement of  $H_2$  and  $O_2$  evolution with increasing the time. The experimental error in the evolution of  $H_2$  and  $O_2$  gas is estimated to be  $\sim \pm 5\%$ , which is ascribed to the manual sampling of the gases.

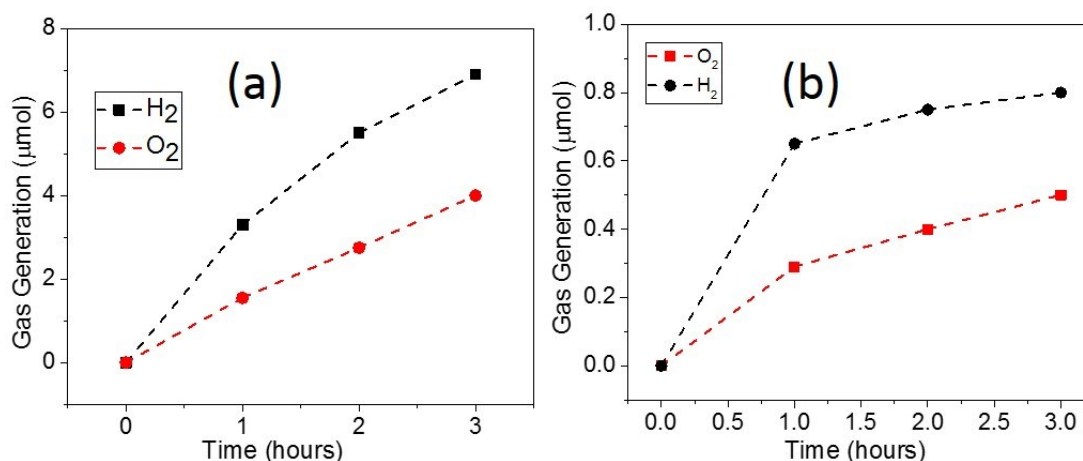


**Figure 5-12** Amount of hydrogen and oxygen evolved by BMO nanostructures (a) and thin films (b) respectively recorded at 0.4 V vs Ag/AgCl under 1 sun illumination. Dot line (red and black) in both images shows the trend of respective gas generation in time.

## 5.5 Conclusions and perspectives

In summary, we grew epitaxial BMO thin films (TF-BMO) and nanostructures (NS-BMO) deposited by PLD on (111)-oriented NSTO substrates. We found that both morphologies can be used as photoanode materials for hydrogen and oxygen evolution. The photoanode properties were further characterized by performing Mott-Schottky experiments which revealed that BMO behaves as an n-type semiconductor. TF-BMO exhibits highest photocurrent density ( $\sim 40 \mu\text{A}/\text{cm}^2$  at 0.4 V vs Ag/AgCl, corresponding to 0.98 V vs RHE) about four times higher under 2 Sun as opposed to 1 Sun. The NS-BMO exhibits the highest photocurrent density ( $\sim 0.9 \text{ mA}/\text{cm}^2$  at 0.8 V vs Ag/AgCl, corresponding to 1.38 V vs RHE) compared to TF-BMO ( $\sim 10 \mu\text{A}/\text{cm}^2$  at 0.4 V vs Ag/AgCl, corresponding to 0.98 V vs RHE) under 1 Sun. Based on the band alignment with respect to the redox potential of water, we showed that TF-BMO and NS-BMO are suitable for oxygen evolution. In both films and nanostructures, the photocurrent is very stable; a variation of only 9%

was detected in thin films over a period of  $\sim 1000$  s whereas negligible changes were observed in nanostructures. The results show great potential for the development of inorganic oxides as light absorbers and stable components for solar to  $O_2/H_2$  energy conversion, which in turn will pave the way towards the development of new type of efficient photoelectrode materials.

# Chapter 6 Conclusions and Perspectives

## 6.1 Conclusions

We conclude that multiferroic (MF) inorganic perovskite materials are viable candidates for use as active elements in photovoltaic (PV) devices for solar energy harvesting. The band gaps (1.1 eV-2.8 eV) of such materials can efficiently harvest the wide range of the visible part of solar spectrum on earth surface. Without the need for *n-p* junctions, ferroelectric (FE) perovskites are capable to convert solar energy into electrical energy by means of bulk photovoltaic (BPV) effect, a fundamentally new route to endow the photon to electron conversion in materials. Although ferroelectric polarization-induced electric field inside the materials are used to describe the photogenerated charge carrier separation, the overall physics behind the PV effect in polar perovskites is still not clearly elucidated. In addition, the overall solar to electrical power conversion efficiency (PCE) in such type of materials is very poor despite showing an excellent mechanism of photocarrier separation. Therefore, a lot more investigation is still needed to make PV effect clear, while simultaneously looking for an efficient way to improve the PCE.

In this work, we succeeded to improve the PCE by engineering the materials, presented in chapter 3. We successfully grew epitaxial BiFeO<sub>3</sub>(BFO)/Bi-Mn-O bilayer thin films on niobium doped (111) oriented SrTiO<sub>3</sub> (STO) single crystalline substrates by pulse laser deposition (PLD), employing a compressive strain in the films due to lattice mismatch. The PCE of ~1.43% with the fill factor (FF) of ~0.72 was reported in the bilayer based devices under 1 Sun illumination which is higher than any PCE ever reported in individual BFO or BMO thin films. We described that the ferroelectric polarization induced internal electric field plays a crucial role to improve the PCE, particularly we described the PV behavior by developing a model based on the energy band

structure of all device components and showed that the band alignment is modulated by polarization switching.

In chapter 4, we reported the PCE of 4.20% under 1 sun illumination for the first time in Bi-Mn-O composite films made of BiMnO<sub>3</sub> and BiMn<sub>2</sub>O<sub>5</sub> crystal phases. The films were grown on (111) oriented niobium-doped STO substrate by PLD. Both phases in the films were characterized by a bunch of characterization tools including transmission electron microscopy (TEM), Raman spectroscopy, atomic force microscopy (AFM), piezoelectric force microscopy (PFM), Kelvin probe force microscopy (KPFM), ellipsometry, and solar simulator. The results showed that grain boundaries (GB) play crucial roles for photocurrent and photovoltages generations and thereby described the PV results with GB barrier potentials.

In chapter 5, we demonstrated the optical and photoelectrochemical (PEC) properties of BiMnO<sub>3</sub> (BMO) thin films and nanostructures grown on (111) oriented niobium-doped STO substrates by PLD. During growth of nanostructures, nanostencils shadow masks with a periodic array of nanometer-scale circular features were mechanically mounted on the substrates before material deposition. Thin films exhibited photocurrent density ( $\sim 40 \mu\text{A}/\text{cm}^2$  at 1.2 V vs Ag/AgCl) about four times higher under 2 Sun as opposed to 1 Sun. The nanostructures exhibited the highest photocurrent density ( $\sim 0.9 \text{ mA}/\text{cm}^2$  at 1.2 V vs Ag/AgCl) compared to TF-BMO ( $\sim 10 \mu\text{A}/\text{cm}^2$  at 0.4 V vs Ag/AgCl) under 1 Sun. The photoanode properties of thin films and nanostructures were further characterized by performing Mott-Schottky experiments which revealed that BMO behaves as the n-type semiconductor. Based on the band alignment with respect to the redox potential of water, we demonstrated that thin films and nanostructures were suitable for hydrogen and oxygen evolution, respectively. In both films and nanostructures, the photocurrent was very stable; only

9% variation was detected in thin films over a period of ~1000 s whereas negligible changes were observed in nanostructures.

## **6.2 Perspectives**

MF BMO perovskites as active material systems in PV devices alone or in conjunction with other perovskites were investigated and found their enormous potentials in green solar energy conversion. Although the structure and physical properties were investigated rigorously, further investigations in the following directions could be more interesting and fruitful in future.

In chapter 3, we described the enhancement of efficiency in BFO/Bi-Mn-O bilayer based solid state PV devices using the model of interface modulation by ferroelectric-polarization induced electric field. However, the optimization of thickness of each layer, and the atomic scale resolution at bilayer interface to observe the possible interfacial layer mixing could be an interesting topic in terms of obtaining high absorption of sunlight. In addition, the interfacial coupling of two ferroelectric layers could be an interesting topic to study. If the evidence of ferroelectric coupling between two layers is found then that would be a holy grail in science, which could be useful in developing future electronic devices including spintronics, and computer memory applications.

In chapter 4, we described the high PCE in composite thin films made of mixed crystal phases using the model of grain boundary barrier potentials. However, the effect of grain sizes on PV effect was not optimized. Grain sizes may alter the physical and chemical properties of material systems and therefore it is important to optimize them to achieve a maximum efficiency. We first described the ferroelectric-semiconducting grain boundaries in the field of inorganic oxide perovskites to the best of our knowledge and subsequently showed their positive impacts on the PV efficiency. Therefore, the results could be useful in future to design efficient solid-state PV

devices in many other material systems as they provide a fundamentally new route to enhance PCE in perovskite thin film based PV devices.

In chapter 5, we described the photocatalytic properties of BMO thin films and nanostructures as photoelectrodes in PEC cells. The results show great potentials for the development of multiferroic oxides as visible light absorbers and stable components in electrochemical reactions for solar to O<sub>2</sub>/H<sub>2</sub> energy conversion, which in turn will pave the way towards the development of new low cost and efficient photoelectrode materials. Although we described the superior PEC performances in nanostructures over thin films, the effect of the thickness of thin films and the effect of the heights and dimensions of nanostructures were not discussed which could be interesting to optimize in improving the device performances.

## References

---

- [1] <http://www.sandia.gov/~jytsao/Solar%20FAQs.pdf>
- [2] A. Gore, *Our choice: a plan to solve the climate crisis*. Push Pop Press: Menlo Park, CA, 2009.
- [3] E. Becquerel, Recherches sur les effets de la radiation chimique de la lumière solaire, au moyen des courants électriques. *C. R. Acad. Sci.* 1839, 9, 145.
- [4] S. Sze, *Semiconductor devices: physics and technology*. Wiley, 2002.
- [5] S. Essig, C. Allebé, T. Remo, J. Geisz, M. Steiner, K. Horowitz, L. Barraud, J. Ward, M. Schnabel, A. Descoeurdes, D. Young, M. Woodhouse, M. Despeisse, C. Ballif, A. Tamboli, Raising the one-sun conversion efficiency of III–V/Si solar cells to 32.8% for two junctions and 35.9% for three junctions. *Nature Energ.* 2017, 2, 17144.
- [6] H. Huang, Solar energy: ferroelectric photovoltaics. *Nature Photon.* 2010, 4, 134.
- [7] W. Shockley, H. Queisser, Detailed balance limit of efficiency of p-n junction solar cells. *J. Appl. Phys.* 1961, 3, 2.
- [8] A. Chynoweth, Surface space-charge layers in barium titanate. *Phys. Rev.* 1956, 102,105.
- [9] F. Chen, Optically induced change of refractive indices in LiNbO<sub>3</sub> and LiTaO<sub>3</sub>. *J. Appl. Phys.* 1969, 40, 8.
- [10] A. Glass, D. Linde, T. Negran, High-voltage bulk photovoltaic effect and the photorefractive process in LiNbO<sub>3</sub>. *Appl. Phys. Lett.* 1974, 25, 233.
- [11] S. Yang, J. Seidel, S. Byrnes, P. Shafer, C. Yang, M. Rossell, P. Yu, Y. Chu, J. Scott, J. Ager, L. Martin, R. Ramesh, Above-bandgap voltages from ferroelectric photovoltaic devices. *Nature Nanotech.* 2010, 5, 143.

- 
- [12] M. Alexe, Local mapping of generation and recombination lifetime in BiFeO<sub>3</sub> single crystals by scanning probe photoinduced transient spectroscopy. *Nano Lett.* 2012, 12, 2193.
- [13] J. Starkiewicz, L. Sosnowski, O. Simpson, Photovoltaic effects exhibited in high-resistance semi-conducting films. *Nature* 1946, 158, 28.
- [14] H. Johnson, R. Williams, C. Mee, The anomalous photovoltaic effect in cadmium telluride. *J. Phys. D: Appl. Phys.* 1975, 8, 1530.
- [15] B. Goldstein, L. Pensak, High-voltage photovoltaic effect. *J. Appl. Phys.* 1959, 30, 155.
- [16] A. Kholkin, O. Boiarkine, N. Setter, Transient photocurrents in lead zirconate titanate thin films. *Appl. Phys. Lett.* 1998, 72, 1.
- [17] R. Nechache, C. Harnagea, S. Li, L. Cardenas, W. Huang, J. Chakrabartty, F. Rosei, Bandgap tuning of multiferroic oxide solar cells. *Nature Photon.* 2015, 9, 61.
- [18] J. Spanier, V. Fridkin, A. Rappe, A. Akbashev, A. Polemi, Y. Qi, Z. Gu, S. Young, C. Hawley, D. Imbrenda, G. Xiao, A. Bennett-Jackson, C. Johnson, Power conversion efficiency exceeding the Shockley–Queisser limit in a ferroelectric insulator. *Nature photon.* 2016, 10, 611.
- [19] K. Maeda, K. Domen, New non-oxide photocatalysts designed for overall water splitting under visible light. *J. Phys. Chem. C* 2007, 111, 7851.
- [20] J. Lee, Photocatalytic water splitting under visible light with particulate semiconductor catalysts. *Catal. Surv. Asia* 2005, 9, 217.
- [21] Y. Tachibana, L. Vayssieres, J. Durrant, Artificial photosynthesis for solar water-splitting. *Nature Photon.* 2012, 6, 511.
- [22] B. James, G. Baum, J. Perez, K. Baum, O. Square, Techno economic analysis of photoelectrochemical (PEC) hydrogen production. DOE report (Contract no. GS-10F-009J), 2009.

- 
- [23] V. Balzani, A. Credi, M. Venturi, Photochemical conversion of solar energy. *Chem. Sus. Chem.* 2008, 1, 26.
- [24] A. Fujishima, K. Honda, Electrochemical photolysis of water at a semiconductor electrode. *Nature* 1972, 238, 37.
- [25] N. Serpone, A. Emeline, Semiconductor photocatalysis — past, present, and future outlook. *J. Phys. Chem. Lett.* 2012, 3, 673.
- [26] M. Grätzel, Photoelectrochemical cells. *Nature* 2001, 414, 338.
- [27] N. Serpone, E. Pelizzetti, Photocatalysis: fundamentals and applications. John Wiley & Sons, New York, 1989.
- [28] Y. Wu, M. Chan, G. Ceder, Prediction of semiconductor band edge positions in aqueous environments from first principles. *Phys. Rev. B* 2011, 83, 235301.
- [29] N. Armaroli, V. Balzani, The future of energy supply: challenges and opportunities. *Angew. Chem. Int. Ed.* 2007, 46, 52.
- [30] K. Benthem, C. Elsässer, R. French, Bulk electronic structure of SrTiO<sub>3</sub>: experiment and theory. *J. Appl. Phys.* 2001, 90, 6156.
- [31] H. Zhang, G. Chen, Y. Li, Y. Teng, Electronic structure and photocatalytic properties of copper-doped CaTiO<sub>3</sub>. *Int. J. Hydrog. Energy* 2010, 35, 2713.
- [32] Y. Qu, W. Zhou, H. Fu, Porous cobalt titanate nanorod: a new candidate for visible light-driven photocatalytic water oxidation. *Chem. Cat. Chem.* 2014, 6, 265.
- [33] Y. Kim, B. Gao, S. Han, M. Jung, A. Chakraborty, T. Ko, C. Lee, W. Lee, Heterojunction of FeTiO<sub>3</sub> nanodisc and TiO<sub>2</sub> nanoparticle for a novel visible light photocatalyst. *J. Phys. Chem. C* 2009, 113, 19179.

- 
- [34] W. Dong, D. Wang, L. Jiang, H. Zhu, H. Huang, J. Li, H. Zhao, C. Li, B. Chen, G. Deng, Synthesis of F doping  $\text{MnTiO}_3$  nanodiscs and their photocatalytic property under visible light. *Mater. Lett.* 2013, 98, 265.
- [35] Y. Qu, W. Zhou, Z. Ren, S. Du, X. Meng, G. Tian, K. Pan, G. Wang, H. Fu, Facile preparation of porous  $\text{NiTiO}_3$  nanorods with enhanced visible-light-driven photocatalytic performance. *J. Mater. Chem.* 2012, 22, 16471.
- [36] Y. Lin, G. Yuan, S. Sheehan, S. Zhou, D. Wang, Hematite-based solar water splitting: challenges and opportunities. *Energy Environ. Sci.* 2011, 4, 4862.
- [37] W. Ji, K. Yao, Y. Lim, Y. Liang, A. Suwardi, Epitaxial ferroelectric  $\text{BiFeO}_3$  thin films for unassisted photocatalytic water splitting. *Appl. Phys. Lett.* 2013, 103, 062901.
- [38] S. Cho, J. Jang, W. Zhang, A. Suwardi, H. Wang, D. Wang, J. MacManus-Driscoll, Single-crystalline thin films for studying intrinsic properties of  $\text{BiFeO}_3$ - $\text{SrTiO}_3$  solid solution photoelectrodes in solar energy conversion. *Chem. Mater.* 2015, 27, 6635.
- [39] D. Jia, J. Xu, H. Ke, W. Wang, Y. Zhou, Structure and multiferroic properties of  $\text{BiFeO}_3$  powders. *J. Eur. Ceram. Soc.* 2009, 29, 3099.
- [40] S. Li, B. AlOtaibi, W. Huang, Z. Mi, N. Serpone, R. Nechache, F. Rosei, Epitaxial  $\text{Bi}_2\text{FeCrO}_6$  multiferroic thin film as a new visible light absorbing photocathode material. *Small* 2015, 11, 4018.
- [41] E. Fabbri, A. Habereeder, K. Waltar, R. Kötz, T. Schmidt, Developments and perspectives of oxide-based catalysts for the oxygen evolution reaction. *Catal. Sci. Technol.* 2014, 4, 3800.
- [42] K. Miura, T. Furuta, First-principles study of structural trend of  $\text{BiMO}_3$  and  $\text{BaMO}_3$ : Relationship between tetragonal and rhombohedral structure and the tolerance factors. *Jpn. J. Appl. Phys.* 2010, 49, 031501.

- 
- [43] M. Suchomel, P. Davies, Predicting the position of the morphotropic phase boundary in high temperature  $\text{PbTiO}_3\text{-Bi}(\text{B}'\text{B}'')\text{O}_3$  based dielectric ceramics. *J. Appl. Phys.* 2004, 96, 4405.
- [44] C. Rao, Transition metal oxides. *Annual Rev. Phys. Chem.* 1989, 40, 291.
- [45] J. Scott, Applications of modern ferroelectrics. *Science* 2007, 315, 954.
- [46] J. Scott, Ferroelectric memories. (Springer series in advanced microelectronics). 2000, 3.
- [47] B. Cullity, C. Graham, Introduction to magnetic materials. Wiley, 2011
- [48] N. Spaldin, S. Cheong, R. Ramesh, Multiferroics: past, present, and future. *Physic. Today.* 2016, 63, 38.
- [49] H. Schmid, Multi-ferroic magnetoelectrics. *Ferroelectrics*, 1994, 162, 317.
- [50] E. Ascher, H. Rieder, H. Schmid, H. Stössel, Some properties of ferromagnetoelectric nickel-iodine boracite,  $\text{Ni}_3\text{B}_7\text{O}_{13}\text{I}$ . *J. Appl. Phys.* 2016, 37, 1404.
- [51] G. Smolenskii, I. Chupis, Ferroelectromagnets. *Sov. Phys. Usp.* 1982, 25, 475.
- [52] M. Fiebig, T. Lottermoser, D. Meier, M. Trassin, The evolution of multiferroics. *Nature Rev. Mater.* 2016, 1, 16046.
- [53] N. Spaldin, M. Fiebig, The Renaissance of magnetoelectric multiferroics. *Science* 2005, 309, 391.
- [54] D. Khomskii, Classifying multiferroics: mechanisms and effects. *Physics*, 2009, 2, 20.
- [55] M. Fiebig, Revival of the magnetoelectric effect. *J. Phys. D Appl. Phys.* 2015, 38, R123.
- [56] W. Eerenstein, N. Mathur, J. Scott, Multiferroic and magnetoelectric materials. *Nature* 2006, 442, 759.
- [57] S. Cheong, M. Mostovoy, Multiferroics: a magnetic twist for ferroelectricity. *Nature Mater.* 2007, 6, 13.

- 
- [58] R. Ramesh, N. Spaldin, Multiferroics: progress and prospects in thin films. *Nature Mater.* 2007, 6, 21.
- [59] J. Wang, J. Neaton, H. Zheng, V. Nagarajan, S. Ogale, B. Liu, D. Viehland, V. Vaithyanathan, D. Schlom, U. Waghmare, N. Spaldin, K. Rabe, M. Wuttig, R. Ramesh, Epitaxial BiFeO<sub>3</sub> multiferroic thin film heterostructures. *Science* 2003, 299, 1719.
- [60] L. Martin, Engineering functionality in the multiferroic BiFeO<sub>3</sub>-controlling chemistry to enable advanced applications. *Dalton Transaction.* 2010, 39, 10813.
- [61] T. Zhao, A. Scholl, F. Zavaliche, K. Lee, M. Barry, A. Doran, M. Cruz, Y. Chu, C. Ederer, N. Spaldin, R. Das, D. Kim, S. Baek, C. Eom, R. Ramesh, Electrical control of antiferromagnetic domains in multiferroic BiFeO<sub>3</sub> films at room temperature. *Nature Mater.* 2006, 5, 823.
- [62] H. Chiba, T. Atou, Y. Syono, Magnetic and electrical properties of Bi<sub>1-x</sub>Sr<sub>x</sub>MnO<sub>3</sub>: hole-doping effect on ferromagnetic perovskite BiMnO<sub>3</sub>. *J. Solid State Chem.* 1997, 132, 139.
- [63] T. Kimura, S. Kawamoto, I. Yamada, M. Azuma, M. Takano, Y. Tokura, Magnetocapacitance effect in multiferroic BiMnO<sub>3</sub>. *Phys. Rev. B* 2003, 67, 180401.
- [64] A. Belik, M. Azuma, T. Saito, Y. Shimakawa, M. Takano, Crystallographic features and tetragonal phase stability of PbVO<sub>3</sub>, a new member of PbTiO<sub>3</sub> family. *Chem. Mater.* 2005, 17, 269.
- [65] D. Efremov, J. Brink, D. Khomskii, Bond- versus site-centred ordering and possible ferroelectricity in manganites. *Nature Mater.* 2004, 3, 853.
- [66] B. Aken, Investigation of charge states and multiferroicity in Fe-doped h-YMnO<sub>3</sub>. *Nature Mater.* 2004, 3, 164.
- [67] T. Kimura, T. Goto, H. Shintani, K. Ishizaka, T. Arima, Y. Tokura, Magnetic control of ferroelectric polarization. *Nature* 2003, 426, 55.

- 
- [68] N. Hur, S. Park, P. Sharma, J. Ahn, S. Guha, S. Cheong, Electric polarization reversal and memory in a multiferroic material induced by magnetic fields. *Nature* 2004, 429, 392.
- [69] N. Ikeda, H. Ohsumi, K. Ohwada, K. Ishii, T. Inami, K. Kakurai, Y. Murakami, K. Yoshii, S. Mori, Y. Horibe, H. Kitô, Ferroelectricity from iron valence ordering in the charge-frustrated system  $\text{LuFe}_2\text{O}_4$ . *Nature* 436, 2005, 1136.
- [70] I. Sergienko, E. Dagotto, Role of the Dzyaloshinskii–Moriya interaction in multiferroic perovskites. *Phys. Rev. B* 2006, 73, 094434.
- [71] R. Johnson, L. Chapon, D. Khalyavin, P. Manuel, P. Radaelli, C. Martin, Giant improper ferroelectricity in the ferroaxial magnet  $\text{CaMn}_7\text{O}_{12}$ . *Phys. Rev. Lett.* 2012, 108, 067201.
- [72] R. Schmidt, E. Langenberg, J. Ventura, M. Varela, Bi containing multiferroic perovskite oxide thin films. *arXiv*. 2014, 1402.1442.
- [73] R. Seshadri, N. Hill, Visualizing the role of Bi 6s “Lone Pairs” in the off-center distortion in ferromagnetic  $\text{BiMnO}_3$ . *Chem. Mater.* 2001, 13, 2892.
- [74] Y. Tokura, N. Nagaosa, Orbital physics in transition-metal oxides. *Science* 2000, 288, 5465.
- [75] [http://guava.physics.uiuc.edu/~nigel/courses/569/essays\\_f2004/files/kim.pdf](http://guava.physics.uiuc.edu/~nigel/courses/569/essays_f2004/files/kim.pdf)
- [76] J. Goodenough, *Magnetism and the chemical bond*. R. E. Krieger Pub. Co., Huntington, 1976.
- [77] N. Hill, K. Rabe, First-principles investigation of ferromagnetism and ferroelectricity in bismuth manganite. *Phys. Rev. B* 1999, 59, 13.
- [78] T. Atou, H. Chiba, K. Ohoyama, Y. Yamaguchi, Y. Syono, Structure determination of ferromagnetic perovskite  $\text{BiMnO}_3$ . *J. Sol. State Chem.* 1999, 145, 639.
- [79] Z. Chi, C. Xiao, S. Feng, F. Li, C. Jin, Manifestation of ferroelectromagnetism in multiferroic  $\text{BiMnO}_3$ . *J. Appl. Phys.* 2005, 98 103519.

- 
- [80] A. Santos, A. Cheetham, W. Tian, X. Pan, Y. Jia, N. Murphy, J. Lettieri, D. Scholm, Epitaxial growth and properties of metastable BiMnO<sub>3</sub> thin films. *Appl. Phys. Lett.* 2004, 84 91.
- [81] M. Gajek, M. Bibes, A. Barthélémy, K. Bouzehouane, S. Fusil, M. Varela, J. Fontcuberta, A. Fert, Spin filtering through ferromagnetic BiMnO<sub>3</sub> tunnel barriers. *Phys. Rev. B* 2005, 72, 020406.
- [82] W. Eerenstein, F. Morrison, J. Scott, N. Mathur, Growth of highly resistive BiMnO<sub>3</sub> films. *Appl. Phys. Lett.* 2005, 87, 101906.
- [83] H. Jeon, G. Bhalla, P. Mickel, K. Voigt, C. Morien, S. Tongay, A. Hebard, A. Biswas, Growth and characterization of multiferroic BiMnO<sub>3</sub> thin films. *J. Appl. Phys.* 2011, 109, 074104.
- [84] F. Sugawara, S. Iiida, Y. Syono, Akimoto, Magnetic properties and crystal distortions in BiMnO<sub>3</sub> and BiCrO<sub>3</sub>. *J. Phys. Soc. Jpn.* 1968, 25, 1553.
- [85] A. Santos, S. Parashar, A. Raju, Y. Zhao, A. Cheetham, C. Rao, Evidence for the likely occurrence of magnetoferroelectricity in the simple perovskite, BiMnO<sub>3</sub>. *Sol. State. Comm.* 2002, 122, 49.
- [86] J. Son, Y. Shin. Multiferroic BiMnO<sub>3</sub> thin films with double SrTiO<sub>3</sub> buffer layers. *Appl. Phys. Lett.* 2008, 93, 062902.
- [87] P. Baettig, R. Seshadri, N. Spaldin, Anti-polarity in ideal BiMnO<sub>3</sub>. *J. Am. Chem. Soc.* 2007, 129, 9854.
- [88] V. Goian, S. Kamba, M. Savinov, D. Nuzhnyy, F. Borodavka, P. Vanek, A. Belik, Absence of ferroelectricity in BiMnO<sub>3</sub> ceramics. *J. Appl. Phys.* 2012, 112, 074112.
- [89] U. Dash, N. Raveendra, C. Jung, A rigorous investigation of BiMnO<sub>3</sub> ferroelectricity through a development of a novel way to stabilize twin free and monoclinic thin film. *J. Alloy. Comp.* 2016, 684, 310.

- 
- [90] A. Belik, S. Iikubo, K. Kodama, N. Igawa, S. Shamoto, M. Maie, T. Nagai, Y. Matsui, S. Stefanovich, I. Bogdan, Lazoryak, E. Takayama-Muromachi, BiScO<sub>3</sub>: centrosymmetric BiMnO<sub>3</sub>-type oxide. *J. Am. Chem. Soc.* 2006, 128, 706.
- [91] T. Yokosawa, A. Belik, T. Asaka, K. Kimoto, E. Takayama-Muromachi, Y. Matsui, Crystal symmetry of BiMnO<sub>3</sub>: electron diffraction study. *Phys. Rev. B* 2008, 77, 024111.
- [92] B. Lee, P. Yoo, V. Nam, K. Toreh, C. Jung, Magnetic and electric properties of stoichiometric BiMnO<sub>3</sub> thin films. *Nanoscal. Res. Lett.* 2015, 10, 47.
- [93] A. Belik, Polar and nonpolar phases of BiMO<sub>3</sub>: a review. *J. Sol. Stat. Chem.* 2012, 195, 32.
- [94] D. Sando, A. Barthel, M. Bibes, BiFeO<sub>3</sub> epitaxial thin films and devices: past, present and future. *J. Phys.: Condens. Matter.* 2014, 26, 473201.
- [95] C. Michel, J. Moreau, G. Achenbach, R. Gerson, W. James, The atomic structure of BiFeO<sub>3</sub>. *Sol. Stat. Comm.* 1969, 7, 701.
- [96] D. Ricinchi, K. Yun, M. Okuyama, A mechanism for the 150  $\mu\text{C. cm}^{-2}$  polarization of BiFeO<sub>3</sub> films based on first-principles calculations and new structural data. *J. Phys. Condens. Matter.* 2006, 18, L97
- [97] H. Béa, B. Dupé, S. Fusil, R. Mattana, E. Jacquet, B. Warot-Fonrose, F. Wilhelm, A. Rogalev, S. Petit, V. Cros, A. Anane, F. Petroff, K. Bouzehouane, G. Geneste, B. Dkhil, S. Lisenkov, I. Ponomareva, L. Bellaiche, M. Bibes, A. Barthélémy, Evidence for room-temperature multiferroicity in a compound with a giant axial ratio. *Phys. Rev. Lett.* 2009, 102, 217603.
- [98] R. Zeches, M. Rossell, J. Zhang, A. Hatt, Q. He, C. Yang, A. Kumar, C. Wang, A. Melville, C. Adamo, G. Sheng, Y. Chu, J. Ihlefeld, R. Erni, C. Ederer, V. Gopalan, L. Chen, D. Schlom, N. Spaldin, L. Martin, R. Ramesh, A strain-driven morphotropic phase boundary in BiFeO<sub>3</sub>. *Science* 2009, 326, 977.

- 
- [99] H. Bea, M. Bibes, X. Zhu, S. Fusil, K. Bouzehouane, S. Petit, J. Kreisel, A. Barthelemy, Crystallographic, magnetic, and ferroelectric structures of bulk like BiFeO<sub>3</sub> thin films. *Appl. Phys. Lett.* 2008, 93, 072901.
- [100] S. Ryu, J. Kim, Y. Shin, B. Park, J. Son, H. Jang, Enhanced magnetization and modulated orbital hybridization in epitaxially constrained BiFeO<sub>3</sub> thin films with rhombohedral symmetry. *Chem. Mater.* 2009, 21, 5050.
- [101] J. Yang, Q. He, S. Suresha, C. Kuo, C. Peng, R. Haislmaier, M. Motyka, G. Sheng, C. Adamo, H. Lin, Z. Hu, L. Chang, L. Tjeng, E. Arenholz, N. Podraza, M. Bernhagen, R. Uecker, D. Schlom, V. Gopalan, L. Chen, C. Chen, R. Ramesh, Y. Chu, Orthorhombic BiFeO<sub>3</sub>. *Phys. Rev. Lett.* 2012, 109, 247606.
- [102] J. Lee, K. Chu, A. Ünal, S. Valencia, F. Kronast, S. Kowarik, J. Seidel, C. Yang, Phase separation and electrical switching between two isosymmetric multiferroic phases in tensile strained BiFeO<sub>3</sub> thin films. *Phys. Rev. B* 2014, 89, 140101.
- [103] G. Xu, H. Hiraka, G. Shirane, Low symmetry phase in (001) BiFeO<sub>3</sub> epitaxial constrained thin films. *Appl. Phys. Lett.* 2005, 86, 182905.
- [104] H. Toupet, F. Marrec, C. Lichtensteiger, B. Dkhil, M. Karkut, Evidence for a first-order transition from monoclinic  $\alpha$  to monoclinic  $\beta$  phase in BiFeO<sub>3</sub> thin films. *Phys. Rev. B* 2010, 81, 140101.
- [105] Z. Chen, Y. Qi, L. You, P. Yang, C. Huang, J. Wang, T. Sritharan, L. Chen, Large tensile-strain-induced monoclinic M<sub>B</sub> phase in BiFeO<sub>3</sub> epitaxial thin films on a PrScO<sub>3</sub> substrate. *Phys. Rev. B* 2013, 88, 054114.
- [106] G. Xu, J. Li, D. Viehland, Ground state monoclinic (Mb) phase in (110)<sub>c</sub> BiFeO<sub>3</sub> epitaxial thin films. *Appl. Phys. Lett.* 2006, 89, 222901.

- 
- [107] L. Yan, H. Cao, J. Li, D. Viehland, Triclinic phase in tilted (001) oriented BiFeO<sub>3</sub> epitaxial thin films. *Appl. Phys. Lett.* 2009, 94, 132901.
- [108] J. Teague, R. Gerson, W. James, Dielectric hysteresis in single crystal BiFeO<sub>3</sub>. *Solid State Commun.* 1970, 8, 1073.
- [109] D. Lebeugle, D. Colson, A. Forget, M. Viret, Very large spontaneous electric polarization in single crystals at room temperature and its evolution under cycling fields. *Appl. Phys. Lett.* 2007, 91, 022907.
- [110] S. Baek, C. Eom, Reliable polarization switching of BiFeO<sub>3</sub>. *Phil. Trans. R. Soc. A* 2012, 370, 4872.
- [111] Y. Popov, A. Kadomtseva, D. Belov, G. Vorob'ev, A. Zvezdin, Magnetic-field-induced toroidal moment in the magnetoelectric Cr<sub>2</sub>O<sub>3</sub>. *J. Exp. Theor. Phys. Lett.* 1999, 69, 330.
- [112] A. Kadomtseva, Y. Popov, G. Vorob'ev, A. Zvezdin, Spin density wave and field induced phase transitions in magnetoelectric antiferromagnets. *Physica B: Cond. Matter* 1995, 211, 327.
- [113] S. Kiselev, R. Ozerov, G. Zhdanov, Detection of magnetic order in ferroelectric BiFeO<sub>3</sub> by neutron diffraction. *Sov. Phys. Dokl.* 1963, 7, 742.
- [114] W. Ratcliff, Z. Yamani, V. Anbusathaiah, T. Gao, P. Kienzle, H. Cao, I. Takeuchi, Electric-field-controlled antiferromagnetic domains in epitaxial BiFeO<sub>3</sub> thin films probed by neutron diffraction. *Phys. Rev. B* 2013, 87, 140405.
- [115] J. Juraszek, O. Zivotsky, H. Chiron, C. Vaudolon, J. Teillet, A setup combining magneto-optical Kerr effect and conversion electron Mössbauer spectrometry for analysis of the near-surface magnetic properties of thin films. *Rev. Sci. Instrum.* 2009, 80, 043905.

- 
- [116] F. Bai, J. Wang, M. Wuttig, J. Li, N. Wang, A. Pyatakov, A. Zvezdin, L. Cross, D. Viehland, Destruction of spin cycloid in (111)<sub>c</sub>-oriented BiFeO<sub>3</sub> thin films by epitaxial constraint: enhanced polarization and release of latent magnetization. *Appl. Phys. Lett.* 2005, 86, 032511.
- [117] J. Ihlefeld, A. Kumar, V. Gopalan, D. Schlom, Adsorption-controlled molecular-beam epitaxial growth of BiFeO<sub>3</sub>. *Appl. Phys. Lett.* 2007, 91, 071922.
- [118] H. Bea, M. Bibes, A. Barthélémy, K. Bouzehouane, E. Jacquet, A. Khodan, J. Contour, S. Fusil, F. Wyczisk, A. Forget, D. Lebeugle, D. Colson, M. Viret, Influence of parasitic phases on the properties of BiFeO<sub>3</sub> epitaxial thin films. *Appl. Phys. Lett.* 2005, 87, 072508.
- [119] U. Würfel, P. Würfel, *Physics of solar cells: from basic principles to advanced concepts.* Wiley, 2009.
- [120] D. Chapin, C. Fuller, G. Pearson, A new p-n junction photocell for converting solar radiation into electrical power. *J. Appl. Phys.* 1954, 25, 676.
- [121] J. Britt, C. Ferekides, Thin film CdS/CdTe solar cell with 15.8% efficiency. *Appl. Phys. Lett.* 1993, 62, 2851.
- [122] M. Contreras, B. Egaas, K. Ramanathan, J. Hiltner, A. Swartzlander, F. Hasoon, R. Noufi, Progress toward 20% efficiency in Cu(In,Ga)Se<sub>2</sub> polycrystalline thin-film solar cells. *Prog. Photovoltaics: Res. Appl.* 1999, 7, 311.
- [123] W. Badawy, A review on solar cells from Si-single crystals to porous materials and quantum dots. *J. Adv. Res.* 2015, 6,123.
- [124] <https://www.nrel.gov/pv/assets/images/efficiency-chart.png>.
- [125] R. Townsend, J. Macchia, Optically induced refractive index changes in BaTiO<sub>3</sub>. *J. Appl. Phys.* 1970, 41, 5188.

- 
- [126] V. Fridkin, Bulk photovoltaic effect in noncentrosymmetric crystals. *Crystal. Rep.* 2001, 46, 654. *Transl. Kristallograp.* 2001, 46, 722.
- [127] W. Koch, R. Munser, W. Ruppel, P. Wurfel, Bulk photovoltaic effect in BaTiO<sub>3</sub>. *Sol. Stat. Commun.* 1975, 17, 847.
- [128] G. Dalba, Y. Soldo, Giant bulk photovoltaic effect under linearly polarized x-ray synchrotron radiation. *Phys. Rev. Lett.* 1995, 74, 988.
- [129] A. Glass, M. Lines, Principles and applications of ferroelectrics and related materials. Clarendon press, Oxford, UK, 1979.
- [130] J. Wei, Phenomena and mechanisms of photovoltaic effects in ferroelectric BiFeO<sub>3</sub> thin films. PhD Thesis, National University of Singapore, 2012.
- [131] P. Brody, F. Crowne, Mechanism for the high voltage photovoltaic effect in ceramic ferroelectrics. *J. Elect. Mater.* 1975, 4, 955.
- [132] M. Qin, K. Yao, Y. Liang, S. Shannigrahi, Thickness effects on photoinduced current in ferroelectric (Pb<sub>0.97</sub>La<sub>0.03</sub>)(Zr<sub>0.52</sub>Ti<sub>0.48</sub>)O<sub>3</sub> thin films. *J. Appl. Phys.* 2007, 101, 014104.
- [133] M. Qin, K. Yao, Y. Liang, Photovoltaic mechanisms in ferroelectric thin films with the effects of the electrodes and interfaces. *Appl. Phys. Lett.* 2009, 95, 022912.
- [134] Q. Meng, Y. Kui, C. Yung, High efficient photovoltaics in nanoscaled ferroelectric thin films. *Appl. Phys. Lett.* 2008, 93, 122904.
- [135] Y. Yang, S. Lee, S. Yi, B. Chae, S. Lee, H. Joo, M. Jang, Schottky barrier effects in the photocurrent of sol-gel derived lead zirconate titanate thin film capacitors. *Appl. Phys. Lett.* 2000, 76, 774.
- [136] B. Meyer, D. Vanderbilt, Ab initio study of ferroelectric domain walls in PbTiO<sub>3</sub>. *Phys. Rev. B* 2002, 65, 104111.

- 
- [137] J. Seidel, L. Martin, Q. He, Q. Zhan, Y. Chu, A. Rother, M. Hawkridge, P. Maksymovych, P. Yu, M. Gajek, N. Balke, S. Kalinin, S. Gemming, F. Wang, G. Catalan, J. Scott, N. Spaldin, J. Orenstein, R. Ramesh, Conduction at domain walls in oxide multiferroics. *Nature Mater.* 2009, 8, 229.
- [138] M. Alexe, D. Hesse, Tip-enhanced photovoltaic effects in bismuth ferrite. *Nature Commun.* 2011, 2, 256.
- [139] F. Zheng, J. Xu, L. Fang, M. Shen, X. Wu, Separation of the schottky barrier and polarization effects on the photocurrent of Pt sandwiched  $\text{Pb}(\text{Zr}_{0.20}\text{Ti}_{0.80})\text{O}_3$  films. *Appl. Phys. Lett.* 2008, 93, 172101.
- [140] D. Cao, C. Wang, F. Zheng, W. Dong, L. Fang, M. Shen, High-efficiency ferroelectric-film solar cells with an n-type  $\text{Cu}_2\text{O}$  cathode buffer layer. *Nano Lett.* 2012, 12, 2803.
- [141] F. Zheng, Y. Xin, W. Huang, J. Zhang, X. Wang, M. Shen, W. Dong, L. Fang, Y. Bai, X. Shen, J. Hao, Above 1% efficiency of a ferroelectric solar cell based on the  $\text{Pb}(\text{Zr,Ti})\text{O}_3$  film. *J. Mater. Chem. A* 2014, 2, 1363.
- [142] R. Nechache, C. Harnagea, S. Licocchia, E. Traversa, A. Ruediger, A. Pignolet, F. Rosei, Photovoltaic properties of  $\text{Bi}_2\text{FeCrO}_6$  epitaxial thin films. *Appl. Phys. Lett.* 2011, 98, 202902.
- [143] P. Lopez-Varo, L. Bertoluzzi, J. Bisquert, M. Alexe, M. Coll, J. Huang, J. Jimenez-Tejada, T. Kirchartz, R. Nechache, F. Rosei, Y. Yuan, Physical aspects of ferroelectric semiconductors for photovoltaic solar energy conversion. *Phys. Report.* 2016, 653, 1.
- [144] T. Cook, D. Dogutan, S. Reece, Y. Surendranath, T. Teets, D. Nocera, Solar energy supply and storage for the legacy and nonlegacy worlds. *Chem. Rev.* 2010, 110, 6474.
- [145] Y. Izumi, Recent advances in the photocatalytic conversion of carbon dioxide to fuels with water and/or hydrogen using solar energy and beyond. *Coord. Chem. Rev.* 2013, 257, 171.

- 
- [146] M. Tahir, N. Amin, Recycling of carbon dioxide to renewable fuels by photocatalysis: Prospects and challenges. *Renew. Sust. Energy Rev.* 2013, 25, 560.
- [147] K. Maeda, Photocatalytic water splitting using semiconductor particles: History and recent developments. *J. Photochem. Photobiol. C* 2011, 12, 237.
- [148] F. Osterloh, Inorganic nanostructures for photoelectrochemical and photocatalytic water splitting. *Chem. Soc. Rev.* 2013, 42, 2294.
- [149] Y. Qu, X. Duan, Progress, challenge and perspective of heterogeneous photocatalysts. *Chem. Soc. Rev.* 2013, 42, 2568.
- [150] A. Singh, S. Chang, R. Hocking, U. Bach, L. Spiccia, Highly active nickel oxide water oxidation catalysts deposited from molecular complexes. *Energy Environ. Sci.* 2013, 6, 579.
- [151] T. Hisatomi, J. Kubota, K. Domen, Recent advances in semiconductors for photocatalytic and photoelectrochemical water splitting. *Chem. Soc. Rev.* 2014, 43, 7520.
- [152] N. Serpone, A. Emeline, V. Ryabchuk, V. Kuznetsov, Y. Artemev, S. Horikoshi, Why do hydrogen and oxygen yields from semiconductor-based photocatalyzed water splitting remain disappointingly low? Intrinsic and extrinsic factors impacting surface redox reactions. *ACS Energy Lett.* 2016, 1, 931.
- [153] A. Fujishima, K. Kohayakawa, K. Honda, Hydrogen production under sunlight with an electrochemical photocell. *J. Electrochem. Soc.* 1975, 122, 1487.
- [154] T. Takata, Y. Furumi, K. Shinohara, A. Tanaka, M. Hara, J. Kondo, K. Domen, Photocatalytic decomposition of water on spontaneously hydrated layered perovskites. *Chem. Mater.* 1997, 9, 1063.
- [155] H. Kato, A. Kudo, New tantalate photocatalysts for water decomposition into H<sub>2</sub> and O<sub>2</sub>. *Chem. Phys. Lett.* 1998, 295, 487.

- 
- [156] M. Machida, J. Yabunaka, T. Kijima, Efficient photocatalytic decomposition of water with the novel layered tantalate  $\text{RbNdTa}_2\text{O}_7$ . *Chem. Commun.* 1999, 0, 1939.
- [157] H. Kato, A. Kudo, Water splitting into  $\text{H}_2$  and  $\text{O}_2$  on alkali tantalate photocatalysts  $\text{ATaO}_3$  (A= Li, Na, and K). *J. Phys. Chem. B* 2001, 105, 4285.
- [158] S. Ikeda, T. Itani, K. Nango, M. Matsumura, Overall water splitting on tungsten-based photocatalysts with defect pyrochlore structure. *Catal. Lett.* 2004, 98, 229.
- [159] M. Ni, M. Leung, D. Leung, K. Sumathy, A review and recent developments in photocatalytic water-splitting using  $\text{TiO}_2$  for hydrogen production. *Renew. Sustain. Energ. Rev.* 2007, 11, 401.
- [160] S. Khan, J. Akikusa, Photoelectrochemical splitting of water at nanocrystalline n- $\text{Fe}_2\text{O}_3$  thin-film electrodes. *J. Phys. Chem. B* 1999, 103, 7184.
- [161] X. Liu, F. Wang, Q. Wang, Nanostructure-based  $\text{WO}_3$  photoanodes for photoelectrochemical water splitting. *Phys. Chem. Chem. Phys.* 2012, 14, 7894.
- [162] R. Gardner, F. Sweett, D. Tanner, The electrical properties of alpha ferric oxide—II: Ferric oxide of high purity. *J. Phys. Chem. Solids* 1963, 24, 1183.
- [163] J. Kennedy, K. Frese, Photooxidation of water at  $\alpha\text{-Fe}_2\text{O}_3$  electrodes. *J. Electrochem. Soc.* 1978, 125, 709.
- [164] M. Butler, Photoelectrolysis and physical-properties of semiconducting electrode  $\text{WO}_3$ . *J. Appl. Phys.* 1977, 48, 1914.
- [165] C. Liu, N. Dasgupta, P. Yang, Semiconductor nanowires for artificial photosynthesis. *Chem. Mater.* 2013, 26, 415.
- [166] T. Townsend, N. Browning, F. Osterloh, Overall photocatalytic water splitting with  $\text{NiO}_x\text{-SrTiO}_3$ —a revised mechanism. *Energy Environ. Sci.* 2012, 5, 9543.

- 
- [167] R. Asai, H. Nemoto, Q. Jia, K. Saito, A. Iwase, A. Kudo, A visible light responsive rhodium and antimony-codoped SrTiO<sub>3</sub> powdered photocatalyst loaded with an IrO<sub>2</sub> cocatalyst for solar water splitting. *Chem. Commun.* 2014, 50, 2543.
- [168] P. Kanhere, J. Zheng, Z. Chen, Site specific optical and photocatalytic properties of Bi-doped NaTaO<sub>3</sub>. *J. Phys. Chem. C* 2011, 115, 11846.
- [169] P. Kanhere, J. Zheng, Z. Chen, Visible light driven photocatalytic hydrogen evolution and photophysical properties of Bi<sup>3+</sup> doped NaTaO<sub>3</sub>. *Int. J. Hydrog. Energy* 2012, 37, 4889.
- [170] P. Kanhere, Z. Chen, A review on visible light active perovskite-based photocatalysts. *Molecules* 2014, 19, 19995.
- [171] Z. Yi, J. Ye, Band gap tuning of Na<sub>1-x</sub>La<sub>x</sub>Ta<sub>1-x</sub>Co<sub>x</sub>O<sub>3</sub> solid solutions for visible light photocatalysis. *Appl. Phys. Lett.* 2007, 91, 254108.
- [172] Z. Zhao, R. Li, Z. Li, Z. Zou, Photocatalytic activity of La-N-codoped NaTaO<sub>3</sub> for H<sub>2</sub> evolution from water under visible-light irradiation. *J. Phys. D: Appl. Phys.* 2011, 44, 165401.
- [173] S. Tijare, M. Joshi, P. Padole, P. Mangrulkar, S. Rayalu, N. Labhsetwar, Photocatalytic hydrogen generation through water splitting on nano-crystalline LaFeO<sub>3</sub> perovskite. *Int. J. Hydrog. Energy* 2012, 37, 10451.
- [174] F. Gao, X. Chen, K. Yin, S. Dong, Z. Ren, F. Yuan, T. Yu, Z. Zou, J. Liu, Visible-light photocatalytic properties of weak magnetic BiFeO<sub>3</sub> nanoparticles. *Adv. Mater.* 2007, 19, 2889.
- [175] P. Dhanasekaran, N. Gupta, Factors affecting the production of H<sub>2</sub> by water splitting over a novel visible-light-driven photocatalyst GaFeO<sub>3</sub>. *Int. J. Hydrog. Energy* 2012, 37, 4897.
- [176] P. Tang, H. Chen, F. Cao, G. Pan, Magnetically recoverable and visible-light-driven nanocrystalline YFeO<sub>3</sub> photocatalysts. *Catal. Sci. Technol.* 2011, 1, 1145.

- 
- [177] P. Borse, C. Cho, S. Yu, J. Yoon, T. Hong, J. Bae, E. Jeong, H. Kim, Improved photolysis of water from Ti incorporated double perovskite  $\text{Sr}_2\text{FeNbO}_6$  lattice. *Bull. Korean Chem. Soc.* 2012, 33, 3407.
- [178] R. Hu, C. Li, X. Wang, Y. Sun, H. Jia, H. Su, Y. Zhang, Photocatalytic activities of  $\text{LaFeO}_3$  and  $\text{La}_2\text{FeTiO}_6$  in p-chlorophenol degradation under visible light. *Catal. Commun.* 2012, 29, 35.
- [179] R. Singh, J. Narayan, Pulsed-laser evaporation technique for deposition of thin films: physics and theoretical model. *Phys. Rev. B* 1990, 41, 8843.
- [180] R. Eason, Pulse laser deposition of thin films: applications-led growth of functional materials. John Wiley & Sons Inc. 2007.
- [181] J. Chakrabarty, Multiferroic materials as active elements for photovoltaic devices. MSc thesis, EMT-INRS, University of Quebec, 2013.
- [182] <http://titan.physx.u-szeged.hu/~lamilab/plden.htm>.
- [183] <http://hyperphysics.phy-astr.gsu.edu/hbase/quantum/bragg.html>
- [184] F. Haguenau, P. Hawkes, J. Hutchison, B. Satiat-Jeunemaître, G. Simon, D. Williams, Key events in the history of electron microscopy. *Microscop. Microanalys.* 2003, 9, 96.
- [185] C. Harnagea, C. Cojocaru, R. Nechache, O. Gautreau, F. Rosei, A. Pignolet, Towards ferroelectric and multiferroic nanostructures and their characterisation. *Int. J. Nanotech.* 2008, 5, 930.
- [186] U. Zerweck, C. Loppacher, T. Otto, S. Grafström, L. Eng, Accuracy and resolution limits of kelvin probe force microscopy. *Phys. Rev. B* 2005, 71, 125424.
- [187] G. Catalan, J. Scott, Physics and applications of bismuth ferrite. *Adv. Mater.* 2009, 21 2463.

- 
- [188] B. Guo, W. Dong, H. Li, H. Liu, Evidence for oxygen vacancy or ferroelectric polarization induced switchable diode and photovoltaic effects in BiFeO<sub>3</sub> based thin films. *Nanotech.* 2013, 24, 27.
- [189] J. Chakrabartty, R. Nechache, C. Harnagea, F. Rosei, Photovoltaic effect in multiphase Bi-Mn-O thin films. *Optics Exp.* 2014, 22 (S1), A80.
- [190] S. Yang, L. Martin, S. Byrnes, T. Conry, S. Basu, D. Paran, L. Reichertz, J. Ihlefeld, C. Adamo, A. Melville, Y. Chu, C. Yang, J. Musfeldt, D. Schlom, J. Ager, R. Ramesh, Photovoltaic effects in BiFeO<sub>3</sub>. *Appl. Phys. Lett.* 2009, 95, 6.
- [191] Z. Fan, K. Yao, J. Wang, Photovoltaic effect in an indium-tin-oxide/ZnO/BiFeO<sub>3</sub>/Pt heterostructure. *Appl. Phys. Lett.* 2014, 105, 16.
- [192] R. Katiyar, P. Misra, F. Mendoza, G. Morell, R. Katiyar, Switchable photovoltaic effect in bilayer graphene/BiFeO<sub>3</sub>/Pt heterostructures. *Appl. Phys. Lett.* 2014, 105, 14.
- [193] D. Kim, H. Lee, M. Biegalski, H. Christen, Large ferroelectric polarization in antiferromagnetic BiFe<sub>0.5</sub>Cr<sub>0.5</sub>O<sub>3</sub> epitaxial films. *Appl. Phys. Lett.* 2007, 91, 4.
- [194] H. Christen, D. Norton, L. Géa, L. Boatner, Pulsed laser deposition of solid-solution films using segmented targets. *Thin Sol. Film.* 1998, 312, 156.
- [195] M. Jung, I. Yang, Y. Jeong, Investigation of the magnetic and the ferroelectric properties of BiMnO<sub>3</sub> thin films. *J. Kor. Phys. Soc.* 2013, 63, 624.
- [196] S. Kalinin, D. Bonnell, Imaging mechanism of piezoresponse force microscopy of ferroelectric surfaces. *Phys. Rev. B* 2002, 65, 125408.
- [197] C. Harnagea, A. Pignolet, M. Alexe, D. Hesse, Higher-order electromechanical response of thin films by contact resonance piezoresponse force microscopy. *IEEE Trans. Ultrason. Ferroelec. Freq. Cont.* 2006, 53, 12.

- 
- [198] X. Xu, T. Guoqiang, R. Huijun, X. Ao, Structural, electric and multiferroic properties of Sm-doped BiFeO<sub>3</sub> thin films prepared by the sol–gel process. *Ceram. Intern.* 2013, 39, 6223.
- [199] E. Pérez, Growth and characterization of Bi-based multiferroic thin films. PhD Thesis, Departament de Física Aplicada i Òptica, Facultat de Física, Universitat de Barcelona, 2013.
- [200] X. Xu, J. Ihlefeld, J. Lee, O. Ezekoye, E. Vlahos, R. Ramesh, V. Gopalan, X. Pan, D. Schlom, J. Musfeldt, Tunable band gap in Bi(Fe<sub>1-x</sub>Mn<sub>x</sub>)O<sub>3</sub> films. *Appl. Phys. Lett.* 2010, 96, 192901.
- [201] X. Wang, G. Koleilat, J. Tang, H. Liu, I. Kramer, R. Debnath, L. Brzozowski, D. Barkhouse, L. Levina, S. Hoogland, E. Sargent, Tandem colloidal quantum dot solar cells employing a graded recombination layer. *Nature Photon.* 2011, 5, 480.
- [202] G. Pethuraja, E. Roger, K. Ashok, L. Changwoo, J. Nicholas, E. Harry, H. Pradeep, L. Jennifer, Current-voltage characteristics of ITO/p-Si and ITO/n-Si contact interfaces. *Adv. Mater. Phys. Chem.* 2012, 2, 2.
- [203] H. Yang, H. Luo, H. Wang, I. Usov, N. Suvorova, M. Jain, D. Feldmann, P. Dowden, R. Paula, Q. Jia, Rectifying current-voltage characteristics of BiFeO<sub>3</sub>/NbBiFeO<sub>3</sub>/Nb-doped SrTiO<sub>3</sub> heterojunction. *Appl. Phys. Lett.* 2008, 92, 10.
- [204] M. Green, *Solar cells-operating principles, technology and system application.* University of NSW, Australia, 1992.
- [205] B. Ray, M. Alam, Achieving fill factor above 80% in organic solar cells by charged interface. 38<sup>th</sup> IEEE Photovol. Special. Conf. (PVSC) 2012, 2, 1.
- [206] C. Yang, J. Seidel, S. Kim, P. Rossen, P. Yu, M. Gajek, Y. Chu, L. Martin, M. Holcomb, Q. He, P. Maksymovych, N. Balke, S. Kalinin, A. Baddorf, S. Basu, M. Scullin, R. Ramesh, Electric modulation of conduction in multiferroic Ca-doped BiFeO<sub>3</sub> films. *Nature Mater.* 2009, 8, 485.

- 
- [207] Z. Liu, F. Yan, The application of bismuth-based oxides in organic-inorganic hybrid photovoltaic devices. *J. Am. Ceram. Soc.* 2012, 95, 1944.
- [208] Z. Yue, K. Zhao, S. Zhao, X. Li, H. Ni, A. Wang, Thickness-dependent photovoltaic effects in miscut Nb-doped SrTiO<sub>3</sub> single crystals. *J. Phys. D: Appl. Phys.* 2010, 43, 015104.
- [209] Y. Muraoka, T. Muramatsu, J. Yamaura, Z. Hiroi, Photogenerated hole carrier injection to YBa<sub>2</sub>Cu<sub>3</sub>O<sub>7-x</sub>/YBa<sub>2</sub>Cu<sub>3</sub>O<sub>7-x</sub> in an oxide heterostructure. *Appl. Phys. Lett.* 2004, 85, 2950.
- [210] D. Neamen, *Semiconductor physics and devices: basic principles*. 3<sup>rd</sup> Ed., McGraw-Hill, New York, 2003.
- [211] C. Wang, K. Jin, Z. Xu, L. Wang, C. Ge, H. Lu, H. Guo, M. He, G. Yang, Switchable diode effect and ferroelectric resistive switching in epitaxial BiFeO<sub>3</sub> thin films. *Appl. Phys. Lett.* 2011, 98, 192901.
- [212] Z. Hu, Q. Li, M. Li, Q. Wang, Y. Zhu, X. Liu, X. Zhao, Y. Liu, S. Dong, Ferroelectric memristor based on Pt/BiFeO<sub>3</sub>/Nb-doped SrTiO<sub>3</sub> heterostructure. *Appl. Phys. Lett.* 2013, 102, 102901.
- [213] V. Belinicher, B. Sturman, The photogalvanic effect in media lacking a center of symmetry. *Sov. Phys. Usp.* 1980, 23, 199.
- [214] E. Loh, A model of dc leakage in ceramic capacitors. *J. Appl. Phys.* 1982, 53, 6229.
- [215] H. Neumann, G. Arlt, Maxwell-wagner relaxation and degradation of SrTiO<sub>3</sub> and BaTiO<sub>3</sub> ceramics. *Ferroelectrics* 1986, 69, 179.
- [216] U. Rau, K. Taretto, S. Siebentritt, Grain boundaries in Cu(In, Ga)(Se, S)<sub>2</sub> thin-film solar cells. *Appl. Phys. A* 2009, 96, 221.

- 
- [217] J. Yun, A. Ho-Baillie, S. Huang, S. Woo, Y. Heo, J. Seidel, F. Huang, Y. Cheng, M. Green, Benefit of grain boundaries in organic–inorganic halide planar perovskite solar cells. *J. Phys. Chem. Lett.* 2015, 6, 875.
- [218] N. Li, K. Yao, G. Gao, Z. Sun, L. Li, Charge, orbital and spin ordering in multiferroic  $\text{BiMn}_2\text{O}_5$ : density functional theory calculations. *Phys. Chem. Chem. Phys.* 2011, 13, 9418.
- [219] E. Nuffield, X-ray diffraction methods. John Wiley, NY, 1966.
- [220] F. Silva Júnior, C. Paschoal, R. Almeida, R. Moreira, W. Paraguassu, M. Castro Junior, A. Ayala, Z. Kann, M. Lufaso, Room-temperature vibrational properties of the  $\text{BiMn}_2\text{O}_5$  mullite. *Vibration. Spectrosc.* 2013, 66, 43.
- [221] D. Shukla, R. Kumar, S. Mollah, R. Choudhary, P. Thakur, S. Sharma, N. Brookes, M. Knobel, Swift heavy ion irradiation induced magnetism in magnetically frustrated  $\text{BiMn}_2\text{O}_5$  thin films. *Phys. Rev. B* 2010, 82, 174432.
- [222] P. Toulemonde, P. Bordet, P. Bouvier, J. Kreisel, Single-crystalline  $\text{BiMnO}_3$  studied by temperature-dependent x-ray diffraction and raman spectroscopy. *Phys. Rev. B* 2014, 89, 224107.
- [223] L. Yin, B. Yuan, J. Chen, D. Zhang, Q. Zhang, J. Yang, J. Dai, W. Song, Y. Sun, Dielectric relaxations and magnetodielectric response in  $\text{BiMn}_2\text{O}_5$  single crystal. *Appl. Phys. Lett.* 2013, 103, 152908.
- [224] S. Hong, J. Woo, H. Shin, J. Jeon, Y. Pak, E. Colla, N. Setter, E. Kim, K. No, Principle of ferroelectric domain imaging using atomic force microscope. *J. Appl. Phys.* 2001, 89, 1377.
- [225] J. Chakrabartty, R. Nechache, C. Harnagae, S. Li, F. Rosei, Enhanced photovoltaic properties in bilayer  $\text{BiFeO}_3$  /Bi-Mn-O thin films. *Nanotech.* 2016, 27, 215402.
- [226] J. Son, C. Park, H. Kim, Room temperature ferroelectric property of  $\text{BiMnO}_3$  thin film with double  $\text{SrTiO}_3$  buffer layers on Pt/Ti/SiO<sub>2</sub>/Si substrate. *Metal. Mater. Int.* 2010, 16, 289.

- 
- [227] J. Scott, Ferroelectrics go bananas. *J. Phys.: Condens. Matter* 2008, 20, 21001.
- [228] L. Pintilie, M. Alexe, Ferroelectric-like hysteresis loop in non-ferroelectric systems. *Appl. Phys. Lett.* 2005, 87, 112903.
- [229] K. Tobe, T. Kimura, Y. Okimoto, Y. Tokura, Anisotropic optical spectra in a detwinned  $\text{LaMnO}_3$  crystal. *Phys. Rev. B* 2001, 64, 184421.
- [230] M. Quijada, J. Simpson, L. Vasiliu-Doloc, J. Lynn, H. Drew, Y. Mukocskii, S. Karabashev, Temperature dependence of low-lying electronic excitations of  $\text{LaMnO}_3$ . *Phys. Rev. B* 2001, 64, 224426.
- [231] J. Lee, X. Ke, R. Misra, J. Ihlefeld, X. Xu, Z. Mei, T. Heeg, M. Roeckerath, J. Schubert, Z. Liu, J. Musfeldt, P. Schiffer, D. Schlom, Adsorption-controlled growth of  $\text{BiMnO}_3$  films by molecular-beam epitaxy. *Appl. Phys. Lett.* 2010, 96, 262905.
- [232] C. Himcinschi, A. Bhatnagar, A. Talkenberger, M. Barchuk, D. Zahn, D. Rafaja, J. Kortus, M. Alexe, Optical properties of epitaxial  $\text{BiFeO}_3$  thin films grown on  $\text{LaAlO}_3$ . *Appl. Phys. Lett.* 2015, 106, 012908.
- [233] C. Himcinschi, I. Vrejoiu, M. Friedrich, L. Ding, C. Cobet, N. Esser, M. Alexe, D. Zahn, Optical characterization of  $\text{BiFeO}_3$  epitaxial thin films grown by pulsed-laser deposition. *Phys. Stat. Solidi C* 2010, 7, 296.
- [234] V. Železný, D. Chvostová, L. Pajasová, I. Vrejoiu, M. Alexe, Optical properties of epitaxial  $\text{BiFeO}_3$  thin films. *Appl. Phys. A* 2010, 100, 1217.
- [235] J. Xu, R. Zhang, Z. Chen, Z. Wang, F. Zhang, X. Yu, A. Jiang, Y. Zheng, S. Wang, L. Chen, Optical properties of epitaxial  $\text{BiFeO}_3$  thin film grown on  $\text{SrRuO}_3$ -buffered  $\text{SrTiO}_3$  substrate. *Nanoscal. Res. Lett.* 2014, 9, 188.

- 
- [236] J. Tauc, R. Grigorovici, A. Vancu, Optical properties and electronic structure of amorphous germanium. *Phys. Stat. Solid. B* 1966, 15, 627.
- [237] J. Chakrabartty, D. Barba, L. Jin, D. Benetti, F. Rosei, R. Nechache, Photoelectrochemical properties of BiMnO<sub>3</sub> thin films and nanostructures. *J. Power Sources* 2017, 365, 162.
- [238] H. Xin, S. Vorpahl, A. Collord, I. Braly, A. Uhl, B. Krueger, D. Ginger, H. Hillhouse, Lithium-doping inverts the nanoscale electric field at the grain boundaries in Cu<sub>2</sub>ZnSn(S,Se)<sub>4</sub> and increases photovoltaic efficiency. *Phys. Chem. Chem. Phys.* 2015, 17, 23859.
- [239] S. Kalinin, D. Bonnell, Surface potential at surface-interface junctions in SrTiO<sub>3</sub> bicrystals. *Phys. Rev. B* 2000, 62, 15.
- [240] Y. Zhou, L. Wang, S. Chen, S. Qin, X. Liu, J. Chen, D. Xue, M. Luo, Y. Cao, Y. Cheng, E. H. Sargent, J. Tang, Thin-film Sb<sub>2</sub>Se<sub>3</sub> photovoltaics with oriented one-dimensional ribbons and benign grain boundaries. *Nature Photon.* 2015, 9, 409.
- [241] J. Li, V. Chawla, B. Clemens, Investigating the role of grain boundaries in CZTS and CZTSSe thin film solar cells with scanning probe microscopy. *Adv. Mater.* 2012, 24, 720.
- [242] S. Hong, S. Tong, W. Parka, Y. Hiranaga, Y. Cho, A. Roelofs, Charge gradient microscopy. *Proc. Natl. Acad. Sci.* 2014, 111, 6566.
- [243] S. Tong, W. Park, Y. Choi, L. Stan, S. Hong, A. Roelofs, Mechanical removal and rescreening of local screening charges at ferroelectric surfaces. *Phys. Rev. Appl.* 2015, 3, 014003.
- [244] W. Melitz, J. Shen, A. Kummel, S. Lee, Kelvin probe force microscopy and its application. *Surface Sci. Report.* 2011, 66, 1.
- [245] K. Zhao, K. Jin, Y. Huang, S. Zhao, H. Lu, M. He, Z. Chen, Y. Zhou, G. Yang, Ultraviolet fast-response photoelectric effect in tilted orientation SrTiO<sub>3</sub> single crystals. *Appl. Phys. Lett.* 2006, 89, 173507.

- 
- [246] X. Zou, L. You, W. Chen, H. Ding, D. Wu, T. Wu, L. Chen, J. Wang, Mechanism of polarization fatigue in BiFeO<sub>3</sub>. ACS Nano 2012, 6, 8997.
- [247] W. Metzger, M. Gloeckler, The impact of charged grain boundaries on thin-film solar cells and characterization. J. Appl. Phys. 2005, 98, 063701.
- [248] J. Scott, C. Araujo, B. Melnick, L. McMillan, R. Zuleeg, Quantitative measurement of space-charge effects in lead zirconate-titanate memories. J. Appl. Phys. 1991, 70, 382.
- [249] X. Chen, C. Jia, Y. Chen, G. Yang, W. Zhang, Ferroelectric memristive effect in BaTiO<sub>3</sub> epitaxial thin films. J. Phys. D: Appl. Phys. 2014, 47, 365102.
- [250] K. Lehovec, G. Shirn, Conductivity injection and extraction in polycrystalline barium titanate. J. Appl. Phys. 1962, 33, 2036.
- [251] H. Lee, L. Burton, Charge carriers and time dependent currents in BaTiO<sub>3</sub>-based ceramic. IEEE Trans. Component. Hybrid. Manufact. Tech. 1986, 9, 469.
- [252] J. Chakrabarty, R. Nechache, S. Li, M. Nicklaus, A. Ruediger, F. Rosei, Photovoltaic properties of multiferroic BiFeO<sub>3</sub>/BiCrO<sub>3</sub> heterostructures. J. Am. Cer. Soc. 2014, 96, 1837.
- [253] A. Bhatnagar, A. Chaudhuri, Y. Kim, D. Hesse, M. Alexe, Role of domain walls in the abnormal photovoltaic effect in BiFeO<sub>3</sub>. Nature Comm. 2013, 4, 2835.
- [254] M. Alexe, C. Harnagea, D. Hesse, U. Gösele, Polarization imprint and size effects in mesoscopic ferroelectric structures. Appl. Phys. Lett. 2001, 79, 242.
- [255] W. Lee, H. Han, A. Lotnyk, M. Schubert, S. Senz, M. Alexe, D. Hesse, S. Baik, U. Gosele, Individually addressable epitaxial ferroelectric nanocapacitor arrays with near Tb inch<sup>-2</sup> density. Nature Nanotech. 2008, 3, 402.

- 
- [256] R. Nechache, C. Cojocaru, C. Harnagea, C. Nauenheim, M. Nicklaus, A. Ruediger, F. Rosei, A. Pignolet, Epitaxial patterning of  $\text{Bi}_2\text{FeCrO}_6$  double perovskite nanostructures: multiferroic at room temperature. *Adv. Mater.* 2011, 23, 1724.
- [257] C. Cojocaru, R. Nechache, C. Harnagea, A. Pignolet, F. Rosei, Nanoscale patterning of functional perovskite-type complex oxides by pulsed laser deposition through a nanostencil. *Appl. Surf. Sci.* 2010, 256, 4777.
- [258] C. Cojocaru, C. Harnagea, A. Pignolet, F. Rosei, Nanostenciling of functional materials by room temperature pulsed laser deposition. *IEEE Trans. Nanotech.* 2006, 5, 470.
- [259] C. Cojocaru, C. Harnagea, F. Rosei, A. Pignolet, M. Boogaart, J. Brugger, Complex oxide nanostructures by pulsed laser deposition through nanostencils. *Appl. Phys. Lett.* 2005, 86, 183107.
- [260] C. Cojocaru, F. Ratto, C. Harnagea, A. Pignolet, F. Rosei, Semiconductor and insulator nanostructures: challenges and opportunities. *Microel. Eng.* 2005, 80, 448.
- [261] C. Cojocaru, A. Bernardi, J. Reparaz, M. Alonso, J. MacLeod, C. Harnagea, F. Rosei, Site-controlled growth of Ge nanostructures on Si(100) via pulsed laser deposition nanostenciling. *Appl. Phys. Lett.* 2007, 91, 113112.
- [262] M. Kato, J. Zhang, N. Paul, E. Reisner, Protein film photoelectrochemistry of the water oxidation enzyme photosystem II. *Chem. Soc. Rev.* 2014, 43, 6485.
- [263] G. Luca, D. Preziosi, F. Chiarella, R. Capua, S. Gariglio, Ferromagnetism and ferroelectricity in epitaxial  $\text{BiMnO}_3$  ultra-thin films. *Appl. Phys. Lett.* 2013, 103, 062902.
- [264] A. Vailionis, H. Boschker, W. Siemons, E. Houwman, D. Blank, G. Rijnders, G. Koster, Misfit strain accommodation in epitaxial  $\text{ABO}_3$  perovskites: lattice rotations and lattice modulations. *Phys. Rev. B* 2011, 83, 064101.

- 
- [265] Z. Luo, C. Li, D. Zhang, T. Wang, J. Gong, Highly-oriented Fe<sub>2</sub>O<sub>3</sub>/ZnFe<sub>2</sub>O<sub>4</sub> nanocolumnar heterojunction with improved charge separation for photoelectrochemical water oxidation. *Chem. Comm.* 2016, 52, 9013.
- [266] N. Rong, M. Chu, Y. Tang, C. Zhang, X. Cui, H. He, Y. Zhang, P. Xiao, Improved photoelectrocatalytic properties of Ti-doped BiFeO<sub>3</sub> films for water oxidation. *J. Mater. Sci.* 2016, 51, 5712.
- [267] Y. Hwang, A. Boukai, P. Yang, High density n-Si/n-TiO<sub>2</sub> core/shell nanowire arrays with enhanced photoactivity. *Nano Lett.* 2008, 9, 410.
- [268] N. Hahn, C. Mullins, Photoelectrochemical performance of nanostructured Ti- and Sn-doped  $\alpha$ -Fe<sub>2</sub>O<sub>3</sub> photoanodes. *Chem. Mater.* 2010, 22, 6474.
- [269] W. Li, J. Li, X. Wang, J. Ma, Q. Chen, Photoelectrochemical and physical properties of WO<sub>3</sub> films obtained by the polymeric precursor method. *Int. J. Hydrog. Energ.* 2010, 35, 13137.
- [270] R. Solarska, R. Jurczakowski, J. Augustynski, A highly stable, efficient visible-light driven water photoelectrolysis system using a nanocrystalline WO<sub>3</sub> photoanode and a methane sulfonic acid electrolyte. *Nanoscale* 2012, 4, 1553.
- [271] Q. Zeng, J. Bai, J. Li, L. Xia, K. Huang, X. Li, B. Zhou, A novel in situ preparation method for nanostructured  $\alpha$ -Fe<sub>2</sub>O<sub>3</sub> films from electrodeposited Fe films for efficient photoelectrocatalytic water splitting and the degradation of organic pollutants. *J. Mater. Chem. A* 2015, 3, 4345.
- [272] R. Krol, M. Grätzel, Photoelectrochemical hydrogen production. Springer, 2011, ISBN 9781461413806.
- [273] J. Krysa, M. Zlamal, S. Kment, M. Brunclikova, Z. Hubicka, TiO<sub>2</sub> and Fe<sub>2</sub>O<sub>3</sub> films for photoelectrochemical water splitting. *Molecules* 2015, 20, 1046.

- 
- [274] H. Uchiyama, S. Igarashi, H. Kozuka, Evaporation-driven deposition of WO<sub>3</sub> thin films from organic-additive-free aqueous solutions by low-speed dip coating and their photoelectrochemical properties. *Langmuir* 2016, 32, 3116.
- [275] K. Gelderman, L. Lee, S. Donne, Flat-band potential of a semiconductor: using the Mott–Schottky equation. *J. Chem. Edu.* 2007, 84, 685.
- [276] D. Scaife, Oxide semiconductors in photoelectrochemical conversion of solar energy. *Solar Energ.* 1980, 25, 41.
- [277] T. Cai, J. Wang, S. Ju, Z. Li, Ferroelectric and multiferroic tunnel junctions. INTECH Open Access Publisher, 2010.
- [278] S. Kalinin, D. Bonnell, Screening phenomena on oxide surfaces and its implications for local electrostatic and transport measurements. *Nano Lett.* 2004, 4, 555.
- [279] K. May, D. Fenning, T. Ming, W. Hong, D. Lee, K. Stoerzinger, M. Biegalski, A. Kolpak, Y. Shao-Hor, Thickness-dependent photoelectrochemical water splitting on ultrathin LaFeO<sub>3</sub> films grown on Nb:SrTiO<sub>3</sub>. *J. Phys. Chem. Lett.* 2015, 6, 977.
- [280] A. Hochbaum, P. Yang, Semiconductor nanowires for energy conversion. *Chem. Rev.* 2010, 110, 527.
- [281] M. Bhatt, J. Lee, Recent theoretical progress in the development of photoanode materials for solar water splitting photoelectrochemical cells. *J. Mater. Chem. A* 2015, 3, 10632.

## Appendix A: List of Acronyms

PV	Photovoltaic
PCE	Power conversion efficiency
FE	Ferroelectric
APV	Anomalous photovoltage
BTO	BaTiO <sub>3</sub>
LNO	LiNbO <sub>3</sub>
BFO	BiFeO <sub>3</sub>
DW	Domain walls
GB	Grain boundaries
PZT	Lead zirconate titanate
J	Current density
V	Voltage
J <sub>sc</sub>	Short-circuit current density
V <sub>oc</sub>	Open circuit voltage
FF	Fill factor
BFCO	Bi <sub>2</sub> FeCrO <sub>6</sub>
BFO	BiFeO <sub>3</sub>
STO	SrTiO <sub>3</sub>
NSTO	Niobium doped SrTiO <sub>3</sub>
ITO	Indium tin oxide
FTO	Fluorine doped tin oxide
PEC	Photoelectrochemical
H <sub>2</sub>	Hydrogen

O <sub>2</sub>	Oxygen
BMO	BiMnO <sub>3</sub>
PZO	PbZrO <sub>3</sub>
PTO	PbTiO <sub>3</sub>
STO	SrTiO <sub>3</sub>
PLD	Pulsed laser deposition
E	Electric field
P	Polarization vector
P <sub>UP</sub>	Upward polarization vector
P <sub>Down</sub>	Downward polarization vector
P <sub>S</sub>	Spontaneous polarization
P <sub>r</sub>	Remnant polarization
E <sub>C</sub>	Coercive field
MF	Multiferroic
BPV	Bulk photovoltaic
E <sub>DP</sub>	Depolarization field
PLZT	(Pb,La)(Zr,Ti)O <sub>3</sub>
VB	Valence band
CB	Conduction band
NHE	Normalized hydrogen electrode
RHE	Reverse hydrogen electrode
UV	Ultraviolet
XRD	X-ray diffraction
TEM	Transmission electron microscopy

XTEM	Cross-sectional transmission electron microscopy
HRTEM	High-resolution transmission electron microscopy
FFT	Fast Fourier Transform
SAED	Selected area diffraction pattern
RS	Raman spectroscopy
AFM	Atomic force microscopy
SEM	Scanning electron microscopy
PFM	Piezoresponse force microscopy
PL	Photoluminescence
RSM	Reciprocal space mapping
C-AFM	Conductive atomic force microscopy
KPFM	Kelvin probe force microscopy
UPS	Ultraviolet photoemission spectroscopy
$\alpha$	Absorption coefficient
EQE	External quantum efficiency
IPCE	Incident photon to current efficiency
CPD	Contact potential difference
RT	Room temperature
TF-BMO	Thin film BiMnO <sub>3</sub>
NS-BMO	Nanostructure BiMnO <sub>3</sub>
E <sub>CB</sub>	Conduction band edge energy
E <sub>VB</sub>	Valence band edge energy
V <sub>fb</sub>	Flat band potential
UV-Vis	Ultraviolet-Visible

## Appendix B: Résumé (in French)

### L'Introduction

En raison de l'augmentation de la population sur notre planète, le taux de consommation énergétique mondiale augmente également. Il devrait être plus que double ( $\sim 27,6$  TW) d'ici à 2050 et triple ( $\sim 43,0$  TW) à 2100 [1]. Actuellement, il y a environ 86% de l'énergie totale du monde qui est produite par la combustion des combustibles fossiles (par exemple, le pétrole, le charbon et le gaz naturel) [2]. Depuis que la production d'énergie à base des combustibles fossiles traditionnels attire l'attention en raison des problèmes environnementaux, un grand intérêt sera vers les sources d'énergie propres et durables. L'énergie solaire est considérée comme l'une des sources d'énergie renouvelable les plus fiables et les plus abondantes pour remplacer les combustibles fossiles, car la lumière du soleil est gratuite, abondante et largement accessible pour tous les pays et tous les personnes au monde entier. L'effet photovoltaïque (PV) [3,4] est utilisé pour convertir directement l'énergie solaire en électricité, mais la conversion effective de l'énergie solaire en électricité dépend entièrement du développement des technologies PV. Les produits PV dans le marché sont dominants par les cellules solaires en silicium (Si). Grâce aux progrès technologiques, un record de la performance sur l'efficacité de conversion d'énergie solaire en l'énergie électrique (PCE) d'environ 27% a été réalisé sous illumination solaire (AM 1.5G) dans des cellules solaires en Si monocristallin [5]. Cependant, les performances de ces cellules solaires basées sur les jonctions p-n sont toujours inférieures à leurs potentiels prévisibles et limitées par plusieurs inconvénients pratiques, tels que le coût élevé des matériaux par rapport à la génération d'énergie conventionnelle basée sur les combustibles fossiles et la complexité de traitement des matériaux.

La découverte de propriétés optoélectroniques sur les pérovskites- $ABO_3$  inorganiques a récemment attiré un grand intérêt dans les scientifiques grâce aux leurs nouvelles méthodes fondamentalement pour la conversion directe du rayonnement solaire en électricité. Spécifiquement, le mécanisme PV dans les pérovskites d'oxyde est complètement différent de celui qui se produit à l'interface de p-n dans les semi-conducteurs traditionnels [4]. Dans les dispositifs PV traditionnels, un champ électrique interne est développé à travers la jonction p-n qui sépare les porteurs de charge photogénérés. Cependant, des cristaux de pérovskite non-centrosymétriques permettent d'une polarisation ferroélectrique (FE) spontanée accompagnée d'un champ électrique interne (champ dépolarisant) dans la direction opposée qui est utilisée pour séparer les porteurs chargés. L'amplitude effective du champ électrique interne induit par la polarisation est supérieure d'environ un ordre de grandeur à celle d'une jonction p-n [6]. Généralement, la phototension dans les cellules PV à la jonction p-n est limitée par la bande interdite des semi-conducteurs (typiquement  $\leq 1$  V) [7]. Cependant, les pérovskites FE peuvent développer des phototensions plus larges que celui de la bande interdite, que l'on appelle la phototension anormale (APV). L'effet PV a été observé pour la première fois dans les cristaux FE  $BaTiO_3$  (BTO) en 1956 [8]. Ensuite, un APV aussi grand que 1000 V a été enregistré dans des cristaux de  $LiNbO_3$  (LNO) qui a été décrit par des changements d'indice de réfraction induits par la lumière sous illumination lumineuse [9,10]. Les couches minces épitaxiales  $BiFeO_3$  (BFO) avec des domaines FE périodiques ordonnés donnent une APV jusqu'à 16 V qui a été décrit par la théorie des parois de domaine (en anglais: DW) [11]. Selon cette théorie (DW), les porteurs de charge photogénérés sont séparés par le champ électrique élevé développant à travers chaque DW. La phototension totale est la somme des phototensions individuelles développée dans chaque DW. Toutefois, la théorie DW a été examinée lorsque les APVs allant jusqu'à 28 V ont été rapportés dans les films BFO avec un seul domaine FE [12]. En

effet, la compréhension des phénomènes physiques exacte qui soutient l'APV dans les FE fait l'objet d'un débat en cours. L'APV, qui n'apparaît jamais sauf dans FEs, a été observé pour la première fois sur des films PbS en 1946, s'élevant à 2 V [13]. Il a ensuite été détecté dans d'autres semi-conducteurs, y compris les couches polycristallines CdTe, ZnTe et InP [14,15], contredisant ainsi essentiellement la théorie de phototension à la bande interdite limitée dans les jonctions p-n conventionnelles. Le phénomène a été décrit en postulant l'existence de barrières aux joints de grains (en anglais : GBs) et en résultant de la concentration asymétrique des centres d'impureté aux interfaces. La superposition des grains orientés en série a été considérée comme étant à l'origine des APV.

Malgré la grande APV, les matériaux de pérovskite polaire présentent de faibles valeurs de la densité de photocourant ( $J_{SC}$ ), typiquement allant de  $nA/cm^2$  à  $\mu A/cm^2$  [11,12] en limitant ainsi leur PCE. En effet, les pérovskites d'oxyde sont typiquement des isolants induisant un transport de porteurs de charge très faible, et ensuit limitant leur  $J_{SC}$ . Par conséquent, les défis pour améliorer la PCE sont principalement liés à l'amélioration de  $J_{SC}$  dans ces pérovskites. Jusqu'à présent, seulement deux rapports ont rapporté l'amélioration de la  $J_{SC}$  qui est dans la gamme de  $mA/cm^2$ , améliorant ainsi la PCE. Premièrement, une valeur  $J_{SC}$  aussi grande que  $\sim 20,60 mA/cm^2$  a été rapportée dans des couches minces épitaxiales  $Bi_2FeCrO_6$  (BFCO) observée sans aucun APV ( $V_{OC} = 0,79 V$ ). Celui-ci conduit à un PCE jusqu'à 3,30% dans des dispositifs basés à la seule couche mince BFCO et 8,10% dans les dispositifs basés à trois couches minces BFCO [17]. L'ordre de cation Fe et Cr dans les couches minces BFCO peut permit d'accorder les bandes interdites de 2,4 à 1,4 eV offrant un grand potentiel pour fabriquer des dispositifs PV à base des multicouches FEs avec des bandes interdites graduées dans l'empilement perpendiculaire aux substrats. En résultat, les structures graduées, dite-on multi-absorbantes, peuvent absorber une large gamme du spectre

solaire conduisant à un photocourant élevé et donc à une PCE élevée jusqu'à 8,1%. Deuxièmement, une valeur de  $J_{SC}$  jusqu'à  $\sim 19.10 \text{ mA/cm}^2$  a été rapportée en utilisant un sondage nanométrique dans un seul cristal en masse BTO conduisant à une PCE de 4,80% sous une illumination solaire [18]. La phénoménologie de l'effet PV en masse (en anglais : BPV) a été utilisée pour illustrer la collection de porteurs non-thermalisés qui donne plus que l'efficacité quantique de l'unité, donc des PCE élevées.

L'application de matériaux à base de pérovskite a récemment s'étendu à la production d'hydrogène et d'oxygène photocatalytique. Contrairement à la production d'énergie électrique utilisant des dispositifs PV à semi-conducteurs, la méthode photocatalytique de la production de combustibles chimiques sous forme gazeuse est largement étudiée comme la méthode potentielle pour exploiter l'énergie solaire [19-21], plus facile à stocker que l'électricité [22,23]. Le procédé photocatalytique se produit dans des cellules photoélectrochimiques (PEC), où un matériau semi-conducteur photoactif forme une jonction au contact avec un électrolyte liquide. Les porteurs de charge photogénérés sont ensuite entraînés principalement par le champ électrique induisant par la jonction dans les électrolytes, ce qui active les réactions PEC [24,25]. La performance des cellules PEC dépend de plusieurs facteurs liés au matériau, dont les paramètres suivants: le coefficient d'absorption de la lumière élevée, la mobilité des porteurs de charge élevée, la stabilité chimique au contact des réactifs et l'adaptation appropriée des énergies de bord de bande avec le potentiel redox de l'eau réactions favorables d'évolution de l'hydrogène ( $H_2$ ) et de l'oxygène ( $O_2$ ) [26-29]. Les matériaux de pérovskite ont montré des propriétés photo-physiques uniques et offrent des avantages distincts par rapport à de nombreux autres systèmes de matériaux. En particulier, ils présentent l'alignement d'énergie de bande approprié avec le potentiel redox de l'eau dans les solutions aqueuses et leur bande interdite semi-conductrice correspond à la lumière visible, ce qui

est intéressé comme un candidat pour les réactions d'évolution de l'hydrogène et de l'oxygène. Par exemple, les composés de pérovskite titanate  $MTiO_3$  (où  $M = Sr, Ba, Ca, Mn, Co, Fe, Pb, Cd, Ni$ ) ont des bandes interdites élevées ( $> 3,5$  eV) et se présentent un bon comportement photocatalytique sous le rayonnement ultraviolet (UV) du spectre solaire [30-35]. Cependant, les titanates dopés aux co-catalyseurs (i.e., Rh ou Ru, ou  $NiO_x$ ) peuvent exploiter les visibles du rayonnement solaire représentant des bons exemples de catalyseurs pour les réactions d'évolution d'hydrogène. Par contre, sans besoin de co-catalyseurs, la plupart des pérovskites à base de ferrite ( $LaFeO_3, BiFeO_3, GaFeO_3$  et  $YFeO_3$ ) possèdent de faibles bandes interdites (au moins de 3 eV) qui correspondent à la large gamme de longueurs d'onde visible du spectre solaire et donc présentent des propriétés photophysiques supérieures à celles de l'hématite et d'autres composés d'oxyde du fer [36]. Parmi eux, les couches FEs BFO ayant une bande interdite de  $\sim 2,7$  eV peuvent agir comme la photoanode dans les cellules PEC montrant la  $J_{SC}$  jusqu'à  $\sim 5 \mu A/cm^2$  sous rayonnement solaire (AM 1.5G) [37-39]. Il est important de parler que le comportement FE exotique des couches BFO peut moduler la flexion de la bande aux interfaces d'entre la couche et l'électrolyte conduisant à un processus de séparation d'électron-trou plus rapide en améliorant ainsi la performance photocatalytique. De même, une amélioration de la performance entraînée par la ferroélectricité a également été observée dans les couches minces  $Bi_2FeCrO_6$  (BFCO), où 50% du site B de cation Fe dans un composé BFO est remplacé par cation Cr. Avec la  $J_{SC}$  jusqu'à  $\sim 1$  mA/cm<sup>2</sup> sous une illumination solaire, BFCO se montre une performance PEC plus élevée que celle des couches BFO [40]. Pour améliorer la performance PEC, il est nécessaire d'explorer ce type de matériaux stables dans les électrolytes (moins corrosifs), possédant de faibles bandes interdites (c'est-à-dire correspondant à la longueur d'onde visible du spectre solaire) et chevauchant les potentiels de réduction et d'oxydation de l'eau dans les électrolytes.

## La motivation et les objectifs

Ce projet est motivé par la demande urgente dans le domaine d'énergie propre et renouvelable pour le développement de nouveaux matériaux (ou systèmes de matériaux) utilisant dans les dispositifs PV avec une performance globale améliorée et viable. Pour la conversion efficace de l'énergie solaire en électricité, l'exploration, la découverte et l'optimisation des systèmes de matériaux sont requises. Les pérovskites polaires inorganiques utilisées comme des matériaux actifs dans les dispositifs PV ont déjà montré des caractéristiques uniques, par exemple, des phototensions les plus grandes que la bande interdite et l'accommodation de photocourant avec la direction de polarisation qui est différente sur des dispositifs PV conventionnels à base de jonction p-n. De plus, de nombreuses pérovskites inorganiques sont utilisées pour des matériaux multifonctionnels, et donc leurs applications peuvent être étendues à de nouveaux dispositifs tels que les transducteurs, les dispositifs à micro-ondes, les photodétecteurs, les diodes électroluminescentes (en anglais : LED), les mémoires d'ordinateur, etc. Dans cette thèse, nous comptons d'étudier les propriétés physiques et chimiques des oxydes de pérovskite inorganiques complexes comme la photoabsorbant actif pour la conversion d'énergie solaire. Pour réaliser ces objectifs, nous avons choisi les composés de pérovskite, comme  $\text{BiMnO}_3$  (BMO) et BFO où les phases cristallines sont stabilisées sur des substrats appropriés par l'ablation du laser pulsé (en anglais : PLD). Lorsque la taille des pérovskites à base de bismuth (BMO, BFO et BFCO) est réduite à l'échelle nanométrique, ils peuvent montrer des propriétés physiques intéressantes par rapport à leur homologue en masse. Parmi toutes les pérovskites FE, nous pouvons dire que le BFO est largement étudié pour les applications PV. Il montre une bonne polarisation FE résiduelle ( $\sim 55 \mu\text{C}/\text{cm}^2$ ) et une faible valeur de bande interdite (2,4 – 2,8 eV) par rapport aux valeurs de bande interdite des FEs traditionnels

(> 3,0 eV). Cependant, la PCE des cellules solaires à base des couches minces BFO est toujours faible (< 0.1%) sous illumination d'un soleil. En revanche, les couches minces BMO avec les épaisseurs de plusieurs centaines de nanomètres présentent des propriétés FE à la température ambiante et une bande interdite relativement faible (~ 1,2 eV). Des études antérieures ont exploré le rôle de la ferroélectricité dans l'effet PV des couches minces des multiphases BMO qui présentaient de faibles PCE ( $\approx 0,11\%$ ). Pour développer le potentiel global des composés BMO dans l'étude d'énergie solaire, il est nécessaire d'étudier leurs propriétés physiques et chimiques à l'échelle nanométrique et macroscopique. Il est également important d'évaluer leur potentiel d'intégration avec d'autres systèmes de matériaux afin d'améliorer l'efficacité de la conversion de l'énergie solaire. Sur cette base, nous avons exploité des propriétés FE et des joints de grains dans les matériaux à base de pérovskite améliorant les PCE dans la collecte de l'énergie solaire. Stimulé par le concept de cellules solaires des multijonctions, et en considérant la flexibilité de fabrication des multicouches minces (hétérostructures) croissant par PLD, nous choisissons des bicouches minces de pérovskite (BFO/BMO) pour étudier les améliorations potentielles de la PCE. Nous montrons une amélioration significative de la ferroélectricité dans les bicouches minces de pérovskite, ce qui améliore la PCE (Chapitre 3). De plus, nous démontrons que les phases cristallines mixtes (BMO et  $\text{BiMn}_2\text{O}_5$ ) présentant dans des couches minces uniques peuvent améliorer la PCE des dispositifs PV à l'état solide (Chapitre 4)

D'autre part, le comportement photocatalytique du composé BMO comme photoélectrodes dans une cellule PEC peut être une étude intéressante en raison de sa faible bande interdite chevauchant le potentiel d'oxydation et/ou de réduction de l'eau en production d'hydrogène gazeux. Comme il est bien connu que les modifications de morphologie des matériaux sont très sensibles aux réactions électrochimiques, il serait également intéressant d'étudier les propriétés

photocatalytiques en relation avec les modifications de morphologie des photoélectrodes BMO dans les cellules PEC. Dans la dernière partie de la thèse (chapitre 5), nous démontrons le concept de stabilisation des nanostructures cristallines BMO sur les substrats par PLD démontrant les performances PEC de ces nanostructures comme photoanodes dans les réactions d'évolution  $H_2$  et  $O_2$  dans les cellules PEC. En particulier, nous comparons les performances PEC des couches minces et nanostructures BMO croissant par PLD démontrant que les nanostructures BMO montent les performances PEC supérieures à celles des couches minces.

En bref, les objectifs de cette thèse sont décrits comme suit,

- (1) Synthèse des couches minces BMO (en forme de monophasés et multiphasés) et l'étude de leurs propriétés FE et PV;
- (2) Étude des propriétés électriques et optiques des joints de grains dans les couches minces BMO multiphasées;
- (3) Synthèse de bicouches minces BFO/BMO et l'étude de leurs propriétés FE et PV;
- (4) Étude du comportement photocatalytique des couches minces BMO et l'exploration des stratégies pour améliorer la performance photocatalytique des photoélectrodes à base de BMO dans l'étude d'énergie solaire.

## **Les résultats et les discussions**

### **Chapitre 3 Des propriétés PV renforcées dans les bicouches minces $BiFeO_3/Bi-Mn-O$**

Dans ce chapitre, nous cherchons à combiner la forte ferroélectricité de BFO avec la faible bande interdite de BMO dans une hétérostructure d'un dispositif unique pour améliorer la PCE. Nous avons combiné BFO et BMO, en fabriquant les bicouches minces BFO/BMO sandwichées les électrodes en haut de l'oxyde d'indium dopé au Sn (ITO) et les substrats conductifs de  $SrTiO_3$

dopés Nb (0.5%) (NSTO) en bas. Les schémas du dispositif et les caractérisations structurales sont représentés sur la figure 1. Le scan  $\theta$ - $2\theta$  de la diffraction des rayons X (DRX, en anglais : XRD) montre la structure pseudo-cubique (pc) préférentielle de l'orientation (111) des phases BMO et l'orientation (111) des phases BFO suivant de la direction (111) du substrat cubique NSTO (figure 1b). Des mesures de  $\Phi$ -scan dans la figure 1c représentent trois fois de la symétrie sur BMO, BFO et NSTO, ce qui démontre la nature épitaxiale des couches minces. Une image transversale de la microscopie électronique en transmission (MET, en anglais: TEM) à la résolution de 10 nm est montrée sur la figure 1e qui représente les interfaces pointues à l'interface BFO/BMO.

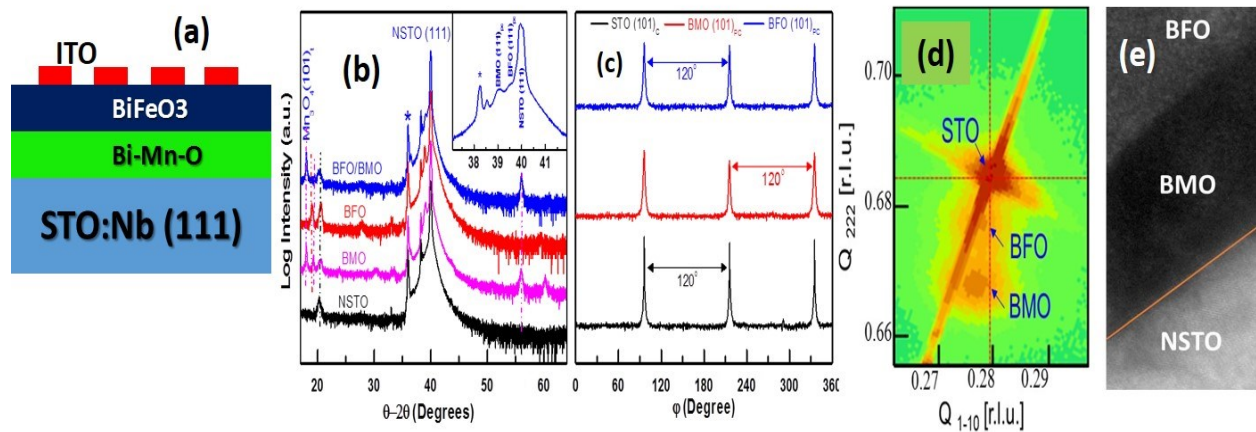


Figure 1 (a) Schéma de l'architecture du dispositif. Un biais externe a été appliqué entre les substrats en haut ITO et NSTO en bas pour les mesures électriques. (b) Les scans DRX- $\theta$  $2\theta$  sur des substrats NSTO, des couches minces croissantes BMO, BFO et BFO, respectivement. Les couches minces respectives crû sur les substrats NSTO orientés (111) montrent des réflexions (1/2, 1/2, 1/2) de BFO, BMO et de petits pourcentages d'orientation (101)<sub>t</sub> des phases Mn<sub>3</sub>O<sub>4</sub>. L'encart montre clairement que l'orientation (111)<sub>pc</sub> des phases BMO et BFO. Le symbole «\*» indique la

contamination par le tungstène de la source du tube à rayons X. (c) Les mesures de  $\Phi$ -scan montrent une symétrie à trois fois de BMO, BFO et NSTO, respectivement, démontrant la nature épitaxiale des couches. (d) La cartographie de l'espace réciproque (CER, en anglais : RSM) autour des réflexions NSTO (312) montre que les deux pointes liées à la coexistence de BMO et BFO. (e) L'image transversale de la MET prise à la résolution de 10 nm montre des interfaces pointues à l'interface BFO/BMO.

Les diagrammes dans la figure 2a montrent une hystérésis de polarisation macroscopique sur la hétérostructure des bicouches déposées. La polarisation restante de hétérostructure des bicouches BFO/BMO est beaucoup plus élevée ( $\sim 98 \mu\text{C}/\text{cm}^2$ ) que celle des couches minces individuelles BMO ( $\sim 1,33 \mu\text{C}/\text{cm}^2$ ). En voyant clairement, la pente de la courbe de polarisation-tension est presque nulle (avec une erreur absolue estimée à environ 20 à cause de courants fuites) pour la hétérostructure des bicouches (figure 1a) lors que nous estimons une valeur de  $\sim 50$  pour la couche BMO uniquement. Sur cette base, nous concluons que la tension diminue à travers le composant BFO est suffisante pour inverser la polarisation, en impliquant (de la condition limite électrostatique à l'interface) que sa permittivité est suffisamment faible. Par conséquent, nous avons conclu que les grandes valeurs de polarisation résiduelle proviennent principalement de la couche BFO.

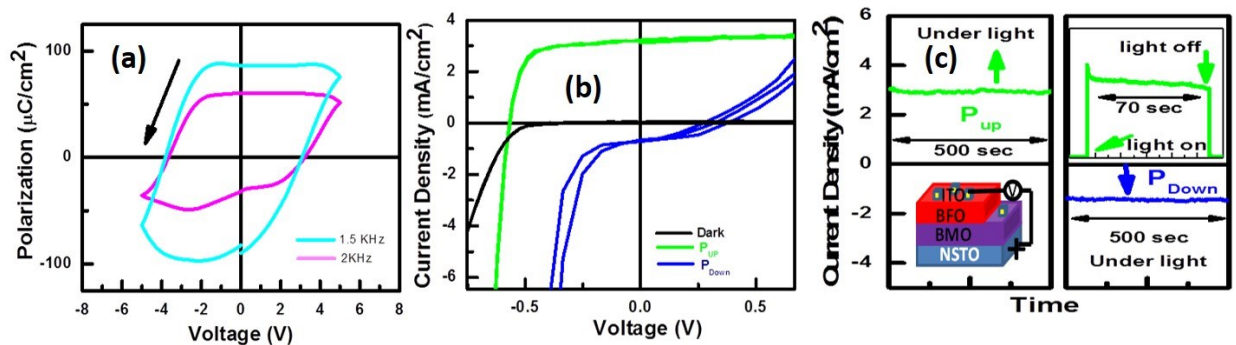


Figure 2 (a) La courbe de tension versus polarisation enregistrée sur hétérostructure aux deux fréquences différentes montre des polarisations FE restantes élevées. (b) Des courbes caractéristiques de  $J$ - $V$  sur hétérostructure avec un pôle électrique positif et négatif démontrant l'effet PV. (c) La densité de photocourant variée avec le temps présente une génération stable de photocourant. L'encart en gauche-bas montre la géométrie de la structure testée. L'encart en droit-haut montre la dynamique de photocourant en circuit court enregistrée pendant 70 s sous la lumière ON (OFF). Les encarts en gauches-haut et en droites-bas montrent une bonne stabilité de la génération de photocourant pendant 500 secondes.

Les performances PV ont été évaluées en enregistrant la courbe de la densité de courant ( $J$ ) avec la tension ( $V$ ) sur des échantillons sous condition avec/sans la lumière (figure 2b). La densité de photocourant et la tension en circuit ouvert enregistrées sont respectivement de  $\sim 3,5$  mA/cm<sup>2</sup> et  $\sim 0,56$  V. La PCE calculée ( $\eta$ ) est de  $\sim 1,43\%$  avec un facteur de remplissage élevé (FF) de  $\sim 0,72$ . Le FF observé est légèrement supérieur à celui précédent dans les dispositifs PV à base d'oxyde FE ( $\sim 0,71$  dans les couches BMO). En comparaison, les paramètres PV sur des hétérostructures ITO/BFO/NSTO, ITO/BMO/NSTO et ITO/BFO/BMO/NSTO sont résumés dans le tableau 1 ci-dessous. La PCE calculée des couches minces BMO est  $\sim 6 \times 10^{-4}\%$  qui est 14-fois moins que les hétérostructures des bicouches. Pour évaluer la stabilité de photocourant en circuit court, nous avons observé l'évolution avec le temps montrant la figure 2c.

Tableau 1. Comparaison des propriétés PV des couches BFO, BMO et bicouches BFO/BMO.

Polarisation vers le haut ( $P_{UP}$ )		Polarisation vers le bas ( $P_{DOWN}$ )	
$J_{sc}$ [cm <sup>-2</sup> ]	$V_{oc}$ [V]	$J_{sc}$ [cm <sup>-2</sup> ]	$V_{oc}$ [V]

ITO/BFO/NSTO	~ 0.032 mA	~0.42 V	~0.011 mA	~0.55 V
ITO/BMO/NSTO[189]	~0.15 mA	~0.53 V	~0.23 mA	~0.56 V
ITO/BFO/BMO/NSTO	~3.50 mA	~0.56 V	~0.70 mA	~0.35 V

#### **Chapitre 4 Phases cristallines mixtes dans des couches minces multiferroïques pour une performance photovoltaïque améliorée**

Dans ce chapitre, nous démontrons le concept d'un dispositif PV basé sur matériau de composite comprenant deux types de phases cristallines différentes:  $\text{BiMnO}_3$  (BMO) et  $\text{BiMn}_2\text{O}_5$ . La première est la phase ferromagnétique [63] à la température inférieure à  $\sim 105$  K et FE [86] avec une bande interdite expérimentale de  $\sim 1,20$  eV mesurée par l'ellipsométrie à la température ambiante lors que le  $\text{BiMn}_2\text{O}_5$  est un semiconducteur avec une bande interdite théorique de  $\sim 1,23$  eV [218] prédite par la théorie fonctionnelle de la densité. Nous montrons que l'incorporation de grains FE dans des matériaux semiconducteurs non-FE (matrice de FE et semiconducteur) dans un même dispositif peut augmenter la densité de courant en circuit court ( $J_{\text{SC}} = \sim 7,03$  mA/cm<sup>2</sup>) ayant une APV ( $V_{\text{OC}} = \sim 1,48$  V) en conduisant à une PCE maximale de  $\sim 4,20\%$  dans un dispositif PV à base de la couche mince FE unique. La phototension enregistrée dépasse de la bande interdite des phases individuelles dans les couches. Nous avons constaté que les porteurs photoexcités sont accumulés principalement aux joints de grains (en anglais : GBs) plutôt qu'à l'intérieur des grains. Les résultats sont décrits dans l'armature des potentiels de barrière des GBs.

Les schémas du dispositif et les connexions de circuit pour toutes les mesures électriques macroscopiques sont illustrés sur la figure 3a. On a fait croître des hétérostructures des composites Bi-Mn-O sur des substrats monocristallins NSTO (100) par PLD. L'épaisseur de la couche est

d'environ 110 nm mesurée par la MET transversale. Comme mentionné ci-dessus, les couches des composites comprennent des phases BMO et  $\text{BiMn}_2\text{O}_5$ , en donnant des GBs et des interfaces observées dans les images de MET (figure 3b). Les structures cristallines de BMO et  $\text{BiMn}_2\text{O}_5$  sont trouvées d'être monocliniques et orthorhombiques.

Pour évaluer l'effet PV, nous avons enregistré la densité de photocourant en circuit court en fonction de la tension DC externe appliquée avec le sombre et l'éclairage sous un soleil (AM 1.5G). Au cours de ces études, 5 échantillons ont été sélectionnés au hasard pour mesurer les réponses PV d'un ensemble de 10 échantillons. Les échantillons ont présenté respectivement des rendements de  $\sim 4,20\%$ ,  $\sim 4,0\%$ ,  $\sim 3,90\%$ ,  $\sim 3,8\%$  et  $\sim 3,96\%$ . Le dispositif PV avec le meilleur rendement ( $\sim 4,20\%$ ) montre un FF de  $\sim 0,58$  (figure 3c). Nous avons discuté dans ce texte les caractéristiques de l'échantillon présentant une PEC d'environ  $3,96\%$  car qu'il est le plus proche du rendement moyenne. La variation des rendements sur des différents échantillons peut provenir de plusieurs facteurs, y compris l'uniformité des couches, la taille de l'électrode en haut, l'uniformité de la lumière incidente, et ainsi la variation des mesures de courant et de tension sur chaque échantillon. Avant la mesure des caractéristiques des courbes  $J$ - $V$ , la polarisation des échantillons primitifs a été changée par appliquer des séquences d'impulsions de tension bipolaires avec une magnitude de 6 V et une durée de 0,1 s pour chaque un, tel que la polarisation a resté l'orientation soit vers STO (ci-après  $P_{\text{down}}$ ) ou vers ITO ( $P_{\text{up}}$ ). Le but de la polarisation est d'observer l'effet FE macroscopique sur l'effet PV. Le cas échéant, les courbes  $J$ - $V$  des échantillons polarisés ont ensuite été enregistrées sous éclairage, comme indiqué sur la figure 3d. Le  $J_{\text{SC}}$  et le  $V_{\text{OC}}$  de l'un des dispositifs étaient d'environ  $7,03 \text{ mA/cm}^2$  et 1,36 V, respectivement. La PCE calculée est d'environ  $3,96\%$  avec un FF de 0,42. Cependant, tous les deux  $J_{\text{SC}}$  et  $V_{\text{OC}}$  ne variaient que légèrement (presque négligeable) lorsque le dispositif était polarisé avec une tension de polarisation inverse (polarisation dans l'état

$P_{\text{down}}$ ), en représentant par la courbe bleue dans la figure 3d. Aucune hystérésis n'a été observée lors des courbes  $I$ - $V$  suggérant l'absence d'effet de l'injection de charge au cours du temps pendant les mesures.

Pour observer les porteurs de charge photoexcités et leur efficacité de séparation, nous avons effectué des mesures d'efficacité quantique externe (EQE) (figure 3e). Une EQE maximale ayant  $\sim 51\%$  est observée dans la région ultraviolette du spectre solaire tandis que  $\sim 15\%$  d'EQE est obtenue dans la région visible. La densité de photocourant en circuit court ( $J_{\text{SC}}$ ) à partir d'EQE a été calculée, en ayant  $\sim 7,08 \text{ mA/cm}^2$  qui est approximativement égale aux valeurs obtenues des courbes  $I$ - $V$  ( $\sim 7,03 \text{ mA/cm}^2$ ). Des mesures d'ellipsométrie optique ont été effectuées pour étudier les propriétés d'absorption des couches. Les coefficients d'absorption ( $\alpha$ ) estimés pour les différentes couches sont présentés en fonction de l'énergie des photons dans la figure 3f. Comme observé dans la figure 3f, les pics apparaissent dans la région de 1,60 à 1,75 eV pour toutes les couches. Des pics relatifs ont ainsi été attribués à des charges d'excitations de transfert entre des états mixtes O  $2p$  et Mn  $3d$ . Les courbes  $(\alpha E)^2$  correspondantes par rapport à  $E$  indiquent une bande interdite directe de tous les couches (BMO =  $\sim 1,27 \pm 0,05 \text{ eV}$ ,  $\text{BiMn}_2\text{O}_5$  =  $\sim 1,24 \pm 0,05 \text{ eV}$ , BMO- $\text{BiMn}_2\text{O}_5$  =  $\sim 1,25 \pm 0,05 \text{ eV}$ ). Les résultats sont proches de la bande estimée de BMO qui se situent d'entre  $\sim 1,15$  et  $1,20 \text{ eV}$  [40,189,225,218]. Malgré que les valeurs soient très proches de leurs bandes interdites, les couches des composites absorbent effectivement les longueurs d'onde lumineuses supérieures à 850 nm, ce qui contribue également à améliorer leurs propriétés PV. La contribution du substrat NSTO à la performance PV mesurée est exclue, puisque les photons incidents d'énergie  $E \geq 3,2 \text{ eV}$  (la bande interdite de NSTO) sont principalement absorbés dans les couches. Les résultats montrent clairement l'absorption plus élevée dans les couches avec deux phases coexistantes. Ceci est cohérent avec les mesures de la courbe  $J$ - $V$ , qui montrent un  $J_{\text{SC}}$  plus

élevé dans le composite (figure 3d) par rapport aux couches avec des phases individuelles. Pour étudier l'effet FE sur la génération de photocharge à l'échelle nanométrique, nous avons mené des expériences de la microscopie à force de sonde Kelvin (en anglais : KPFM) pour observer le profil de charge de surface dans des conditions d'obscurité et d'illumination. La zone spécifique de l'échantillon a été polarisée successivement en appliquant une impulsion de tension positive et négative et a mesuré le profil de charge de surface par KPFM après chaque polarisation. Les résultats n'ont montré aucun effet de la ferroélectricité sur la génération de porteurs de photocharge. Sur la base de ces résultats, nous suggérons que les interfaces de grains dans la couche de nanocomposite jouent un rôle crucial dans l'amélioration de l'absorption optique qui est décrite ci-dessous.

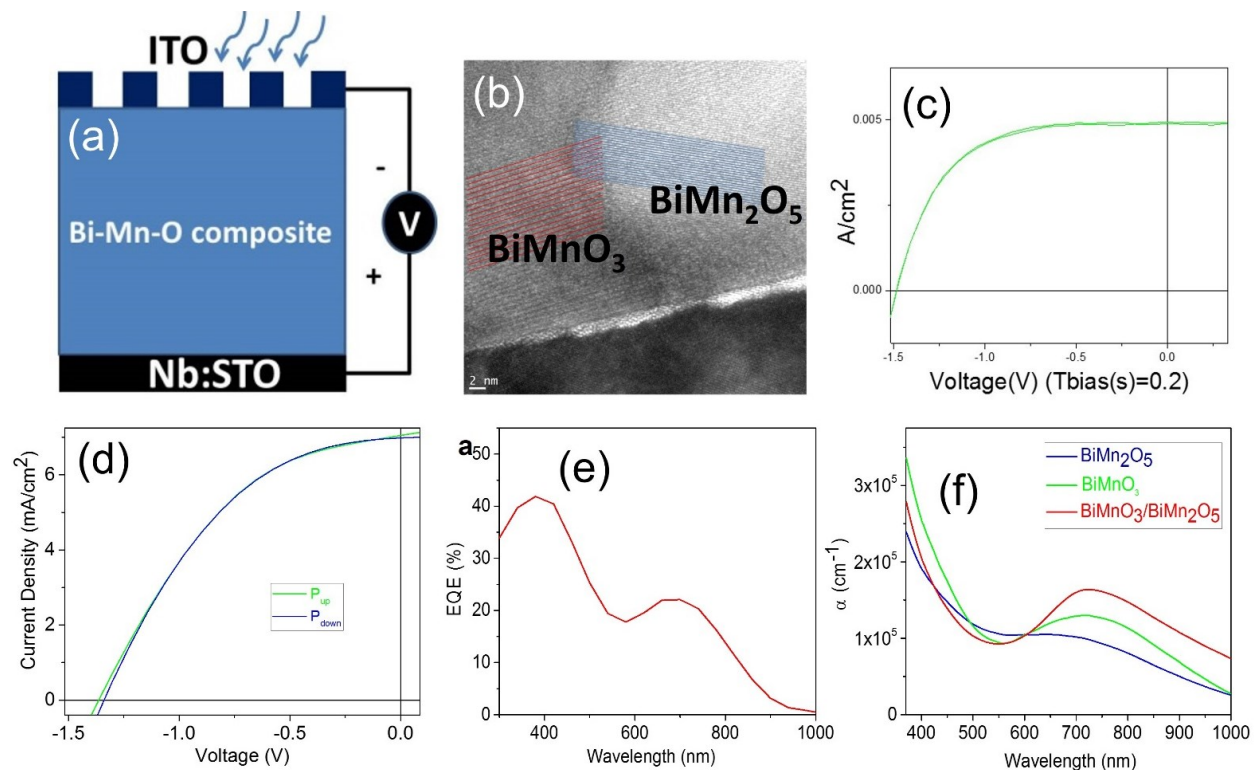


Figure 3 (a) Schémas des connexions des dispositifs pour les mesures électriques. (b) Des images transversales de MET montrant deux phases différentes. (c) Des courbes  $J$ - $V$  enregistrées dans le meilleur échantillon sous l'éclairage après commutation avec l'impulsion de tension bipolaire. (d) La courbe  $J$ - $V$  enregistrée dans l'échantillon présentant une efficacité proche de l'efficacité moyenne sur tous les échantillons testés sous illumination pour différentes orientations de polarisation. (e) Les mesures d'EQE sur un seul échantillon révèlent des efficacités supérieures à 51% sous la lumière UV. (f) Les spectres d'absorption optique des couches comprenant respectivement les phases BMO-BiMn<sub>2</sub>O<sub>5</sub>, BMO et BiMn<sub>2</sub>O<sub>5</sub>.

Pour décrire l'effet des interfaces des grains, nous étudions le comportement PV des GBs et des grains en masse à l'échelle nanométrique en utilisant la microscopie à force atomique conductrice (en anglais : C-AFM). Les propriétés de génération de photocourant des GBs ont été étudiées en utilisant C-AFM et sont illustrés sur la figure 4. Les figures 4a et b montrent la topographie et l'image de photocourant correspondantes enregistrées simultanément. Pendant l'acquisition, l'illumination de l'échantillon (fourni par une source laser avec la longueur d'onde de ~632 nm) au-dessous de la pointe d'AFM était initialement OFF (en haut de l'image) puis ON (la bande au milieu) et OFF (en bas). On peut voir sur le profil présent (figure 4c), la génération de courant est négligeable sous sans lumière, et il existe un courant en circuit court important mesuré pendant l'illumination. Cela démontre clairement l'apparition de l'effet PV dans nos couches, et exclut également les artefacts topographiques [238]. Dans une mesure de grossissement plus élevée réalisée dans une autre zone sous un éclairage laser constant (Fig. 4d, e), nous observons que le contraste n'est pas uniformément réparti sur la surface de la couche, mais plutôt sur les emplacements correspondants aux interfaces des GBs. En GBs, l'intensité de courant atteint des valeurs de 25 pA, un ordre de grandeur plus élevé que dans le grain en masse, en illustrant dans

un profil de balayage linéaire traversant les GBs (figure 4e, f). D'autres travaux montrent que l'intensité de photocourant augmente en valeur absolue avec l'intensité lumineuse, atteignant environ de 1000 pA (figure 4h, i), quand en restant confiné au voisinage des GBs. Ils démontrent clairement l'effet des GBs sur l'effet PV. Pour vérifier l'effet d'un éventuel artefact topographique, le résultat est confirmé par des mesures de photocourant à haute résolution, comme montré dans la figure 4j-l. L'amplitude de photocourant (qui atteint ~600 pA dans cette zone) est la plus élevée en GBs et n'est pas corrélée avec la topographie de surface ni avec la pente locale. Cela peut être clairement déduit en comparant les régions encerclées. La boucle verte marque un GB "lisse", où le photocourant est au haut de partout dans le GB, alors que dans la boucle rouge, indiquant un GB raide, le courant est élevé seulement qu'où les grains adjacents sont en contact direct. Ces observations montrent que les pics de courant ne dépendent pas de la géométrie du contact avec la pointe-l'échantillon et nous excluons donc le rôle possible des artefacts topographiques dans nos mesures.

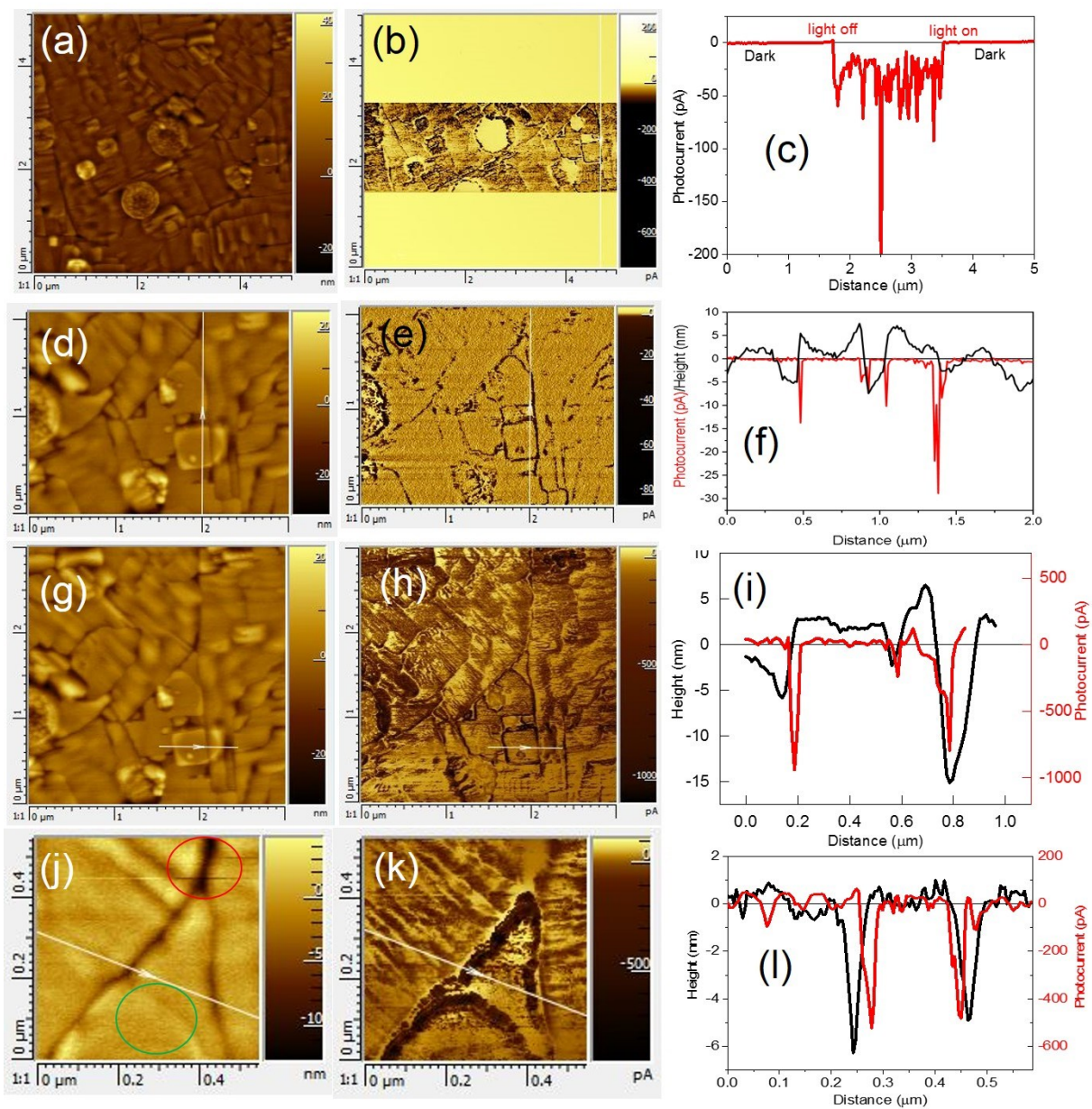


Figure 4 Des mesures de photocourant de surface par C-AFM effectuées sur des échantillons croissants: (a) L'image topographique. (b) L'image actuelle enregistrée quand en changeant sous l'éclairage on/off au biais 0 V. (c) Le profil de ligne actuel à travers l'image. L'image topographique (d) et l'image actuelle sous illumination au biais 0 V (e) enregistrée dans une autre zone à la surface de l'échantillon, (f) des profils de lignes de courant topographique et

correspondant montrant un courant élevé en GBs. Les mêmes mesures effectuées lors de l'illumination de la surface de l'échantillon à haute intensité. (g) L'image topographique, (h) l'image de courant en circuit court. (i) Comparaison des profils de ligne extraits de courant en circuit court et des images topographiques. Des images de topographie (j) et de courant en circuit court, (k) à plus haute résolution sous éclairage, et (l) comparaison de profils de lignes extraits du courant en circuit court et d'images topographiques. Tailles de balayage:  $(5 \times 5) \mu\text{m}^2$  à a, b;  $(3 \times 2) \mu\text{m}^2$  à d, e;  $(3 \times 3) \mu\text{m}^2$  à g et h; et  $(0.54 \times 0.54) \mu\text{m}^2$  à j et k.

## **Chapitre 5 Propriétés photoélectrochimiques des couches minces et des nanostructures de $\text{BiMnO}_3$**

Dans ce chapitre, nous démontrons la croissance contrôlée de nanostructures BMO (NS-BMO) sur des substrats NSTO (111) en utilisant PLD par des nanostencils [257-259] (des masques d'ombre avec un réseau périodique de caractéristiques circulaires à l'échelle nanométrique). Le substrat NSTO conductrice a été choisi pour promouvoir la croissance épitaxiale de BMO favorisée par la petite discordance des réseaux cristallins, et en fait sa conductivité est un bon candidat comme l'électrode en bas. Nous rapportons également les propriétés optiques et PEC sur NS-BMO obtenu en comparaison avec les couches minces BMO (en anglais : TF-BMO) croissantes sur des substrats NSTO par PLD. Nous montrons que les effets de taille (i.e., des couches minces versus des nanostructures) permettent de démontrer les photosélectrodes BMO obtenant une position de la bande variable en faveur de l'évolution de l'hydrogène et de l'oxygène, respectivement, en fonction de l'alignement de la bande. Nous avons constaté que les deux photoélectrodes conviennent à l'évolution d'oxygène.

Des hétérostructures de composites en couches minces BMO ont été croit sur des substrats NSTO (111) monocristallins par PLD. L'épaisseur des couches était d'environ  $60 \pm 10$  nm estimé par la réflectivité aux rayons X (en anglais : XRR). La nanostructure BMO a été croit sur des substrats NSTO (111) en utilisant la même cible et la même chambre de PLD que pour les couches minces BMO, mais les paramètres croissants de la PLD étaient différents. Un masque à pochoir avec des ouvertures à l'échelle nanométrique acquises par Aqua Marijn Filtration (aux Pays-Bas) a été monté mécaniquement sur le substrat pour croître la nanostructure configurée.

La figure 5 montre un diagramme typique des scans DRX- $\theta 2\theta$  des couches minces obtenues. Le modèle révèle que la phase cristalline BMO avec une structure monoclinique a une orientation préférentielle avec la direction pseudo-cubique  $(111)_{pc}$ . L'analyse de  $\Phi$ -scan autour de la réflexion NSTO (101) suggère une croissance épitaxiale des couches avec une symétrie triplée (voir figure 5b.). La figure 5c montre des images de MEB sur des échantillons NS-BMO. Les structures cristallines sont confirmées par des scans DRX- $\theta 2\theta$  (figure 5d) qui montrent des phases cristallines BMO fortement orientées à  $(111)_{pc}$ . Les résultats indiquent les mêmes structures cristallines que celles obtenues dans les couches.

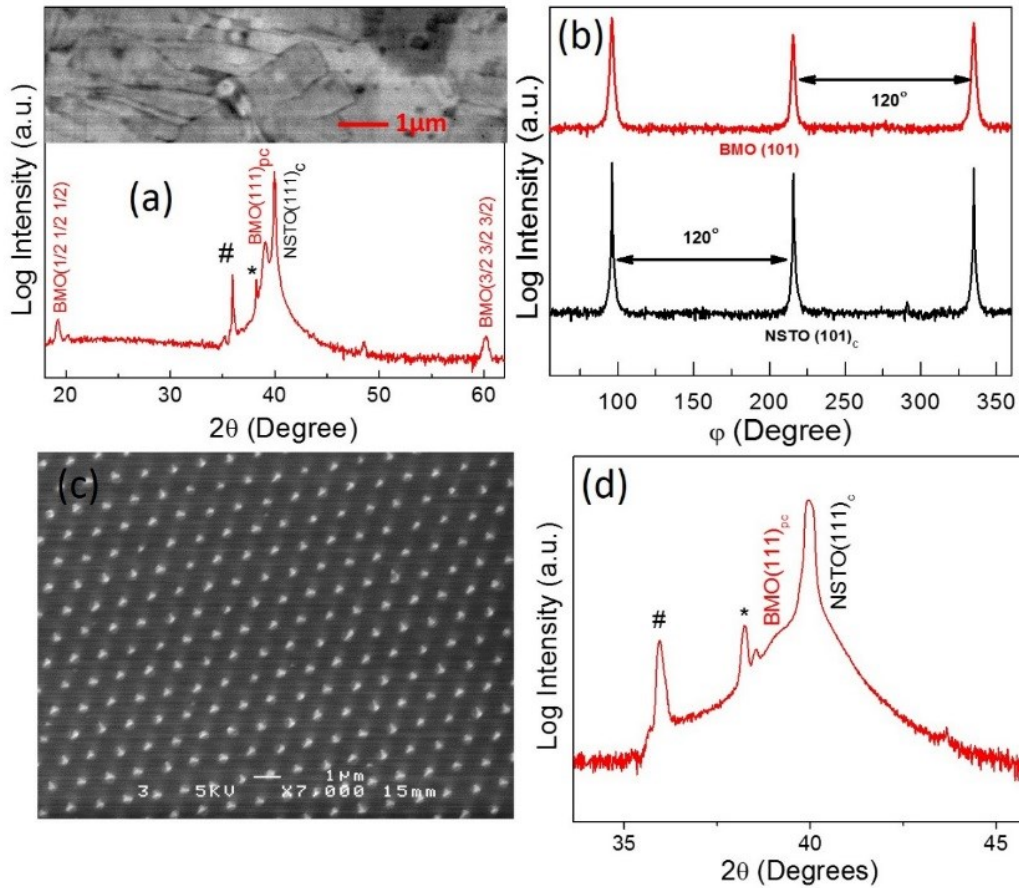


Figure 5 (a) Des scans DRX- $\theta$ 2 $\theta$  de couches BMO croissantes sur des substrats NSTO (111). Le symbole "#" indique une contamination par le tungstène des sources du tube à rayons X. L'encart montre l'image MEB des couches BMO déposées. (b) Des mesures de balayage montrent une symétrie à trois fois de BMO, démontrant la nature épitaxiale des couches (c) L'image MEB des nanostructures BMO croissantes sur NSTO (111)<sub>c</sub> orienté en utilisant un masque stencil. (d) Des scans DRX- $\theta$ 2 $\theta$  montrent l'orientation de (111)<sub>pc</sub> des nanostructures BMO.

Pour une surveillance simultanée de courant avec/sans la lumière sur nos dispositifs, les propriétés PEC de TF-BMO et de NS-BMO ont été étudiées par le voltamètre à balayage linéaire (en anglais : LSV) sous illumination de lumière discontinue (voir figure 6). Les figures 6a et b montrent la

densité de photocourant ( $J_{sc}$ ) en fonction du potentiel appliqué enregistré respectivement dans TF-BMO et NS-BMO. Le potentiel d'apparition est déterminé comme étant  $\sim -0,6$  V vs. Ag/AgCl ( $\sim -0,02$  V vs RHE, l'électrode d'hydrogène inverse) pour les couches alors qu'un déplacement vers des potentiels plus négatifs  $\sim -0,9$  V vs. Ag/AgCl ( $\sim -0,30$  V vs. RHE) est observée dans les nanostructures BMO. En comparaison, le déplacement des potentiels initiaux du photocourant anodique de  $-0,209$  V vs. Ag/AgCl à  $-0,366$  V vs. Ag/AgCl est décrit par l'effet du dopage Ti sur le photocourant amélioré dans les couches BFO [260]. Dans TF-BMO, le  $J_{sc}$  le plus élevé de  $\sim 10$   $\mu\text{A}/\text{cm}^2$  à  $0,4$  V par rapport à Ag/AgCl ( $0,98$  V par rapport à RHE) a été enregistré à une illumination solaire ( $100$   $\text{mW}/\text{cm}^2$ ). Le  $J_{sc}$  a augmenté jusqu'à environ  $40$   $\mu\text{A}/\text{cm}^2$  à  $0,4$  V par rapport à Ag/AgCl lorsque les mêmes couches ont été exposés à une illumination aux deux soleils. Dans les couches épitaxiales BFO avec l'épaisseur de  $223$  nm, les  $J_{sc}$  les plus élevés de  $\sim 10$   $\mu\text{A}/\text{cm}^2$  ont été rapportés sous illumination avec des intensités de  $250$   $\text{mW}/\text{cm}^2$  ( $2,5$  soleils) [37]. Dans notre cas, la couche BMO avec l'épaisseur de  $60$  nm donne les mêmes valeurs de  $J_{sc}$  que BFO sous un soleil et augmente jusqu'à 4 fois sous deux soleils. La tension en circuit ouvert observée ( $V_{oc} = \sim 0,38$  V) augmente du potentiel positif au potentiel négatif sous illumination (voir l'encart de la figure 6a) qui sont les caractéristiques typiques des photoélectrodes semiconductrices de type n [267]. En illustrant dans la figure 6b, le plus élevé de  $J_{sc}$  d'environ  $\sim 900$   $\mu\text{A}/\text{cm}^2$  à  $0,8$  V par rapport à Ag/AgCl ( $1,38$  V par rapport à RHE) a été enregistré sous un soleil dans NS-BMO. De même, la densité de photocourant la plus élevée de  $0,4$   $\text{mA}/\text{cm}^2$  et de  $2,7$   $\text{mA}/\text{cm}^2$  à  $1,4$  V par rapport à RHE a été rapportée dans les couches  $\alpha\text{-Fe}_2\text{O}_3$  dopés au Ti et les couches  $\text{WO}_3$  respectivement [268,269]. La densité de photocourant des nanostructures BMO est assez faible ( $\sim 12$   $\mu\text{A}/\text{cm}^2$ ) en potentiel négatif et augmente de manière significative dans les potentiels positifs ( $\sim 900$   $\mu\text{A}/\text{cm}^2$ ). De même que pour les couches BMO, la phototension des nanostructures BMO

augmente vers un potentiel négatif ( $V_{OC} = \sim 0,32$  V). Ceci suggère que les nanostructures croissantes se comportent comme des matériaux de photoanodes de type n. Des réponses de PEC négligeables ont été observées à partir de substrats NSTO «nuls» (couleur verte sur la figure 6a), ce qui implique que les propriétés de PEC observées proviennent principalement de couches.

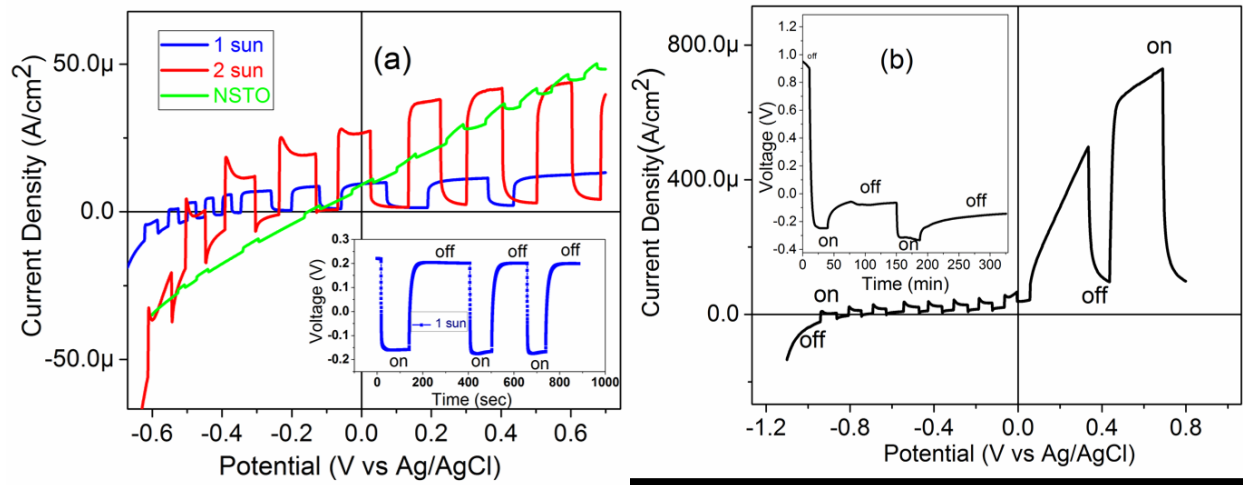


Figure 6 (a) Variations de la densité de courant avec la tension appliquée (vs Ag / AgCl) dans 1 M de  $\text{Na}_2\text{SO}_4$  à pH 6,8 sous un et deux soleils des couches BMO. (b) Variations de la densité de courant avec la tension appliquée (vs Ag / AgCl) dans 1 M de  $\text{Na}_2\text{SO}_4$  à pH 6,8 sous un soleil de la lumière hachée des nanostructures BMO. L'encart montre la réponse de la tension en circuit ouvert sous sans lumière et un soleil de la lumière.

Les niveaux d'énergie de BMO sont alignés sur les niveaux d'oxydoréduction (en anglais : redox) montrant dans les figures 7c et d. Pour obtenir une image complète de l'alignement de la bande de BMO, les largeurs d'énergie entre le potentiel de la bande plate et le potentiel de la bande de conduction (CB) sont estimées à -0.10 eV pour les couches minces et -0.13 eV pour les nanostructures vs. NHE (l'électrode à hydrogène normalisée). Pour calculer ces largeurs d'énergie, il faut connaître l'un des niveaux d'énergie de la bande valence (VB) ou de CB des TF-BMO et des

NS-BMO. Dans notre cas, nous avons estimé la position de la CB de TF-BMO et de NS-BMO en utilisant l'équation suivante:  $E_{CB} = V_{fb} + K_B T \ln (N_D/N_{CB})$  [276], où  $E_{CB}$  et  $N_{CB}$  sont le bord d'énergie et la densité effective d'états en CB, respectivement. La bande interdite optique des échantillons de BMO a été déterminée à partir des spectres de transmittance de la mesure de spectroscopie UV-Vis, estimée à environ 1,2 eV, valeurs similaires observées précédemment dans TF-BMO. Selon l'alignement complet de la bande par rapport aux réactions d'évolution de l'oxygène et de l'hydrogène, le TF-BMO et le NS-BMO conviennent tous deux à la réaction d'évolution de l'O<sub>2</sub> (figures 7c, d).

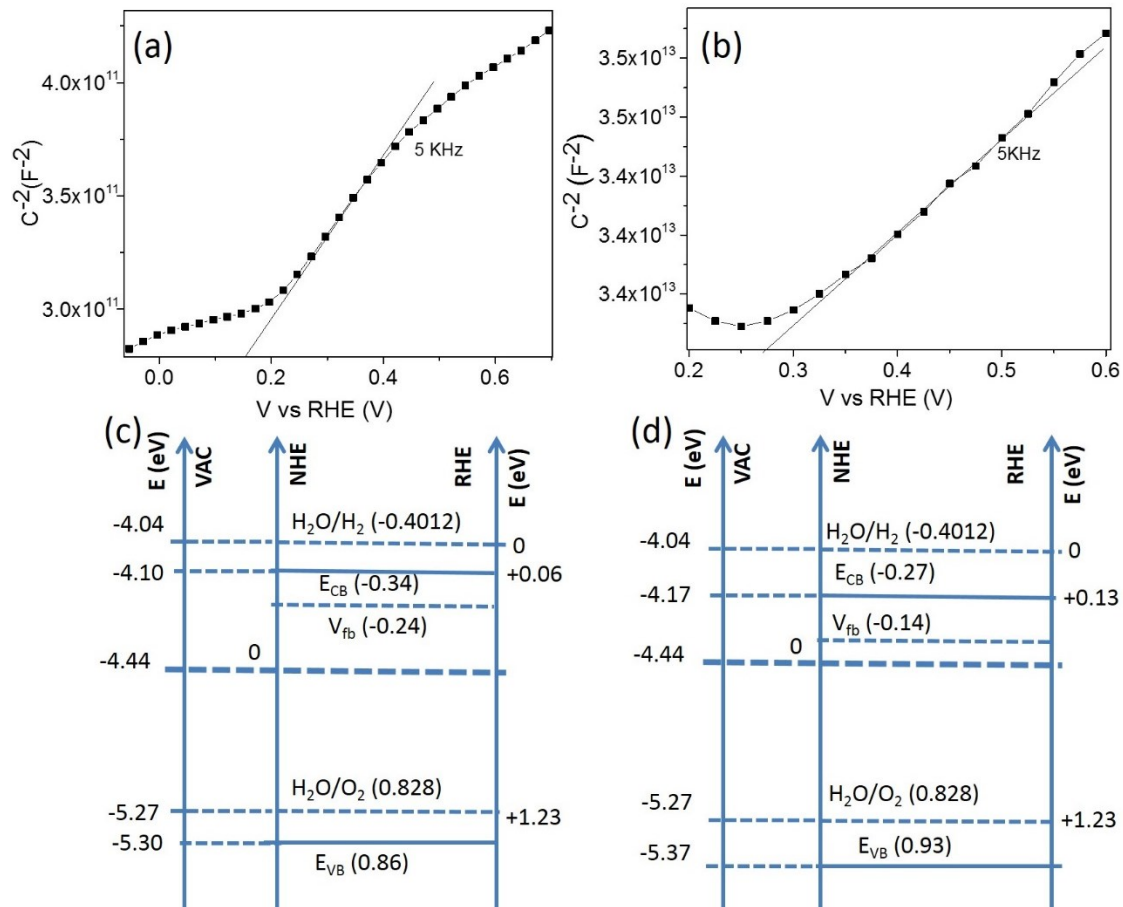


Figure 7 L'analyse de Mott-Schottky ( $1/C^2$  par rapport au potentiel appliqué, où 'C' est la capacité) des photoelectrodes de BMO en couches minces (a) et nanostructures (b). L'intersection de la ligne pointillée ( $1/C^2 = 0$ ) peut être utilisée pour déterminer le  $V_{fb}$  des photoelectrodes BMO. Diagramme du niveau d'énergie calculé basé sur les résultats de Mott-Schottky montrant les niveaux d'énergie de  $V_{fb}$ , le bord de VB et de CB des photoelectrodes des couches BMO (c) et nanostructures BMO (d), respectivement.

## Les conclusions et les perspectives

Nous concluons que les matériaux de pérovskite multiferroïques sont des candidats comme éléments actifs dans les dispositifs PV pour la collecte de l'énergie solaire. Les interstices de bande (1,1 – 2,7 eV) de tels matériaux peuvent efficacement récolter la large gamme de partie visible du spectre solaire sur la surface de la terre. Dans ce travail, nous avons réussi à améliorer la PCE en développant les matériaux présentés au chapitre 3. Nous avons développé avec succès des bicouches minces épitaxiales BFO/Bi-Mn-O sur des substrats NSTO(111) monocristallin par PLD, employant une contrainte de compression dans les couches en raison d'une discordance de réseau. Nous avons rapporté la PCE de ~1,43% avec le FF de ~0,72 sur les dispositifs basés à bicouches minces sous un soleil, qui est plus élevée que tout PCE jamais rapporté dans les couches minces individuelles BFO ou BMO. Nous avons décrit que le champ électrique interne induit par la polarisation FE joue un rôle crucial pour améliorer la PCE. Cependant, l'optimisation de l'épaisseur de chaque couche et le mélange possible de couches interfaciales pourraient être un sujet intéressant en termes d'obtention d'une absorption élevée de la lumière solaire.

Dans le chapitre 4, nous avons rapporté la PCE de ~4,20% sous un soleil pour la première fois dans des couches composites Bi-Mn-O comprenant des phases cristallines BMO et  $\text{BiMn}_2\text{O}_5$ . Les

couches ont été développées sur un substrat de NSTO orienté (111) par PLD. Les deux phases des couches ont été caractérisées par un ensemble d'outils de caractérisation comprenant la MET, la spectroscopie Raman, l'AFM, la microscopie à force piézoélectrique (PFM), la KPFM, l'ellipsométrie et le simulateur d'énergie solaire. Les résultats ont montré que les GBs jouent un rôle crucial pour les générations de photocellules et ont ainsi décrit les résultats PV avec des potentiels de barrière GB. Nos résultats peuvent fournir une nouvelle voie fondamentalement pour améliorer la PCE dans les dispositifs PV à base des couches minces pérovskites.

Dans le chapitre 5, nous avons démontré les propriétés photoélectrochimiques (PEC) des couches minces et des nanostructures de BMO croissantes sur des substrats NSTO (111) par PLD. Les couches minces montrent une densité de photocourant ( $\sim 40 \mu\text{A}/\text{cm}^2$  à 1,2 V vs Ag/AgCl) d'environ quatre fois plus élevée sous deux soleils par opposition et un seul soleil. Les nanostructures montrent la plus élevée la densité de photocourant ( $\sim 0,9 \text{ mA}/\text{cm}^2$  à 1,2 V vs Ag/AgCl) par rapport à TF-BMO ( $\sim 10 \mu\text{A}/\text{cm}^2$  à 0,4 V vs Ag/AgCl) sous un soleil. Selon l'alignement de la bande par rapport au potentiel redox de l'eau, nous avons démontré que les couches minces et les nanostructures étaient appropriées pour l'évolution de l'oxygène. Les résultats montrent un grand potentiel pour le développement d'oxydes inorganiques en tant qu'absorbeurs de lumière et de composants stables pour la conversion de l'énergie solaire en  $\text{O}_2/\text{H}_2$ , ce qui ouvrira la voie au développement de nouveaux types de matériaux des photoélectrodes efficaces.